



Aerospace and Mechanical Engineering Department
Space Structures and Systems Laboratory

SATELLITE ORBITS IN THE ATMOSPHERE: UNCERTAINTY QUANTIFICATION, PROPAGATION AND OPTIMAL CONTROL

Thesis submitted in fulfilment of the requirements for the degree of
Doctor in Engineering Sciences

by

Lamberto DELL'ELCE, Ir.
Research fellow of the F.R.S. – FNRS

February 2015

Author's contact details

Lamberto DELL'ELCE

Space Structures and Systems Laboratory
Aerospace and Mechanical Engineering Department
University of Liège

1, Chemin des chevreuils
4000 Liège, Belgium

Email: lamberto.dellelce@ulg.ac.be
Phone: +32 4 3669449

Members of the Examination Committee

Prof. Olivier BRÜLS (President of the Committee)
University of Liège (Liège, BE)
Email: o.bruls@ulg.ac.be

Prof. Gaëtan KERSCHEN (Advisor)
University of Liège (Liège, BE)
Email: g.kerschen@ulg.ac.be

Prof. Maarten ARNST
University of Liège (Liège, BE)

Prof. Pini GURFIL
Technion – Israel Institute of Technology (Haifa, IL)

Prof. Heiner KLINKRAD
Technical University of Braunschweig (Braunschweig, D)

Prof. Thierry MAGIN
Von Karman Institute for Fluid Dynamics (Brussels, BE)

Prof. Pierre ROCHUS
University of Liège (Liège, BE)

Prof. Daniel J. SCHEERES
University of Colorado Boulder (Boulder, CO)

Abstract

From the massive international space station to nanosatellites, all space missions share a common principle: orbiting an object requires energy. The greater the satellite's mass, the higher the launch cost. In astrodynamics, this translates into the motto “use whatever you can”. This concept encompasses a broad spectrum of missions, e.g., Earth’s oblateness is exploited for sun-synchronous orbits and the kinetic energy of a planet is used to accomplish fly-by maneuvers. Nowadays, the same paradigm is coming on stream in the context of distributed space systems, where complex missions are envisaged by splitting the workload of a single satellite into multiple agents. Orbital perturbations – often regarded as disturbances – can be turned into an opportunity to control the relative motion of the agents in order to reduce or even remove the need for on-board propellant.

This thesis combines uncertainty quantification, analytical propagation, and optimal control of satellite trajectories in the atmosphere to effectively and robustly exploit the aerodynamic force. Specifically, by means of a probabilistic estimation and prediction of the aerodynamic force and an efficient and consistent propagation of low-Earth orbits, a robust reference trajectory for the realization of relative maneuvers between two satellites in a realistic environment can be generated.

The main contributions of the dissertation consist of: a probabilistic modeling and inference of satellite aerodynamics with applications to orbit propagation and lifetime assessment; an analytical solution of satellite motion in the atmosphere of an oblate planet; a novel methodology for trajectory planning of uncertain dynamical system and its application to propellantless orbital rendez-vous using differential drag.

Acknowledgements

The first person I want to acknowledge is my advisor, Prof. Gaetan Kerschen who believed in me since the very beginning and gave me the opportunity to accomplish this PhD in a highly qualified and friendly environment. I thank you for your invaluable advices and ideas, for being an exemplary leader and motivator, for your ceaseless enthusiasm for my research, and for being always available and willing to help me.

I am grateful to Professors Olivier Brüls, Maarten Arnst, Pini Gurfil, Heiner Klinkrad, Thierry Magin, Pierre Rochus, and Daniel Scheeres, who kindly accepted to serve on my examination committee.

I am thankful to Prof. Pini Gurfil for your warm hospitality during my research period at the Technion and for introducing me to your talented team. These two months were a marvelous scientific and cultural experience I will never forget.

I am grateful to Prof. Thierry Magin for giving me the opportunity to participate to the ESA project UQ4AERO and for inviting me to join VKI as a collaborative PhD student.

I acknowledge Dr Vladimir Martinusi for the fundamental contribution to Chapter 4. I am thankful to you not only for our precious professional collaboration, but also for being a good friend for making everyday life in the office amusing.

A special thanks is for my family, especially my mother, for continuously supporting me during these years abroad.

Finally I thank Jessica. You always support me and motivate me with love and you accept all my decisions, even if they cause us to live far away for long periods.

Contents

Introduction	1
Challenges	2
Outline of the dissertation	3
1 Satellite Mechanics in Low-Earth Orbits	7
1.1 Introduction	8
1.2 The inertial motion	8
1.3 Coordinates and reference frames	10
1.4 The relative motion	13
1.5 Aerodynamic force modeling	14
1.5.1 Atmospheric density	14
1.5.2 True airspeed	16
1.5.3 Aerodynamic coefficient	17
1.6 High-fidelity orbital propagation	19
1.7 The QB50 and QARMAN missions	21
1.8 Conclusion	22
2 Uncertainty Quantification of Satellite Drag	23
2.1 Introduction	24
2.2 Modeling assumptions and uncertainty source identification	27
2.3 Stochastic methods for uncertainty characterization	28
2.3.1 Maximum likelihood estimation	29
2.3.2 Maximum entropy	30
2.4 Uncertainty characterization of initial conditions	31
2.5 Uncertainty characterization of atmospheric drag	34
2.5.1 Atmospheric model	35
2.5.2 Ballistic Coefficient	43
2.6 Uncertainty propagation via Monte Carlo	45
2.7 Stochastic sensitivity analysis	48
2.8 Conclusion	49
3 Aerodynamic Force Estimation	51
3.1 Introduction	52
3.2 Particle filtering for mixed parameter and state estimation	53
3.3 Non-gravitational force estimation	58

3.3.1	States and parameters	58
3.3.2	Proposal and prior distributions	60
3.3.3	Measurement model	60
3.3.4	Recommendations for the choice of filter's parameters	61
3.4	High-fidelity simulations	63
3.5	Conclusion	67
4	Analytical Propagation of Low-Earth Orbits	69
4.1	Introduction	70
4.2	Variational method and averaging	72
4.3	Analytical solution for the absolute motion	75
4.3.1	The case of small eccentricity ($e^4 \simeq 0$)	76
4.3.2	The case of very small eccentricity ($\bar{e}^2 \simeq 0$)	79
4.4	Analytical solution for the relative motion	81
4.5	Validation of the analytical propagator	82
4.5.1	Inertial motion	83
4.5.2	Relative motion	86
4.6	Conclusion	88
5	Differential Drag: an Optimal Control Approach	89
5.1	Introduction	90
5.2	Modeling assumptions	92
5.3	Optimal maneuvers using differential drag	93
5.3.1	Drag estimator	94
5.3.2	Maneuver planner	95
5.3.3	On-line compensator	99
5.4	Rendez-vous between two satellites of the QB50 constellation	100
5.4.1	Drag estimator	103
5.4.2	Maneuver planner	104
5.4.3	On-line compensator	105
5.5	Conclusion	108
6	Robust Maneuver Planning	111
6.1	Introduction	112
6.2	Robust maneuver planning	114
6.2.1	The robust deterministic trajectory	114
6.2.2	Inclusion of the tracking error	118
6.3	Discretization of the problem	119
6.3.1	Semi-infinite formulation	120
6.3.2	Discrete formulation	123
6.4	Step-by-step implementation	126
6.4.1	Flat formulation	127
6.4.2	Choice of the polynomial basis	128
6.4.3	Discretization of the path constraints	129
6.4.4	Solution of the problem	129
6.5	Orbital rendez-vous using differential drag	131

6.5.1	Flat formulation	134
6.5.2	Choice of the polynomial basis	135
6.5.3	Discretization of the path constraints	135
6.5.4	Results	135
6.6	Conclusion	141
Conclusions		141
	Contributions	143
	Perspectives	144
A Maximum Entropy: a Numerical Approach		147
B Linearized equations of motion		151
C QARMAN		159

List of Figures

1	Outcome of each chapter together with the considered analytical and numerical methods (in italics)	4
1.1	Order of magnitude of the perturbations in LEO. Non-gravitational perturbations assume cross-section-to-mass ratio equal to $5 \cdot 10^{-3} \frac{\text{m}^2}{\text{kg}}$. The reflectivity coefficient ranges from 1 to 2. Atmospheric density is computed with the Jacchia 71 model with extreme (min-max) solar and geomagnetic activity.	9
1.2	Reference frames used in the thesis. Purple denotes the ECI frame. Red denotes the perifocal frame. Blue denotes the LVLH frame. Green denotes the body frame (of the deputy).	11
1.3	Curvilinear relative states.	14
1.4	Structure of the atmosphere.	15
1.5	Vertical structure of the atmosphere: density number and mass concentration of the species. NRLMSISE-00 averaged over the latitude and longitude on January the 1 st 2013 00:00 UTC, $F_{10.7} = \bar{F}_{10.7} = 150$ sfu, $K_p = 4$	16
1.6	Physical principles of gas-surface interaction in free molecular flow. .	18
1.7	Our MATLAB propagator.	20
1.8	QARMAN's mission timeline. DiffDrag, AeroSDS, and Reentry correspond to the differential drag, aerodynamic stability and deorbiting, and reentry phases, respectively.	21
1.9	Architecture of QARMAN.	22
2.1	Proposed uncertainty quantification approach.	26
2.2	Schematic representation of uncertainty quantification of orbital lifetime in LEO. White box: deterministic modeling, gray box: stochastic modeling, black box: unmodeled dynamics.	28
2.3	Error on the orbital lifetime in the nominal case in function of the order of the gravity model.	29
2.4	probability density function (PDF) of the initial altitude and eccentricity before deployment (maximum entropy principle).	33
2.5	Observed daily solar activity.	37
2.6	Marginal distributions of the geomagnetic and solar activity proxies (identified with maximum likelihood).	38
2.7	Correlation matrix of the Gaussian copula used to model the solar and geomagnetic proxies. Axes labels denote elapsed days.	39
2.8	Solar flux trajectories. The red curve are observed data. The blue curve is generated with the Gaussian copula.	40

2.9	PDF of the model correction factor of the temperature in function of the external temperature (maximum entropy principle).	42
2.10	Convergence of the mean of the orbital lifetime. The shaded area indicates $3 - \sigma$ confidence bounds on the mean.	46
2.11	Kernel density estimations of the PDF and CCDF of the orbital lifetime.	47
3.1	Algorithm for the recursive estimation of states and parameters. At every time step, this loop is repeated for the n particles.	56
3.2	Comparison between the mean equinoctial elements \bar{a} and \bar{P}_1 computed with the first-order Brouwer model and with a Gaussian quadrature. The input parameters are listed in Table 3.2 but the aerodynamic force and solar radiation pressure (SRP) are turned off.	61
3.3	Autocorrelation of the process noise of averaged elements using the analytical propagator.	63
3.4	Non-gravitational force estimation assuming constant space weather proxies in the simulations. The red-dashed curve is the norm of the true non-gravitational force. The blue-solid curve is its median estimate. The shaded region depicts 90% confidence bounds.	64
3.5	Convergence of the parameters for the estimation of drag and SRP. .	65
3.6	Results at 600km altitude. The other simulation parameters are listed in Table 3.2. In the top plot: the red-dashed curve is the norm of the true non-gravitational force, the blue-solid curve is its median estimate, and the shaded region depicts 90% confidence bounds.	66
4.1	Proposed orbit propagation.	83
4.2	Numerical simulations for the absolute motion. The blue-solid curves depict the error of our analytical propagator. The red-dashed curves are the error made by neglecting drag.	85
4.3	Comparison of the drift of our propagator when the simulation environment accounts for or neglects the atmospheric drag. The black line is the median of the Monte Carlo samples. The grey region indicates 90% confidence bounds.	86
4.4	Numerical simulations for the relative motion. The blue-solid curves depict the relative distance estimated by our analytical propagator. The red-dashed curves – essentially superimposed – are the true relative distance. The norm of the position error is depicted in the bottom plots.	87
5.1	Nominal attitude of deputy (left) and chief (right).	92
5.2	High-level optimal control strategy. The asterisk denotes the reference trajectory and control.	93
5.3	Schematic representation of the estimation of the ballistic coefficient.	95
5.4	Drag force of the chief. The solid line is the real drag. The dashed line is the estimated drag with the simple atmospheric model. The dash-dot line is the estimated drag with the Jacchia 71 model.	103
5.5	Minimum-differential-drag off-line (i.e., scheduled) maneuver. In the upper figure, the color indicates the elapsed time since the beginning of the maneuver, including the drag estimation time. The trajectory is illustrated with relative curvilinear states (defined in Section 1.4). .	104

5.6	'Flattest trajectory' off-line maneuver (i.e., scheduled). In the upper figure, the color indicates the elapsed time since the beginning of the maneuver, including the drag estimation time. The trajectory is illustrated with relative curvilinear states (defined in Section 1.4).	105
5.7	Minimum-differential-drag on-line maneuver. In the upper figure, the black-dotted and the colored line are the planned and the on-line trajectories, respectively. The color indicates the elapsed time since the beginning of the maneuver, including the drag estimation time. In the bottom figure, the dashed and the solid lines are the scheduled and the on-line pitch angles, respectively. The trajectory is illustrated with relative curvilinear states (defined in Section 1.4).	106
5.8	Minimum-differential-drag on-line maneuver. Zoom of the terminal phase. The black-dotted and the colored line are the planned and the on-line trajectories, respectively. The color indicates the time since the beginning of the maneuver.	107
5.9	Minimum-differential-drag on-line maneuver without tracking of the reference pitch angle. In the upper figure, the black-dotted and the colored line are the planned and the on-line trajectories, respectively. The color indicates the elapsed time since the beginning of the maneuver, including the drag estimation time. In the bottom figure, the dashed and the solid lines are the scheduled and the on-line pitch angles, respectively.	107
5.10	'Flattest trajectory' maneuver. In the upper figure, the black-dotted and the colored line are the planned and the on-line trajectories, respectively. The color indicates the elapsed time since the beginning of the maneuver, including the drag estimation time. In the bottom figure, the dashed and the solid lines are the scheduled and the on-line pitch angles, respectively. The trajectory is illustrated with relative curvilinear states (defined in Section 1.4).	108
6.1	Conceptual difference between the existing and the proposed approaches to robust maneuver planning.	113
6.2	Schematic representation of the sets. From the lightest to the darkest, the gray regions indicate the feasible sets of Problems (6.1), (6.12), (6.27), and (6.29), respectively. The notation $\mathcal{I}(\Delta)$ is used to indicate $\bigcap_{\delta \in \Delta} \mathcal{I}(\delta)$.	117
6.3	Theoretical framework of the proposed methodology.	120
6.4	Notation of the car steering example.	126
6.5	Steering a car. Inner approximation of the feasible set. The dark and light grey regions are related to the maximum and minimum samples of the drag coefficient, respectively. The dashed lines are the hidden edges of the light-grey regions.	130
6.6	Steering a car. Solution of the chance constrained optimization problem.	132
6.7	Steering a car. Influence of the risk parameter on the performance index.	133
6.8	Differential drag bounds. The colored region is the envelop of the samples required by the scenario approach. Solid red lines are the worst case of these samples.	136
6.9	Scheduled reference trajectory in curvilinear coordinates.	137

6.10	Planned differential drag. The red and blue curves depict the robust and nominal feasible regions. The black curve in the first and second plots depicts the differential drag required to accomplish the robust and nominal trajectory, respectively. The third plot superimposes the robust bounds to the planned differential drag in the nominal case. 138
6.11	Satisfaction of the rendez-vous conditions. From the lighter to the darker, the colored regions indicate 90%, 50%, and 10% confidence bounds. Red regions refer to the robust trajectory. The blue regions are related to the nominal one.	138
6.12	Probability density distribution of the root mean square distance between planned and on-line trajectory. Red and blue are related to the tracking of the robust and of the nominal reference path, respectively.	139
6.13	Comparison between the reference trajectories and the Monte Carlo samples. The colored regions indicate 99% confidence bounds on the trajectory of the samples. The tracking of the reference path is better with the robust reference path.	140
1	Contributions of the thesis.	143
A.1	Numerical implementation of the maximum entropy principle.	149
C.1	cumulative distribution function (CDF) of the root-mean-squared distance between the reference and the executed trajectories.	160
C.2	Satisfaction of the rendez-vous conditions. From the lighter to the darker, the shaded regions indicate 90%, 50%, and 10% confidence regions.	160
C.3	Median (blue) and 90% confidence bounds (red) of the satisfaction of the rendez-vous conditions when additional time is added after the planned maneuvering time.	161

List of Tables

1.1	Sources of variation of the atmospheric density.	15
2.1	Nominal parameters for the simulations.	26
2.2	Global biases and standard deviations of the model correction factors of the outputs of NRLMSISE-00 for all levels of geomagnetic activity and an altitude range of [200, 400]km.	42
2.3	Errors between the analytic and DSMC-based numerical predictions for the ballistic coefficient. Full accommodation of the energy is considered for both the analytical and the numerical approaches.	44
2.4	Summary of uncertainty characterization.	46
2.5	Total effect Sobol indices of the orbital lifetime. Only the indices above 0.01 are listed.	49
3.1	Influence of the filter's parameters on the quality of the estimation. .	62
3.2	Simulation parameters.	67
4.1	Input parameters for the simulations of the absolute motion. The same inputs are used for the chief in the simulations of the relative motion.	84
4.2	Input parameters for the deputy.	86
5.1	Simulation parameters.	101
5.2	Differences between the simulation environment and the plant of the controller.	102
6.1	Steering a car. Simulation parameters.	127
6.2	Initial space weather proxies.	136

Abbreviations and acronyms

AoP	argument of perigee
CCDF	complementary cumulative distribution function
CDF	cumulative distribution function
DMC	dynamic model compensation
DoF	degree-of-freedom
DSMC	direct simulation Monte Carlo
ECI	Earth-centered inertial
EoM	Equations of Motion
ESA	European Space Agency
GMM	Gaussian mixture Model
GPS	global positioning system
GVE	Gauss variational equations
HMM	hidden Markov model
IADC	Inter-Agency Space Debris Coordination Committee
IoD	in-orbit demonstration
IVP	initial value problem
LEO	low-Earth orbits
LMI	linear matrix inequalities
LVLH	local-vertical-local-horizontal
MC	Monte Carlo
MLE	maximum likelihood estimation
MPC	model predictive control
NRL	Naval Research Laboratory
NLP	non-linear programming
OoM	order of magnitude

PCE	polynomial chaos expansion
PDF	probability density function
PSD	power spectral density
RAAN	right ascension of the ascending node
ROE	relative orbital elements
SMC	sequential Monte Carlo
SRP	solar radiation pressure
SSA	space situational awareness
STK	Systems Tool Kit
TAS	true airspeed
TLE	two-line elements
ToD	true of date
TPBVP	two-point boundary value problem
ULg	University of Liège
UQ	uncertainty quantification
VKI	Von Karman Institute for Fluid Dynamics
VoI	variable of interest
VoP	variation of parameters

Introduction

From the massive international space station to nanosatellites, all space missions share a common principle: orbiting an object requires energy. The greater the satellite's mass, the higher the launch cost. In astrodynamics, this translates into the motto “use whatever you can”. This concept encompasses a broad spectrum of missions, e.g., the Earth’s oblateness is exploited for sun-synchronous orbits, the kinetic energy of a planet is used to accomplish fly-by maneuvers, and the stability of Lagrangian points enables low-cost trips to the Moon. Nowadays, the same paradigm is coming on stream in the context of distributed space systems, where complex missions are envisaged by splitting the workload of a single satellite into multiple agents. Orbital perturbations – often regarded as disturbances – can be turned into an opportunity to control the relative motion of the agents in order to reduce or even remove the need for on-board propellant.

For low-Earth orbits (LEO), the residual atmosphere is responsible for a monotonic dissipation of the satellite’s energy, resulting in a slow but continuous “fall” toward the Earth’s surface. Exploiting the residual aerodynamic force is not a recent idea, see, e.g., natural-decay-based deorbiting strategies [Petro, 1992, Roberts and Harkness, 2007] or drag-assisted relative maneuvers [Leonard et al., 1989]. Although these concepts date back to a couple of decades, their practical realization is still largely unexplored. The reason is that, owing to outstanding challenges in satellite aerodynamics modeling and estimation, e.g., lack of knowledge and experimental data on gas-surface interaction principle, uncertainties in attitude determination, and stochastic dynamics of the upper atmosphere, *a deterministic assessment of satellite trajectories in the atmosphere is likely to be bound to considerable errors*. This is not only true for long-term propagations, for which the uncertainty in the aforementioned monotonic energy dissipation cumulates in time, but it is also a major concern for short-term – read few days – high-fidelity predictions. For example, on October the 21st 2013 European Space Agency (ESA) announced that the satellite GOCE was expected to re-enter in about two weeks¹. Eventually, because of uncertainties due to attitude control limitations, re-entry occurred on November the 11th, which represents a 30% error in a twenty-day-long estimation.

This thesis addresses different issues related to uncertainty characterization, efficient propagation, and robust control of satellite trajectories in the atmosphere. The

¹http://www.esa.int/For_Media/Press_Releases/ESA_s_GOCE_mission_comes_to_an_end.

proposed methodologies are used for developing a propellantless technique based on the differential drag concept. By controlling the surface exposed to the residual atmosphere, it is possible to change the magnitude of the atmospheric drag and therefore to create a differential force, between one spacecraft (the deputy) and either another spacecraft (the chief) or a desired target point. This force can be exploited to control the relative position between the deputy and the target in the orbital plane, which enhances the maneuverability of small satellites in LEO.

Three main questions are addressed in the thesis:

- how can we *characterize the uncertainty sources* affecting the evolution of satellite orbits in the atmosphere by using physical considerations and available experimental data?
- how can we *efficiently propagate* the trajectory of a satellite in the atmosphere?
- how can we *exploit the aerodynamic force* for accomplishing complex propellantless maneuvers?

Challenges

In order to answer these questions, we have to tackle several important challenges.

Dominant sources of parametric uncertainties and modeling errors in aerodynamic force estimation include atmospheric properties, physical properties of the satellite, and gas-surface interaction in free molecular flow. The uncertainty quantification (UQ) of satellite trajectories is highly dependent on the characterization of these uncertainties. For this reason, the probabilistic model of the sources should be inferred only from experimental data and available information. In addition, the model must be consistent with mechanical modeling considerations.

Targeting efficient but physically meaningful orbital propagation requires that all dominants effects are modeled. In LEO this includes the perturbations due both to the Earth's oblateness and the atmosphere. Their combined effect causes the orbit to dramatically drift from the Keplerian unperturbed model. While the oblateness perturbation falls in the range of conservative forces, allowing the classical perturbation methods to be applied, this is not the case for the atmospheric force, which is non-conservative. For this reason, using the tools of analytical mechanics to accomplish analytical propagation in LEO is, at best, challenging.

The realization of orbital maneuvers relies on a broad spectrum of propulsive means ranging from impulsions to low thrust. This latter is aimed at accomplishing the maneuver by means of the integral effect of a continuous – but very small – control force, which results in long-period control arcs during the maneuver. Targeting the optimization of the available resources, an adequate planning of the whole maneuver is generally envisaged before its realization. The exploitation of drag as a control force falls into this category. In this case, planning the maneuvers is challenging because the control force is uncertain. Existing approaches for robust

maneuver planning lead to a deterministic control action associated to a probabilistic description of the reference path. When the dynamics of the system is extremely sensitive to the outcome of the uncertain environment, as it is the case for drag-assisted maneuvers, the confidence bounds of the trajectory might be too large to make it of practical interest.

Outline of the dissertation

The outline of the thesis is presented in Figure 1.

Chapter 1 opens with preliminaries on orbital dynamics in LEO with a special focus on satellite aerodynamics modeling. The coordinates and reference frames used in the thesis are also detailed. The QB50 and QARMAN missions, which serve as case study in the other chapters, are introduced.

Chapter 2 proposes an UQ study of LEO trajectories. In view of the stochastic nature of the thermosphere and of the complexity of drag modeling, a deterministic assessment of LEO trajectories is likely to be bound to failure. Uncertainties in the initial state of the satellite and in the atmospheric drag force, as well as uncertainties introduced by modeling limitations associated with atmospheric density models, are considered. Firstly, a probabilistic model of these variables is inferred from experimental data and atmospheric density models by means of mathematical statistics methods like maximum likelihood estimation and maximum entropy. Secondly, this probabilistic characterization of inputs is mapped through orbital propagation into a probabilistic characterization of the variable of interest (VoI), e.g., trajectory, lifetime, or position at the end of a maneuver; this can be achieved in several ways, which include Monte Carlo simulation and stochastic expansion methods such as those based on polynomial chaos. Lastly, the probabilistic model thus obtained is used to gain insight into the impact that the input uncertainties have on the VoI, for example, by carrying out stochastic sensitivity analyses. The developments are exploited for the lifetime estimation of a nanosatellite. The same characterization of the uncertainty sources also proves useful in Chapters 3 and 6.

Chapter 3 discusses the recursive estimation and prediction of non-gravitational forces. For this purpose, a particle filter is developed. The generation of the proposal distributions for the particles relies on the developments of Chapter 2. Slow-dynamics parameters are used to build a model for the non-gravitational forces, and they are estimated by the filter. The current estimation can be exploited for short-term predictions, i.e., of the order of few orbits. By averaging the effects of the perturbations, it is shown that the filter can accurately estimate the aerodynamic force from global positioning system (GPS) observations without using accelerometers, enhancing the general interest in the filter.

Chapter 4 offers a closed-form solution for the motion of a satellite about an oblate planet with a uniform atmosphere. Specifically, osculating orbital elements are projected into their mean counterparts by means of a Brouwer-Lyddane contact transformation. Assuming that the orbit is near-circular, i.e., the fourth power of

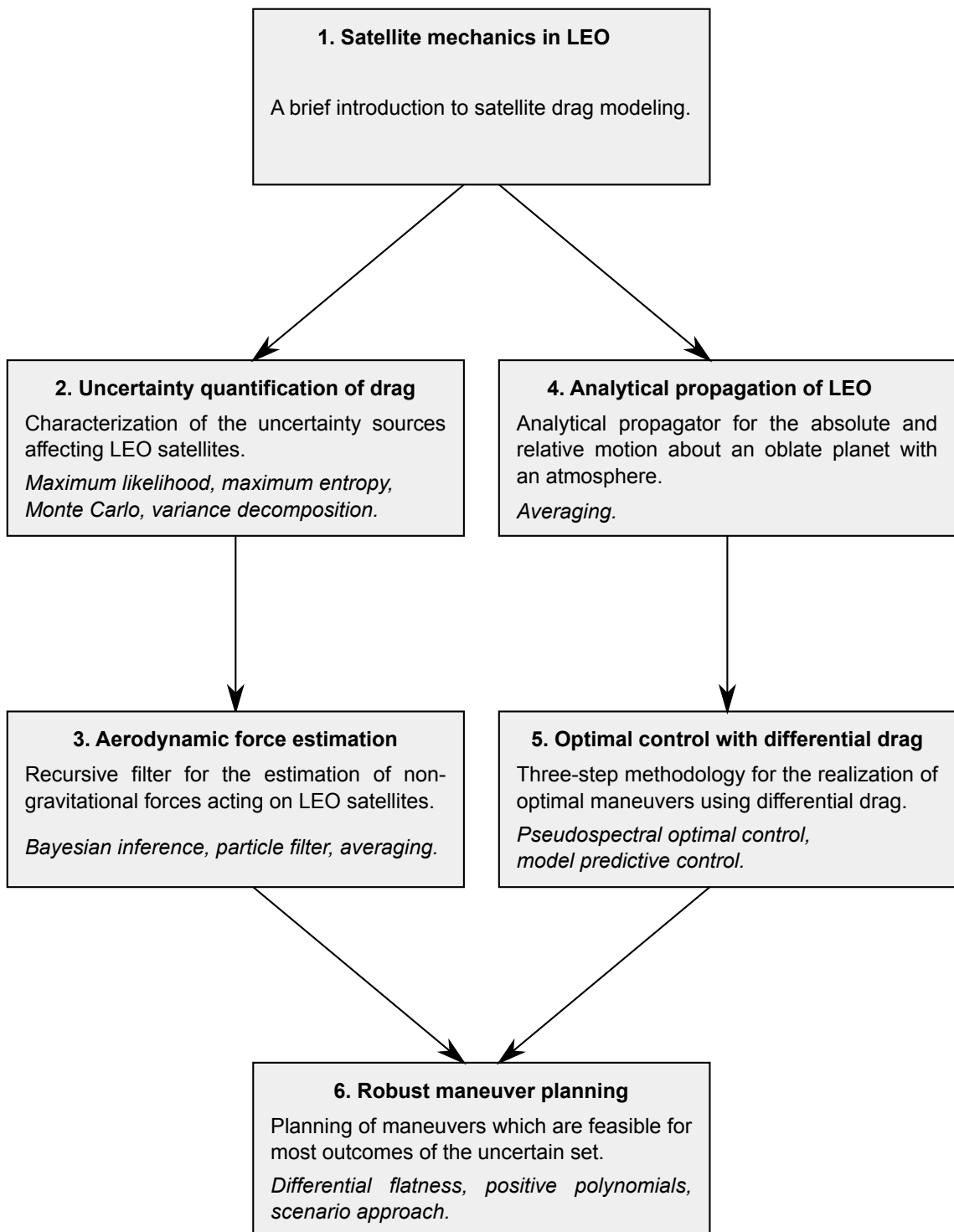


Figure 1: Outcome of each chapter together with the considered analytical and numerical methods (in italics)

the eccentricity is neglected, a time-explicit solution of the averaged equations of motion is derived. Finally, without further assumptions, a closed-form solution for the relative dynamics is also achieved by using simple tensorial transformations. The analytical predictions are validated against numerical simulations.

Chapter 5 is devoted to the exploitation of the aerodynamic force for differential-drag-based maneuvers. A three-step optimal control approach to the problem is proposed. At first, the inertial position of the chief and the deputy are observed to deduce their ballistic properties. An optimal maneuver is then planned by means of a pseudo-spectral transcription of the optimal control problem. The method is flexible in terms of cost function and can easily account for constraints of various nature. Finally, the on-line tracking of the reference trajectory is achieved by means of model predictive control (MPC). These developments are illustrated using high-fidelity simulations including a coupled 6-degree-of-freedom model with advanced aerodynamics.

Chapter 6 bridges the gap between Chapters 2, 3, 4, and 5 to offer a general-purpose methodology for the maneuver planning of dynamical systems in the presence of uncertainties. After introducing the novel concept of *robust deterministic trajectory* as the solution of an infinite-dimensional optimization problem, sufficient conditions for its existence are outlined. For this purpose, the notion of differential flatness is used. Then, a discretization of the infinite-dimensional problem guaranteeing the feasibility of the trajectory over an arbitrary user-defined portion of the uncertain set is proposed. Taking advantage of the formalism of squared functional systems and of the scenario approach, the methodology does not require a temporal grid and is able to include uncertainty sources of various nature. The usefulness of the proposed methodology is demonstrated in the framework of differential-drag-based maneuvers.

A discussion on the achievements of this work closes the thesis. Limitations and perspectives for future research are also discussed.

Chapter 1

Satellite Mechanics in Low-Earth Orbits

Abstract

LEO is arguably the most perturbed dynamical environment for satellites in geocentric orbits. Specifically, perturbations due to the Earth's oblateness and residual atmosphere dominate satellite dynamics below 600 km. This chapter provides an introduction to orbital dynamics in LEO and describes the coordinates and reference frames used in the thesis. The physical principles governing satellite aerodynamics and the resulting mathematical models are outlined. This survey encompasses the structure of the upper atmosphere and gas-surface interaction principles in free molecular flow, and it serves as a foretaste of the challenges related to drag modeling and estimation encountered in the thesis.

1.1 Introduction

The region ranging from the Earth's surface up to 2000 km altitude is referred to as LEO. Because of its privileged position, e.g., for global monitoring, telecommunications, and astronomical observations, and because of the relatively low cost for the launch (compared to any other space mission), most existing satellites are orbiting in this region. However, LEO is also the most perturbed dynamical environment for satellites in geocentric orbits.

Perturbations due to the Earth's oblateness and residual atmosphere strongly affect satellite dynamics below 600 km. If the accurate assessment of the effects of non-spherical harmonics is possible thanks to the gravitational maps provided by the GOCE and GRACE missions, long-term aerodynamic prediction is, at best, challenging owing to complex physical phenomena governing gas-surface interaction mechanisms and the dynamical behavior of the upper atmosphere.

This chapter offers an introduction to orbital dynamics in LEO. The physical principles governing satellite aerodynamics and the resulting mathematical models are outlined. This survey encompasses the structure of the upper atmosphere and gas-surface interaction principles in free molecular flow, and it serves as a foretaste of the challenges about drag modeling and estimation encountered in the thesis.

The chapter is organized as follows. Section 1.2 introduces the perturbed Kepler problem. The coordinates and reference frames used in the thesis are defined in Section 1.3. The equations governing the relative motion are detailed in Section 1.4. An overview of satellite aerodynamics modeling is proposed in Section 1.5. Section 1.6 describes the high-fidelity computational environment exploited in this thesis to carry out numerical simulations. Finally, Section 1.7 introduces the QARMAN CubeSat and the QB50 mission, which serve as case studies in the thesis.

1.2 The inertial motion

The initial value problem (IVP) governing the motion of the inertial position, \mathbf{r} , of a non-propelled satellite in LEO, is:

$$\begin{aligned} \ddot{\mathbf{r}} + \frac{\mu}{r^3} \mathbf{r} &= \mathbf{f}_p(\mathbf{r}, \dot{\mathbf{r}}, t), \\ \mathbf{r}(t_0) &= \mathbf{r}_0, \\ \dot{\mathbf{r}}(t_0) &= \dot{\mathbf{r}}_0, \end{aligned} \tag{1.1}$$

where μ , \mathbf{r}_0 , $\dot{\mathbf{r}}_0$, and \mathbf{f}_p denote the Earth's gravitational parameter, the inertial position and velocity at the initial time t_0 , and the perturbing specific force, respectively. The dot indicates the derivative with respect to the time variable $t \geq t_0$.

Targeting accurate orbital prediction in LEO, the perturbing force has to accommodate the effects of the non-spherical gravitational field, residual atmosphere, solar radiation pressure, and third-body perturbations of Sun and Moon. In addition, general relativity, albedo, and tidal effects may also be relevant for very

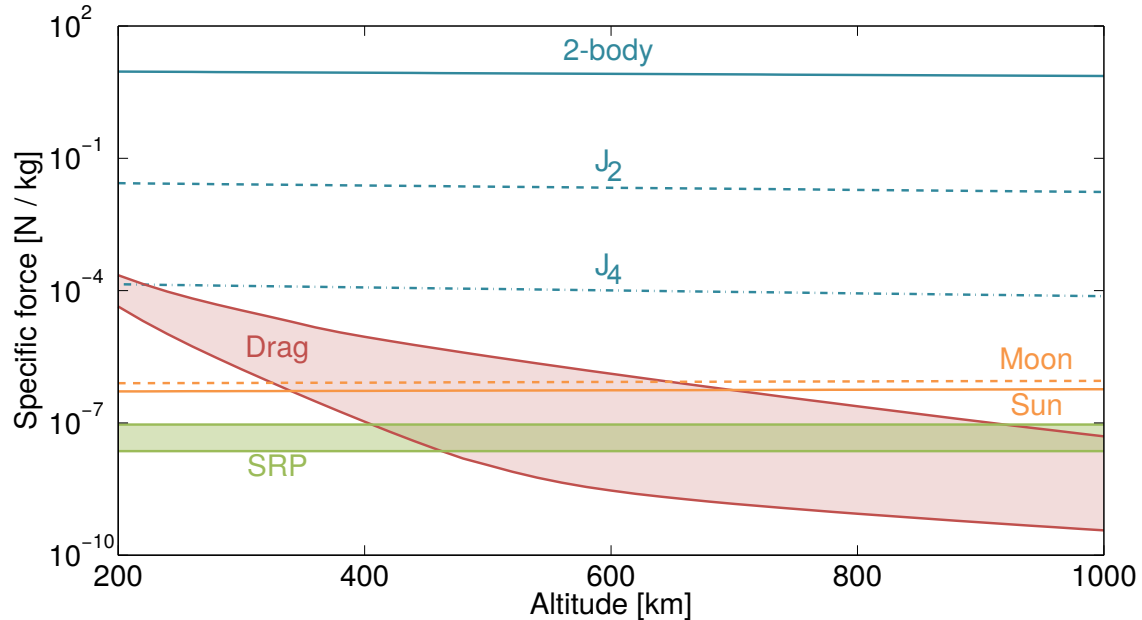


Figure 1.1: Order of magnitude of the perturbations in LEO. Non-gravitational perturbations assume cross-section-to-mass ratio equal to $5 \cdot 10^{-3} \frac{\text{m}^2}{\text{kg}}$. The reflectivity coefficient ranges from 1 to 2. Atmospheric density is computed with the Jacchia 71 model with extreme (min-max) solar and geomagnetic activity.

accurate predictions. In particular, tides could be evident for very long-term propagations due to tidal friction. Perturbations of the polar axis, i.e., precession, nutation, and polar wandering, need to be considered as well¹. Their modeling is discussed in [Montenbruck and Gill, 2000, Vallado, 2001]. Figure 1.1 illustrates the order of magnitude (OoM) of the perturbations in LEO emphasizing the variability of non-gravitational forces. Beyond the OoM, we stress that the way perturbations act is crucial for the long-term evolution of the orbit, i.e., *secular effects*. For example, aerodynamic drag provides a continuous dissipation of the energy resulting in a monotonic decrease of the semi-major axis and circularization of the orbit.

The unperturbed problem associated to Equation (1.1), i.e., when $\mathbf{f}_p = \mathbf{0}$, is Kepler's problem, which has the classic first integrals:

$$\begin{aligned}\mathbf{h} &= \mathbf{r} \times \dot{\mathbf{r}}, \\ \mathbf{e} &= \frac{1}{\mu} \dot{\mathbf{r}} \times \mathbf{h} - \hat{\mathbf{r}}, \\ \epsilon &= \frac{1}{2} \dot{\mathbf{r}}^2 - \frac{\mu}{r},\end{aligned}\tag{1.2}$$

namely the specific angular momentum, the eccentricity vector and the specific total energy, respectively. In this thesis, the notation $\hat{\boldsymbol{\alpha}}$ denotes the unit vector in the

¹Neglecting the precession, nutation, and polar wandering results into inconsistent modeling of non-spherical gravitational effects.

direction $\boldsymbol{\alpha}$, i.e., $\hat{\boldsymbol{\alpha}} = \frac{\boldsymbol{\alpha}}{\|\boldsymbol{\alpha}\|}$.

If $\epsilon < 0$, then the unperturbed trajectory is an ellipse with eccentricity $e = \|\boldsymbol{e}\|$ and semimajor axis $a = -\frac{\mu}{2\epsilon}$. Kepler's problem is super-integrable and, indeed, only five of the aforementioned first integrals are independent.

The use of the vectorial orbital elements \boldsymbol{h} and \boldsymbol{e} together with the specific total energy \mathcal{E} to study the perturbed motion provides insight into the geometrical evolution of the orbit before solving the IVP. Such an approach is inspired by [Hestenes, 1999] and [Condurache and Martinusi, 2013].

1.3 Coordinates and reference frames

The following reference frames are used in the thesis (see Figure 1.2(a)):

Earth-centered inertial (ECI) $\{\hat{\mathbf{i}}, \hat{\mathbf{j}}, \hat{\mathbf{k}}\}$: the origin is in the center of the Earth.

The $\hat{\mathbf{i}}$ and $\hat{\mathbf{k}}$ -axis are toward the true vernal equinox and north pole at Epoch January 1st 2000 12:00 UTC, respectively; $\hat{\mathbf{j}}$ completes the right-hand frame.

true of date (ToD) $\{\hat{\mathbf{i}}_{ToD}, \hat{\mathbf{j}}_{ToD}, \hat{\mathbf{k}}_{ToD}\}$: it is analogous to the ECI but the $\hat{\mathbf{i}}_{ToD}$

and $\hat{\mathbf{k}}_{ToD}$ axes are toward the true equinox and north pole at the current epoch, respectively. This frame evolves very slowly with respect to the ECI, so that gyroscopic effects are safely neglected.

perifocal (PF) $\{\hat{\mathbf{e}}, \hat{\mathbf{p}}, \hat{\mathbf{h}}\}$: the origin is in the center of the Earth. The $\hat{\mathbf{e}}$ and $\hat{\mathbf{h}}$ -axis are toward the instantaneous eccentricity vector and angular momentum, respectively; $\hat{\mathbf{p}}$ completes the right-hand frame.

local-vertical-local-horizontal (LVLH) $\{\hat{\mathbf{r}}, \hat{\mathbf{t}}, \hat{\mathbf{h}}\}$: the origin is in the center of mass of the satellite. The $\hat{\mathbf{r}}$ and $\hat{\mathbf{h}}$ -axis are toward the instantaneous position and angular momentum, respectively; $\hat{\mathbf{t}}$ completes the right-hand frame, i.e.,

$$\hat{\mathbf{r}} = \frac{\mathbf{r}}{\|\mathbf{r}\|}, \quad \hat{\mathbf{h}} = \frac{\mathbf{r} \times \dot{\mathbf{r}}}{\|\mathbf{r} \times \dot{\mathbf{r}}\|}, \quad \hat{\mathbf{t}} = \hat{\mathbf{h}} \times \hat{\mathbf{r}}. \quad (1.3)$$

body frame $\{\hat{\mathbf{x}}_b, \hat{\mathbf{y}}_b, \hat{\mathbf{z}}_b\}$: the origin is in the center of mass of the satellite. The axes are aligned toward the principal axes of inertia of the satellite.

Beside vectorial representation, Keplerian and equinoctial elements are used to describe the state of the satellite.

Keplerian elements, $\mathcal{E} = (a, e, i, \Omega, \omega, M)$, yield an intuitive geometrical interpretation of the orbit (see Figure 1.2(b)):

- the semi-major axis, a , and the eccentricity, e , define the geometry of the orbit;

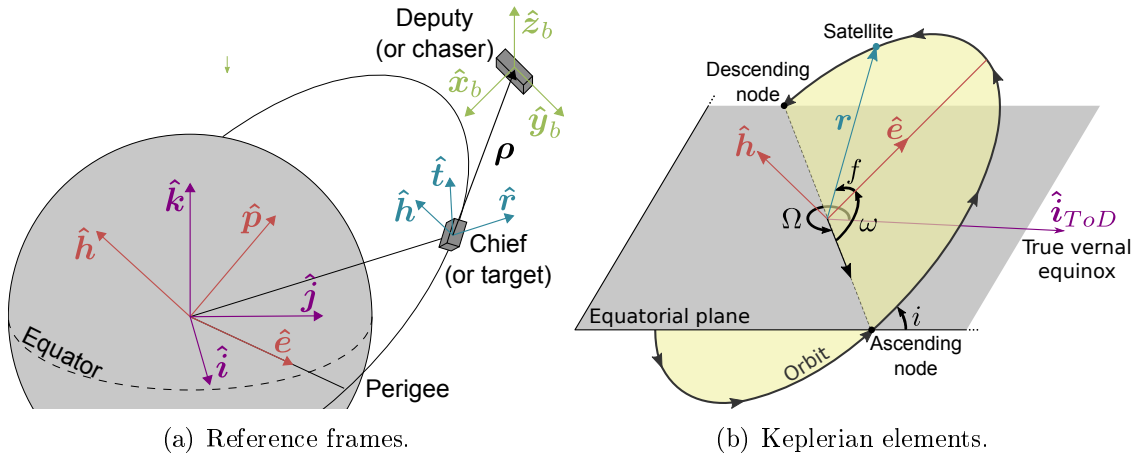


Figure 1.2: Reference frames used in the thesis. Purple denotes the ECI frame. Red denotes the perifocal frame. Blue denotes the LVLH frame. Green denotes the body frame (of the deputy).

- the inclination, i , and the right ascension of the ascending node (RAAN), Ω , locate the orbital plane in the space;
- the argument of perigee (AoP), ω , positions the orbit within its plane;
- the mean anomaly, M , locates the satellite on the orbit. Specifically, given the true anomaly, f , Kepler equation is used to compute M as follows:

$$M = E - e \sin(E), \quad (1.4)$$

where the eccentric anomaly, E , is defined as

$$\tan \frac{E}{2} = \sqrt{\frac{1-e}{1+e}} \tan \frac{f}{2}. \quad (1.5)$$

Let ${}^B\mathbf{R}_A$ denote the rotation matrix from the reference frame A to B , and define the elementary rotation matrices:

$$\begin{aligned} \mathbf{R}_1(\alpha) &= \begin{bmatrix} 1 & 0 & 0 \\ 0 & \cos \alpha & -\sin \alpha \\ 0 & \sin \alpha & \cos \alpha \end{bmatrix}; \quad \mathbf{R}_2(\alpha) = \begin{bmatrix} \cos \alpha & 0 & \sin \alpha \\ 0 & 1 & 0 \\ -\sin \alpha & 0 & \cos \alpha \end{bmatrix}; \\ \mathbf{R}_3(\alpha) &= \begin{bmatrix} \cos \alpha & -\sin \alpha & 0 \\ \sin \alpha & \cos \alpha & 0 \\ 0 & 0 & 1 \end{bmatrix}. \end{aligned} \quad (1.6)$$

The following relations hold:

$$\begin{aligned} {}^{PF}\mathbf{R}_{ToD} &= {}^{ToD}\mathbf{R}_{PF}^T = \mathbf{R}_3(\omega) \mathbf{R}_1(i) \mathbf{R}_3(\Omega), \\ {}^{LVLH}\mathbf{R}_{PF} &= {}^{PF}\mathbf{R}_{LVLH}^T = \mathbf{R}_3(f), \end{aligned} \quad (1.7)$$

We note that in this thesis the orbital elements are referred to the ToD frame.

The position and velocity vectors are given by:

$$\begin{aligned} \mathbf{r} &= \frac{a(1-e^2)}{1+e\cos f} (\cos f \hat{\mathbf{e}} + \sin f \hat{\mathbf{p}}) \\ \dot{\mathbf{r}} &= \sqrt{\frac{\mu}{a(1-e^2)}} (-\sin f \hat{\mathbf{e}} + (e+\cos f) \hat{\mathbf{p}}) \end{aligned} \quad (1.8)$$

Gauss variational equations (GVE) for the Keplerian elements are singular for circular and equatorial orbits. On the contrary, equinoctial elements [Broucke and Cefola, 1972],

$$\begin{aligned} \boldsymbol{\mathcal{E}}_{eq} = \left(a, P_1 = e \sin(\omega + \Omega), P_2 = e \cos(\omega + \Omega), Q_1 = \tan \frac{i}{2} \sin \Omega, \right. \\ \left. Q_2 = \tan \frac{i}{2} \cos \Omega, L = \omega + \Omega + f \right)^T, \end{aligned} \quad (1.9)$$

are singularity-free. GVE for the equinoctial elements are [Battin, 1999]:

$$\begin{aligned} \dot{a} &= \frac{2a^2}{h} \left[(P_2 \sin L - P_1 \cos L) f_{p,r} + \frac{p}{r} f_{p,t} \right] \\ \dot{P}_1 &= \frac{r}{h} \left[-\frac{p}{r} \cos L f_{p,r} + \left(P_1 + \left(1 + \frac{p}{r} \right) \sin L \right) f_{p,t} - P_2 (Q_1 \cos L - Q_2 \sin L) f_{p,h} \right] \\ \dot{P}_2 &= \frac{r}{h} \left[\frac{p}{r} \sin L f_{p,r} + \left(P_2 + \left(1 + \frac{p}{r} \right) \cos L \right) f_{p,t} + P_1 (Q_1 \cos L - Q_2 \sin L) f_{p,h} \right] \\ \dot{Q}_1 &= \frac{r}{2h} (1 + Q_1^2 + Q_2^2) \sin L f_{p,h} \\ \dot{Q}_2 &= \frac{r}{2h} (1 + Q_1^2 + Q_2^2) \cos L f_{p,h} \\ \dot{L} &= \frac{h}{r^2} - \frac{r}{h} (Q_1 \cos L - Q_2 \sin L) f_{p,h} \end{aligned} \quad (1.10)$$

where $p = a(1-e^2)$, $h = \|\mathbf{h}\|$, and $f_{p,r}$, $f_{p,t}$, and $f_{p,h}$ are the components of \mathbf{f}_p in the LVLH frame, respectively. In some chapters, the argument of true longitude, L , is replaced by the argument of mean longitude, $l = \omega + \Omega + M$.

The mean counterpart of Keplerian and equinoctial elements is denoted by $\bar{\boldsymbol{\mathcal{E}}}$ and $\bar{\boldsymbol{\mathcal{E}}}_{eq}$, respectively. Mean elements are computed by means of a Brouwer-Lyddane contact transformation [Schaub and Junkins, 2003].

1.4 The relative motion

Consider two satellites, a *chief* (or target) and a *deputy* (or chaser). In the following, the subscripts $(\cdot)_C$ and $(\cdot)_D$ denote anything related to the chief and the deputy, respectively. Let $\Delta\mathbf{r} = {}^{LVLH}\mathbf{R}_{ECI}(\mathbf{r}_D - \mathbf{r}_C)$ be the relative position of the deputy with respect to the chief in the LVLH frame of the chief.

Let $\boldsymbol{\omega}$ be the instantaneous velocity of the LVLH frame, and assume that the absolute motion of the chief, i.e., referred to ECI, is known. Consequently, \mathbf{r}_C and $\boldsymbol{\omega}$ are considered to be known functions of time. Let t_0 denote the initial time, and $\Delta\mathbf{r}_0$, $\Delta\dot{\mathbf{r}}_0$ denote the initial relative position and velocity vectors of the deputy with respect to the chief.

The IVP governing the relative motion is:

$$\begin{aligned} \Delta\ddot{\mathbf{r}} + 2\boldsymbol{\omega} \times \Delta\dot{\mathbf{r}} + \boldsymbol{\omega} \times (\boldsymbol{\omega} \times \Delta\mathbf{r}) + \dot{\boldsymbol{\omega}} \times \Delta\mathbf{r} &= -\mu \left(\frac{\mathbf{r}_C + \Delta\mathbf{r}}{\|\mathbf{r}_C + \Delta\mathbf{r}\|^3} - \frac{\Delta\mathbf{r}}{\|\Delta\mathbf{r}\|^3} \right) + \Delta\mathbf{f}_p, \\ \Delta\mathbf{r}(t_0) &= \Delta\mathbf{r}_0, \\ \Delta\dot{\mathbf{r}}(t_0) &= \Delta\dot{\mathbf{r}}_0, \end{aligned} \tag{1.11}$$

where $\Delta\mathbf{f}_p(\Delta\mathbf{r}, \Delta\dot{\mathbf{r}}, \mathbf{r}_C, \dot{\mathbf{r}}_C, t) = \mathbf{f}_{p,D} - \mathbf{f}_{p,C}$.

Relative states

The following relative coordinates are used in the thesis [Alfriend et al., 2009]:

Cartesian states are the position and velocity in the LVLH frame, i.e., $\Delta\mathbf{r} = x\hat{\mathbf{r}} + y\hat{\mathbf{t}} + z\hat{\mathbf{h}}$ and $\Delta\dot{\mathbf{r}} = \dot{x}\hat{\mathbf{r}} + \dot{y}\hat{\mathbf{t}} + \dot{z}\hat{\mathbf{h}}$, respectively.

mean equinoctial relative orbital elements (ROE) are defined as

$$\Delta\bar{\mathcal{E}}_{eq} = \bar{\mathcal{E}}_{eq,D} - \bar{\mathcal{E}}_{eq,C}.$$

Mean equinoctial ROE are used in the control plant. The advantage over LVLH Cartesian states is that $\Delta\bar{\mathcal{E}}_{eq}$ is constant in the unperturbed motion and it evolves linearly in time in the presence of J_2 [Schaub et al., 2000, Schaub, 2003]. In addition, differently from Keplerian ROE, variational equations in the equinoctial ROE are singularity-free.

curvilinear states are defined in Figure 1.3 as:

$$\begin{aligned} \tilde{x} &= r_D - r_C & \tilde{v}_x &= \dot{x} \cos \Delta\theta - \dot{y} \sin \Delta\theta \\ \tilde{y} &= r_D \Delta\theta & \tilde{v}_y &= \dot{x} \sin \Delta\theta + \dot{y} \cos \Delta\theta \end{aligned} \tag{1.12}$$

where $\Delta\theta = \cos^{-1}(\hat{\mathbf{r}}_D \cdot \hat{\mathbf{r}}_C)$. These coordinates are used to illustrate the relative trajectories in the thesis.

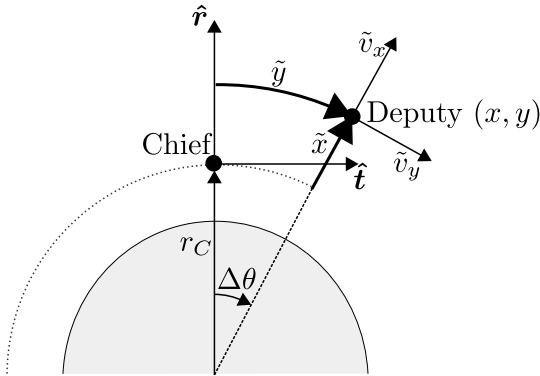


Figure 1.3: Curvilinear relative states.

1.5 Aerodynamic force modeling

This overview on satellite aerodynamics is inspired by [Klinkrad, 2006, Doornbos, 2012, Hughes, 2012, Prieto et al., 2014].

The aerodynamic specific force is modeled as:

$$\mathbf{f}_{drag} = -\frac{1}{2} \mathbf{C}_a \frac{S}{m} \rho v_{TAS}^2 \quad (1.13)$$

where \mathbf{C}_a , S , m , ρ , and v_{TAS} are the dimensionless aerodynamic coefficient, the projected surface of the satellite in the direction $\hat{\mathbf{v}}_{TAS}$, the satellite's mass, the atmospheric density, and the true airspeed (TAS), i.e., the velocity of the spacecraft with respect to the atmosphere.

The component of the aerodynamic force toward $\hat{\mathbf{v}}_{TAS}$ is referred to as *drag*. The subscript *drag* in Equation (1.13), emphasizes that drag is the major component of the aerodynamic force acting on satellites, i.e., $\mathbf{f}_{drag} \cdot \hat{\mathbf{v}}_{TAS} \approx \|\mathbf{f}_{drag}\|$. Although not rigorous, referring to “drag force” instead of “aerodynamic force” is common practice in astrodynamics.

The component of the aerodynamic coefficient toward $\hat{\mathbf{v}}_{TAS}$ is referred to as *drag coefficient*, $C_d = \mathbf{C}_a \cdot \hat{\mathbf{v}}_{TAS}$. Finally, $C_b = C_d \frac{S}{m}$ denotes the *ballistic coefficient*.

High-fidelity modeling of \mathbf{C}_a , ρ , and v_{TAS}^2 is challenging. The following sections recall the physical principles behind their modeling.

1.5.1 Atmospheric density

The main contributors to the determination of the structure and dynamics of the atmosphere are summarized in Table 1.1.

Let P_j , ρ_j , m_j , T , R be the partial pressure, density and molecular weight of the j -th constituent, the temperature, and the universal gas constant, respectively. The *vertical rarefaction* of the atmosphere is obtained by differentiating the equation of

Table 1.1: Sources of variation of the atmospheric density.

Source	
Spatial variations	
Vertical rarefaction	Hydrostatic equilibrium
Day-night bulge	Direct heating of the Sun
Seasonal-latitudinal variations	Sun's declination
Space weather	
Solar activity	Extreme ultraviolet radiation
Geomagnetic activity	Coulomb heating through charged solar wind particles
Temporal variations	
Semianual	Eccentricity of Earth's heliocentric orbit More complex, not fully understood, phenomena

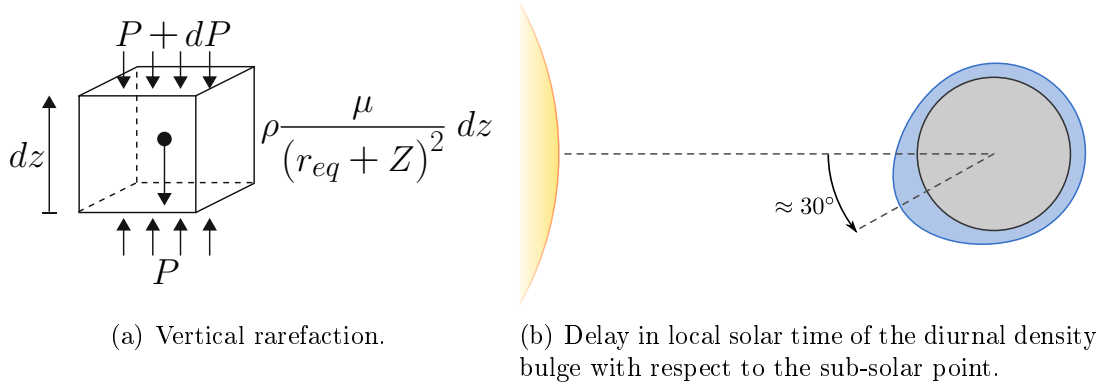


Figure 1.4: Structure of the atmosphere.

ideal gases

$$\frac{P_j}{\rho_j} = \frac{R}{m_j} T \Rightarrow \frac{dP_j}{dz} = \frac{R}{m_j} \frac{dT}{dz} + \frac{\rho_j}{m_j} \frac{R}{dz}, \quad (1.14)$$

and by combining it with the hydrostatic equation of an infinitesimal cube of air at altitude Z (see Figure 1.4(a)). Introducing thermal diffusion, the diffusive equilibrium atmospheric state equation is thus obtained:

$$\frac{1}{\rho_j} \frac{d\rho_j}{dZ} + \frac{1 + \alpha_j}{T} \frac{dT}{dZ} + \frac{m_j}{R T} \frac{\mu}{(r_{eq} + Z)^2} = 0 \quad (1.15)$$

where r_{eq} denotes the equatorial radius and α_j is the thermal diffusion coefficient, which is equal to -0.4 for He and H and zero for the remaining species. Integration of Equation (1.15) yields

$$\rho_j(Z) = \rho_j(Z_0) \left(\frac{T(Z_0)}{T(Z)} \right)^{1+\alpha_j} \exp \left(- \int_{Z_0}^Z \frac{m_j}{R T} \frac{\mu}{(r_{eq} + Z)^2} dz \right). \quad (1.16)$$

Because the argument of the integral in Equation (1.16) decreases with the molecular mass m_j , the number density of lightweight species like helium and hydrogen decreases with slower rate than heavy species like molecular oxygen and nitrogen, as

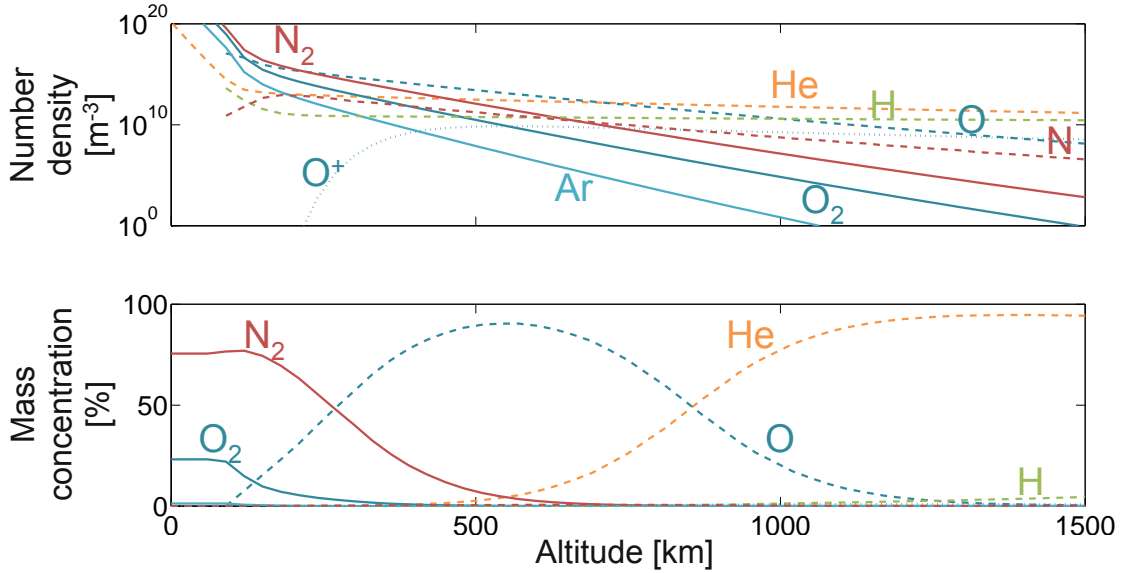


Figure 1.5: Vertical structure of the atmosphere: density number and mass concentration of the species. NRLMSISE-00 averaged over the latitude and longitude on January the 1st 2013 00:00 UTC, $F_{10.7} = \bar{F}_{10.7} = 150$ sfu, $K_p = 4$.

illustrated in Figure 1.5. The mass concentration at very high altitude is essentially constituted by lightweight species only.

The temperature profile, $T(Z)$, depends on the specific atmospheric model. It can account for the direct heating of the Sun, i.e., the day-night bulge in Figure 1.4(b) and seasonal-latitudinal variations, for the variations of the Earth-Sun distance, and for the current space weather.

1.5.2 True airspeed

The TAS is the relative velocity of the satellite with respect to the atmosphere. It is given by three contributions: (1) inertial velocity of the satellite, (2) co-rotating atmosphere, (3) wind, i.e.,

$$\mathbf{v}_{TAS} = \underbrace{\dot{\mathbf{r}}}_{\text{inertial velocity}} - \underbrace{\omega_e \hat{\mathbf{i}}_{ToD} \times \mathbf{r}}_{\text{co-rotating atmosphere}} - \underbrace{\mathbf{v}_w}_{\text{wind}} \quad (1.17)$$

where ω_e is the angular velocity of the Earth sidereal rotation rate.

Thermospheric winds can be of several hundreds of meters per second [Doornbos, 2012], but they are most often neglected in numerical simulations. In first approximation, their gross effect on the semi-major axis is compensated throughout one revolution in near-circular orbits.

1.5.3 Aerodynamic coefficient

The computation of the ballistic coefficient is a challenging and important problem for LEO propagation. The drag coefficient is itself a function of the atmospheric conditions, i.e., gas composition and external temperature, of the ballistic properties of the spacecraft, i.e., geometry and attitude, of the wall temperature, and of the gas-surface interaction.

Two complementary approaches exist for the determination of drag coefficients. *Fitted drag coefficients* are deduced from observation of the orbital dynamics of the spacecraft. This method is not based on physical modeling of the aerodynamic force, but it just requires an underlying atmospheric model. The result is a coefficient that is consistent with the observed dynamics and that rectifies the bias of the atmospheric model. However, fitted coefficients can be computed only after the launch. On the contrary, *physical drag coefficients* are based on physical models of the gas-surface interaction in free molecular flow regime. These methods do not require an atmospheric model and they are appropriate for pre-launch analyses. However, the resulting coefficient is generally biased with respect to observations.

A large body of literature on the determination of physical drag coefficients is available, see, e.g., [Storz et al., 2005, Marcos, 2006]. For non-convex geometries, Monte Carlo (MC) based methods are arguably the only way to compute physical drag coefficients, e.g., direct simulation Monte Carlo (DSMC), test-particle MC, and ray-tracing method. These methods use probabilistic MC simulations to solve Boltzmann's equation for fluid flows with finite Knudsen number. However, this technique is extremely computationally intensive. For simple convex geometries, semi-empirical analytic methods relying on the decomposition into elementary panels provide an accurate and computationally-effective alternative.

The semi-analytic method discussed herein is based upon the research of Sentman [Sentman, 1961] and Cook [Cook, 1965] and upon the more recent contributions of Moe [Moe and Moe, 2005], Sutton [Sutton, 2009], Fuller [Fuller and Tolson, 2009], and Pilinski [Pilinski et al., 2011a].

The following notions are used to model gas-surface interaction (Figure 1.6):

- Impacting particles exchange energy with the surface. The *accommodation coefficient*, α , determines whether the impacting particles are reflected and retain their mean kinetic energy (for $\alpha = 0$) or they acquire the spacecraft wall temperature T_w (for $\alpha = 1$). At low altitudes, a layer of atomic oxygen covers the surface and it “captures” the largest part of impacting particles². Full accommodations of the energy is a good approximation in this case. When the partial pressure of the atomic oxygen decreases, partial accommodation occurs. It is responsible for an increase of the drag coefficient³ and for a misalignment of the force with respect to TAS. Advanced gas-surface interaction models

²This layer is softer at atomic level than materials like aluminum. This causes impacting particles to remain in this soft layer.

³Full vs partial accommodation of the energy can be compared with perfectly elastic and non-elastic impacts, respectively.

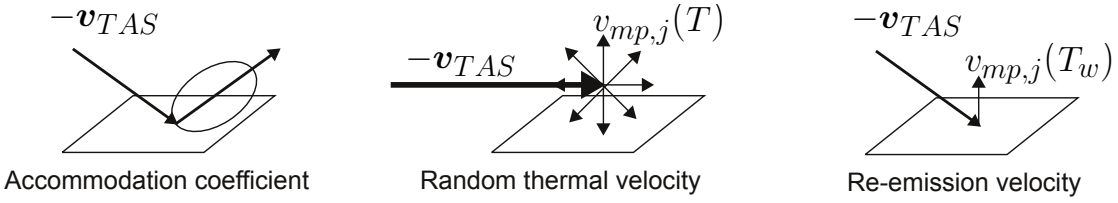


Figure 1.6: Physical principles of gas-surface interaction in free molecular flow.

also consider the way non-accommodated particles are reflected, e.g., diffuse or specular reflection.

- The *most-probable-thermal velocity*, $v_{mp,j}$, is an indicator of the isotropic random velocity of the particles of the j -th gas species. This velocity is added to the TAS, so that some particles can also impact surfaces whose outward normal, $\hat{\mathbf{n}}$, is orthogonal to \mathbf{v}_{TAS} or even such that $\hat{\mathbf{n}} \cdot \mathbf{v}_{TAS} < 0$. For this reason, long-shaped satellites flying “as an arrow” have larger drag coefficients as compared to shorter satellites with similar cross-section-to-mass ratio. Because the thermal velocity is inversely proportional to the square root of the molecular mass, this effect is more pronounced at high altitudes, where the atmosphere is mostly composed by lightweight particles.
- Accommodated particles assume the temperature of the surface, T_w . Subsequently, they are re-emitted with most-probable thermal velocity corresponding to such temperature. This causes a force toward the normal of the surface – which is not generally aligned toward \mathbf{v}_{TAS} – and an increase of the aerodynamic coefficient at high altitude.

Consider a one-sided elementary panel, say the k -th spacecraft panel, with outward normal $\hat{\mathbf{n}}$ and provided with surface S_k . Define $\psi_k = \hat{\mathbf{v}}_{TAS} \cdot \hat{\mathbf{n}}$ and $\phi_k = \|\hat{\mathbf{v}}_{TAS} \times \hat{\mathbf{n}}\|$. Given the TAS to most-probable thermal velocity ratio of the j -th gas species

$$W_j = \frac{v_{TAS}}{v_{mp,j}} = v_{TAS} \left(2 \frac{B}{m_j} T \right)^{-\frac{1}{2}}, \quad (1.18)$$

where B is the Boltzmann constant, the dimensionless drag and lift coefficients are provided by Sentman’s equation

$$\begin{aligned} C_d^{(k,j)} &= \left[\frac{P_{k,j}}{\sqrt{\pi}} + \psi_k \left(1 + \frac{1}{2W_j^2} \right) Z_{k,j} + \frac{\psi_k}{2} \frac{v_{re}}{v_{TAS}} (\sqrt{\pi} Z_{k,j} \psi_k + P_{k,j}) \right] \frac{S_k}{S}, \\ C_l^{(k,j)} &= \left[\phi_k \frac{1}{2W_j^2} Z_{k,j} + \frac{\phi_k}{2} \frac{v_{re}}{v_{TAS}} (\sqrt{\pi} Z_{k,j} \psi_k + P_{k,j}) \right] \frac{S_k}{S}, \end{aligned} \quad (1.19)$$

with

$$\begin{aligned} P_{k,j} &= \frac{\exp(-W_j^2 \psi_k^2)}{W_j}, \\ Z_{k,j} &= 1 + \operatorname{erf}(W_j \psi_k), \\ \frac{v_{re}}{v_{TAS}} &= \sqrt{\frac{1}{2} \left(1 + \alpha \left(\frac{4RT_w}{m_j v_{TAS}^2} - 1 \right) \right)}, \end{aligned} \quad (1.20)$$

where v_{re} is the velocity of the re-emitted particles.

Summing up the contributions of all the panels and of the different gas species yields the aerodynamic coefficient:

$$\mathbf{C}_a = \sum_{k,j} \left[\frac{\rho_j}{\rho} \left(C_d^{(k,j)} \hat{\mathbf{v}}_{TAS} + C_l^{(k,j)} \frac{\hat{\mathbf{v}}_{TAS} \times \hat{\mathbf{n}}}{\|\hat{\mathbf{v}}_{TAS} \times \hat{\mathbf{n}}\|} \times \hat{\mathbf{v}}_{TAS} \right) \right]. \quad (1.21)$$

Missions may assume that the drag coefficient is constant and the aerodynamic force proportional to the projected cross section and toward $\hat{\mathbf{v}}_{TAS}$. Although convenient for most applications, these assumptions are only rigorous when considering hyper-velocity, free-molecular flow, i.e., $\frac{v_{TAS}}{v_{mp,j}} \rightarrow \infty$, full accommodation of the energy, and negligible re-emission velocity.

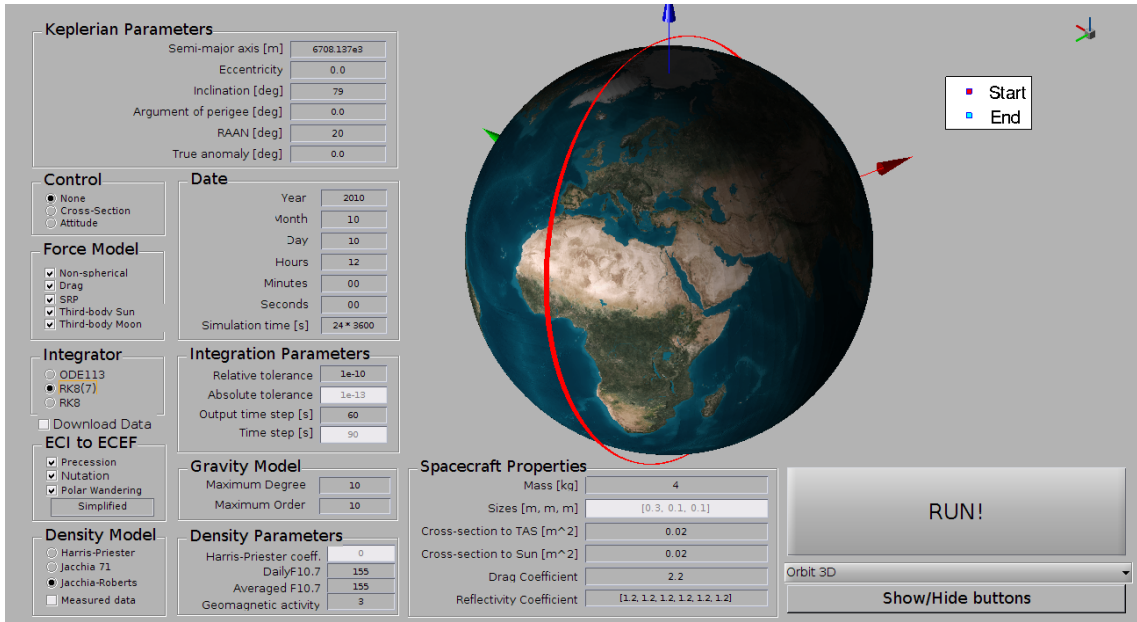
1.6 High-fidelity orbital propagation

The numerical simulations performed in Chapters 2, 3, 5, and 6 are carried out in a highly-detailed environment. Both attitude and orbital dynamics of the satellites are propagated in their complete nonlinear coupled dynamics by means of our homemade MATLAB propagator (Figure 1.7(a)). Figure 1.7(b) shows a validation of our code against Systems Tool Kit (STK).

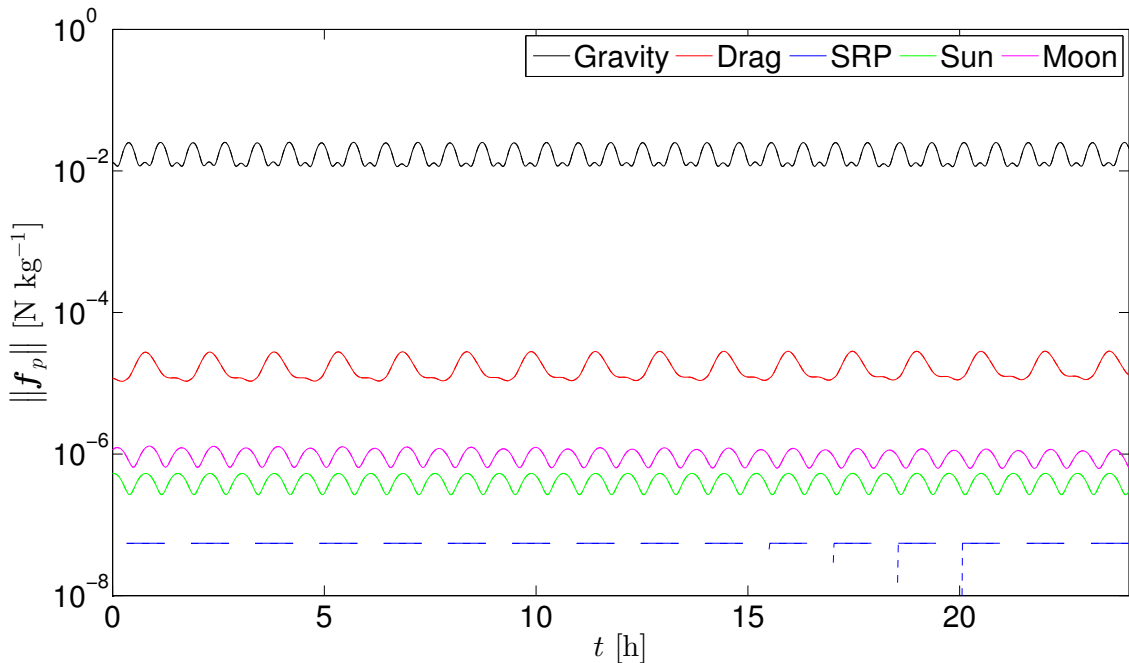
The orbital perturbations include aerodynamic force, a detailed gravitational field with harmonics up to order and degree 10, SRP and third-body perturbations of Sun and Moon. The external torques are due to aerodynamics and gravity gradient, and the models proposed by [Wertz, 1978] for the reaction wheels and magnetic rods are exploited. The control torque is computed with the quaternion feedback algorithm [Wie, 2008].

The aerodynamic coefficient is computed by means of Equations (1.21) at every time step. This model assumes free-molecular flow, random thermal velocity, variable accommodation of the energy, and non-zero re-emission velocity. An analogous model is used for the aerodynamic torque [Hughes, 2012].

The atmospheric model is NRLMSISE-00 [Picone, 2002]. Short-term random variations are included by adding a second-order stationary stochastic process to the total mass density. The power spectral density of the process is the one proposed by Zijlstra [Zijlstra et al., 2005] rescaled for the altitude of the maneuver. The



(a) Graphical user interface.



(b) Validation against STK. Solid lines are computed with our propagator. Dashed lines (almost superimposed to the solid ones) are computed with STK.

Figure 1.7: Our MATLAB propagator.

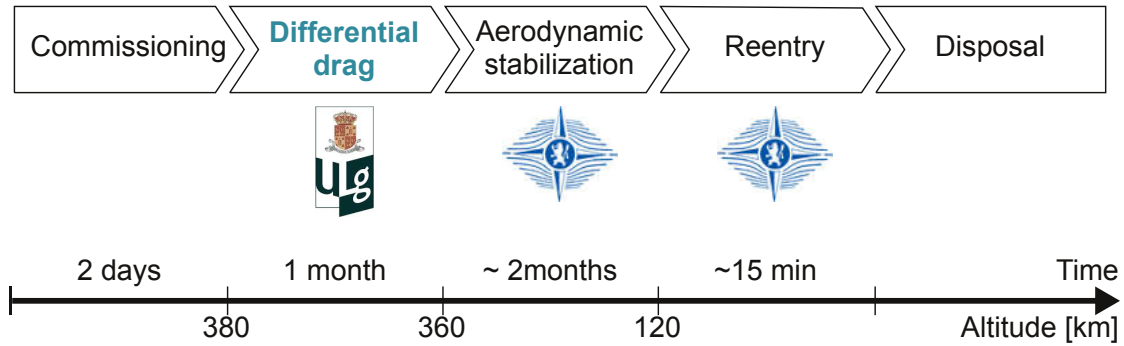


Figure 1.8: QARMAN’s mission timeline. DiffDrag, AeroSDS, and Reentry correspond to the differential drag, aerodynamic stability and deorbiting, and reentry phases, respectively.

atmosphere is assumed to co-rotate with the Earth, but thermospheric winds are neglected.

Precession, nutation, and wandering of the polar axis are modeled according to [Montenbruck and Gill, 2000].

1.7 The QB50 and QARMAN missions

The QB50 Project initiated by the Von Karman Institute for Fluid Dynamics (VKI) aims at being the biggest network of CubeSats for scientific research and technology demonstration in orbit. QB50 has the scientific objective to study in situ the temporal and spatial variations of a number of key constituents and parameters in the lower thermosphere (100-400 km) with a network of about 40 double CubeSats, separated by tens to few hundreds kilometers and carrying identical sensors. QB50 will also study the reentry process by measuring a number of key parameters during reentry and by comparing predicted and actual CubeSat trajectories and orbital lifetimes. QB50 will also accommodate about 10 double or triple CubeSats for in-orbit demonstration (IoD) of novel technologies.

One satellite of the constellation is QARMAN (QubeSat for Aerothermodynamic Research and Measurements on AblatioN), a triple-unit CubeSat developed by a joint collaboration between VKI and University of Liège (ULg). The primary mission objective of QARMAN is to carry out research during the reentry phase. Other mission objectives involve the validation of an aerodynamic stabilization and deorbiting system and the in-orbit demonstration of propellantless maneuvers using differential drag. The fulfillment of these objectives corresponds to different phases of the operational lifetime of QARMAN, as illustrated in Figure 1.8. Specifically, the first month of the lifetime of QARMAN is devoted to differential drag maneuvers.

The architecture of QARMAN is depicted in Figure 1.9.

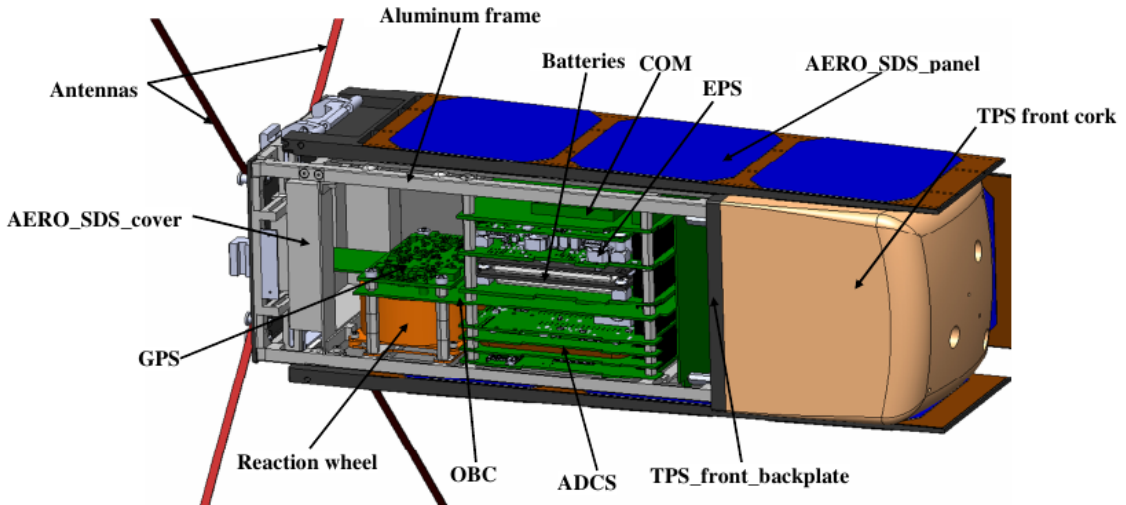


Figure 1.9: Architecture of QARMAN.

1.8 Conclusion

This chapter offered an overview on modeling of satellite orbits in LEO. Owing to complex physical phenomena governing gas-surface interaction in free molecular flow and the structure of the upper atmosphere, accurate satellite aerodynamics modeling is a challenging task and accommodating its underlying uncertainties is mandatory when propagating trajectories in LEO. For this reason, Chapters 2 and 3 are devoted to the uncertainty characterization and estimation of the aerodynamic force, respectively.

Chapter 2

Uncertainty Quantification of Satellite Drag

Abstract

In view of the stochastic nature of the thermosphere and of the complexity of drag modeling, a deterministic assessment of medium-to-long term predictions of the dynamics of a satellite in low-Earth orbit is likely to be bound to failure. The present chapter performs a probabilistic characterization of the dominant sources of uncertainty inherent to low-altitude satellites. Uncertainties in the initial state of the satellite and in the atmospheric drag force, as well as uncertainties introduced by modeling limitations associated with atmospheric density models, are considered. Mathematical statistics methods in conjunction with mechanical modeling considerations are used to infer the probabilistic characterization of these uncertainties from experimental data and atmospheric density models. This characterization step facilitates the application of uncertainty propagation and sensitivity analysis methods, which, in turn, allow gaining insight into the impact that these uncertainties have on the variables of interest. The probabilistic assessment of the orbital lifetime of a CubeSat of the QB50 constellation is used to illustrate the methodology. The same uncertainty characterization also proves useful in Chapters 3 and 6.

2.1 Introduction

In view of the stochastic nature of the thermosphere and of the complexity of drag modeling, the LEO region is arguably the most perturbed region for satellites in geocentric orbit, and a deterministic assessment of medium-to-long term predictions of the dynamics of a satellite in LEO is likely to be bound to failure. An outstanding example concerns orbital lifetime estimation: the continuing growth of space debris is a problem of great concern to the astrodynamics community. Most national space agencies and the Inter-Agency Space Debris Coordination Committee (IADC) now firmly accept a maximum orbital lifetime [iad, 2010]. Specifically, spacecraft must be able to deorbit within 25 years from protected regions, namely from LEO and geostationary orbits. Spacecraft most often exploit chemical propulsion for this purpose, although novel deorbiting strategies, including electrical propulsion [Ryden et al., 1997], solar sails [Johnson et al., 2011], and tethers [Bombardelli et al., 2013], are currently being investigated as well. In other cases, proving through supporting long-term orbit propagations that the natural orbital decay of the spacecraft requires less time than the prescribed 25-year limit may suffice to satisfy the requirement. In this context, the design and optimization of deorbiting strategies require reliable orbital lifetime estimation.

Lifetime estimation began with the early space age with the method developed by Sterne [Sterne, 1958], which was based upon analytical expressions for the rate of change of apogee and perigee. Ladner and Ragsdale [Ladner and Ragsdale, 1995] improved this method and through recommendations in the choice of the most sensitive parameters, they emphasized the importance of uncertainties. Orbital propagation efficiency was then improved by Chao and Platt [Chao and Platt, 1991] thanks to a novel set of simplified averaged equations of classical orbital elements. The adequate treatment of atmospheric density led to renewed interest in lifetime estimation. For instance, Fraysse *et al.* [Fraysse et al., 2012] described good practices for lifetime computation of LEO satellites where drag may be significant and introduced the concept of equivalent solar activity.

However, owing to various experimental and modeling limitations, various parametric uncertainties and modeling errors impede accurate orbital lifetime estimation. For example, Monte Carlo simulations performed in the position paper on space debris mitigation [pos, 2006] indicated that the orbital lifetime of a spacecraft with an initial $36,000 \times 250$ km orbit can vary between about 8 years (with a relative frequency of 5%) to about 70 years (with a relative frequency also of 5%). Oltrogge and Leveque [Oltrogge et al., 2011] provided another example of the variability of three different lifetime estimation tools in the analysis of orbital decay of CubeSats. Variations of the order of 50% were observed between predicted and observed lifetime.

Dominant sources of parametric uncertainties and modeling errors in orbital lifetime estimation include atmospheric properties, the initial state of the satellite, and the physical properties of the satellite. First, although remarkable efforts were performed to gain insight into the nature of the atmosphere [Jacchia, 1965, 1971,

Hedin, 1991], a complete and thorough understanding of the mechanisms that determine the gas composition, the temperature, and other atmospheric properties has not been achieved yet; even if further detailed models were available, their efficient numerical implementation would probably be prohibitive. In addition, most atmospheric models available in the literature rely on the correlation of the density with solar and geomagnetic activity indicators, which are subject to uncertainties themselves. Next, uncertainty in the initial state of the satellite may arise either because the mission design status, e.g., some initial orbital parameters, is not known yet or because of experimental limitations, e.g., limitations associated with GPS or two-line elements (TLE) datasets. Finally, uncertainties in the physical properties of the satellite may include the drag and reflectivity coefficients, the mass, and the geometry. Although all these uncertainties exist for every mission, their relative importance is case-dependent.

Although there is a large body of literature concerning lifetime estimation, UQ of orbital propagation is a more recent research topic. By expressing the analytical solution with a Taylor series expansion and by solving the Fokker-Planck equation, Park and Scheeres [Park and Scheeres, 2006] were able to propagate Gaussian uncertainty in the initial states of a non-linear deterministic evolution problem. Non-linear dynamics propagation resulted in a progressive distortion of the probability distribution of the states, which became non-Gaussian. Further work on the propagation of the uncertainty in the initial states by means of the Fokker-Planck equation was performed by Giza *et al.* [Giza et al., 2009], who were also able to efficiently propagate uncertainty by considering a simplified drag model. Analytical propagation of uncertainties in the two-body problem was then achieved by Fujimoto *et al.* [Fujimoto et al., 2012]. Concerning uncertainty propagation techniques, Doostan *et al.* introduced the polynomial chaos expansion (PCE) method in astrodynamics [Jones et al., 2012, 2013]. Important issues in lifetime estimation are summarized by Saleh [Saleh et al., 2002], while Scheeres *et al.* [Scheeres et al., 2006] pointed out the existence of a rigorous and fundamental limit in squeezing the state vector uncertainty. In summary, non-linear and long-period dynamics propagation [Junkins et al., 1996] as well as severe uncertainty sources make UQ of orbital lifetime a difficult problem.

We view probabilistic UQ of orbital lifetime estimation as a three-step problem. The first step involves using methods from mathematical statistics in conjunction with mechanical modeling considerations to characterize the uncertainties involved in the orbital lifetime estimation problem as one or more random variables. The second step is to map this probabilistic characterization of inputs through the orbital propagator into a probabilistic characterization of the orbital lifetime; this can be achieved in several ways, which include MC simulation [Casella and Casella, 2013] and stochastic expansion methods such as those based on polynomial chaos [Ghanem and Spanos, 1991, Le Maître and Knio, 2010]. Lastly, the third step involves using the probabilistic model thus obtained to gain insight into the impact that the input uncertainties have on the orbital lifetime, for example, by carrying out stochastic sensitivity analyses. The three-step methodology is illustrated in Figure 2.1

In this chapter, we focus mainly on the first step, i.e., the probabilistic charac-

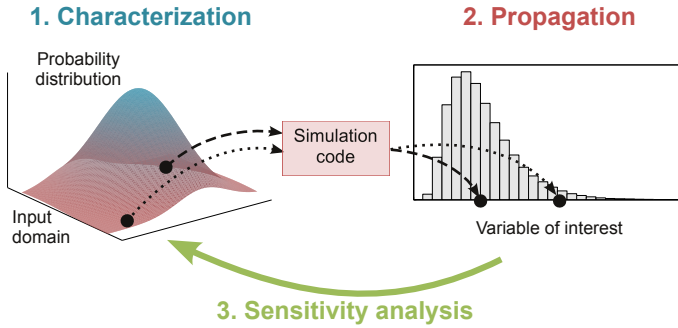


Figure 2.1: Proposed uncertainty quantification approach.

Table 2.1: Nominal parameters for the simulations.

	Variable	Value
Initial conditions	Initial altitude	380 km
	Eccentricity	10^{-3}
	Orbital inclination	98 deg
	Launch date	2016
Spacecraft properties	Mass	2 kg
	Size	$0.2 \text{ m} \times 0.1 \text{ m} \times 0.1 \text{ m}$

terization of the dominant sources of uncertainty involved in the lifetime estimation of low-altitude satellites. Uncertainties in the initial state of the satellite and in the atmospheric drag force, as well as uncertainties introduced by modeling limitations associated with atmospheric density models, are considered. A brief outline of the results of the propagation and sensitivity analysis is also provided; a more detailed description is available in [Dell'Elce and Kerschen, 2014a].

To illustrate the proposed methodology, the standard two-unit (2U) CubeSat of the QB50 constellation is considered. This case study is particularly relevant for two reasons. First, the objective of the constellation is to study in situ the spatial and temporal variations in the lower thermosphere. The initial circular orbit will have an altitude of 380 km where atmospheric drag is significant. Second, it is a real-life mission that should be launched in 2016; hence, the results described here can be useful not only to the astrodynamics community but also to the CubeSat developers. The simulation parameters are summarized in Table 2.1.

The chapter is organized as follows. Section 2.2 details the modeling assumptions and identifies the dominant sources of uncertainty. Section 2.3 summarizes two stochastic methods for uncertainty characterization. Subsequently, the characterization of the uncertainties in the initial conditions and in the drag force is examined in Sections 2.4 and 2.5, respectively. Finally, Sections 2.6 and 2.7 briefly outline the uncertainty propagation and sensitivity analysis steps, respectively.

2.2 Modeling assumptions and uncertainty source identification

The motion of the center of gravity of a non-propelled Earth orbiting spacecraft is governed by the IVP (1.1), which we rewrite here for convenience:

$$\ddot{\mathbf{r}} = -\frac{\mu}{r^3} \mathbf{r} + \mathbf{f}_p(\mathbf{r}, \dot{\mathbf{r}}, t, \mathbf{p}, \mathbf{q}), \quad (2.1)$$

with the following initial conditions

$$\begin{aligned} \mathbf{r}(t_0) &= \mathbf{r}_0, \\ \dot{\mathbf{r}}(t_0) &= \dot{\mathbf{r}}_0; \end{aligned} \quad (2.2)$$

here, $\mathbf{p}(t)$ and $\mathbf{q}(t)$ are a vector of parameters, e.g., geometrical and inertial properties of the satellite, and the spacecraft attitude quaternion, respectively.

The gravitational constant is known with high accuracy, $\mu = 3.986 \cdot 10^{14} \text{ m}^3 \text{s}^{-2} \pm 8 \cdot 10^5 \text{ m}^3 \text{s}^{-2}$ [Ries et al., 1992]; hence, it is supposed to be deterministic in this work. Thus, the uncertainties in the spacecraft dynamics, and, in particular, in the orbital lifetime, originate from the initial conditions and the perturbing forces, as shown in Figure 2.2. The main perturbations for a LEO spacecraft are due to the gravitational forces, i.e., non-spherical harmonics of the Earth's gravitational field and third-body disturbances of sun and moon, \mathbf{f}_g , to the atmospheric drag \mathbf{f}_{drag} , and to the SRP \mathbf{f}_{SRP} ; hence, $\mathbf{f}_p \simeq \mathbf{f}_g + \mathbf{f}_{drag} + \mathbf{f}_{SRP}$. Their respective OoM depend on the considered orbit. Figure 1.1 illustrates the amplitude of these perturbations for a 2U CubeSat for various LEO altitudes. Minor perturbing forces include radiation pressure of the Earth's albedo which is due to the diffuse reflection of the sunlight, Earth infrared radiation, relativistic accelerations, tides, and third-body perturbations of the planets. Nonetheless, they are at least one OoM smaller than SRP, so that their influence can be safely neglected in most applications.

Both the Earth's gravitational attraction and third-body perturbations are considered as deterministic quantities in this study because they can be modeled with high accuracy. Concerning the Earth's attraction, Fraysse *et al.* [Fraysse et al., 2012] reported that it is sufficient to include zonal harmonics up to J_4 for lifetime estimation¹. Figure 2.3 provides the numerical evidence that this recommendation is valid for our QB50 case study. Because of the strong non-linearity of this problem and possible chaotic dynamics, the convergence of the relative error is not monotonic, especially if zonal-only perturbations are considered. As a result, the relative error tends to stabilize at a value of about 0.1% beyond order 4; this error can be safely neglected with respect to the large uncertainties inherent to orbital lifetime

¹Special cases may require a more complete modeling of the perturbing agents. For instance, if sectorial perturbations have very little influence on long-term propagations in LEO, we note that some special orbits could require a more detailed modeling of the gravity field, e.g., it is recommended to include zonal harmonics up to J_{15} for orbits with inclination close to 63.4deg. Lamay *et al.* propose a survey of these resonance effects in [Lamy et al., 2012].

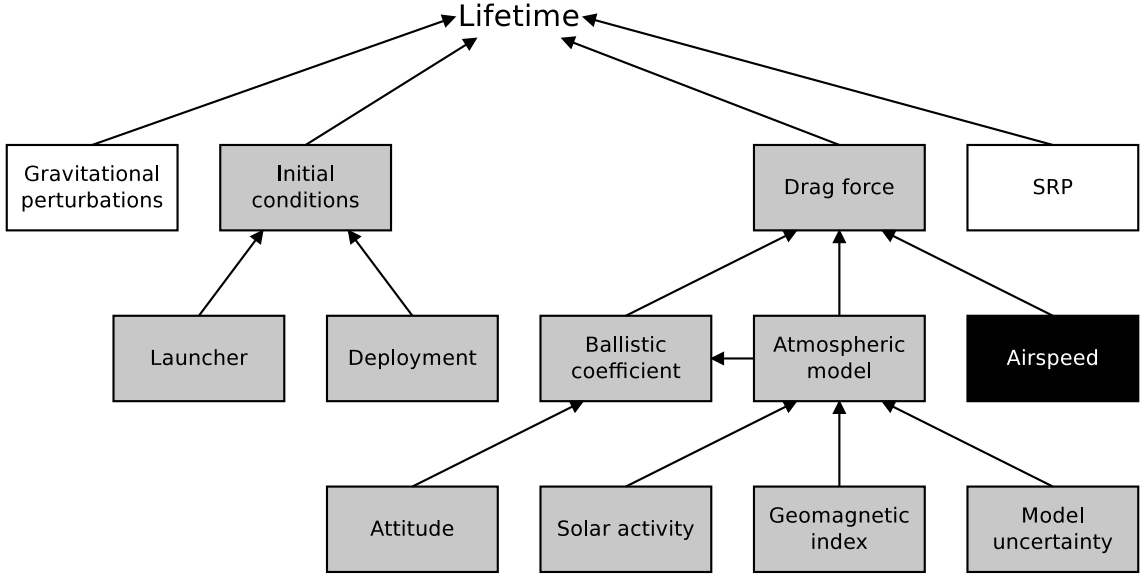


Figure 2.2: Schematic representation of uncertainty quantification of orbital lifetime in LEO. White box: deterministic modeling, gray box: stochastic modeling, black box: unmodeled dynamics.

estimation. The modeling of the perturbing force due to SRP is a challenging and demanding task. However, SRP can usually be neglected for very low altitudes, as confirmed in Figure 1.1, and it is also considered deterministic in this work. We therefore assume in the context of this study that *only the perturbations due to atmospheric drag play an important role for UQ of orbital lifetime estimation*. Besides the great magnitude of drag perturbations in LEO, this assumption is supported by the fact that drag is uncertain in nature and does not exhibit any relevant compensation throughout one orbit, e.g., it is responsible for a monotonic decrease of the semi-major axis.

The popular Runge-Kutta 8(7) [Montenbruck and Gill, 2000] is exploited as numerical integrator for orbital propagation. To reduce the computational burden, the relative precision was set to 10^{-9} , which provides a relative error of $\mathcal{O}(10^{-2})$ on the lifetime with respect to a precision of 10^{-13} .

2.3 Stochastic methods for uncertainty characterization

Within a probabilistic framework, the objective of characterization is to model the sources of uncertainty involved in the problem under study as one or more random variables² X with values in the support \mathcal{I}_X . The extension of the methods dis-

²It is common practice in statistics to use uppercase letters to denote random variables; by contrast, lower-case letters indicate deterministic variables. We use this system of notation only

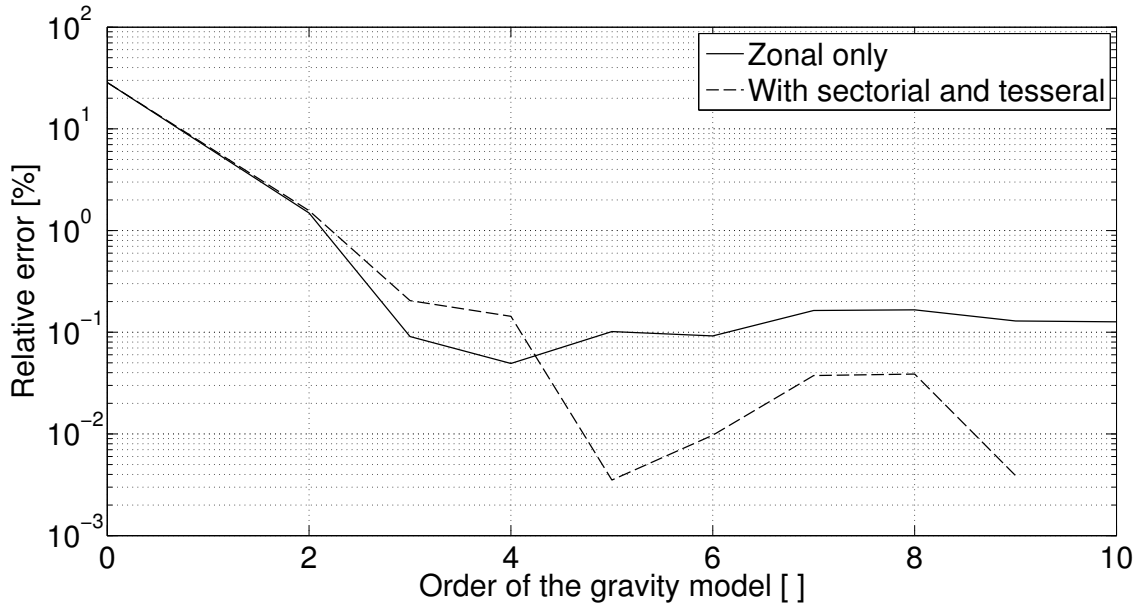


Figure 2.3: Error on the orbital lifetime in the nominal case in function of the order of the gravity model.

cussed in this section to the multivariate case is straightforward, but we preferred to illustrate the scalar case to ease the notation. This requires that an adequate probability distribution, or, if X is continuous, its PDF, $p_X : \mathcal{I}_X \rightarrow \mathbb{R}^+$, be assigned to these random variables. The information available for obtaining this distribution typically consists of one or more of the following sources. First, various types of experimental data can be available. Next, there can be mechanical laws that impose constraints on the values that the random variables may take, e.g., mechanical laws can require that the uncertain atmospheric density is positive. These constraints act as sources of information because the inferred probability distribution must assign a vanishing probability to those values of the random variables that do not satisfy the constraints. Finally, various other sources can contribute information, for example, in the form of nominal values.

Methods from mathematical statistics are most often used in conjunction with mechanical modeling considerations to infer a characterization of uncertainties from the available information. Providing an exhaustive account of all available methods from mathematical statistics is beyond the scope of this chapter. Instead, we confine ourselves to a succinct presentation of two fundamental methods.

2.3.1 Maximum likelihood estimation

The first method involves selecting an adequate ‘labeled’ probability distribution, followed by inferring suitable values for its parameters from data, for example, by

in this section, which focuses on the mathematical aspects.

using the method of maximum likelihood estimation (MLE). By labeled probability distribution we mean Gaussian, uniform, and other probability distributions given in catalogs in the literature. Consider a set of n samples x_1, \dots, x_n of a random variable X and a PDF $p_X(x; \vartheta_1, \dots, \vartheta_d)$, where $\vartheta_1, \dots, \vartheta_d$ are the parameters defining the distribution, e.g., the mean and the standard deviation for the normal distribution. According to the maximum likelihood method, the d parameters of the PDF have to be chosen such that they are consistent, e.g., they have a positive standard deviation, and maximize the likelihood function

$$\mathcal{L}(\vartheta_1, \dots, \vartheta_d) = \prod_{j=1}^n p_X(x_j; \vartheta_1, \dots, \vartheta_d). \quad (2.3)$$

In practice, the logarithm of the likelihood function is generally considered as the objective function in order to reduce numerical errors due to the product of small numbers.

Care should be taken to select a labeled PDF that is consistent with the physical constraints; for example, the Gaussian probability distribution should not be selected to characterize an uncertain atmospheric density because its support is \mathbb{R} , and its selection would thus lead to the assignment of a non-vanishing probability to negative values.

2.3.2 Maximum entropy

If no adequate labeled probability distribution is available, the possibility of constructing a new adequate distribution can be considered, using, for example, the maximum entropy principle [Shannon, 1948]. The maximum entropy principle states that the probability distribution with the largest entropy should be selected from among those that are consistent with the available information. The entropy of a continuous random variable X with PDF $p_X(x)$ and support \mathcal{I}_X is defined as

$$s_X = - \int_{\mathcal{I}_X} p_X(x) \log p_X(x) dx. \quad (2.4)$$

For most of the sources of uncertainty that we characterize using the principle of maximum entropy, the probability distribution is obtained as the one that maximizes entropy,

$$\max_{p_X} s_X(p_X), \quad (2.5)$$

from among those that are consistent with available information of the following

form

$$\begin{aligned} \int_{\mathcal{I}_X} p_X(x) dx - 1 &= 0, \\ \int_{\mathcal{I}_X} x p_X(x) dx - \mu_X &= 0, \\ \int_{\mathcal{I}_X} (x - \mu_X)^2 p_X(x) dx - \sigma_X^2 &= 0; \end{aligned} \quad (2.6)$$

here $\mathcal{I}_X = [x_{min}, x_{max}]$, μ_X and σ_X are a given support, a given mean, and a given standard deviation, respectively. The exact analytical solution to this constrained optimization problem can be obtained using Lagrange multipliers, and it is the truncated Gaussian distribution with support \mathcal{I}_X and with second-order statistical descriptors μ_X and σ_X ³.

$$p_X(x; \tilde{\mu}_X, \tilde{\sigma}_X, x_{min}, x_{max}) = \frac{1}{\tilde{\sigma}_X} \frac{p_N\left(\frac{x-\tilde{\mu}_X}{\tilde{\sigma}_X}\right)}{c_N\left(\frac{x_{max}-\tilde{\mu}_X}{\tilde{\sigma}_X}\right) - c_N\left(\frac{x_{min}-\tilde{\mu}_X}{\tilde{\sigma}_X}\right)}; \quad (2.7)$$

here p_N , c_N , $\tilde{\mu}_X$ and $\tilde{\sigma}_X$ are the PDF and the CDF of the standard Gaussian distribution, and the parameters of the associated unbounded Gaussian distribution, respectively. $\tilde{\mu}_X$ and $\tilde{\sigma}_X$, are obtained by solving

$$\begin{aligned} \tilde{\mu}_X + [p_X(x_{min}) - p_X(x_{max})] \tilde{\sigma}^2 &= \mu_X, \\ \left[1 + (x_{min} - \tilde{\mu}_X) p_X(x_{min}) - (x_{max} - \tilde{\mu}_X) p_X(x_{max}) \right. \\ \left. - (p_X(x_{min}) - p_X(x_{max}))^2 \tilde{\sigma}_X^2 \right] \tilde{\sigma}_X^2 &= \sigma_X^2, \end{aligned} \quad (2.8)$$

where the dependency of p_X on its parameters are omitted for the sake of conciseness.

For more general applications of the maximum entropy principle, the numerical solution of the problem is an alternative. An interesting approach that is particularly suitable for high-dimensional problems was proposed by Soize [Soize, 2008]. A simple numerical implementation is proposed in Appendix A, and it is illustrated for the characterization of the initial altitude.

2.4 Uncertainty characterization of initial conditions

As discussed in Section 2.2, the two main sources of uncertainties considered in the present study are those in the initial states and atmospheric drag. Uncertainty characterization of the initial states is strongly related to the current status of the mission. Two scenarios may occur:

- The spacecraft is in orbit. The uncertainty in the initial states depends on

³These are the second-order descriptors of the actual PDF, i.e., the truncated normal distribution, and not of the associated unbounded normal distribution.

measured data, while the initial epoch can generally be considered as deterministic. TLE and GPS are two common measurement techniques. The former is responsible for wider dispersion than the latter, but it is often the only option available for debris and nanosatellites. Relevant work on TLE uncertainty was performed by Vallado [Vallado et al., 2011] and Flohrer *et al.* [Flohrer et al., 2008]. Kahr *et al.* [Kahr et al., 2013] estimated the uncertainty in the TLE-based positioning of nano and micro-satellites by means of GPS data. In the same paper, it is shown that the exploitation of intermittent GPS data in conjunction with TLE can enhance the accuracy of few-day predictions by one order of magnitude.

- The mission is still in a design phase, which is the scenario studied in this paper. In this case, uncertainty in the initial states is related to the launch vehicle injection accuracy and to the deployment strategy. The set of nominal initial conditions may also not be fully defined, e.g., the initial RAAN may be unknown.

For the QB50 network, the reference initial conditions before the deployment are $h_{0,l}^{ref} = 380 \text{ km}$, $i_{0,l}^{ref} = 98 \text{ deg}$, and $e_{0,l}^{ref} = 10^{-3}$, where $h_{0,l}^{ref}$, $i_{0,l}^{ref}$ and $e_{0,l}^{ref}$ are the initial altitude above the equatorial radius, the orbital inclination, and the eccentricity, respectively. Keplerian elements are used for orbit parametrization because the mean anomaly is the only fast variable in this parameter set. Mean elements, instead of osculating elements, are considered to avoid an important sensitivity of the lifetime with respect to the initial anomaly resulting from short-period variations of the semi-major axis. Doing so, we can remove the initial anomaly from the uncertainty sources. Since the reference orbit is circular, the characterization of the initial AoP is not relevant either. As no information is available yet, the initial RAAN is modeled as an aleatory variable with uniform uncertainty between 0 and 360 deg, in accordance with the maximum entropy principle.

The uncertainty in $h_{0,l}$, $i_{0,l}$, and $e_{0,l}$ depends on the accuracy of the launcher. Standard deviations of the Keplerian elements consistent with the performance of current launchers used for LEO are considered, namely, $\sigma_h = 2.5 \text{ km}$, $\sigma_i = 0.03 \text{ deg}$, and $\sigma_e = 3.5 \cdot 10^{-4}$. These three variables are supposed to be independent because no information about their correlation is usually provided, and univariate PDFs are constructed in the following.

The initial altitude of the spacecraft is a non-negative random variable, so that its support is \mathbb{R}^+ . The mean and standard deviation of the PDF are constrained to be equal to the nominal values $h_{0,l}^{ref}$ and σ_h , respectively. Thus, according to the maximum entropy principle, $h_{0,l}$ is modeled as a truncated Gaussian distribution with support \mathbb{R}^+ and with the imposed second-order descriptors, as shown in Figure 2.4(a). A similar problem is solved for the initial orbital eccentricity (Figure 2.4(b)) and inclination. For these variables the support is $[0, 1]$ and \mathbb{R} , respectively.

The initial date t_0 is the last parameter necessary to fully define the initial state right before the deployment of the constellation. The launch is foreseen for early 2016. However, because of the frequent delays in space missions, t_0 is modeled

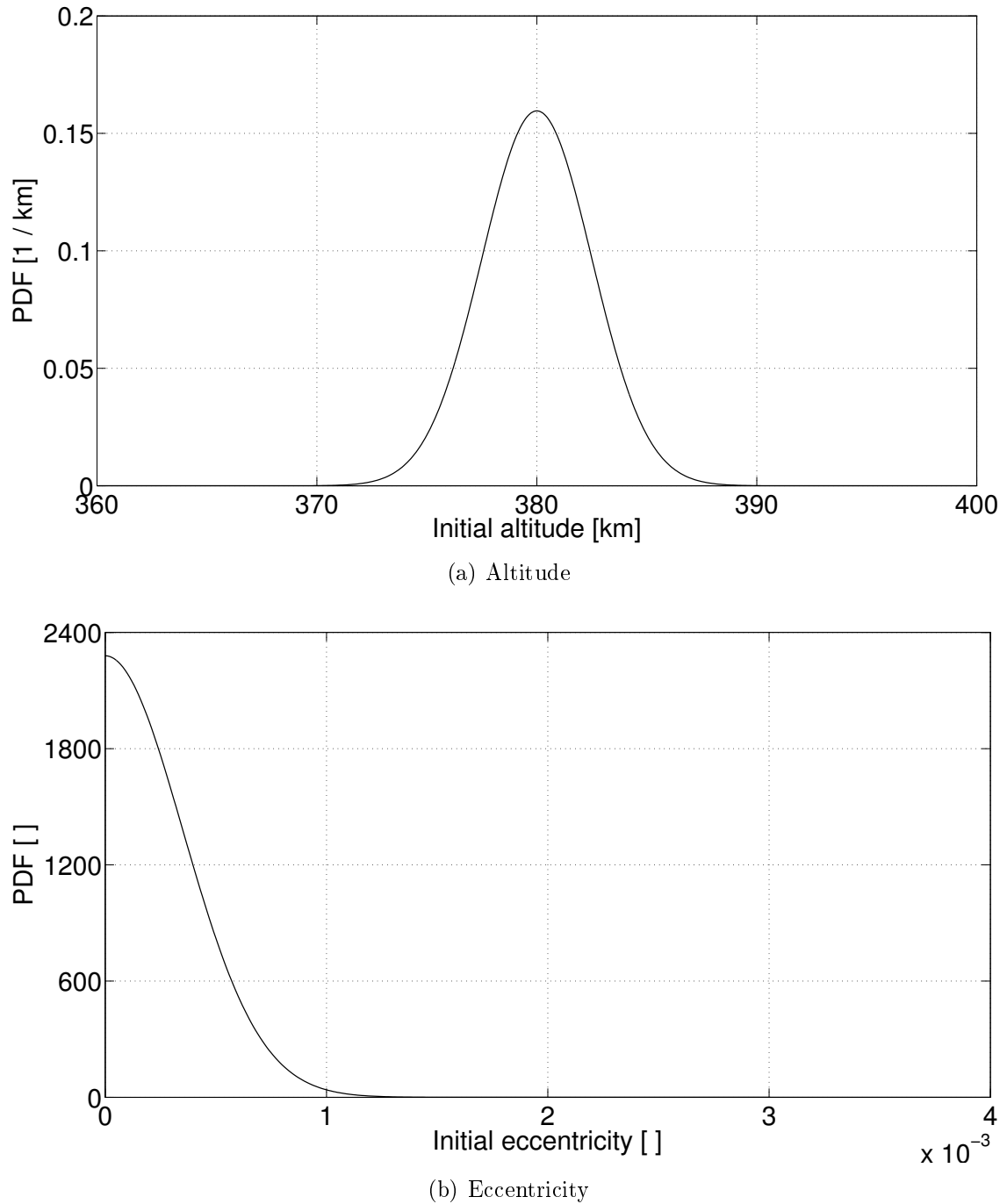


Figure 2.4: PDF of the initial altitude and eccentricity before deployment (maximum entropy principle).

as a uniform random variable between January the 1st 2016 and January the 1st 2017. A wider launch window is not necessary, since the long-term variations in the atmospheric models are not considered herein.

A second source of uncertainty for the initial conditions is the deployment of the QB50 constellation. Even though the exact strategy for deployment is still unknown, the nanosatellites will be ejected thanks to a spring-loaded pusher plate with an ejection velocity between 1 and 1.5 m.s^{-1} . Though negligible with respect to the orbital speed, the ejection velocity may be responsible for uncertainties of the order of launcher accuracy. For example, an ejection velocity in the flight direction leads to an increment of the semi-major axis of 2.6 km , which is larger than σ_h . Therefore, the ejection velocity is modeled as a vector with norm, v_{ej} , and direction uniformly distributed in $[1.0, 1.5] \text{ ms}^{-1}$ and in the space, respectively. Parameterizing the direction with azimuth, Θ , and elevation, χ , yields

$$p_{\Theta,\chi}(\Theta, \chi) = \frac{1}{360} \frac{\cos \chi}{2} \quad [\text{deg}^{-2}]; \quad (2.9)$$

here Θ and χ are defined in $[0, 360] \text{ deg}$ and $[-90, 90] \text{ deg}$, respectively. This distribution is uniform over the radian sphere, and it is obtained by considering that the infinitesimal surface with these parameters is given by $\cos \chi d\Theta d\chi$.

2.5 Uncertainty characterization of atmospheric drag

The second main source of uncertainty considered herein is the atmospheric drag. The aerodynamic force per unit of mass is computed using the Equation (1.13). According to Vallado [Vallado, 2001], all the terms involved in Equation (1.13) and the equation itself are affected by uncertainties.

In this work, the TAS is calculated using the assumption of a co-rotating atmosphere, i.e.,

$$\mathbf{v}_{TAS} = \dot{\mathbf{r}} - \boldsymbol{\omega}_E \times \mathbf{r}, \quad (2.10)$$

where $\boldsymbol{\omega}_E$ is the Earth's angular velocity. This means that we do not consider the upper-thermosphere winds, which can be of the order of several hundreds of meters per second [Häusler et al., 2007, Wu et al., 1994, Liu et al., 2006]. However, the basic dynamics of the wind involves a movement from daylight to night-time, which approximately results in a compensation of their effects throughout one orbit. Relevant work on the determination of these winds from experimental data is performed in [Doornbos, 2012], and different models are available in the literature [Hedin et al., 1988, Killeen et al., 1987]. The thermospheric cooling trend [Emmert et al., 2008] is also ignored herein.

We stress that the drag force is just one component of the aerodynamic force. Lift forces are also considered in our simulations, although their OoM and influence on lifetime are much smaller.

2.5.1 Atmospheric model

The dominant uncertainty source in the drag estimation is the atmospheric density. One of the most advanced atmospheric models is NRLMSISE-00, which is a global, i.e., from ground to exosphere, empirical model developed by the US Naval Research Laboratory (NRL). The model is calibrated by means of mass spectrometer, incoherent scatter, and accelerometer measurements. Two important inputs of the model are the daily and 81-day averaged radio flux indices, $F_{10.7}$ and $\bar{F}_{10.7}$. The 3-hour geomagnetic index, a_p , is another input of the model, but, for long-period propagations, its daily average, A_p , can be exploited. The other inputs required by NRLMSISE-00 are the position of the spacecraft and the Julian date, which are computed throughout the numerical integration of the equations of motion. Although they depend on random variables, e.g., $JD(t) = t + t_0$, they are not primary sources of uncertainty. Given these inputs, NRLMSISE-00 is able to estimate the number densities of helium, atomic and molecular oxygen, atomic and molecular nitrogen, argon, and hydrogen, together with the local atmospheric temperature. The total mass density is deduced directly from these outputs.

Solar and geomagnetic proxies

Correlation between gas density and space weather proxies, e.g., solar radio flux and geomagnetic index, is crucial in the development of an atmospheric model. The sensitivity of the orbital lifetime with respect to these variables is very substantial [Naasz et al., 2007]. This section focuses on the characterization of the solar and geomagnetic random variables. Different approaches were proposed in the literature to address this important problem. Among them, Ashrafi *et al.* [Ashrafi et al., 1993] developed a prediction tool based on chaos theory, and they proved that it is more suitable than statistical approaches for short-term prediction. Watari [Watari, 1996] and Loskutov *et al.* [Loskutov et al., 2001] introduced methodologies for the identification of periodic and chaotic components and for solar activity forecasting based on singular spectrum analysis. To generate realizations of realistic future solar flux trajectories (geomagnetic activity was not considered), Woodburn [Woodburn and Lynch, 2005] proposed to superpose to the trend of the trajectory a scalar exponential Gauss-Markov sequence.

The consideration of time-varying series complicates the uncertainty propagation because the problem belongs to the family of stochastic differential equations [Øksendal, 1992]. As an alternative for orbital lifetime estimation, Fraysse *et al.* introduced the concept of *constant equivalent solar activity* [Fraysse et al., 2012]. The idea is to consider a constant solar flux and geomagnetic index throughout the propagation. If the satellite has a 25-year lifetime for the chosen constant equivalent solar activity, then its lifetime for possible future solar activities will also be 25 years with a probability of 50%. The equivalent solar flux is a function of the ballistic coefficient C_b and of the altitude of the apogee h_p , whereas the daily geomagnetic index is set to 15. This technique is particularly appropriate for very long prop-

agations in the order of one or several solar cycles. In [Dell'Elce et al., 2014], we proposed another approach to the problem. It was also based upon the idea of using an effective solar activity, but it was more suitable for propagations of the order of a fraction of the solar cycle. Instead of a deterministic effective solar activity we considered a random effective solar activity. The main underlying assumption was that neglecting variations of the space weather proxies with respect to their averaged value in time does not yield drastic variations of the orbital lifetime. This approach has the effect to reduce the dimension of the uncertainty source set, enabling the possibility to use efficient techniques for uncertainty propagation, e.g., polynomial chaos expansion (PCE) was used in [Dell'Elce and Kerschen, 2014a] thanks to the exploitation of the random effective solar activity.

Because this thesis also focuses on short-term propagations, e.g., rendez-vous maneuvers lasting a couple of weeks, we model solar activity by means of a stochastic process also in this chapter. In this way, the same probabilistic model will be also exploited in Chapters 3 and 6.

$F_{10.7}$, $\bar{F}_{10.7}$, and A_P are characterized using the data measured over the last 50 years provided by the Celestrack database⁴. Bearing in mind that QB50 has a lifetime of a few months and that the launch window is [January 2016, January 2017], the portion of the solar cycle between [January 2014, January 2018] is considered to be a conservative mission window. Thus, only the data of the previous cycles corresponding to the same portion of the solar cycle are exploited for uncertainty characterization. Because of the important variations in correspondence of the solar maxima and of the variability in the period of the solar activity, the identification of the selected data set is achieved by identifying the minima of the solar flux curve smoothed by a moving-average filter of 2-year width. These minima are then used to define a dimensionless position between two consecutive minima of the solar cycle. This process is illustrated for the daily solar flux in Figure 2.5; a similar process can be carried out for $F_{10.7}$ and A_p . The data in the shaded windows are retained for uncertainty characterization of the solar weather proxies.

Given the relatively short time span of the lifetime, i.e., $\mathcal{O}(1 \text{ year})$, compared to the solar cycle, the processes are assumed to be reasonably stationary within the maneuvering time, i.e., the random variables used for the modeling of the sequence of each of the three proxies are assumed to have the same marginal distribution, and all the points of the selected dataset are exploited for its generation. The statistical model must be able to represent both the marginal distributions and the correlation between the three variables. In addition, because the proxies are modeled as stochastic processes, the autocorrelation of the time series must also be accounted for.

Let t_{proc} be a temporal window large enough to accommodate all the relevant autocorrelations of the processes. In other words, it is assumed that the values of the proxies at time t are correlated to their past history until $t - t_{proc}$. In this study we set t_{proc} to 20 days. The selected dataset is split into sequences of length

⁴<http://www.celestrak.com/SpaceData/sw19571001.txt>

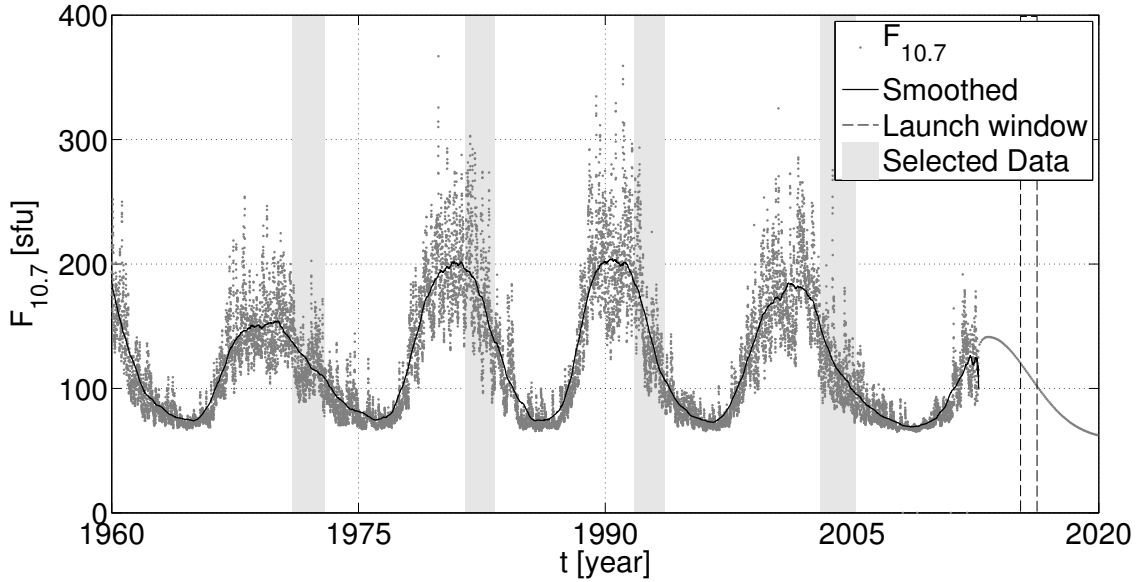


Figure 2.5: Observed daily solar activity.

$n_{kn} = \text{ceil}(t_{proc})$. The stochastic processes are modeled by means of three n_{kn} -elements vectors of random variables, $\mathbf{F}_{10.7}$, $\bar{\mathbf{F}}_{10.7}$, and \mathbf{A}_p , such that the generic k -th element is the value of the proxy evaluated at time $t = k \text{ ceil}(t_f)$.

The Gaussian copula [Marriott and Eaton, 1984]

$$\left\{ \begin{array}{l} \mathbf{Z}_1 \\ \mathbf{Z}_2 \\ \mathbf{Z}_3 \end{array} \right\} \xrightarrow{\text{chol}(\mathcal{C})} \left\{ \begin{array}{l} \boldsymbol{\Xi}_1 \xrightarrow{c_N(\xi_1)} \mathbf{U}_1 \xrightarrow{\mathcal{F}_{F_{10.7}}^{-1}(\mathbf{u}_1; \boldsymbol{\vartheta}_{F_{10.7}})} \mathbf{F}_{10.7} \\ \boldsymbol{\Xi}_2 \xrightarrow{c_N(\xi_2)} \mathbf{U}_2 \xrightarrow{\mathcal{F}_{\bar{F}_{10.7}}^{-1}(\mathbf{u}_2; \boldsymbol{\vartheta}_{\bar{F}_{10.7}})} \bar{\mathbf{F}}_{10.7} \\ \boldsymbol{\Xi}_3 \xrightarrow{c_N(\xi_3)} \mathbf{U}_3 \xrightarrow{\mathcal{F}_{A_p}^{-1}(\mathbf{u}_3; \boldsymbol{\vartheta}_{A_p})} \mathbf{A}_p \end{array} \right. ; \quad (2.11)$$

is used to account for the statistical dependence both within and among $\mathbf{F}_{10.7}$, $\bar{\mathbf{F}}_{10.7}$, and \mathbf{A}_p . Here

- \mathbf{Z}_1 , \mathbf{Z}_2 , and \mathbf{Z}_3 are n_{kn} -element vectors of independent standard Gaussian random variables,
- $\boldsymbol{\Xi}_1$, $\boldsymbol{\Xi}_2$, and $\boldsymbol{\Xi}_3$ are n_{kn} -element vectors of correlated standard Gaussian random variables; $\text{chol}(\mathcal{C})$ is the Cholesky decomposition of their correlation matrix. It holds $[\boldsymbol{\Xi}_1^T, \boldsymbol{\Xi}_2^T, \boldsymbol{\Xi}_3^T] = [\mathbf{Z}_1^T, \mathbf{Z}_2^T, \mathbf{Z}_3^T] \text{chol}(\mathcal{C})$,
- \mathbf{U}_1 , \mathbf{U}_2 , and \mathbf{U}_3 are n_{kn} -element vectors of correlated uniform random variables with support $[0, 1]$,
- $\mathcal{F}_{(\cdot)}$ is the CDF of the marginal distribution that is chosen to fit the model, and $\boldsymbol{\vartheta}_{(\cdot)}$ is the vector of parameters defining the distribution.

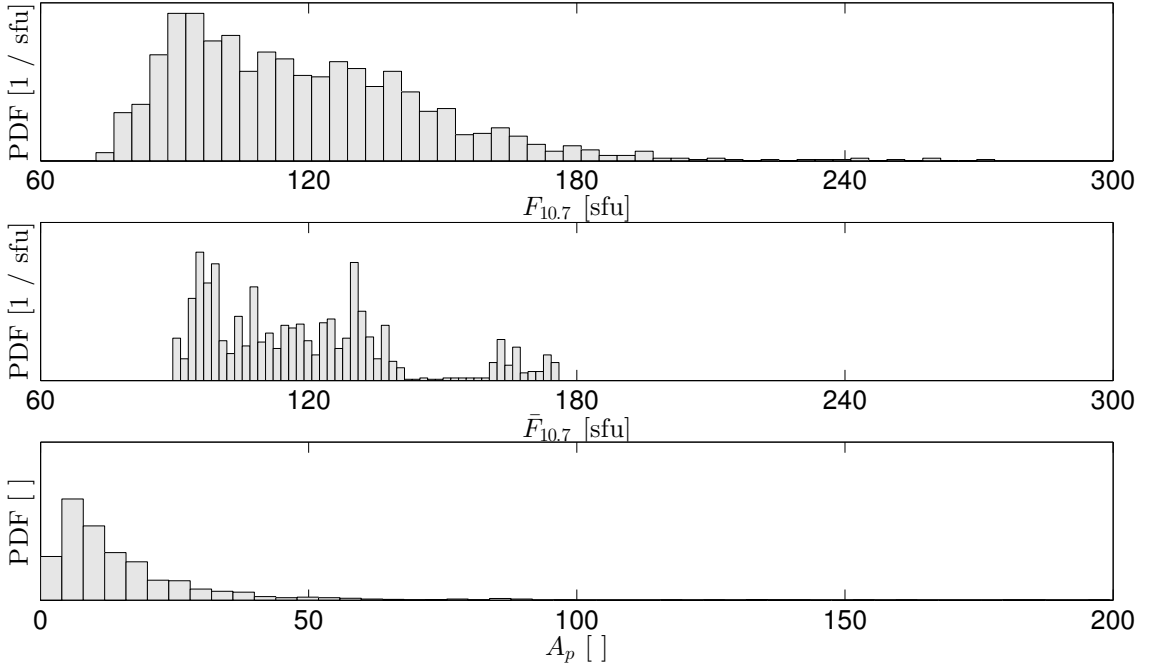


Figure 2.6: Marginal distributions of the geomagnetic and solar activity proxies (identified with maximum likelihood).

The identification of the parameters of the statistical model is achieved by means of the MLE. The design variables of the MLE problem are the parameters of the marginal PDF and the correlation matrix:

$$p_{\mathbf{F}_{10.7}, \bar{\mathbf{F}}_{10.7}, \mathbf{A}_p} = p_{\mathbf{F}_{10.7}, \bar{\mathbf{F}}_{10.7}, \mathbf{A}_p} (\mathbf{F}_{10.7}, \bar{\mathbf{F}}_{10.7}, \mathbf{A}_p; \boldsymbol{\vartheta}_{F_{10.7}}, \boldsymbol{\vartheta}_{\bar{F}_{10.7}}, \boldsymbol{\vartheta}_{A_p}, \mathcal{C}) \quad (2.12)$$

Physical constraints impose that the chosen distributions of the solar flux proxies are defined on \mathbb{R}^+ , whereas the support of the geomagnetic indicator is $[0, 400]$. In addition, the correlation matrix is symmetric with ones on the diagonal and off-diagonal terms with modulus smaller than one by definition. These constraints have to be considered, as well.

Several labeled PDF and histogram distributions were tested to model the marginal PDF. On the one hand, labeled distributions are interesting because the resulting model can be tuned with a very limited number of parameters. On the other hand, histogram distributions are able to represent with the highest fidelity the statistical content of the dataset, but several parameters are necessary to tune the model, i.e., the height of each bin. Histogram distributions for the marginal PDF are used herein. Figure 2.6 depicts the obtained marginal distributions.

Figure 2.7 presents the values of the correlation matrix. The autocorrelation of the daily solar flux smoothly decreases with the time increment, while the one of the 81-day averaged flux is always close to one. This is due to the fact that the averaged flux exhibits negligible variations within the window $t_{f,max}$. Nonetheless, large variations can be expected from one realization of the process to the other

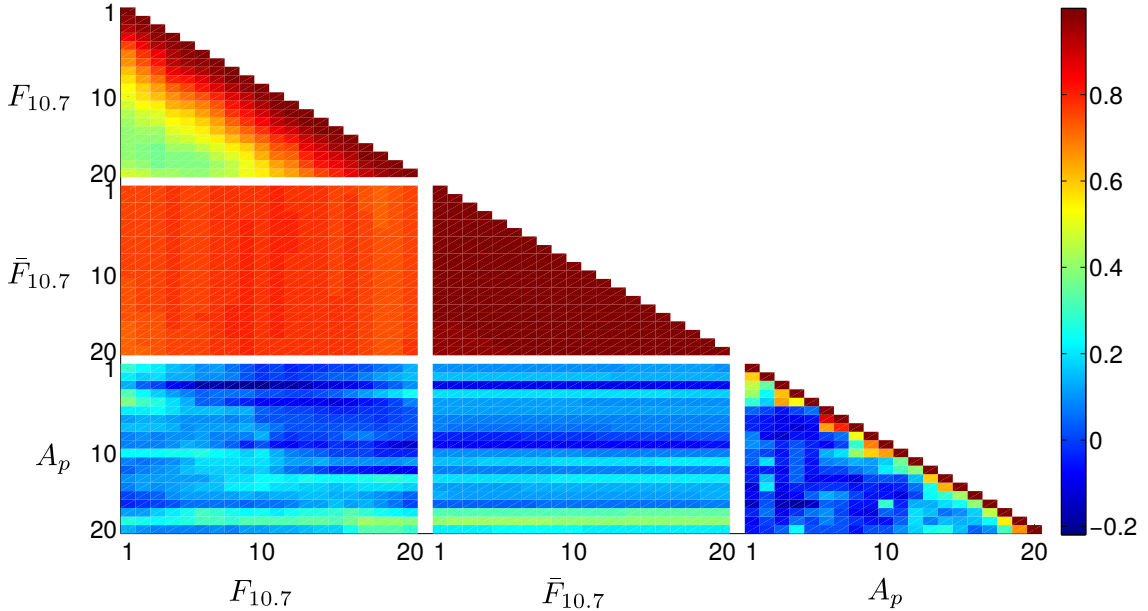


Figure 2.7: Correlation matrix of the Gaussian copula used to model the solar and geomagnetic proxies. Axes labels denote elapsed days.

according to the marginal distribution. Indeed, high values of the daily flux are expected when its average is also high. This consideration is consistent with the high cross-correlation between daily and averaged values.

Once the probabilistic model of $p_{\mathbf{F}_{10.7}, \bar{\mathbf{F}}_{10.7}, \mathbf{A}_p | \mathbf{F}_{10.7, \sim n_k}, \bar{\mathbf{F}}_{10.7, \sim n_k}, \mathbf{A}_{p, \sim n_k}}$ is available, it is possible to propagate the stochastic processes. Specifically, the values of $F_{10.7}$, $\bar{F}_{10.7}$, and A_p at time t are computed by means of the conditional probability

$$p_{F_{10.7}, \bar{F}_{10.7}, A_p | \mathbf{F}_{10.7, \sim n_k}, \bar{\mathbf{F}}_{10.7, \sim n_k}, \mathbf{A}_{p, \sim n_k}} \quad (2.13)$$

of the Gaussian copula. Here the notation $\mathbf{F}_{10.7, \sim n_k}$ indicates the vector of $\mathbf{F}_{10.7}$ without the n_k -th element. Figure 2.8 illustrates a sample trajectory generated with the probabilistic model and a real one.

Model uncertainty

Targeting practicality and efficient numerical computation, the most popular atmospheric models exploit a limited number of proxies to take the correlation between density and stochastic processes into account. This is why the uncertainty characterization of the density should also consider the uncertainty related to the discrepancy of the model with respect to reality. For instance, Scholz *et al.* compared the atmospheric densities given by different models including NRLMSISE-00, DTM-2009, JB-2008 and GITM [Scholz *et al.*, 2012]. They observed deviations in the order of 50% considering the same environmental conditions. In addition to the discrepancies among different models, Pardini *et al.* [Pardini *et al.*, 2012] and Bowman *et al.*

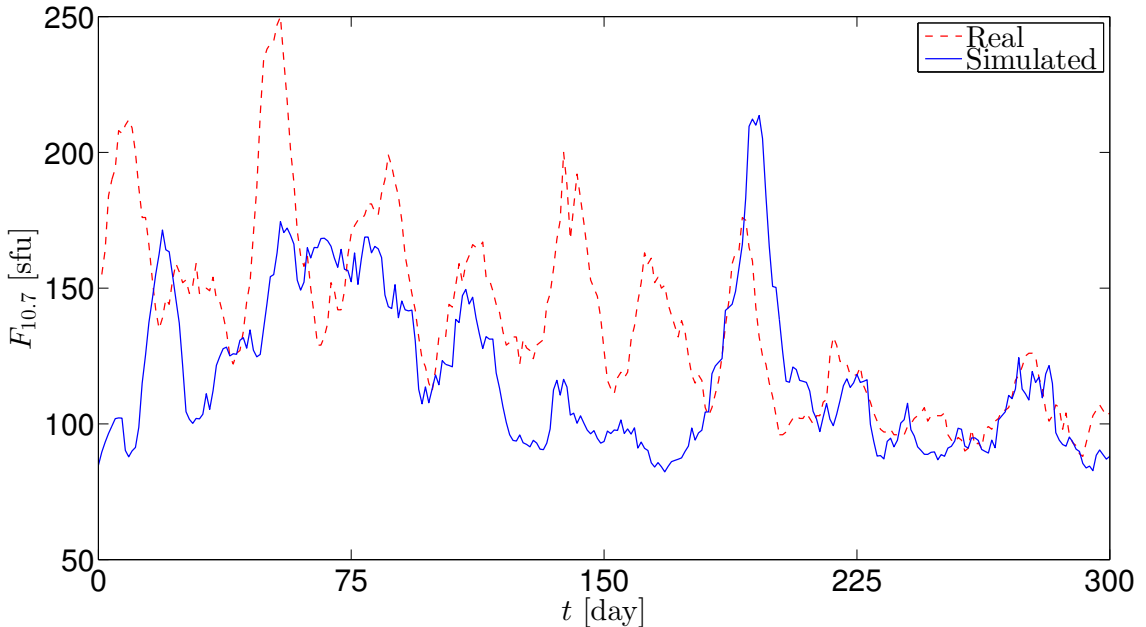


Figure 2.8: Solar flux trajectories. The red curve are observed data. The blue curve is generated with the Gaussian copula.

[Bowman and Moe, 2005, Bowman and Hrcic, 2008] studied the biases of different models by comparing physical and fitted drag coefficients. Overestimation of the density at low altitudes was observed for all models with peaks of the order of 20%. The oversimplified physical drag modeling exploited for the tuning of old models and the absence of long-term thermospheric cooling are responsible for this systematic overestimation.

To cope with model uncertainty of NRLMSISE-00, the work of Picone *et al.* [Picone, 2002] is exploited in this chapter. They performed a statistical analysis between the NRLMSISE-00 model and experimental data, and they tabulated the biases and standard deviations of the gas composition and temperature for different ranges of altitudes, for in-situ and ground based measurements, and for quiet ($A_p \leq 10$), active ($A_p \geq 50$) and all geomagnetic conditions. Biases for number density of gas species n_j and for the temperature T are defined as

$$\beta_{n_j}^{(k)} = \exp \left[E \left(\log \frac{n_j^{(data,k)}}{n_j^{(model)}} \right) \right] - 1, \quad (2.14)$$

$$\beta_T^{(k)} = E (T^{(data,k)} - T^{(model)}), \quad (2.15)$$

respectively. Superscripts *model* and *data* correspond to the outputs of the NRLMSISE-00 model and experimental data, respectively. $E[\cdot]$ denotes the expectation operator with respect to the different measurements within a single dataset, k . The corre-

sponding standard deviations are

$$\sigma_{n_j}^{(k)} = \sqrt{E\left(\log^2 \frac{n_j^{(data,k)}}{n_j^{(model)}}\right) - \log^2(\beta_{n_j}^{(k)} + 1)}, \quad (2.16)$$

$$\sigma_T^{(k)} = \sqrt{E\left((T^{(data,k)} - T^{(model)})^2\right) - \beta_T^{(k) 2}}. \quad (2.17)$$

In what follows, the measurements for all levels of geomagnetic activity in the altitude range [200, 400]km are considered⁵. To account for this variability, we define random variables, denoted η_{n_j} and η_T , for each output of NRLMSISE-00 such that the corrected atmospheric properties are given by

$$n_j = n_j^{(model)} \exp(\eta_{n_j}), \quad (2.18)$$

$$T = T^{(model)} + \eta_T. \quad (2.19)$$

These random variables are considered constant throughout a single orbit propagation and are characterized using the maximum entropy principle. Because the available information is given in terms of the bias and standard deviation and because their support is \mathbb{R} , the random variables η_{n_j} are characterized by a normal distribution with second-order descriptors

$$\mu_{n_j} = E\left(\log\left(1 + \beta_{n_j}^{(k)}\right)\right), \quad (2.20)$$

$$\sigma_{n_j} = \sqrt{E\left(\sigma_{n_j}^{(k) 2} + \mu_{n_j}^{(k) 2}\right) - \mu_{n_j}^2}; \quad (2.21)$$

here the expectation operator is with respect to the different datasets.

For the random variable η_T , non-negativity of the temperatures must be enforced, i.e., $\mathcal{I}_{\eta_T} = [-T, \infty)$. The resulting distribution depends on the temperature T and no feasible solution exists for $T < -\beta_T$, β_T being the mean value of $\beta_T^{(k)}$ across the different datasets. In practice, however, this temperature range is not physically meaningful; it is never reached using the NRLMSISE-00 model. The resulting distribution is a truncated Gaussian with left bound equal to $-T$ and second-order descriptors β_T and σ_T . We note that the distributions converge to the unbounded normal distribution for $T \gg -\beta_T + 3\sigma_T$, as illustrated in Figure 2.9.

The obtained second-order statistical descriptors of η_{n_j} and η_T are listed in Table 2.2.

⁵This is where most of the lifetime will be spent in our test case. The residual lifetime below 200km is of the order of one day.

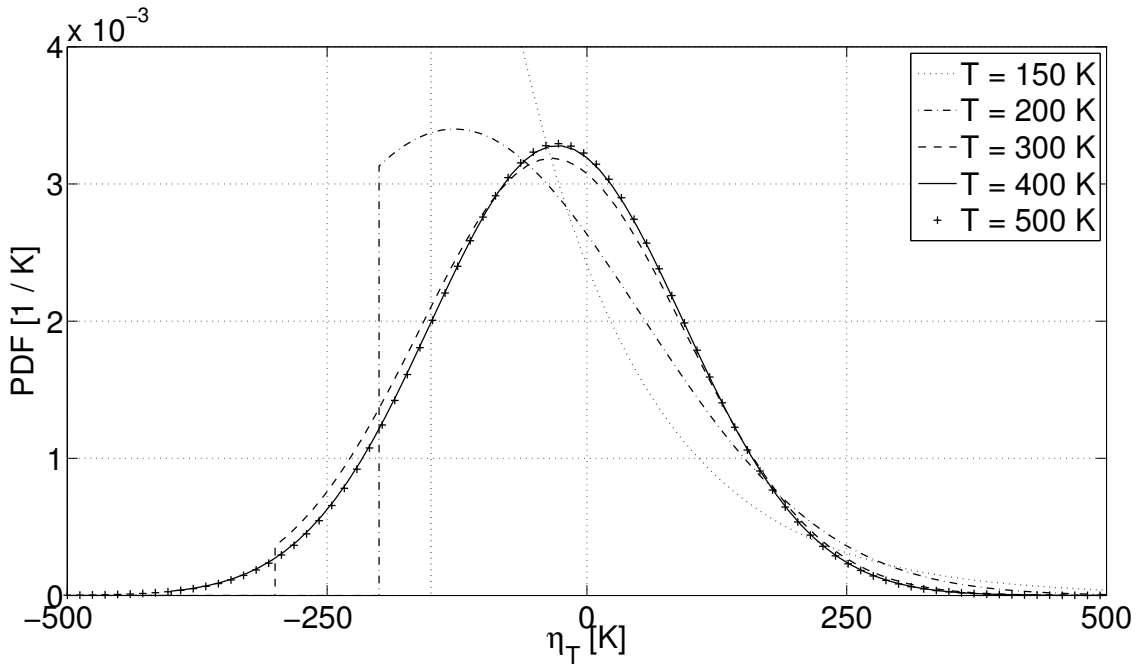


Figure 2.9: PDF of the model correction factor of the temperature in function of the external temperature (maximum entropy principle).

Table 2.2: Global biases and standard deviations of the model correction factors of the outputs of NRLMSISE-00 for all levels of geomagnetic activity and an altitude range of [200, 400]km.

Output	Mean	Std
Temperature (K)	-27.9	121.2
Helium (%)	8.0	34.7
Total oxygen (%)	1.6	25.4
Molecular nitrogen (%)	-1.1	35.9
Argon (%)	18.6	52.0
Hydrogen (%)	4.0	31.4
Atomic nitrogen (%)	-15.7	53.0

2.5.2 Ballistic Coefficient

We consider the model of physical ballistic coefficients presented in Section 1.5.3. According to this theory, the drag coefficient is determined as a function of the atmospheric conditions, i.e., gas composition and external temperature, of the physical properties of the spacecraft, i.e., the mass and geometry, of the wall temperature T_w , of the gas-surface interaction, and of its attitude, i.e.,

$$C_b = C_b(n_j, T, m, \text{geometry}, T_w, \alpha, \delta, \epsilon), \quad (2.22)$$

where α , δ , and ϵ are the energy flux accommodation coefficient, the angle of attack⁶, and the side slip angle, respectively. The accommodation coefficient is an indicator of the gas-surface interaction. It determines whether the reflected particles retain their mean kinetic energy (for $\alpha = 0$) or they acquire the spacecraft wall temperature T_w (for $\alpha = 1$) [Doornbos, 2012].

Numerical simulations we carried out pointed out that the term $4RT_w v_{TAS}^{-2}$ in Equation (1.20) is very small with respect to 1. We therefore consider it as deterministic with $T_w = 300$ K. For the energy accommodation coefficient, to our knowledge, data for its stochastic characterization are not available, and we model it as

$$\alpha = 5 \cdot 10^{-7} n_O T (1 + 10^{-7} n_O T)^{-1}, \quad (2.23)$$

as suggested by Pilinski [Pilinski et al., 2011b].

The main contribution to uncertainty depends on the outputs of the atmospheric model, which were already characterized in the previous section. Another contribution is spacecraft attitude, which determines the coefficients ψ_k and ϕ_k in Equation (1.19). The requirements for a standard QB50 spacecraft impose that the angle δ between the CubeSat's long axis and the velocity be smaller than 5 deg with 3- σ confidence [Muylaert, 2012]. There is no requirement on the side slip angle ϵ . According to the maximum entropy principle, the attitude angles δ and ϵ are modeled as a Gaussian random variable with zero mean and a standard deviation of $\frac{5}{3}$ deg, and a uniform random variable with values in [0, 360] deg, respectively. We emphasize that this analysis does not account for the commissioning, which in the case of QB50 is required to be within the first two orbiting days. For other spacecraft, commissioning might last several weeks, especially for nanosatellites with limited attitude control. During commissioning, the spacecraft is tumbling and considering this phase would require 6 degree-of-freedom propagation and the characterization of the initial angular rates, which is beyond the scope of this paper.

The results of the discussed analytical method were compared with full-blown DSMC simulations performed at the VKI. Table 2.3 shows that errors of the order of 1% were achieved, thus validating our approach. Another interesting finding from this table is that the ballistic coefficient is indeed insensitive with respect to wall temperature.

⁶For a 2U CubeSat it is defined as the angle between the long axis and the TAS direction.

Table 2.3: Errors between the analytic and DSMC-based numerical predictions for the ballistic coefficient. Full accommodation of the energy is considered for both the analytical and the numerical approaches.

Altitude [km]	AoA [deg]	Wall temperature [K]	Analytical C_b [$\frac{\text{m}^2}{\text{kg}}$]	Relative error [%]
120	0.00	273.15	1.21e-02	0.36
120	0.00	298.15	1.21e-02	0.38
120	0.00	323.15	1.21e-02	0.38
120	5.00	273.15	1.34e-02	1.34
120	5.00	298.15	1.34e-02	1.33
120	5.00	323.15	1.34e-02	1.34
120	10.00	273.15	1.51e-02	0.89
120	10.00	298.15	1.51e-02	0.86
120	10.00	323.15	1.51e-02	0.85
120	15.00	273.15	1.69e-02	1.10
120	15.00	298.15	1.69e-02	1.08
120	15.00	323.15	1.69e-02	1.05
200	0.00	273.15	1.33e-02	-0.03
200	0.00	298.15	1.34e-02	-0.02
200	0.00	323.15	1.34e-02	-0.02
200	5.00	273.15	1.46e-02	3.40
200	5.00	298.15	1.47e-02	3.39
200	5.00	323.15	1.47e-02	3.38
200	10.00	273.15	1.59e-02	0.66
200	10.00	298.15	1.59e-02	0.66
200	10.00	323.15	1.60e-02	0.65
200	15.00	273.15	1.76e-02	0.03
200	15.00	298.15	1.76e-02	0.04
200	15.00	323.15	1.76e-02	0.04
280	0.00	273.15	1.38e-02	0.01
280	0.00	298.15	1.38e-02	0.01
280	0.00	323.15	1.38e-02	-0.01
280	5.00	273.15	1.51e-02	4.11
280	5.00	298.15	1.51e-02	4.10
280	5.00	323.15	1.52e-02	4.09
280	10.00	273.15	1.63e-02	1.22
280	10.00	298.15	1.63e-02	1.21
280	10.00	323.15	1.63e-02	1.22
280	15.00	273.15	1.79e-02	0.16
280	15.00	298.15	1.79e-02	0.16
280	15.00	323.15	1.79e-02	0.16
350	0.00	273.15	1.40e-02	-0.02
350	0.00	298.15	1.40e-02	-0.01
350	0.00	323.15	1.41e-02	-0.01
350	5.00	273.15	1.54e-02	4.43
350	5.00	298.15	1.54e-02	4.40
350	5.00	323.15	1.54e-02	4.41
350	10.00	273.15	1.65e-02	1.50
350	10.00	298.15	1.65e-02	1.49
350	10.00	323.15	1.65e-02	1.49
350	15.00	273.15	1.80e-02	0.20
350	15.00	298.15	1.80e-02	0.20
350	15.00	323.15	1.81e-02	0.21

2.6 Uncertainty propagation via Monte Carlo

The MC algorithm is now used to compute the orbital lifetime of one nanosatellite of the QB50 constellation considering the uncertainty sources discussed in the previous sections and summarized in Table 2.4.

The mapping $y = g(\mathbf{x})$ is considered for which the stochastic input vector \mathbf{x} and the (scalar) VoI y are defined on the supports \mathcal{I}_X and \mathcal{I}_Y , respectively. MC propagation is a means of quantifying uncertainty in the VoI by mapping uncertainties in the inputs through the model $g(\cdot)$. The generation of a set of N realizations $\mathbf{x}_1, \mathbf{x}_2, \dots, \mathbf{x}_N$ of the stochastic vector \mathbf{X} according to the joint PDF of its elements is the first step of the MC propagation.

The direct evaluation of the mapping for each generated sample leads to N samples of the VoI from which statistics can be computed. Specifically, the second-order descriptors are given by

$$\mu_Y^{(N)} = \frac{1}{N} \sum_{j=1}^N y_j, \quad (2.24)$$

$$\sigma_Y^{(N)} = \frac{1}{N} \sum_{j=1}^N (y_j - \mu_Y^{(N)})^2. \quad (2.25)$$

The convergence and rate of convergence of MC propagation are ensured by the law of large numbers and the central limit theorem under limited assumptions. If the mean value μ_Y of the VoI exists, the law of large numbers states that the sample mean $\mu_Y^{(N)}$ converges almost surely to μ_Y as N increases. If the standard deviation σ_Y of the VoI exists and if Lindeberg's condition is satisfied, the central limit theorem states that the error $\mu_Y^{(N)} - \mu_Y$ is a normally distributed random variable with zero mean and standard deviation $\frac{\sigma_Y}{\sqrt{N}}$.

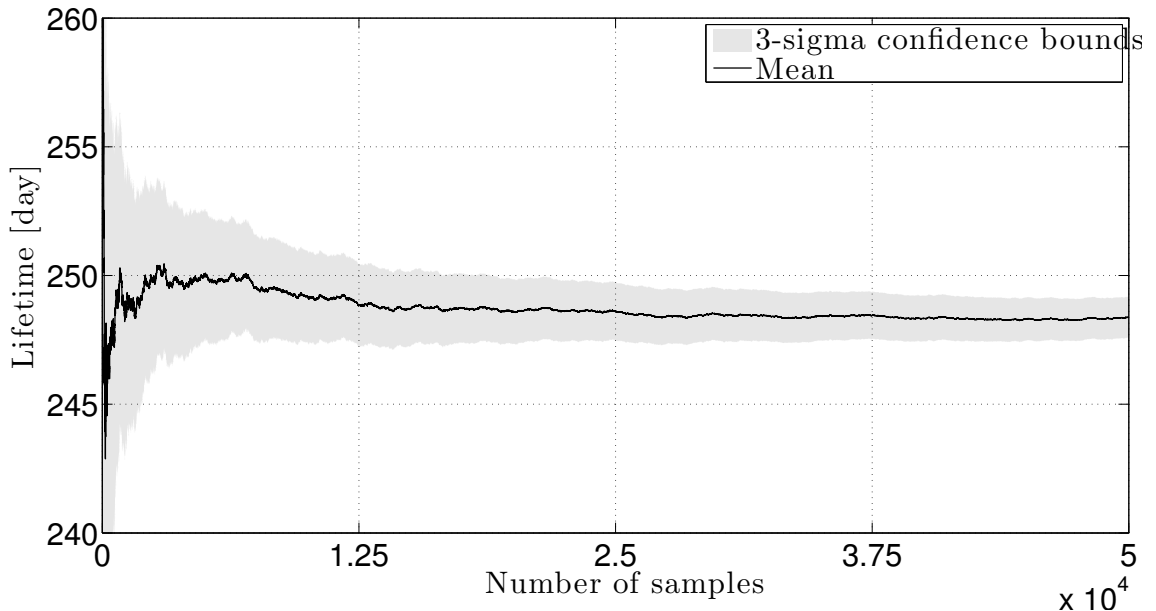
Figure 2.10 shows that 50000 evaluations were necessary for achieving the convergence of the mean value within ± 1 day with a confidence level of 3σ . Because a single orbital propagation lasts 10 minutes on average, the complete propagation was run on a computer cluster; it resulted in an accumulated computational burden of about 350 days.

Kernel density evaluation is implemented to derive a non-parametric representation of the PDF and CDF of orbital lifetime. It is presented in Figure 2.11. Useful information can be inferred from Figures 2.10 and 2.11:

- The mean orbital lifetime is 248.4 days, which is enough considering the minimum desired lifetime of 3 months.
- The standard deviation amounts to 59.0 days, which results in standard deviation to mean ratio of about 0.24. This reflects a substantial, but expected, variability of orbital lifetime that invalidates a deterministic estimation of this quantity.

Table 2.4: Summary of uncertainty characterization.

Variable	Symbol	Units	Stochastic modeling
Launch date	t_0	day	Uniform in [1/01/2016, 1/01/2017].
Altitude before injection	$h_{0,l}$	km	Truncated Gaussian $[0, +\infty)$, 380km mean, 2.5km std
Inclination before injection	$i_{0,l}$	deg	Normal with 98deg mean and 0.03deg std
Eccentricity before injection	$e_{0,l}$	-	Truncated Gaussian $[0, +\infty)$, 10^{-3} mean, $3.5 \cdot 10^{-4}$ std
RAAN before injection	$\Omega_{0,l}$	deg	Uniform in $[0, 360]$ deg
Ejection velocity (norm)	v_{ej}	m/s	Uniform in $[1, 1.5] \text{ms}^{-1}$
Ejection velocity (azimuth)	Θ	deg	Uniform in $[0, 360]$ deg
Ejection velocity (elevation)	χ	deg	Cosine distribution in $[-90, 90]$ deg
Daily solar activity	$F_{10.7}$	sfu	Gaussian cupola (Figures 2.6 and 2.7)
81-day averaged solar activity	$\bar{F}_{10.7}$	sfu	Gaussian cupola (Figures 2.6 and 2.7)
Geomagnetic index	A_p	-	Gaussian cupola (Figures 2.6 and 2.7)
Model error density	η_{n_j}	-	Gaussian with parameters listed in Table 2.2
Model error temperature	η_T	K	Truncated Gaussian, temperature dependent (Figure 2.9)
Angle of attack	δ	deg	Gaussian with 0deg mean and 5/3deg std
Roll angle	ϵ	deg	Uniform in $[0, 360]$ deg

Figure 2.10: Convergence of the mean of the orbital lifetime. The shaded area indicates $3 - \sigma$ confidence bounds on the mean.

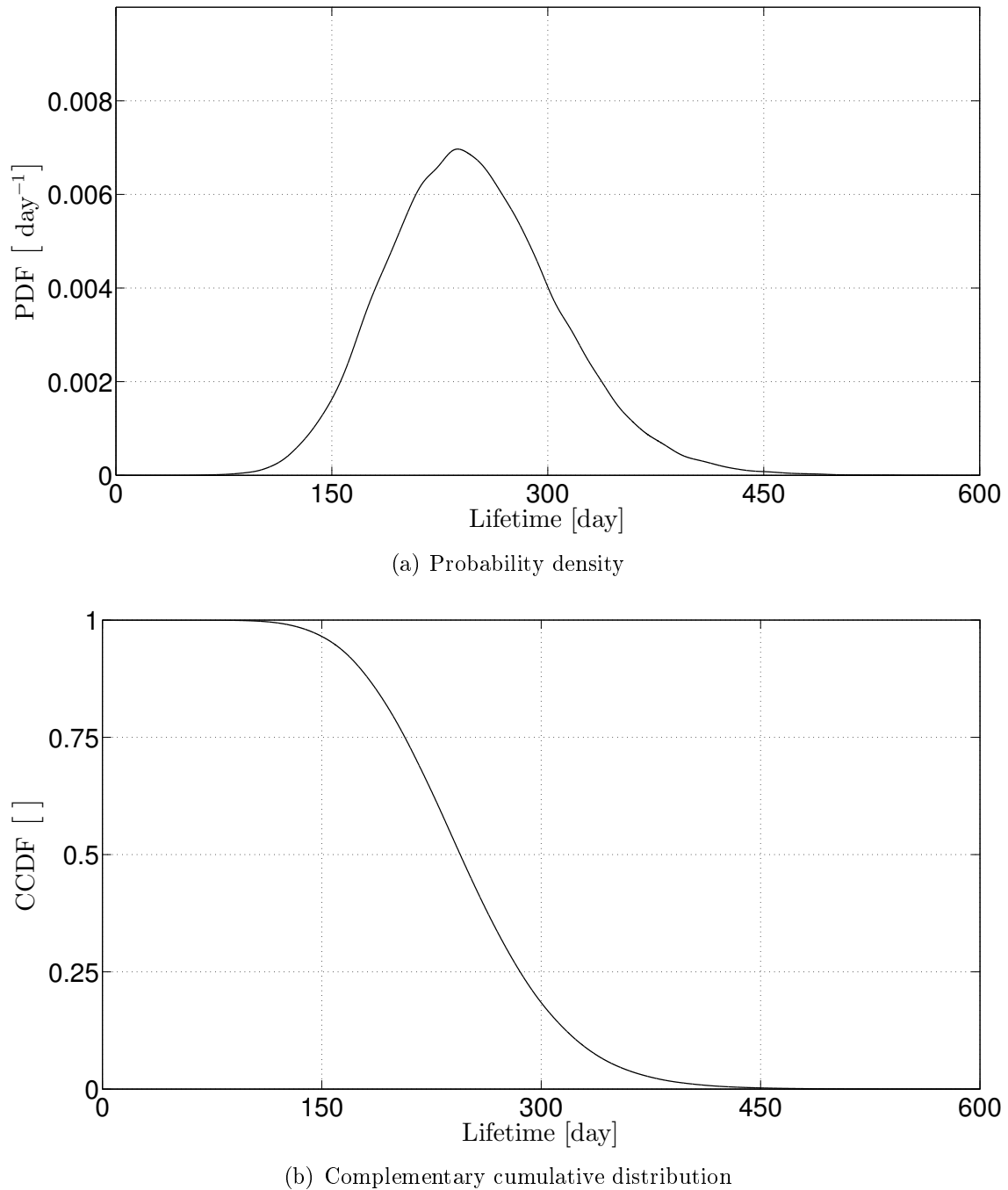


Figure 2.11: Kernel density estimations of the PDF and CCDF of the orbital lifetime.

- The lifetime can be as short as 55 days and as long as 597 days depending on the considered input sample. The fact that lifetime can vary over an entire order of magnitude emphasizes the interest of this study.

2.7 Stochastic sensitivity analysis

Uncertainty propagation allows us to obtain a statistical description of the VoI, which is useful for estimating precisely the variability affecting this quantity. The present section is devoted to stochastic sensitivity analysis for gaining insight into the nature of the propagation itself. Such an analysis is relevant for engineering purposes, particularly for decision making and for assessing the efforts needed to reduce uncertainties on the VoI. In this section, we focus on the so-called *global sensitivity analysis* [Saltelli et al., 2007]. For the sake of completeness, results on local sensitivity analysis are discussed in [Dell'Elce and Kerschen, 2014a].

The objective of global sensitivity analysis is to measure the contribution of each stochastic source in the generation of the uncertainty of the VoI, measured through its variance. The total-effect sensitivity index for the input X_j is the expected value of the variance of the VoI given all the variables but X_j .

$$\mathbb{E}\left(\text{Var}(Y|\mathbf{X}_{\sim j})\right) \quad (2.26)$$

where $\mathbf{X}_{\sim j}$ means all the elements of \mathbf{X} except the component j . The sensitivity index can be interpreted as the portion of the uncertainty in the VoI that can be attributed to the input X_j and its interactions with other variables. The sensitivity indices are often normalized with the variance of the VoI. These dimensionless coefficients are referred to as *total-effect Sobol indices* in the literature [Sobol', 1990].

The numerical computation consists in the integration of:

$$\begin{aligned} \mathbb{E}\left(\text{Var}(Y|\mathbf{X}_{\sim j})\right) &= \int_{\mathcal{I}_{\mathbf{X}_{\sim j}}} \left[\int_{\mathcal{I}_{X_j}} g(\mathbf{x})^2 p_{X_j|\mathbf{X}_{\sim j}}(x_j|\mathbf{x}_{\sim j}) dx_j \right. \\ &\quad \left. - \left(\int_{\mathcal{I}_{X_j}} g(\mathbf{x}) p_{X_j|\mathbf{X}_{\sim j}}(x_j|\mathbf{x}_{\sim j}) dx_j \right)^2 \right] p_{\mathbf{X}_{\sim j}}(\mathbf{x}_{\sim j}) d\mathbf{x}_{\sim j} \end{aligned} \quad (2.27)$$

where $p_{X_j|\mathbf{X}_{\sim j}}(x_j|\mathbf{X}_{\sim j}) \equiv \frac{p_{\mathbf{x}}}{p_{\mathbf{X}_{\sim j}}}$ is the conditional probability of x_j given $\mathbf{X}_{\sim j}$. For a set of independent variables,

$$p_{\mathbf{X}_{\sim j}}(\mathbf{x}_{\sim j}) = \prod_{k=1, k \neq j}^N p_{X_k}(x_k). \quad (2.28)$$

Both deterministic and non-deterministic integration techniques can be implemented for the numerical computation of Equation 2.27. When numerical simulation is computationally demanding, the computation of the Sobol indices might be unfeasible. It is possible to speed up the evaluation by means of a surrogate

Table 2.5: Total effect Sobol indices of the orbital lifetime. Only the indices above 0.01 are listed.

Variable	Sobol index
Launch date	
Altitude before injection	0.05
Inclination before injection	
Eccentricity before injection	
RAAN before injection	
Ejection velocity (norm)	
Ejection velocity (azimuth)	
Ejection velocity (elevation)	
Daily solar activity (mean)	0.43
81-day averaged solar activity (mean)	0.37
Geomagnetic index (mean)	0.35
Model error $O + O_2$	0.43
Model error N_2	0.08
Model error other species	
Model error temperature	
Angle of attack	
Roll angle	

model. For this purpose, we fitted a neural network surrogate model. The input for the model were all the scalar uncertain variables listed in Table 2.4 and the mean of each realization of the solar and geomagnetic activity proxies. The idea to replace the time series of the proxies with an effective solar and geomagnetic activity to reduce the dimension of the UQ problem was investigated in [Dell'Elce et al., 2014]. With 99% confidence, this model predicts the VoI within 6% accuracy. In our opinion, such precision is sufficient to estimate an OoM of the sensitivity indices.

Table 2.5 lists the Sobol indices obtained in the case study. Model error on partial density of oxygen is the main contributor to the uncertainty in the lifetime. This result confirms that a more profound knowledge of drag in rarefied flows and of thermospheric models would be highly beneficial, as heavily stressed in the literature, e.g., [Saleh et al., 2002, Moe and Moe, 2005, Woodburn and Lynch, 2005, Doornbos et al., 2005, Doornbos and Klinkrad, 2006, Naasz et al., 2007]. However, solar and geomagnetic activities are also major contributors. This is why stochastic modeling of this problem is particularly relevant and important: although some uncertainty sources might be more influential in other case study, e.g., attitude could play a more important role for tumbling spacecraft, the uncertainty due to space weather proxies is always present and it cannot be cancelled because of the stochastic nature of solar and geomagnetic activity.

2.8 Conclusion

Although some assumptions were introduced, e.g., neglecting thermospheric winds, the first challenge discussed in the Introduction of the thesis was addressed and

yielded a probabilistic characterization of the uncertainties in satellite aerodynamic modeling. This characterization was used to propagate uncertainties in the lifetime of a LEO satellite. The results obtained confirm the relevance and importance of UQ of LEO trajectories.

Chapters 3 and 6 will make use of the same characterization for other purposes, i.e., recursive drag estimation and UQ of relative maneuvers.

Chapter 3

Aerodynamic Force Estimation

Abstract

Thanks to accurate ephemerides and detailed gravitational maps, third-body and non-spherical gravitational perturbations can be modeled with sufficient precision for most applications in LEO. On the contrary, computational models of satellite aerodynamics and SRP are bound to be biased with respect to in-situ observations. Targeting accurate maneuvers and high-fidelity on-board propagation, the real-time estimation of these perturbations is desired. In this chapter, we develop a particle filter for the recursive estimation and prediction of non-gravitational forces. Although the integration of accelerometer data in the filter is straightforward, we offer a formulation that requires only GPS data. This feature makes the proposed algorithm a valuable resource for small satellites which often cannot afford accelerometers.

3.1 Introduction

Thanks to high-fidelity ephemeris and detailed gravitational maps, third-body and non-spherical gravitational perturbations can be modeled with sufficient precision for most applications in LEO. On the contrary, owing to severe uncertainty sources and modeling limitations, mathematical models of the main non-gravitational forces – namely, aerodynamics and SRP – are generally biased even when advanced formulations are considered.

To date, accurate satellite drag and SRP estimation is only envisaged in challenging missions and the recursive estimation of non-gravitational forces is generally carried out by means of high-sensitivity accelerometers [Gotlib et al., 2004]. Nonetheless, unmodeled force estimators using satellite observations only were also proposed. The method of dynamic model compensation (DMC) is arguably the most popular example of this class [Tapley et al., 2004]: first, an underlying parametric model of the unknown perturbation is adopted; then, the parameters of such model are assumed to be first-order Gauss-Markov processes and they are appended to the state vector of a recursive estimator (most often an extended Kalman filter). Provided accurate¹ and sufficiently dense satellite observations, DMC was successfully applied to the estimation of atmospheric force [Tapley et al., 1975]. In that study, no other process noise but the one in the atmospheric force itself was considered. On the other end of the spectrum, when no non-keplerian perturbation is included in the filter model and similar measurement noise is considered, DMC was shown to properly estimate forces of the order of $10^{-3} \frac{\text{N}}{\text{kg}}$ [Winn, 1975]. Similar accuracy was obtained when basic differentiation of GPS data is implemented [Zhang et al., 2006]. Nonetheless, this is far from being sufficient to estimate drag or SRP which, in general, are 3 or more orders of magnitude smaller. Batch estimators were used for ground-based estimation using observations [Bowman and Moe, 2005]. In this case, measurement noise could be largely relaxed – e.g., TLE were used in [Saunders et al., 2012] – but they were not suitable for recursive implementation. An alternative approach based on optimal control policies was recently developed in [Lubey and Scheeres, 2014]. This technique was able to account for both atmospheric drag and SRP and it could be naturally extended to complex models of the force, but it did not lend itself to recursive estimation, neither.

In the broader context of Bayesian estimation of dynamical systems, sequential Monte Carlo (SMC) algorithms – which include the popular particle filters – are valuable tools to optimally approximate the posterior distribution of hidden Markov processes [Doucet et al., 2000, 2001]. Compared to Kalman filtering techniques, particle filters do not require any assumption on either the linearity of the system nor the nature of the noise. Such generality is obtained at the price of a greater computational burden. Particle filters were used in several problems in astrodynamics, e.g., space object tracking [McCabe and DeMars, 2014], orbit determination [Kim et al., 2012, Mashiku et al., 2012], and relative state estimation [Zeng et al., 2012,

¹Standard deviations of 5m for the position and $1 \frac{\text{mm}}{\text{s}}$ for the velocity.

Hwang and Speyer, 2011]. However, to the best of our knowledge, no attempt of non-gravitational force estimation using particle filters is available in the literature.

In this chapter, we propose an SMC algorithm for the recursive inference of non-gravitational perturbations from satellite observations with no supporting in-situ acceleration measurements. Our approach is conceptually similar to DMC but, on the top of the aforementioned advantages and drawbacks of SMC, we show that it provides good estimates of the non-gravitational perturbations even when fairly inaccurate measurements and a modest underlying propagator are used. The filter works by updating the empirical distribution of a prescribed number of weighted particles. Each particle consists of some dynamical states – read one set of orbital elements and non-gravitational perturbations – and some parameters involved in the computation of unknown forces, e.g., drag and reflectivity coefficients. Weights are assigned to the particles based on the agreement between propagated states and observations. Secular effects of the non-gravitational perturbations allow ‘good’ particles to emerge when weights are recursively updated.

Mean orbital elements are exploited as the only measurements. They can be obtained either by converting GPS states with a contact transformation – as in the present chapter – or by using TLE. This feature has a twofold interest: first, TLE of most LEO objects are available; second, analytical and semi-analytical propagators, e.g., SGP4, can be naturally integrated in the algorithm to propagate particles. For these reasons, this work can be a valuable resource both for space situational awareness (SSA) applications, e.g., space debris’ orbit determination and propagation from TLE, and to enhance short-term trajectory predictions on-board small satellites with moderate computational resources.

The chapter is organized as follows. Section 3.2 discusses the mathematical background on SMC and it outlines the algorithm of the filter. Section 3.3 details the different ‘ingredients’ of the specific problem of non-gravitational force estimation. Insight and caveats on the choice of the parameters of the filter are discussed, as well. Finally, numerical simulations in high-fidelity environment are carried out in Section 3.4.

3.2 Particle filtering for mixed parameter and state estimation

Let $\mathbf{P} \in \mathcal{I}_{\mathbf{P}}$ and $\{\mathbf{X}_\tau \in \mathcal{I}_{\mathbf{X}}, \tau \in \mathbb{N}^+\}$ be an $\mathcal{I}_{\mathbf{P}}$ -valued vector² of uncertain parameters and an $\mathcal{I}_{\mathbf{X}}$ -valued discrete-time m -th order Markov process provided with *transitional prior distribution*

$$\mathbf{X}_{\tau+1} \mid (\mathbf{x}_\tau, \mathbf{x}_{\tau-1}, \dots, \mathbf{x}_{\tau-m}, \mathbf{p}) \sim f(\mathbf{x}_{\tau+1} \mid \mathbf{x}_\tau, \dots, \mathbf{x}_{\tau-m}, \mathbf{p}) \quad \forall t \geq m, \quad (3.1)$$

²Column vectors are considered throughout the whole chapter.

respectively; here, $f(\mathbf{x}_{\tau+1} \mid \mathbf{x}_\tau, \dots, \mathbf{x}_{\tau-m}, \mathbf{p})$ is the PDF defining how the process evolves given outcomes of the parameters' vector and the past $m+1$ realizations of the state, i.e., $\mathbf{P} = \mathbf{p}$, $\mathbf{X}_{\tau-j} = \mathbf{x}_{\tau-j} \forall j = 0, \dots, m$. The tilde means “distributed according to”. Some \mathcal{I}_Y -valued observations $\{Y_\tau \in \mathcal{I}_Y, \tau \in \mathbb{N}^+\}$ are available. Given the outcomes of the current and past states and of the parameters, measurements are assumed to be conditionally independent in time:

$$\mathbf{Y}_\tau \mid (\mathbf{x}_\tau, \dots, \mathbf{x}_0, \mathbf{p}) \sim g(\mathbf{y}_\tau \mid \mathbf{x}_\tau, \mathbf{p}) \quad \forall t \geq 0; \quad (3.2)$$

the PDF $g(\mathbf{y}_\tau \mid \mathbf{x}_\tau, \mathbf{p})$ is referred to as *marginal likelihood distribution*. Equations (3.1) and (3.2) define a hidden Markov model (HMM).

The filtering problem consists in estimating the *marginal posterior distribution* of the process³, which is the joint PDF of \mathbf{P} and \mathbf{X}_τ conditional to the observations $\mathbf{Y}_0, \dots, \mathbf{Y}_\tau$ [Doucet et al., 2001]:

$$\text{pdf}(\mathbf{x}_\tau, \mathbf{p} \mid \mathbf{y}_0, \dots, \mathbf{y}_\tau) \propto g(\mathbf{y}_\tau \mid \mathbf{x}_\tau, \mathbf{p}) \text{pdf}(\mathbf{x}_\tau, \mathbf{p} \mid \mathbf{y}_0, \dots, \mathbf{y}_{\tau-1}). \quad (3.3)$$

Closed-form solution of Equation (3.3) is not generally available. Particle filters approximate the posterior by means of SMC sampling of Equation (3.3). If direct sampling from $\text{pdf}(\mathbf{x}_\tau, \mathbf{p} \mid \mathbf{y}_0, \dots, \mathbf{y}_{\tau-1})$ is not possible or inconvenient, an auxiliary proposal distribution, $q(\mathbf{x}_{\tau+1}, \mathbf{p} \mid \mathbf{y}_{\tau+1}, \mathbf{x}_\tau, \dots, \mathbf{x}_{\tau-m})$, is used yielding the *importance sampling* approach. In theory, any PDF can be used as importance distribution provided that its support covers \mathcal{I}_X and \mathcal{I}_P . However, the adequate choice of the proposal distribution is crucial to achieve good performance of the filter and avoid degeneracy [Daum, 2005].

Several SMC formulations exist [Doucet et al., 2000, 2001], but most of them do not consider parameters estimation. Our algorithm is mainly inspired by the work of Liu *et al.* [Liu and West, 2001], which combines state and parameter estimation by means of *artificial evolution* and *kernel smoothing* of parameters. The filter works by propagating a set of n particles from τ to $\tau+1$. Each particle consists of the last $m+1$ states, a set of parameters, and a weight:

$$j\text{-th particle} := \left\{ \mathbf{x}_\tau^{(j)}, \dots, \mathbf{x}_{\tau-m}^{(j)}; \mathbf{p}_\tau^{(j)}; w_\tau^{(j)} \right\} \quad j = 1, \dots, n; \quad (3.4)$$

weights are nonnegative and such that $\sum_{j=0}^1 w_\tau^{(j)} = 1$. The notation $\mathbf{p}_\tau^{(j)}$ indicates the outcome of \mathbf{P} for the j -th particle at time τ . However, we stress that \mathbf{P} is a multivariate random variable and it is not part of the dynamical states.

Monte Carlo approximation of the posterior at time t is given by the empirical

³The analogy with Kalman filtering is established by considering f and g as non-linear and non-Gaussian generalizations of the predictor and innovation equations, respectively, and the marginal of the posterior distribution as the updated state and covariance estimates.

measure⁴

$$\text{pdf}(\mathbf{x}_\tau, \mathbf{p} \mid \mathbf{y}_0, \dots, \mathbf{y}_\tau) \approx \sum_{j=1}^n w_\tau^{(j)} \delta(\mathbf{x}_\tau - \mathbf{x}_\tau^{(j)}) \delta(\mathbf{p} - \mathbf{p}_\tau^{(j)}), \quad (3.5)$$

where $\delta(\cdot)$ is the multi-dimensional Dirac delta function.

Figure 3.1 depicts the procedure for the recursive update of the particles, which consists of three steps:

Prediction prediction of the states is provided by their expected value at time $\tau + 1$:

$$\tilde{\mathbf{x}}_{\tau+1}^{(j)} = \int_{\mathcal{I}_{\mathbf{x}}} \mathbf{x}_{\tau+1} q(\mathbf{x}_{\tau+1}, \mathbf{p}_\tau^{(j)} \mid \mathbf{y}_{\tau+1}, \mathbf{x}_\tau^{(j)}, \dots, \mathbf{x}_{\tau-m}^{(j)}) d\mathbf{x}_{\tau+1}, \quad j = 1, \dots, n. \quad (3.6)$$

Artificial evolution of the parameters using kernel smoothing consists of using a Gaussian mixture Model (GMM) to update $\mathbf{p}_\tau^{(j)}$ [Liu and West, 2001]. Prior update is given by the location of GMM's kernels

$$\tilde{\mathbf{p}}_{\tau+1}^{(j)} = \gamma \mathbf{p}_\tau^{(j)} + \frac{1-\gamma}{n} \sum_{i=1}^n \mathbf{p}_\tau^{(i)}, \quad j = 1, \dots, n; \quad (3.7)$$

where $\gamma \in [0, 1]$ is a discount factor for the dispersion of the variance of the parameters. Section 3.3 provides with further insight into this parameter.

The weights of the mixture's kernels are computed with the outcomes of Equations (3.6) and (3.7):

$$\tilde{w}_{\tau+1}^{(j)} \propto w_\tau^{(j)} \alpha(\mathbf{y}_{\tau+1}, \tilde{\mathbf{x}}_{\tau+1}^{(j)}, \mathbf{x}_\tau^{(j)}, \dots, \mathbf{x}_{\tau-m}^{(j)}, \tilde{\mathbf{p}}_{\tau+1}^{(j)}). \quad (3.8)$$

Here, function α is defined as

$$\begin{aligned} \alpha(\mathbf{y}_{\tau+1}, \mathbf{x}_{\tau+1}, \mathbf{x}_\tau, \dots, \mathbf{x}_{\tau-m}, \mathbf{p}) &= \\ \frac{f(\mathbf{x}_{\tau+1} \mid \mathbf{x}_\tau, \dots, \mathbf{x}_{\tau-m}, \mathbf{p}) g(\mathbf{y}_{\tau+1} \mid \mathbf{x}_{\tau+1}, \mathbf{p})}{q(\mathbf{x}_{\tau+1}, \mathbf{p} \mid \mathbf{y}_{\tau+1}, \mathbf{x}_\tau, \dots, \mathbf{x}_{\tau-m})}. \end{aligned} \quad (3.9)$$

Re-sampling when multiple recursive updates are performed, weights might become unevenly distributed, with most of them approaching zero. When this happens, only one to very few particles efficiently contribute to the measure of Equation (3.5) – whose variance degenerates – and the quality of the posterior's approximation to computational cost ratio is necessary poor. In layman's terms, huge effort is devoted to propagate particles which inadequately

⁴We refer to this measure as a PDF with an abuse of notation.

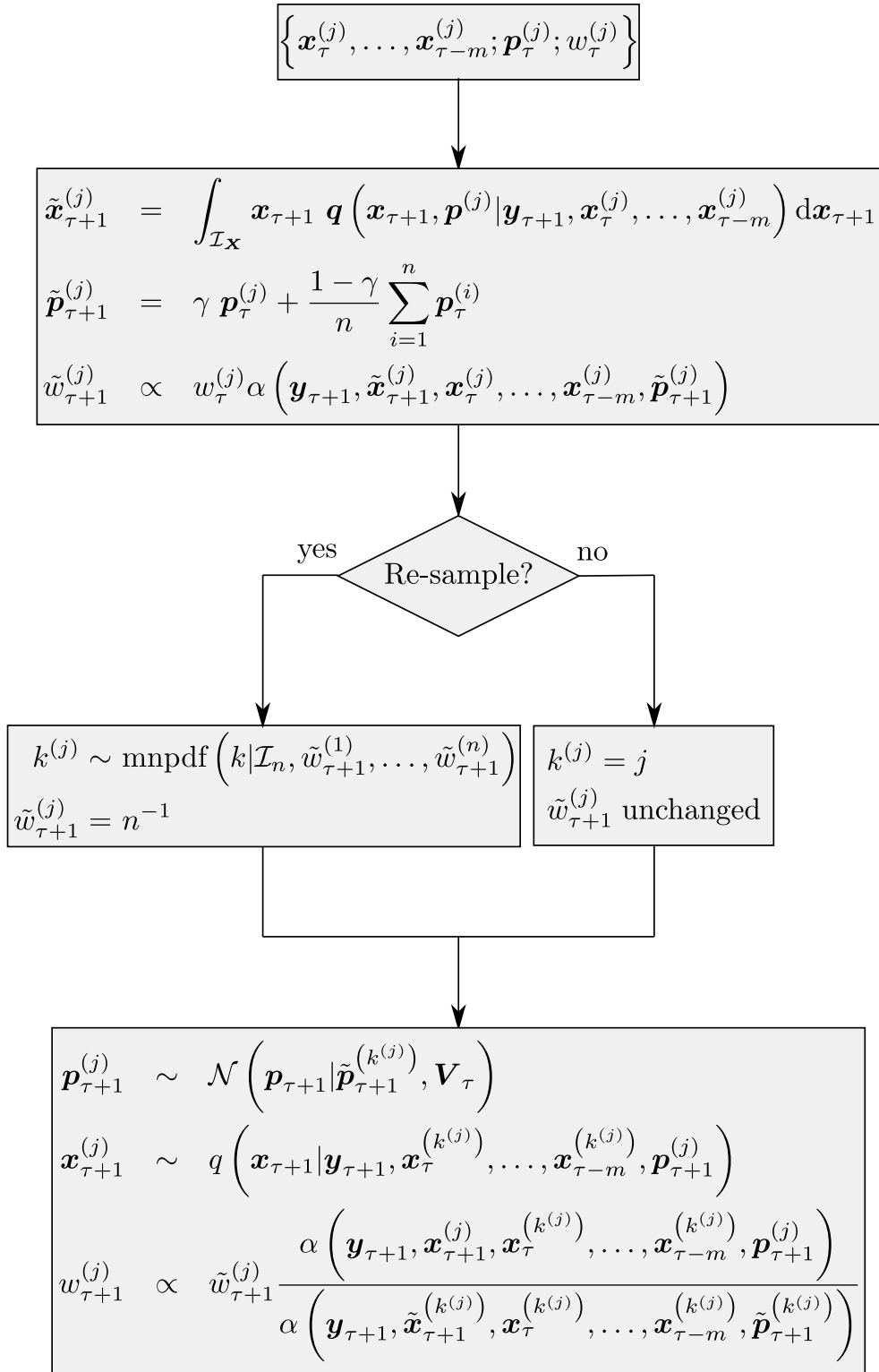


Figure 3.1: Algorithm for the recursive estimation of states and parameters. At every time step, this loop is repeated for the n particles.

contribute to approximate the posterior⁵. This issue is referred to as *degeneracy*.

To prevent degeneracy from occurring, a new set of uniformly-weighted particles is re-sampled from Equation (3.5). This is achieved by sampling n integer coefficients, $k^{(j)} j = 1, \dots, n$, with values in $\mathcal{I}_n = \{1, 2, \dots, n\}$ and corresponding probabilities $\{\tilde{w}_{\tau+1}^{(1)}, \tilde{w}_{\tau+1}^{(2)}, \dots, \tilde{w}_{\tau+1}^{(n)}\}$:

$$k^{(j)} \sim \text{mnpdf}\left(k | \mathcal{I}_n, w_{\tau+1}^{(1)}, \dots, w_{\tau+1}^{(n)}\right), \quad j = 1, \dots, n. \quad (3.10)$$

Here, $\text{mnpdf}\left(\cdot | \mathcal{I}_n, w_{\tau+1}^{(1)}, \dots, w_{\tau+1}^{(n)}\right)$ denotes the \mathcal{I}_n -valued multinomial distribution. After re-sampling, predicted weights are reset to $\hat{w}_{\tau+1}^{(j)} = \frac{1}{n}, j = 1, \dots, n$.

Several existing algorithms perform re-sampling at each time step. Because secular effects of non-gravitational forces need long observation windows to become appreciable, recursive updates are needed to identify good particles⁶. For this reason, we discourage systematic re-sampling in this problem. Hence, we re-sample only if both of the following conditions are satisfied:

1. at least r time steps elapsed since the last re-sampling;
2. the degeneracy indicator, $\frac{1}{\sum_{j=1}^n (\tilde{w}_{\tau+1}^{(j)})^2}$, is below a prescribed threshold⁷.

If re-sampling does not occur, weights $\tilde{w}_{\tau+1}^{(j)}$ are not modified and $k^{(j)} = j \forall j \in [1, n]$.

Update all kernels of the GMM used for artificial evolution share the same variance,

$$\mathbf{V}_\tau = (1 - \gamma^2) \frac{1}{n-1} \sum_{j=1}^n (\mathbf{p}_\tau^{(j)} - \bar{\mathbf{p}}_\tau) (\mathbf{p}_\tau^{(j)} - \bar{\mathbf{p}}_\tau)^T, \quad (3.11)$$

where $\bar{\mathbf{p}}_\tau = \frac{1}{n} \sum_{i=1}^n \mathbf{p}_\tau^{(i)}$. Coefficient $(1 - \gamma^2)$ is introduced so that both mean and variance of the sample $[\mathbf{p}_\tau^{(1)}, \mathbf{p}_\tau^{(2)}, \dots, \mathbf{p}_\tau^{(n)}]$ are preserved by the unweighted mixture.

Hence, states and parameters are updated by sampling from the GMM and

⁵We emphasize that the memory to store a particle and the computations involved in its update is the same regardless the specific value of the weight.

⁶To put it another way, good particles have to collect multiple ‘good marks’ before we are able to distinguish them from bad ones.

⁷We note that, because weights are nonnegative and sum to one, the indicator is in the range $[1, n]$. In addition, it equals the two corner case 1 and n if all weights but one are equal to zero and if particles are uniformly weighted, respectively.

importance distribution, respectively,

$$\mathbf{p}_{\tau+1}^{(j)} \sim \mathcal{N}\left(\mathbf{p}_{\tau+1}|\tilde{\mathbf{p}}_{\tau+1}^{(k(j))}, \mathbf{V}_t\right), \quad (3.12)$$

$$\mathbf{x}_{\tau+1}^{(j)} \sim q\left(\mathbf{x}_{\tau+1}|\mathbf{y}_{\tau+1}, \mathbf{x}_{\tau}^{(k(j))}, \dots, \mathbf{x}_{\tau-m}^{(k(j))}, \mathbf{p}_{\tau+1}^{(j)}\right), \quad (3.13)$$

$$w_{\tau+1}^{(j)} \propto \tilde{w}_{\tau+1}^{(j)} \frac{\alpha\left(\mathbf{y}_{\tau+1}, \mathbf{x}_{\tau+1}^{(j)}, \mathbf{x}_{\tau}^{(k(j))}, \dots, \mathbf{x}_{\tau-m}^{(k(j))}, \mathbf{p}_{\tau+1}^{(j)}\right)}{\alpha\left(\mathbf{y}_{\tau+1}, \tilde{\mathbf{x}}_{\tau+1}^{(k(j))}, \mathbf{x}_{\tau}^{(k(j))}, \dots, \mathbf{x}_{\tau-m}^{(k(j))}, \tilde{\mathbf{p}}_{\tau+1}^{(k(j))}\right)}, \quad (3.14)$$

for $j = 1, \dots, n$.

3.3 Non-gravitational force estimation

The exploitation of the algorithm in Figure 3.1 requires the definition of:

- the states, \mathbf{x} , and parameters, \mathbf{p} , to be estimated,
- the proposal distribution, $f(\mathbf{x}_n|\mathbf{x}_{n-1}, \mathbf{p})$ and $f_0(\mathbf{x}_0|\mathbf{p})$,
- the measurement model,

This section is devoted to the assessment of these entities. In addition, recommendations on the choice of the parameters of the filter are provided.

3.3.1 States and parameters

The main objective of this study is to obtain a probabilistic model for non-gravitational forces which is consistent with the observations of the satellite's motion and, if possible, which yields short-to-medium period predictions of these quantities, i.e., of the order of a couple of orbits or days, respectively. For this reason, the aerodynamic force, \mathbf{f}_{drag} , and SRP, \mathbf{f}_{SRP} , are included in the states. In addition, in view of the measurement model discussed in Section 3.3.3, also the mean equinoctial states, \mathcal{E}_{eq} are included, so that

$$\mathbf{x} = \begin{bmatrix} \mathbf{f}_{drag} \\ \mathbf{f}_{SRP} \\ \mathcal{E}_{eq} \end{bmatrix}. \quad (3.15)$$

Targeting a flexible parametric modeling of the aerodynamic force, the n_{exp} -th order harmonic expansion

$$\mathbf{f}_{drag} = -\frac{1}{2}\lambda(\mathbf{r}, t)\frac{\rho_0 C_D}{m}(S_D + S_0) \sum_{j=1}^{n_{exp}} (a_j \cos(j\theta) + b_j \sin(j\theta)) \mathbf{v}_{TAS} \quad (3.16)$$

is considered. Here, θ is the argument of latitude, while a_j , b_j , S_0 , and $\lambda(\mathbf{r}, t)$ are a set of coefficients which locally capture the principal features of the atmospheric drag, i.e.,

- a_j and b_j model the short-period variations ($\mathcal{O}(t_{orb})$) due to the day-night atmospheric bulge and the variations of the altitude of the satellite due to the orbit's eccentricity and Earth's oblateness,
- S_0 models the variable energy accommodation, which causes drag not to be proportional to the cross section S_D ,
- λ models medium-period variations ($\mathcal{O}(\text{day})$) due to variations in the solar and geomagnetic activity indices, $F_{10.7}$, $\bar{F}_{10.7}$, A_p . It is defined as:

$$\lambda(\mathbf{r}, t) = \frac{\rho_{J71}(\mathbf{r}, t, F_{10.7}(t), \bar{F}_{10.7}(t), A_p(t))}{\rho_{J71}(\mathbf{r}, t, F_{10.7}(0), \bar{F}_{10.7}(0), A_p(0))} \quad (3.17)$$

where the ρ_{J71} denotes the Jacchia-71 atmospheric model [Jacchia, 1971]. Indeed, any model accounting for space weather can serve this purpose.

When filtering, it is reasonable to assume that the information on the current space weather is available so that, given the GPS position, λ is known. On the contrary, the other coefficients have to be estimated by the filter. We note that, for completeness, an exponential term should be included to fully capture the local behavior of the atmosphere. However, we did not observe any relevant improvement when including the exponential decay in our simulations. Possibly, the exponential term should be included for long propagations. On the contrary, the drag coefficient is not included in the vector of parameters because its influence cannot be distinguished from ρ_0 .

The detailed modeling of SRP is beyond the scope of this thesis. For this reason, we model SRP with a single reflectivity coefficient, C_r . When the satellite is in sunlight, the SRP is evaluated as [Montenbruck and Gill, 2000]:

$$\mathbf{f}_{SRP} = -P_{Sun} C_r \frac{S_{SRP}}{m} \frac{\mathbf{r}_{Sun}}{r_{Sun}^3} AU^2 \quad (3.18)$$

where $P_{Sun} = 4.56 \cdot 10^{-6} \frac{N}{m^2}$, S_{SRP} , and \mathbf{r}_{Sun} are the radiation pressure, the cross section toward the Sun direction, and the sun position vector, respectively. Both the information on S_{SRP} and on P_{Sun} are assumed to be available when filtering.

The vector of parameters is thus:

$$\mathbf{p} = [\rho_0, S_0, a_1, \dots, a_m, b_1, \dots, b_m]. \quad (3.19)$$

Medium-period predictions

We open a brief digression to note that when the estimated parameters are available, it is possible to use Equation (3.16) in conjunction with the characterization of the

space weather proxies proposed in Chapter 2 to generate stochastic medium-period predictions of the atmospheric drag, i.e., of the order of a couple of days.

For this purpose, it is sufficient to introduce random time series of the space weather proxies in the coefficient $\lambda(t)$. MC analysis can be implemented to estimate statistical descriptors of the probability distribution.

We will use this feature in Chapter 6.

3.3.2 Proposal and prior distributions

The proposal distribution is aimed at generating the samples $\tilde{\mathbf{x}}$ in the second block of Figure 3.1.

First, the proposal of the mean elements is computed as:

$$\tilde{\boldsymbol{\varepsilon}}_{eq,t+1} \approx \tilde{\boldsymbol{\varepsilon}}_{eq,t} + \frac{t_{pf}}{t_{orb}} \int_0^{t_{orb}} \dot{\boldsymbol{\varepsilon}}_{eq} dt \quad (3.20)$$

where t_{orb} and t_{pf} are the orbital period and the time step of the filter, respectively. The integral is approximated with high-order Gaussian quadrature rules, so that arbitrary perturbations like Equations (3.16) and (3.18) can be accommodated in the integral.

Equations (3.16) and (3.18) are then used to update the drag and SRP, respectively.

Concerning the prior distributions, $f(\mathbf{x}_{t+1} | \mathbf{x}_t, \mathbf{p})$, a second-order stationary stochastic process with the power spectral density (PSD) proposed by [Zijlstra et al., 2005] is added to Equation 3.16. In addition, process noise for the mean elements is inferred by means of the maximum likelihood principle from the time series of the “real” mean elements obtained by integrating the osculating elements with high-order Gaussian quadratures (blue curves in Figure 3.2)

Because these two sources of noise are not correlated, the prior is given by their product.

3.3.3 Measurement model

In this Thesis, we stressed in several occasions that the aerodynamic force is a dominant perturbation in LEO. Nonetheless, this is not evident by considering its OoM in Figure 1.1. For example, we note that neglecting a tenth-order harmonic of the gravity field or introducing a three-meter measurement error on the position result in perturbations of the same OoM of the atmospheric force. What makes drag a dominant perturbation is its integral action, which results in a systematic dissipation of the energy.

For this reason, owing to measurement errors and unmodeled perturbations, estimating drag by differentiating the GPS position is not an option. For this reason, the likelihood function, $g(\mathbf{y}_t | \mathbf{x}_t)$ must account for the integral action of the drag.

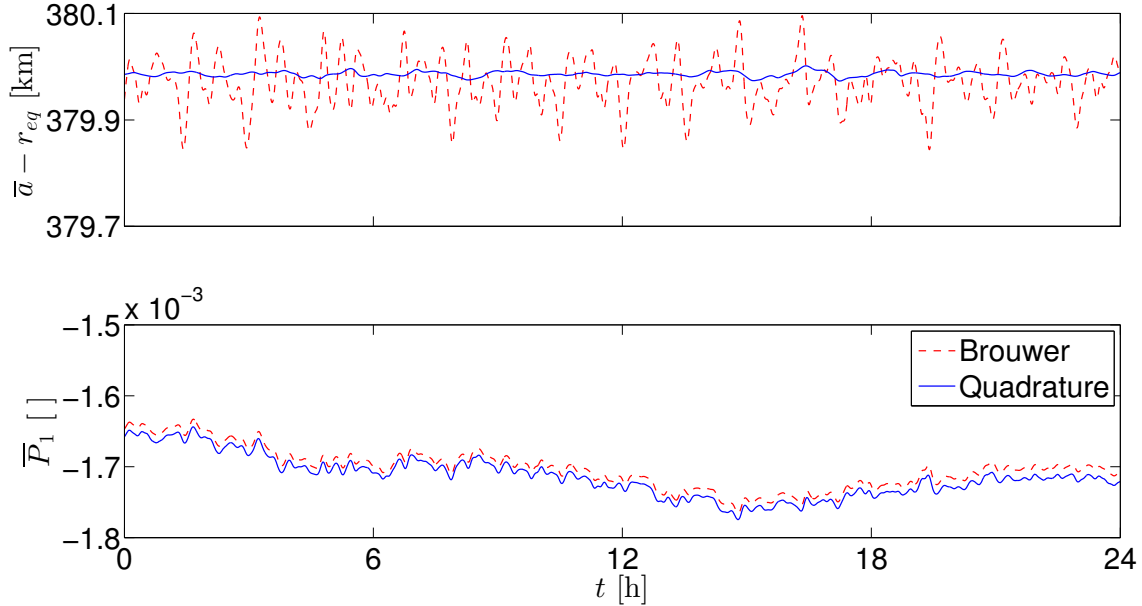


Figure 3.2: Comparison between the mean equinoctial elements \bar{a} and \bar{P}_1 computed with the first-order Brouwer model and with a Gaussian quadrature. The input parameters are listed in Table 3.2 but the aerodynamic force and SRP are turned off.

In this context, the measurements \mathbf{y} we consider are the mean elements computed from the Brouwer-Lyddane contact transformation [Lyddane, 1963].

The distribution, g , is estimated by means of the MLE by comparing the observed and "true" mean elements, i.e., first-order Brouwer against numerical integration.

According to Figure 3.2, the measurement noise is much larger than the process noise for the semi-major axis. In addition, bias occurs for other elements, e.g., the equinoctial element P_1 in the figure. For this reason we cannot afford systematic re-sampling as discussed in the introduction. In fact, when resampling we reset the weights of the particle filter. Because of the huge measurement error compared to the process noise, if re-sampling occurs periodically, i.e., no more than once per orbit, the errors of the contact transformation are partially compensated, so that the good particles can emerge.

We finally note that GPS noise is negligible compared to the noise injected by the contact transformation. In this study it was neglected.

3.3.4 Recommendations for the choice of filter's parameters

A satisfactory trade-off between accurate and rapid convergence is achieved by carefully setting up the parameters of the filter. The first parameter to consider is clearly the number of particles, n . Increasing n nearly-linearly grows up the overall computational burden. However, particles must be enough to adequately represent the posterior distribution and to delay degeneracy. This is particularly true dur-

Table 3.1: Influence of the filter's parameters on the quality of the estimation.

Parameter	Benefits when increased	Drawbacks when increased
n	Enhanced representation of the posterior Convergence when \mathbf{p} has large variance	Computational cost increases
Δt	Improved signal-to-noise ratio	Low sensitivity to short-period variations
r	Improved signal-to-noise ratio	Degeneracy might occur
m	Reduced sensitivity to process noise	Increased memory to store particles
γ	Enhanced convergence Enhanced identification of good particles	Increased complexity PDFs Diversify particles after multiple updates

ing the early phase of the estimation, when uncertainty in the parameters \mathbf{p} is still very large. Adaptive choice of n is encouraged. This can be achieved during the re-sampling step.

Because of the aforementioned secular effects of non-gravitational perturbations and because measurement are statistically independent of time, increasing filter's time step, Δt , and re-sampling rate, r , enhances signal-to-noise ratio and, as such, improves the convergence of the estimation. Augmenting r is preferred when high-fidelity models of the non-gravitational force are used since large time steps would reduce sensitivity to short-period variations. Nonetheless, degeneracy may occur for large r . Based on our experience, the product $r \Delta t$ should be of the order of one-to-few orbital periods⁸.

Neglected gravitational harmonics are the major source of process noise for averaged orbital elements. The order of the HMM, m , is a crucial parameter to mitigate their impact. Specifically, Earth's rotation causes relevant correlations in the time series of the noise after about one-day. For example, Figure 3.3 depicts the auto-correlation of the process noise for the case-study detailed in Section 3.4. Ideally, the order of the HMM should be large enough to cover this interval, but this may dramatically increase the required memory to store particles and augment the complexity of the importance and marginal prior distribution. Autocorrelations below few minutes lag – say $\Delta t \leq 10\text{min}$ – are close to one, so that we suggest using $m = 1$ if filter's time step is of this order of magnitude⁹.

Finally, the parameter γ regulates the memory of the particles: according to Equations (3.7) and (3.11), parameters \mathbf{p} are nearly unchanged after being updated if $\gamma \simeq 1$; on the contrary, they lose most memory of their previous value if $\gamma \simeq 0$. According to [Liu and West, 2001], values between 0.96 and 0.99 are valuable for this parameter. We sustain this recommendation herein, owing to the need for multiple updates to identify ‘good’ particles.

Table 3.1 summarizes all these caveats.

⁸One being sufficient for orbits below 500km.

⁹In this case, using $m = 0$ would result in extremely severe process noise, while larger m would be an unnecessary waste of computational resources.

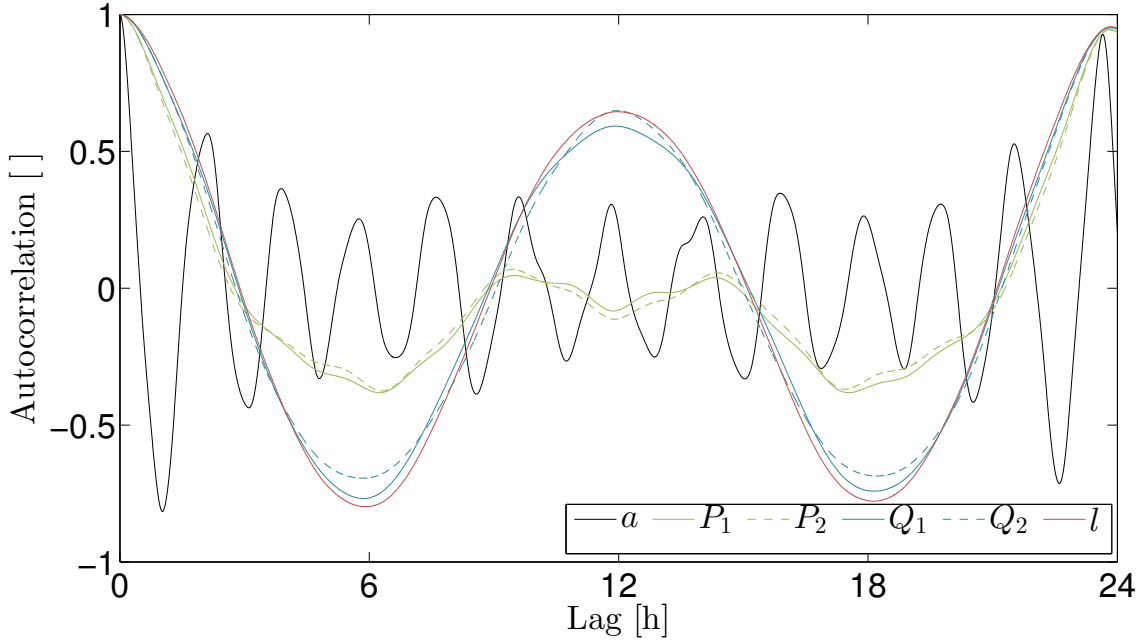


Figure 3.3: Autocorrelation of the process noise of averaged elements using the analytical propagator.

3.4 High-fidelity simulations

The highly-detailed environment described in Section 1.6 is exploited to validate the developments. The atmospheric density of the propagator is modeled by means of NRLMSISE-00. We note that λ was defined on purpose with a different model. The simulation parameters are listed in Table 3.2.

In order to train both S_0 and ρ_0 , an attitude maneuver is performed after 6 hours. The maneuver works by re-orientating the satellite from its minimum to its maximum drag configuration.

Figure 3.4 illustrates the filtered and true non-gravitational force. Thanks to the variable λ , the filter is agile to follow variations due to the solar activity. The close-up zoom of the initial and terminal phases show important difference in the width of the 90% confidence bounds. This is because the parameters need about 50 hours to converge adequately, as shown in Figure 3.5. Nonetheless, the true signal is captured in the bounds since the earliest phases of the simulation.

Finally, Figure 3.6 proves that the filter performs well also at higher altitude. Owing to the vertical rarefaction of the atmosphere, the convergence of the parameters is slower compared to Figure 3.4. However, also in this case the true force is captured in the 90% confidence bounds since the early phase of the simulation and, eventually, the accuracy at the end of the simulation is comparable to the one obtained at lower altitude.

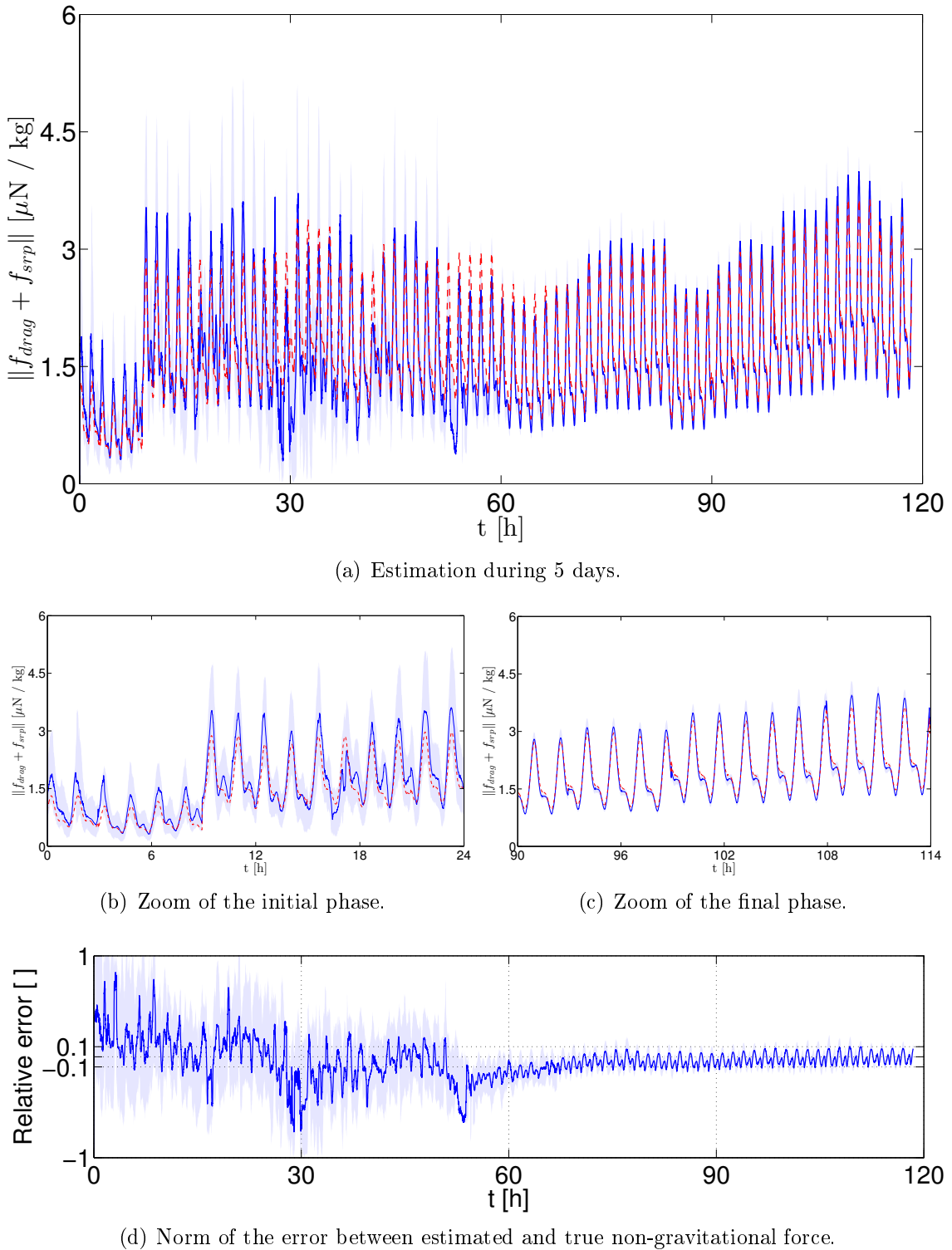


Figure 3.4: Non-gravitational force estimation assuming constant space weather proxies in the simulations. The red-dashed curve is the norm of the true non-gravitational force. The blue-solid curve is its median estimate. The shaded region depicts 90% confidence bounds.

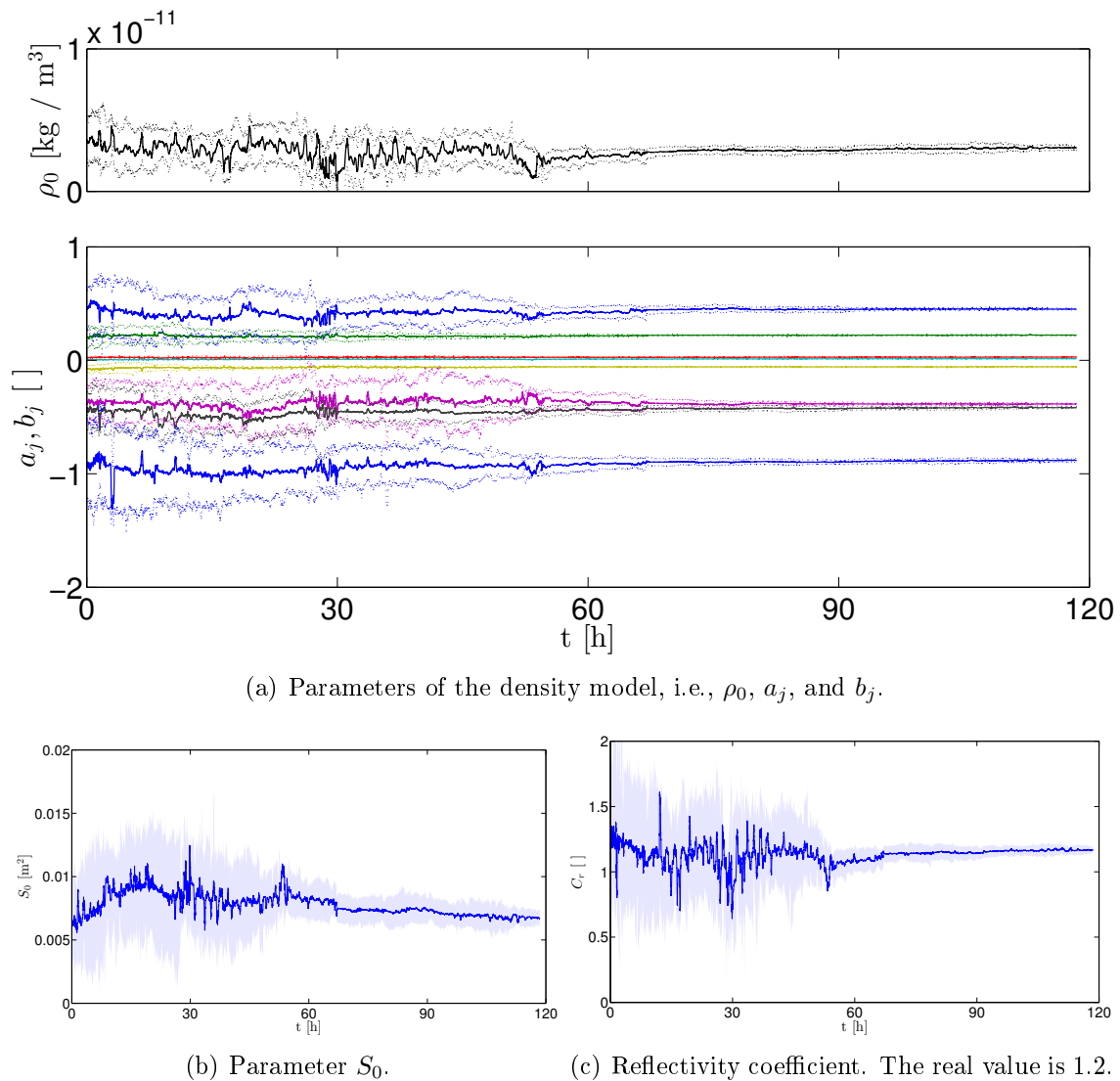
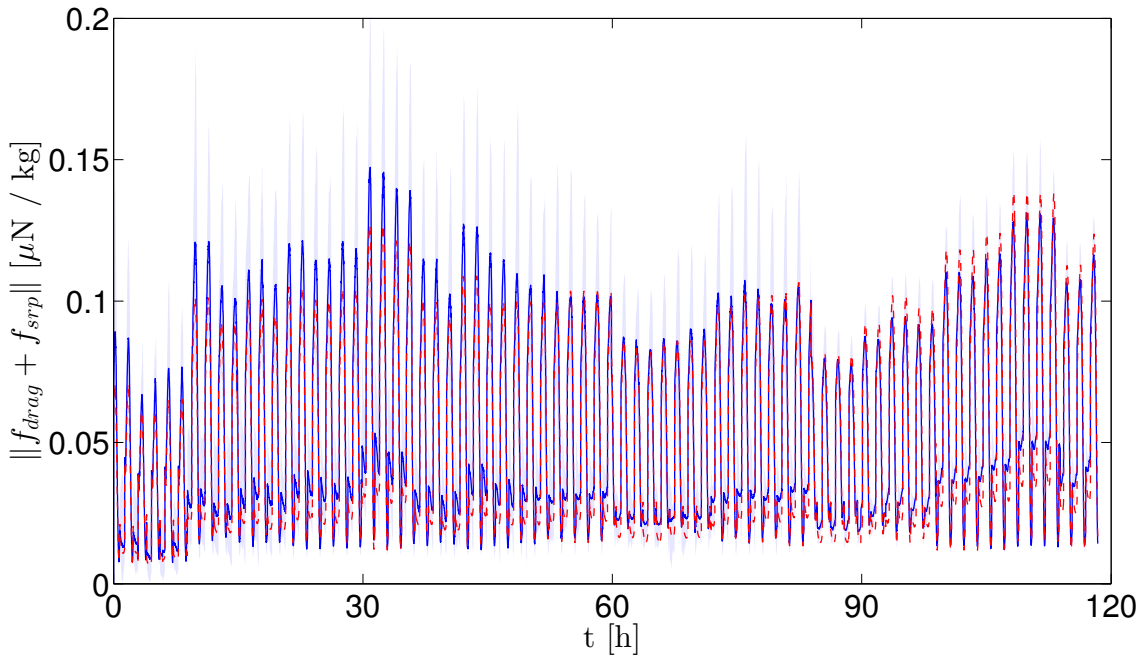
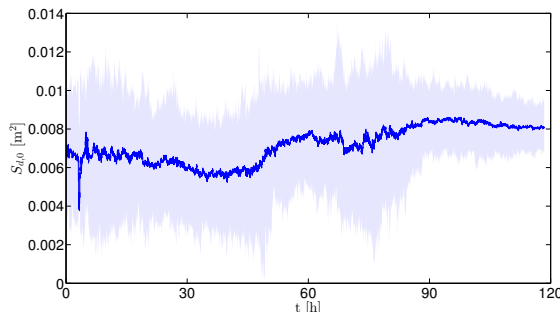
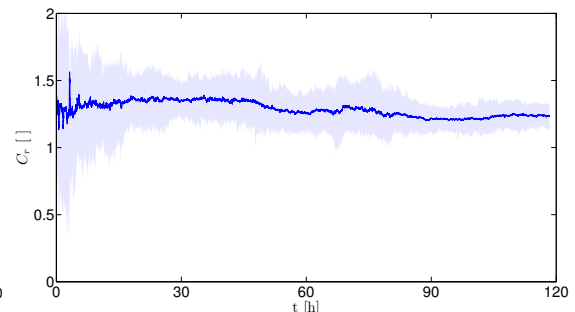


Figure 3.5: Convergence of the parameters for the estimation of drag and SRP.



(a) Estimation of the non-conservative force during 5 days.

(b) Parameter S_0 .

(c) Reflectivity coefficient. The real value is 1.2.

Figure 3.6: Results at 600km altitude. The other simulation parameters are listed in Table 3.2. In the top plot: the red-dashed curve is the norm of the true non-gravitational force, the blue-solid curve is its median estimate, and the shaded region depicts 90% confidence bounds.

Table 3.2: Simulation parameters.

Initial osculating elements	semi-major axis	$r_{eq} + 380$	km
	eccentricity	0.001	
	inclination	98	deg
	RAAN	30	deg
	argument of perigee	120	deg
	true anomaly	15	deg
Space weather proxies	Epoch	1/04/2013	
	observed time history at Epoch		
Spacecraft's properties	mass	4	kg
	dimensions (parallelepiped)	$0.1 \times 0.3 \times 0.1$	m^3
	drag coefficient	2.2	
Particle filter	reflectivity coefficient	1.2	
	particles, n	200	
	time step, Δt	30	s
	re-sampling rate, r	round $\left(\frac{2t_{orb}}{\Delta t}\right)$	
	HMM's order, m	1	
discount factor, γ			0.99

3.5 Conclusion

A particle filter for the recursive estimation of non-gravitational forces was proposed. By using GPS data only, the filter is able to estimate these forces with an adequate accuracy, which makes it interesting for small satellites which cannot afford high-sensitivity accelerometers. The performance of the filter can be improved by considering a second-order contact transformation which could reduce the measurement noise.

The medium-period prediction capabilities of the filter are exploited in Chapter 6 to generate sample predictions of the drag.

Chapter 4

Analytical Propagation of Low-Earth Orbits

Abstract

This chapter offers a time-explicit solution for the motion of a satellite under the influence of the two dominant perturbations in LEO, namely the Earth's oblateness and the atmospheric drag. Averaging technique and series expansions are used to obtain the analytical solution assuming constant atmosphere and either small or very small orbital eccentricity, i.e., $e^4 \approx 0$ and $e^2 \approx 0$, respectively. Thanks to a vectorial formulation, the methodology is singularity-free and results can be expressed, for example, in osculating Keplerian and equinoctial elements. Then, an analytical propagator for the relative motion is obtained by means of the inertial solution and a succession of rotations with the advantage that no simplifying assumption is made on the relative dynamics. Numerical simulations show that the accuracy of the propagator is dominated by the underlying Brouwer-Lyddane contact transformation used to map initial conditions from osculating to mean elements. The loss of accuracy due to the introduction of drag in the model is negligible. In the propagator for the relative motion, most errors due to the contact transformation are compensated. The practical outcome of the chapter is an efficient orbit propagator suitable for on-board implementation.

4.1 Introduction

The main perturbations affecting LEO are due to the planet's oblateness and to the atmosphere. Their combined effect causes the orbit to dramatically drift from the Keplerian unperturbed model. While the oblateness perturbation falls in the range of conservative forces, allowing the classical perturbation methods to be applied, the atmospheric drag is a non-conservative force, so that using the tools of analytical mechanics is, at best, challenging.

While the search for analytical models that accommodate the planet's oblateness – referred to as *the main problem in artificial satellite theory* – brought a multitude of approximate solutions [Garfinkel, 1959, Brouwer, 1959, Kozai, 1959, Lyddane, 1963, Vinti, 1960, Lara and Gurfil, 2012], the analytical solutions for the atmospheric drag are present in a much less significant amount. In most cases they are not suitable for realistic orbit propagation.

The study of the effect of atmospheric drag on satellite orbits dates back to the early spaceflight era. One of the initial and most important contributions in this area belongs to [King-Hele, 1964]. Although the effects of the atmospheric drag were approached thoroughly, the effects of the other perturbations were neglected. [Battin, 1999] developed closed-form expressions for the averaged variation of semi-major axis and eccentricity in terms of modified Bessel functions of the first kind. [Vallado, 2001] and [Roy, 2004] presented approximate variational equations for eccentricity and semi-major axis, deriving expressions for the secular rates of change of the orbital elements which are suitable for series expansion in powers of the eccentricity. [Mittleman and Jezewski, 1982] offered the solution to a modified problem, where an approximate expression for the drag acceleration was used such that the problem becomes integrable. [Vinh et al., 1979] also derived closed-form expressions for the variational equations of the orbital elements with respect to a new independent variable, and then used numerical techniques to integrate the equations of motion. All aforementioned studies either treat the atmospheric drag exclusively, and hence ignore the Earth's oblateness, or they do not provide analytical closed-form solution, but offer instead numerical techniques to integrate them.

Combining the effects of the two major perturbations is challenging, and few attempts were made so far. [Brouwer and Hori, 1961] extended the Poincaré-von Zeipel-based method developed previously by [Brouwer, 1959] to accommodate the atmospheric drag, failing to reach closed-form equations of motion, but rather focusing on the separation of the variables in order to ease numerical integration. [Parks, 1983] included the averaged effects of the atmospheric drag in the contact transformation developed in [Brouwer, 1959], but this methodology rises issues regarding the possibility to invert the contact transformation, which is needed to propagate osculating elements. [Franco, 1991] developed an approximate model for the motion about an oblate planet with atmosphere, but only for the equatorial case.

With the emergence of distributed space systems flying in LEO, the problem of the relative motion between satellites is also of significant importance [Alfriend et al., 2009]. Reliable propagators for the relative dynamics in LEO cannot neglect the

two dominant perturbations, especially when the satellites have different ballistic properties. The relative equations of motion in the unperturbed case were first deduced by Clohessy and Wiltshire [Clohessy and Wiltshire, 1960] by assuming an approximate linearized model and a circular reference trajectory. They were then extended to an elliptic reference trajectory by Tschauner and Hempel [Tschauner and Hempel, 1964]. The solution to the full nonlinear model of the unperturbed relative motion was derived by several authors [Gurfil and Kasdin, 2004, Condurache and Martinusi, 2007a,b], then extended to the relative motion in a general central force field [Condurache and Martinusi, 2007c]. The effect of the J_2 zonal harmonic term on the relative motion of satellites was approached by several authors, and a closed-form solution expressed in mean orbital elements was also provided [Condurache and Martinusi, 2009]. To our knowledge, a closed-form solution of the relative motion of satellites in the presence of both J_2 and atmospheric drag perturbations is still missing in the literature.

The first objective of this chapter is to develop a *new analytical propagator for the absolute motion* suitable for on-board implementation and for short-term predictions under J_2 and drag perturbations. A second objective is to obtain a *closed-form solution for the relative motion*. The latter can be directly obtained from the inertial solution without any further assumption by using kinematic transformations inspired by [Condurache and Martinusi, 2007a,b].

The present approach is based on the so-called *perturbation averaging method*, which consists of an expansion in trigonometric series (with respect to the mean anomaly) where only the first term is retained. This approach already exists for the J_2 -only perturbation, namely the Brouwer first-order model, and it is possible to develop it by simple manipulations, as in [Hestenes, 1999, Condurache and Martinusi, 2013]. The same averaging technique can be applied to the drag acceleration, obtaining the variational equations for the orbital elements with the combined effect of J_2 and drag. Assuming that (i) the atmospheric density is constant and (ii) the orbit eccentricity is small (both situations $e^2 \approx 0$ and $e^4 \approx 0$ are addressed), a new *time-explicit solution to the equations of motion for the averaged classical orbital elements* is achieved. Thanks to the vectorial formalism, the solution is singularity-free.

The chapter is organized as follows. Section 4.2 details the modeling assumptions inherent to this chapter and describes the approach for the solution of the problem. The analytical solution for the inertial motion is detailed in Section 4.3, and Section 4.4 shows how it can be used to obtain closed-form solution for the relative motion by means of a simple change of frame. Finally, the numerical validation of the developments is discussed in Section 4.5.

Dr Martinusi was the main contributor to this study. This chapter is the result of the close collaboration with him [Martinusi et al., 2014, 2015].

4.2 Variational method and averaging

Consider the IVP (1.1) with:

$$\mathbf{f}_p = \mathbf{f}_{J_2} + \mathbf{f}_d \quad (4.1)$$

where \mathbf{f}_{J_2} and \mathbf{f}_d model the specific forces due to the Earth's oblateness and to the drag, respectively. Assuming a constant atmospheric density, ρ_0 , and neglecting the co-rotating component of the TAS in Equation (1.17) and the lift, the expressions of the perturbing accelerations are:

$$\mathbf{f}_{J_2} = -\frac{3k_2}{r^4} \left[\left(1 - 5\frac{z^2}{r^2} \right) \hat{\mathbf{r}} + 2\frac{z}{r} \hat{\mathbf{k}}_{ToD} \right] \quad (4.2a)$$

$$\mathbf{f}_{drag} = -C_0 \|\dot{\mathbf{r}}\| \dot{\mathbf{r}} \quad (4.2b)$$

with the notations:

$$k_2 = \frac{\mu J_2 r_{eq}^2}{2}, \quad C_0 = \frac{1}{2} C_D \frac{S_{ref}}{m} \rho_0$$

Here, J_2 and z are the second zonal harmonic – $J_2 = 1.08263 \cdot 10^{-3}$ for the Earth – and the projection of the position vector on the Earth's rotation axis, i.e., $z = \mathbf{r} \cdot \hat{\mathbf{k}}_{ToD}$, respectively.

If the perturbing specific force \mathbf{f}_p is taken into account, the integral of motion defined in Equation (1.2), i.e., \mathbf{h} , \mathbf{e} , and ϵ , are no longer constant. The motion can still be referred to these quantities, but their variations must be accounted for. A classical perturbation method of averaging is used, where the averages over one period of the unperturbed motion are computed for the aforementioned integrals of motion. For computational purposes, it is more convenient to use the semi-major axis a instead of the specific energy ϵ . The derivatives of \mathbf{h} , \mathbf{e} , and a are [Hestenes, 1999]:

$$\begin{aligned} \dot{\mathbf{h}} &= \mathbf{r} \times \mathbf{f}_p, \\ \dot{\mathbf{e}} &= \frac{1}{\mu} [\mathbf{f}_p \times \mathbf{h} - (\mathbf{r} \times \mathbf{f}_p) \times \dot{\mathbf{r}}], \\ \dot{a} &= \frac{2a^2}{\mu} (\dot{\mathbf{r}} \cdot \mathbf{a}_d). \end{aligned} \quad (4.3)$$

Denote by T_{orb} the main period of the unperturbed motion, and by n the mean motion, i.e.,

$$T_{orb} = \frac{2\pi}{\sqrt{\mu}} a^{3/2} = \frac{2\pi}{n}.$$

The averages over one period T_{orb} of the unperturbed motion of the derivatives

expressed in Equations (4.3) are defined as follows:

$$\dot{\bar{\mathbf{h}}} = \frac{1}{T_{orb}} \int_0^{T_{orb}} (\mathbf{r} \times \mathbf{f}_p) dt \quad (4.4a)$$

$$\dot{\bar{\mathbf{e}}} = \frac{1}{\mu T_{orb}} \int_0^{T_{orb}} [\mathbf{f}_p \times \bar{\mathbf{h}} - (\mathbf{r} \times \mathbf{f}_p) \times \dot{\mathbf{r}}] dt \quad (4.4b)$$

$$\dot{\bar{a}} = \frac{2a^2}{\mu T_{orb}} \int_0^{T_{orb}} (\dot{\mathbf{r}} \cdot \mathbf{f}_p) dt \quad (4.4c)$$

It is convenient to refer all the vector functions used in Equations (4.4) to a reference frame, which is classically chosen to be the averaged perifocal frame, $\{\hat{\bar{\mathbf{e}}}, \hat{\bar{\mathbf{p}}}, \hat{\bar{\mathbf{h}}}\}$, defined in Section 1.3.

Unless stated otherwise, all the vectors which are expressed as column matrices are referred to this particular reference frame. The position and velocity vectors in the perifocal frame are:

$$\mathbf{r} = r \begin{bmatrix} \cos f \\ \sin f \\ 0 \end{bmatrix}; \quad \mathbf{v} = \frac{h}{p} \begin{bmatrix} -\sin f \\ e + \cos f \\ 0 \end{bmatrix}$$

if expressed with respect to the true anomaly, and:

$$\mathbf{r} = \begin{bmatrix} a(\cos E - e) \\ b \sin E \\ 0 \end{bmatrix}; \quad \mathbf{v} = \frac{na}{r} \begin{bmatrix} -a \sin E \\ b \cos E \\ 0 \end{bmatrix}$$

if expressed with respect to the eccentric anomaly. Here, $b = a\sqrt{1-e^2}$ denotes the semi-minor axis.

In the right-hand side of Equations (4.4), the expressions are linear with respect to \mathbf{f}_p , and therefore they may be separated as:

$$\frac{d}{dt}(\bar{}) = \frac{d}{dt}(\bar{})_{J_2} + \frac{d}{dt}(\bar{})_{drag}$$

The expressions of $\dot{\bar{\mathbf{h}}}_{J_2}$, $\dot{\bar{\mathbf{e}}}_{J_2}$ and $\dot{\bar{a}}_{J_2}$ are computed as [Condurache and Martinusi, 2013]:

$$\dot{\bar{\mathbf{h}}}_{J_2} = -\frac{3k_2}{\bar{b}^3} (\hat{\mathbf{k}}_{ToD} \cdot \hat{\bar{\mathbf{h}}}) (\hat{\mathbf{k}}_{ToD} \times \hat{\bar{\mathbf{h}}}) \quad (4.5a)$$

$$\dot{\bar{\mathbf{e}}}_{J_2} = \frac{3\bar{e}k_2}{2\bar{h}\bar{b}^3} \left\{ - \left[1 - 3(\hat{\mathbf{k}}_{ToD} \cdot \hat{\bar{\mathbf{h}}})^2 \right] \hat{\bar{\mathbf{p}}} + 2(\hat{\mathbf{k}}_{ToD} \cdot \hat{\bar{\mathbf{p}}})(\hat{\mathbf{k}}_{ToD} \cdot \hat{\bar{\mathbf{h}}}) \hat{\bar{\mathbf{h}}} \right\} \quad (4.5b)$$

$$\dot{\bar{a}}_{J_2} = 0 \quad (4.5c)$$

where

$$\bar{b} = \bar{a}\sqrt{1 - \bar{e}^2}$$

As expected, the magnitudes of vectors $\bar{\mathbf{h}}_{J_2}$ and $\bar{\mathbf{e}}_{J_2}$ remain constant, based on the fact that:

$$\frac{d}{dt} \|\bar{\mathbf{h}}_{J_2}\|^2 = 2\bar{h}_{J_2} (\hat{\bar{\mathbf{h}}} \cdot \dot{\bar{\mathbf{h}}}_{J_2}) = 0 \quad \frac{d}{dt} \|\bar{\mathbf{e}}_{J_2}\|^2 = 2\bar{e}_{J_2} (\hat{\bar{\mathbf{e}}} \cdot \dot{\bar{\mathbf{e}}}_{J_2}) = 0$$

For this reason, the magnitudes \bar{h} and \bar{e} are only affected by the atmospheric drag. Their derivatives are computed in the following.

Let $K(\cdot)$ and $E(\cdot)$ be the complete elliptic integrals of the first and second kinds, respectively [Abramowitz and Stegun, 1964]:

$$K(w) = \int_0^1 \frac{du}{\sqrt{1 - w^2 u^2}}, \quad E(w) = \int_0^1 \frac{\sqrt{1 - u^2}}{\sqrt{1 - w^2 u^2}} du \quad 0 \leq w \leq 1$$

Then, the variations of \mathbf{h} , \mathbf{e} and a that are due to the atmospheric drag are computed from Equations (4.4) by using the equality:

$$\frac{1}{T_{orb}} \int_0^T \mathcal{F}(E(t)) dt = \frac{1}{2\pi a} \int_0^{2\pi} r \mathcal{F}(E) dE,$$

which is valid for any continuous vector or scalar function \mathcal{F} , and is deduced from $dE = (na/r)dt$. It follows:

$$\begin{aligned} \dot{\bar{\mathbf{h}}}_{drag} &= -\frac{\mu C_0 \sqrt{1 - e^2}}{2\pi} \left(\int_0^{2\pi} \sqrt{1 - e^2 \cos E} dE \right) \hat{\bar{\mathbf{h}}} \\ \dot{\bar{\mathbf{e}}}_{drag} &= -\frac{4C_0 \sqrt{\mu} (1 - \bar{e}^2)}{\pi \sqrt{\bar{a}}} \left[\left(\int_0^{2\pi} \frac{\sqrt{1 - e^2 \cos E}}{1 - e \cos E} \cos E dE \right) \hat{\bar{\mathbf{e}}} \right. \\ &\quad \left. + \left(\frac{1}{\sqrt{1 - e^2}} \int_0^{2\pi} \frac{\sqrt{1 - e^2 \cos E}}{1 - e \cos E} \sin E dE \right) \hat{\bar{\mathbf{p}}} \right] \\ \dot{\bar{a}}_{drag} &= -\frac{C_o}{2\pi} \sqrt{\frac{\mu}{\bar{a}^3}} \int_0^{2\pi} \frac{\sqrt{1 - e^2 \cos E}}{1 - e \cos E} (1 + e \cos E) dE \end{aligned}$$

After manipulations, the closed-form expressions for the variations of \mathbf{h} , \mathbf{e} and a due to the atmospheric drag are obtained as:

$$\dot{\bar{\mathbf{h}}}_{drag} = -\frac{2C_0 \mu \sqrt{1 - \bar{e}^2}}{\pi} E(\bar{e}) \hat{\bar{\mathbf{h}}} \quad (4.6a)$$

$$\dot{\bar{\mathbf{e}}}_{drag} = -\frac{4C_0 \sqrt{\mu} (1 - \bar{e}^2)}{\pi \bar{e} \sqrt{\bar{a}}} [K(\bar{e}) - E(\bar{e})] \hat{\bar{\mathbf{e}}} \quad (4.6b)$$

$$\dot{\bar{a}}_{drag} = -\frac{4C_0 \sqrt{\mu \bar{a}}}{\pi} [2K(\bar{e}) - E(\bar{e})] \quad (4.6c)$$

The variations due to drag of the magnitudes of vectors \bar{h} and \bar{e} are determined based on Equations (4.6) as follows:

$$\dot{\bar{h}} = -\frac{2C_0\mu\sqrt{1-\bar{e}^2}}{\pi}E(\bar{e}), \quad \dot{\bar{e}} = -\frac{4C_0\sqrt{\mu}(1-\bar{e}^2)}{\pi\bar{e}\sqrt{\bar{a}}}[K(\bar{e}) - E(\bar{e})]. \quad (4.7)$$

The variation of the averaged semi-major axis, namely Equation (4.6c), is used instead of $\dot{\bar{h}}$, because one of the Equations (4.7) is redundant, i.e.,

$$\dot{\bar{h}} = \sqrt{\mu} \left(\frac{\sqrt{1-\bar{e}^2}}{2\sqrt{\bar{a}}} \dot{\bar{a}} - \frac{\bar{e}\sqrt{\bar{a}}}{\sqrt{1-\bar{e}^2}} \dot{\bar{e}} \right).$$

Using the average variation of the angular momentum yields the same results.

Equations (4.7) govern the evolution of the orbit, without any reference to the specific motion on the trajectory. For this purpose, the variational equation for one of the anomalies (true, eccentric or mean) is required:

$$\frac{d}{dt}(\) = \frac{\partial}{\partial t}(\) + \left[\frac{\partial}{\partial \mathbf{r}}(\) \right] \cdot \mathbf{f}_p \quad (4.8)$$

where $()$ is any of the anomalies f , E or M [Battin, 1999] (pp. 501–503). The *mean anomaly* M is subjected to the averaging procedure in this work, since it contains the sixth constant of the unperturbed motion, related to the time of periapsis passage, t_P . The closed-form expressions for the variation of the mean anomaly is [Battin, 1999] (pp. 502-503):

$$\dot{M} = n + \frac{rb}{ha^2e} \left[\cos f(\mathbf{r} \cdot \mathbf{f}_p) - \frac{a}{h}(r+p) \sin f(\dot{\mathbf{r}} \cdot \mathbf{f}_p) \right]. \quad (4.9)$$

Averaging over one period of the unperturbed motion yields:

$$\dot{\bar{M}} = \bar{n} + C_u \sqrt{1-\bar{e}^2} (3 \cos^2 \bar{i} - 1), \quad (4.10)$$

where C_u is defined as:

$$C_u = \frac{3k_2}{2b^3h} = \frac{3}{4} \bar{n} J_2 \left(\frac{r_{eq}}{\bar{p}} \right)^2. \quad (4.11)$$

4.3 Analytical solution for the absolute motion

By means of few manipulations of Equations (4.7) and (4.10) [Martinusi et al., 2014], the IVP governing the motion of the satellite can be reformulated in terms of GVE:

$$\dot{\bar{a}} = \dot{\bar{a}}_{J_2} + \dot{\bar{a}}_{drag} = -4C_0\sqrt{\mu\bar{a}}\frac{2K(\bar{e}) - E(\bar{e})}{\pi}, \quad \bar{a}(t_0) = \bar{a}_0, \quad (4.12a)$$

$$\dot{\bar{e}} = \dot{\bar{e}}_{J_2} + \dot{\bar{e}}_{drag} = -\frac{4C_0\sqrt{\mu}}{\sqrt{\bar{a}}}\frac{(1-\bar{e}^2)[K(\bar{e}) - E(\bar{e})]}{\pi\bar{e}}, \quad \bar{e}(t_0) = \bar{e}_0, \quad (4.12b)$$

$$\dot{\bar{i}} = \dot{\bar{i}}_{J_2} + \dot{\bar{i}}_{drag} = 0, \quad \bar{i}(t_0) = \bar{i}_0, \quad (4.12c)$$

$$\dot{\bar{M}} = \dot{\bar{M}}_{J_2} + \dot{\bar{M}}_{drag} = \bar{n} + C_u\sqrt{1-\bar{e}^2}(3c^2-1), \quad \bar{M}(t_0) = \bar{M}_0 \quad (4.12d)$$

$$\dot{\bar{\omega}} = \dot{\bar{\omega}}_{J_2} + \dot{\bar{\omega}}_{drag} = C_u(5c^2-1), \quad \bar{\omega}(t_0) = \bar{\omega}_0, \quad (4.12e)$$

$$\dot{\bar{\Omega}} = \dot{\bar{\Omega}}_{J_2} + \dot{\bar{\Omega}}_{drag} = -2C_u c, \quad \bar{\Omega}(t_0) = \bar{\Omega}_0, \quad (4.12f)$$

where $c = \cos \bar{i}$. The expression of $C_u = C_u(\bar{a}, \bar{e}, r_{eq}, J_2)$ is given in Equation (4.11). Equations (4.12a) and (4.12b) need to be solved first, since the quantities \bar{a} and \bar{e} are involved in all other equations.

In order to obtain the closed-form solution to Equations (4.12), Taylor series expansions with respect to the averaged eccentricity \bar{e} are performed, together with the introduction of a new independent variable τ , defined by:

$$dt = \frac{d\tau}{\mathcal{R}(\bar{a}, \bar{e})}, \quad \tau(t_0) = \bar{a}_0, \quad (4.13)$$

where the expression of $\mathcal{R}(\bar{a}, \bar{e})$ is a regularization factor. A new system of differential equations emerges, where the derivatives, denoted with $()'$, are computed with respect to the new independent variable τ :

$$()' = \frac{d}{d\tau}() = \frac{1}{\mathcal{R}(\bar{a}, \bar{e})} \frac{d}{dt}(),$$

A new differential equation, which links the time variable t to the independent variable τ (similar to Kepler's equation in the unperturbed case), is to be derived and solved explicitly.

4.3.1 The case of small eccentricity ($e^4 \simeq 0$)

Since the averaged inclination remains constant, its differential equation is omitted. By choosing the regularizing factor $\mathcal{R}(\bar{a}, \bar{e})$ to be:

$$\mathcal{R}(\bar{a}, \bar{e}) = -\frac{1}{2}C_0\sqrt{\mu}\sqrt{\bar{a}}(4+3\bar{e}^2) \quad (4.14)$$

Equations (4.12) are recast into:

$$\bar{a}' = -4C_0\sqrt{\mu}\bar{a} \frac{2K(\bar{e}) - E(\bar{e})}{\pi\mathcal{R}(\bar{a}, \bar{e})} \quad (4.15a)$$

$$\bar{e}' = -\frac{4C_0\sqrt{\mu}}{\sqrt{\bar{a}}} \frac{(1 - \bar{e}^2)[K(\bar{e}) - E(\bar{e})]}{\pi\bar{e}\mathcal{R}(\bar{a}, \bar{e})} \quad (4.15b)$$

$$\bar{M}' = \frac{\bar{n}}{\mathcal{R}(\bar{a}, \bar{e})} + \frac{C_u\sqrt{1 - \bar{e}^2}(3c^2 - 1)}{\mathcal{R}(\bar{a}, \bar{e})} \quad (4.15c)$$

$$\bar{\omega}' = \frac{C_u(5c^2 - 1)}{\mathcal{R}(\bar{a}, \bar{e})} \quad (4.15d)$$

$$\bar{\Omega}' = -\frac{2C_u c}{\mathcal{R}(\bar{a}, \bar{e})} \quad (4.15e)$$

$$t' = \frac{1}{\mathcal{R}(\bar{a}, \bar{e})} \quad (4.15f)$$

After expanding the right-hand sides of Equations (4.15a)–(4.15e) in Taylor series and assuming that $\mathcal{O}(\bar{e}^4) = 0$, the system becomes:

$$\bar{a}' = 1 \quad (4.16a)$$

$$\bar{e}' = \frac{\bar{e}}{2\bar{a}} \quad (4.16b)$$

$$\bar{M}' = -\frac{1}{8C_0} \frac{4 - 3\bar{e}^2}{\bar{a}^2} - \frac{3k_2(3c^2 - 1)}{16\mu C_0} \frac{(4 + 3\bar{e}^2)}{\bar{a}^4} \quad (4.16c)$$

$$\bar{\omega}' = -\frac{3k_2(5c^2 - 1)}{16\mu C_0} \frac{(4 + 5\bar{e}^2)}{\bar{a}^4} \quad (4.16d)$$

$$\bar{\Omega}' = \frac{3k_2 c}{8\mu C_0} \frac{(4 + 5\bar{e}^2)}{\bar{a}^4} \quad (4.16e)$$

$$t' = -\frac{2}{C_0\sqrt{\mu}} \frac{1}{\sqrt{\bar{a}}(4 + 3\bar{e}^2)} \quad (4.16f)$$

The solutions to Equations (4.16a) and (4.16b) are:

$$\bar{a} = \tau \quad (4.17a)$$

$$\bar{e} = \alpha_0\sqrt{\tau}, \quad \alpha_0 = \frac{\bar{e}_0}{\sqrt{\bar{a}_0}} \quad (4.17b)$$

From Equation (4.16f), the time-explicit expression of the averaged semi-major axis is obtained:

$$\beta_0 = \frac{\sqrt{3}}{2}\bar{e}_0$$

$$\bar{a} = \frac{\bar{a}_0}{\beta_0^2} \tan^2 [\arctan(\beta_0) - \beta_0 \bar{n}_0 \bar{a}_0 C_0 (t - t_0)] \quad (4.18)$$

The remaining differential equations are solved by simple integration, yielding:

$$\bar{e} = \frac{2}{\sqrt{3}} \tan [\arctan(\beta_0) - \beta_0 \bar{n}_0 \bar{a}_0 C_0 (t - t_0)] \quad (4.19a)$$

$$\begin{aligned} \bar{M} - \bar{M}_0 &= \frac{1}{8} \frac{1}{C_0} \left[\frac{4}{\tau} + 3\alpha_0^2 \ln \frac{\tau}{\bar{a}_0} \right] \Big|_{\tau=\bar{a}_0}^{\tau=\bar{a}} + \\ &\quad \frac{3k_2(3c^2 - 1)}{16\mu} \frac{1}{C_0} \left[\frac{3\alpha_0^2}{2} \frac{1}{\tau^2} + \frac{4}{3\tau^3} \right] \Big|_{\tau=\bar{a}_0}^{\tau=\bar{a}} \end{aligned} \quad (4.19b)$$

$$\bar{\omega} - \bar{\omega}_0 = \frac{3k_2(5c^2 - 1)}{16\mu} \frac{1}{C_0} \left[\frac{5\alpha_0^2}{2} \frac{1}{\tau^2} + \frac{4}{3\tau^3} \right] \Big|_{\tau=\bar{a}_0}^{\tau=\bar{a}} \quad (4.19c)$$

$$\bar{\Omega} - \bar{\Omega}_0 = -\frac{3k_2 c}{8\mu} \frac{1}{C_0} \left[\frac{5\alpha_0^2}{2} \frac{1}{\tau^2} + \frac{4}{3\tau^3} \right] \Big|_{\tau=\bar{a}_0}^{\tau=\bar{a}} \quad (4.19d)$$

In order to avoid the singularities inherent to classical orbital elements, the equations of motion may be written in terms of equinoctial variables:

$$\bar{a} = \frac{\bar{a}_0}{\beta_0^2} \tan^2 [\arctan(\beta_0) - \beta_0 \bar{n}_0 \bar{a}_0 C_0 (t - t_0)] \quad (4.20a)$$

$$\bar{P}_1 = \frac{2}{\sqrt{3}} \tan [\arctan(\beta_0) - \beta_0 \bar{n}_0 \bar{a}_0 C_0 (t - t_0)] \sin \bar{\varpi} \quad (4.20b)$$

$$\bar{P}_2 = \frac{2}{\sqrt{3}} \tan [\arctan(\beta_0) - \beta_0 \bar{n}_0 \bar{a}_0 C_0 (t - t_0)] \cos \bar{\varpi} \quad (4.20c)$$

$$\bar{Q}_1 = \bar{u}_0 \sin \bar{\Omega} \quad (4.20d)$$

$$\bar{Q}_2 = \bar{u}_0 \cos \bar{\Omega} \quad (4.20e)$$

$$\bar{l} = \bar{l}_0 + \frac{1}{8C_0} \left[\frac{4}{\tau} + 3\alpha_0^2 \ln \frac{\tau}{\bar{a}_0} \right] \Big|_{\tau=\bar{a}_0}^{\tau=\bar{a}} + \quad (4.20f)$$

$$\frac{k_2}{16\mu C_0} \left[\frac{3\alpha_0^2(17c^2 - 5c - 4)}{\tau^2} + \frac{8(4c^2 - c - 1)}{\tau^3} \right] \Big|_{\tau=\bar{a}_0}^{\tau=\bar{a}}$$

where $\bar{\Omega}$ is defined in Equation (4.19d), and:

$$\bar{u}_0 = \tan \frac{\bar{i}_0}{2}; \quad \bar{\varpi}_0 = \bar{\omega}_0 + \bar{\Omega}_0; \quad \bar{l}_0 = \bar{\omega}_0 + \bar{\Omega}_0 + \bar{M}_0; \quad (4.21a)$$

$$\bar{\varpi} = \bar{\varpi}_0 + \frac{k_2(5c^2 - 2c - 1)}{32\mu C_0} \left[\frac{15\alpha_0^2}{\tau^2} + \frac{8}{\tau^3} \right] \Big|_{\tau=\bar{a}_0}^{\tau=\bar{a}} \quad (4.21b)$$

The coefficient C_0 in the denominator of Equations (4.19) introduces a singularity. However, it is only an apparent singularity, due to the fact that expressions of the type $(\bar{a} - \bar{a}_0) g(\bar{a}, \bar{a}_0)$, $g(\bar{a}, \bar{a}_0) \neq 0$, are present in the numerators. By taking into

account Equation (4.18), it follows that:

$$\lim_{C_0 \rightarrow 0} \frac{\bar{a} - \bar{a}_0}{C_0} = -2\bar{n}_0 \bar{a}_0^2 (1 + \beta_0^2) (t - t_0) \quad (4.22)$$

If the limit $C_0 \rightarrow 0$ is made in Equations (4.19), the classical averaged variational equations for J_2 only are obtained. The singularity is therefore removed. For numerical purposes, in order to avoid small values of C_0 in Equations (4.19), the series expansion of the difference $\bar{a} - \bar{a}_0$ in powers of C_0 , is considered, which is deduced from Equation (4.18):

$$\bar{a} - \bar{a}_0 = \bar{a}_0 (1 + \beta_0^2) \sum_{k=1}^{\infty} [\bar{n}_0 \bar{a}_0 C_0 (t - t_0)]^k d_k \quad (4.23)$$

where the first relevant values of the coefficients d_k are:

$$\begin{aligned} d_1 &= -2 \\ d_2 &= 1 + 3\beta_0^2 \\ d_3 &= -\frac{4}{3}\beta_0^2 (2 + 3\beta_0^2) \\ d_4 &= \frac{1}{3}\beta_0^2 (15\beta_0^4 + 15\beta_0^2 + 2) \\ d_5 &= -\frac{2}{15}\beta_0^2 (45\beta_0^4 + 60\beta_0^2 + 17) \end{aligned}$$

For the logarithmic term in Equation (4.19b), a series expansion should be used:

$$\frac{1}{C_0} \ln \frac{\bar{a}}{\bar{a}_0} = \bar{n}_0 \bar{a}_0 (1 + \beta_0^2) (t - t_0) \sum_{k=1}^{\infty} [\bar{n}_0 \bar{a}_0 C_0 (t - t_0)]^k g_k \quad (4.24)$$

where the first relevant values of the coefficients g_k are:

$$\begin{aligned} g_1 &= -2 \\ g_2 &= -1 + \beta_0^2 \\ g_3 &= -\frac{2}{3}(1 + \beta_0^4) \\ g_4 &= \frac{1}{6}(1 - \beta_0^2)(3\beta_0^4 + 4\beta_0^2 + 3) \\ g_5 &= -\frac{2}{15}\beta_0^2(3\beta_0^8 + 2\beta_0^6 + 2\beta_0^2 + 3) \end{aligned}$$

4.3.2 The case of very small eccentricity ($\bar{e}^2 \simeq 0$)

Simpler expressions may be obtained if a more restrictive assumption is made, namely that the eccentricity is such that $\mathcal{O}(\bar{e}_0^2) = 0$. Expanding in Taylor series

Equations (4.18) and (4.19) yield:

$$\begin{aligned}\bar{a} &= \bar{a}_0 - 2C_0\sqrt{\mu}(t-t_0)\sqrt{\bar{a}_0} + \mu C_0^2(t-t_0)^2\bar{a}_0 + \mathcal{O}(\bar{e}_0^2), \\ \bar{e} &= \left[1 - \frac{C_0\sqrt{\mu}}{\sqrt{\bar{a}_0}}(t-t_0)\right]\bar{e}_0 + \mathcal{O}(\bar{e}_0^3),\end{aligned}$$

so that the closed-form solution becomes:

$$\bar{a} = [\sqrt{\bar{a}_0} - C_0\sqrt{\mu}(t-t_0)]^2 \quad (4.25a)$$

$$\bar{e} = \bar{e}_0\sqrt{\frac{\bar{a}}{\bar{a}_0}} \quad (4.25b)$$

$$\bar{M} - \bar{M}_0 = \frac{1}{2C_0}\left(\frac{1}{\bar{a}} - \frac{1}{\bar{a}_0}\right) + \frac{k_2(3c^2-1)}{4\mu C_0}\left(\frac{1}{\bar{a}^3} - \frac{1}{\bar{a}_0^3}\right) \quad (4.25c)$$

$$\bar{\omega} - \bar{\omega}_0 = \frac{k_2(5c^2-1)}{4\mu C_0}\left(\frac{1}{\bar{a}^3} - \frac{1}{\bar{a}_0^3}\right) \quad (4.25d)$$

$$\bar{\Omega} - \bar{\Omega}_0 = -\frac{k_2 c}{2\mu C_0}\left(\frac{1}{\bar{a}^3} - \frac{1}{\bar{a}_0^3}\right) \quad (4.25e)$$

The inconvenience of having C_0 in the denominator is removed by accounting for Equation (4.25a):

$$\frac{1}{C_0}\left(\frac{1}{\bar{a}} - \frac{1}{\bar{a}_0}\right) = \frac{\sqrt{\mu}(\sqrt{\bar{a}_0} + \sqrt{\bar{a}})}{\bar{a}_0\bar{a}}(t-t_0) \quad (4.26a)$$

$$\frac{1}{C_0}\left(\frac{1}{\bar{a}^3} - \frac{1}{\bar{a}_0^3}\right) = \frac{\sqrt{\mu}(\bar{a}_0^2 + \bar{a}\bar{a}_0 + \bar{a}^2)(\sqrt{\bar{a}_0} + \sqrt{\bar{a}})}{\bar{a}_0^3\bar{a}^3}(t-t_0) \quad (4.26b)$$

The singularities occurring at low inclinations and small eccentricities are removed by expressing the solution in terms of equinoctial elements. Using Equations (4.24), Equations (4.25) are recast into:

$$\bar{P}_1 = \frac{\bar{e}_0}{\sqrt{\bar{a}_0}}[\sqrt{\bar{a}_0} - C_0\sqrt{\mu}(t-t_0)]\sin\bar{\varpi} \quad (4.27a)$$

$$\bar{P}_2 = \frac{\bar{e}_0}{\sqrt{\bar{a}_0}}[\sqrt{\bar{a}_0} - C_0\sqrt{\mu}(t-t_0)]\cos\bar{\varpi} \quad (4.27b)$$

$$\bar{Q}_1 = \bar{u}_0 \sin \bar{\Omega} \quad (4.27c)$$

$$\bar{Q}_2 = \bar{u}_0 \cos \bar{\Omega} \quad (4.27d)$$

$$\begin{aligned}\bar{l} &= \bar{l}_0 + \frac{\sqrt{\mu}(\sqrt{\bar{a}_0} + \sqrt{\bar{a}})}{2\bar{a}_0\bar{a}} \\ &\quad \left[1 - \frac{k_2(-4c^2+c+1)}{\mu}\frac{(\bar{a}_0^2 + \bar{a}\bar{a}_0 + \bar{a}^2)}{\bar{a}_0^2\bar{a}^2}\right](t-t_0)\end{aligned} \quad (4.27e)$$

where \bar{u}_0 , $\bar{\omega}_0$, \bar{l}_0 are defined in Equation (4.21a) and

$$\bar{\omega} = \bar{\omega}_0 - \frac{k_2(-5c^2 + 2c + 1)}{4\sqrt{\mu}\bar{a}_0^3\bar{a}^3} (\bar{a}_0^2 + \bar{a}\bar{a}_0 + \bar{a}^2) (\sqrt{\bar{a}_0} + \sqrt{\bar{a}}) (t - t_0) \quad (4.28)$$

4.4 Analytical solution for the relative motion

Consider two satellites (chief and deputy) orbiting the Earth, under the influence of oblateness and atmospheric drag perturbations. Given the time-explicit expressions of the orbital elements obtained in Section 4.3, and based on some simple geometric considerations, the time-explicit equations of the relative orbital motion are expressed via the sets of orbital elements of the two satellites.

Recalling Section 1.4, the motion of the deputy with respect to the LVLH reference frame attached to the center of mass of the chief, $\{\hat{\mathbf{r}}_C, \hat{\mathbf{t}}_C, \hat{\mathbf{h}}_C\}$, is given by:

$$\Delta\mathbf{r}(t) = r_D {}^C\mathbf{R}_D \hat{\mathbf{r}}_D - r_C \hat{\mathbf{r}}_C, \quad (4.29)$$

where the position vectors are defined in the LVLH frame of each satellite, and ${}^C\mathbf{R}_D$ is the rotation matrix from the LVLH of the deputy to the LVLH of the chief.

The expression of ${}^C\mathbf{R}_D$ is given by Equations (1.7), i.e.,

$$\begin{aligned} {}^C\mathbf{R}_D &= ({}^{LVLH}\mathbf{R}_{PF} {}^{PF}\mathbf{R}_{ToD})_C ({}^{ToD}\mathbf{R}_{PF} {}^{PF}\mathbf{R}_{LVLH})_D \\ &= \mathbf{R}_3(-\theta_C) \mathbf{R}_1(-i_C) \mathbf{R}_3(-\Omega_C) \mathbf{R}_3(\Omega_D) \mathbf{R}_1(i_D) \mathbf{R}_3(\theta_D), \end{aligned} \quad (4.30)$$

where the total anomaly, θ , is defined as $\theta = \omega + f$.

The components of vector $\Delta\mathbf{r}$ in the chief's LVLH frame are obtained from Equations 4.29 and 4.30:

$$\begin{aligned} x &= r_D [(L_1 \sin \Omega_C + L_2 \cos \Omega_C) \cos \Omega_D + (L_2 \sin \Omega_C - L_1 \cos \Omega_C) \cos \Omega_D \\ &\quad + \sin i_C \sin i_D \sin \theta_C \sin \theta_D] - r_C, \end{aligned} \quad (4.31a)$$

$$\begin{aligned} y &= r_D [(M_1 \sin \Omega_C + M_2 \cos \Omega_C) \cos \Omega_D + (M_2 \sin \Omega_C - M_1 \cos \Omega_C) \cos \Omega_D \\ &\quad + \sin i_C \sin i_D \cos \theta_C \sin \theta_D], \end{aligned} \quad (4.31b)$$

$$\begin{aligned} z &= r_D [(N_1 \sin \Omega_C + N_2 \cos \Omega_C) \cos \Omega_D + (N_2 \sin \Omega_C - N_1 \cos \Omega_C) \cos \Omega_D \\ &\quad + \cos i_C \sin i_D \sin \theta_D], \end{aligned} \quad (4.31c)$$

where $L_{1,2}$, $M_{1,2}$ and $N_{1,2}$ are defined as:

$$L_1 = -\cos(i_C) \sin(\theta_C) \cos(\theta_D) + \cos(\theta_C) \cos(i_D) \sin(\theta_D), \quad (4.32a)$$

$$L_2 = \cos(\theta_C) \cos(\theta_D) + \cos(i_C) \sin(\theta_C) \cos(i_D) \sin(\theta_D), \quad (4.32b)$$

$$M_1 = -\cos(i_C) \cos(\theta_C) \cos(\theta_D) - \sin(\theta_C) \cos(i_D) \sin(\theta_D), \quad (4.32c)$$

$$M_2 = -\sin(\theta_C) \cos(\theta_D) + \cos(i_C) \cos(\theta_C) \cos(i_D) \sin(\theta_D), \quad (4.32d)$$

$$N_1 = \sin(i_C) \cos(\theta_D), \quad (4.32e)$$

$$N_2 = -\sin(i_C) \cos(i_D) \sin(\theta_D). \quad (4.32f)$$

For non-polar and non-equatorial orbits of the chief, Equation (4.31) can be simplified by noting that:

$$\begin{aligned} L_1^2 + L_2^2 &= (1 - \sin^2 i_C \sin^2 \theta_C) (1 - \sin^2 i_D \sin^2 \theta_D) = \sin^2 \phi_C \sin^2 \phi_D \\ M_1^2 + M_2^2 &= (1 - \sin^2 i_C \cos^2 \theta_C) (1 - \sin^2 i_D \sin^2 \theta_D) = (1 - \sin^2 i_C \cos^2 \theta_C) \sin^2 \phi_D \\ N_1^2 + N_2^2 &= \sin^2 i_C (1 - \sin^2 i_D \sin^2 \theta_D) = \sin^2 i_C \sin^2 \phi_D \end{aligned}$$

where $\phi_{(.)} \in [0, \pi]$ denotes the collatitudes of the satellites and satisfies the relation [Battin, 1999]:

$$\cos \phi_{(.)} = \sin i_{(.)} \sin \theta_{(.)}$$

Denote:

$$\begin{aligned} A_L &= \sin \phi_C \sin \phi_D; & B_L &= \sin i_C \sin i_D \sin \theta_C \sin \theta_D \\ A_M &= \sqrt{1 - \sin^2 i_C \cos^2 \theta_C} \sin \phi_D; & B_M &= \sin i_C \sin i_D \cos \theta_C \sin \theta_D \\ A_N &= \sin i_C \sin \phi_D; & B_N &= \cos_C \sin i_D \sin \theta_D \end{aligned} \quad (4.33)$$

and define the quantities $\alpha_U \in [0, 2\pi)$, $U \in \{L, M, N\}$ by their sines and cosines:

$$\cos \alpha_U = \frac{U_1 \sin \Omega_C + U_2 \cos \Omega_C}{A_U}; \quad \sin \alpha_U = \frac{U_2 \sin \Omega_C - U_1 \cos \Omega_C}{A_U}. \quad (4.34)$$

Then Equations (4.31) become:

$$x = r_D [A_L \sin(\alpha_L + \Omega_C - \Omega_D) + B_L] - r_C \quad (4.35a)$$

$$y = r_D [A_M \sin(\alpha_M + \Omega_C - \Omega_D) + B_M] \quad (4.35b)$$

$$z = r_D [A_N \sin(\alpha_N + \Omega_C - \Omega_D) + B_N] \quad (4.35c)$$

Substituting Equations (4.18) and (4.19) or (4.25) in Equations 4.32–4.35 yields the time-explicit solution for the relative motion.

4.5 Validation of the analytical propagator

The time-explicit solution obtained in Section 4.3 describes the averaged motion under the influence of J_2 and atmospheric drag. After averaging, the new varia-

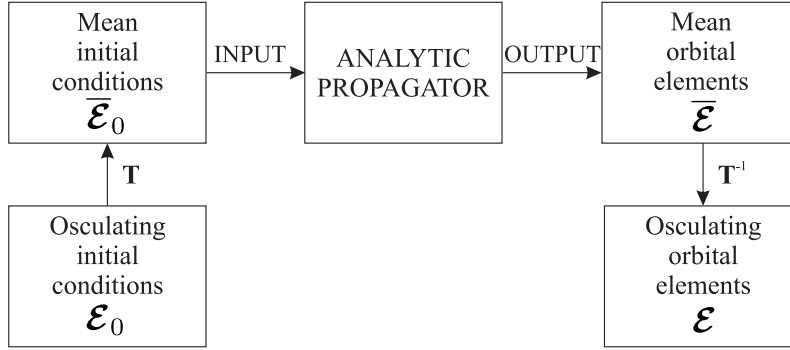


Figure 4.1: Proposed orbit propagation.

tional equations do not belong to the space of osculating orbital elements – which describe the real motion of the satellite – but to a new set of variables often referred to as *mean elements* in astrodynamics [Cain, 1962], or *new variables* in classical mechanics. A mapping between the *old* and the *new variables* needs to be established via a *canonical contact transformation*. This can either be of Jacobian type or infinitesimal, e.g., as in the Poincaré-von Zeipel method [Brouwer, 1959] or in [Deprit, 1969, 1981], respectively. In the context of short-term orbit prediction, using the canonical contact transformation of the Hamiltonian system (in this case the J_2 -only dynamical system) appears legitimate. In other words, the new dynamical system, corresponding to the averaged equations of motion, takes into account the effects of the atmospheric drag, while the transformation back to the (approximate) osculating elements is made by ignoring the drag effect. In this work, the Brouwer’s first-order canonical contact transformation [Brouwer, 1959] is used. For the sake of precision, to avoid the singularity of the Brouwer’s contact transformation occurring at small orbital eccentricity, a slightly-modified version is used [Lyddane, 1963, Schaub and Junkins, 2003].

The orbit propagation paradigm is illustrated in Figure 4.1. At the initial epoch, $t = t_0$, the input is the set of osculating orbital elements $\mathcal{E}_0 = (a_0, e_0, i_0, \omega_0, \Omega_0, M_0)$. The osculating to mean transformation is applied to these coordinates to obtain the mean initial conditions $\bar{\mathcal{E}}_0 = (\bar{a}_0, \bar{e}_0, \bar{i}_0, \bar{\omega}_0, \bar{\Omega}_0, \bar{M}_0)$. The equations derived in Section 4.3 are used to propagate the averaged orbital elements, starting from $\bar{\mathcal{E}}_0$. At each step of the propagation, the inverse contact transformation is applied in order to recover the osculating orbital elements, which constitute the output of the propagation.

In the case of relative motion, the same paradigm is applied both to the chief and the deputy.

4.5.1 Inertial motion

The validation of our analytical propagator is carried out by comparing its predictions with the brute-force numerical integration of the equinoctial GVE. The

Table 4.1: Input parameters for the simulations of the absolute motion. The same inputs are used for the chief in the simulations of the relative motion.

Initial conditions		
Altitude	400, 600	km
Eccentricity	0.001	
Inclination	98	deg
AoP	0	deg
RAAN	0	deg
True anomaly	20	deg
Drag model		
Ballistic coefficient	0.022	$\text{m}^2 \text{ kg}$
Density	$5 \cdot 10^{-12}, 1 \cdot 10^{-13}$	kg m^{-3}
Gravitational model		
Equatorial radius	6378.137	km
Gravitational parameter	$3.986004418 \cdot 10^{14}$	$\text{m}^3 \text{s}^{-2}$
Second zonal harmonic	$1.08263 \cdot 10^{-3}$	

analytical propagator for very-small-eccentric orbits, i.e., the one developed in Section 4.3.2, is used in this validation. Similar accuracy is achieved with the more advanced propagator developed in Section 4.3.1.

Table 4.1 lists the parameters exploited in the simulations. Two case studies are analyzed, namely at 400 and 600 kilometers altitude.

Figure 4.2 depicts the norm of the error in the position made by our analytical propagator and by neglecting the aerodynamic force. The substantial divergence between the two curves motivates the interest in the present work, especially at very low altitude, where the drift after two days of propagation is two OoM greater when drag is neglected.

Because of the vertical exponential rarefaction of the atmosphere, the error when drag is neglected is drastically reduced at higher altitude. On the contrary, the error of our analytical propagator is essentially unchanged at 400 and 600 km, i.e., slightly more than one kilometer after 2 days. This means that the drift of our propagator is dominated by the J_2 effects, while the drift obtained when neglecting drag is indeed dominated by drag itself.

To support this claim, we note that the same one-kilometer drift of our propagator is observed if ρ_0 is set to zero in the simulations. In addition, the fact that the error of our propagator evolves nearly linearly – and with non-horizontal initial slope – is another indicator that the drift is imputable to the Earth’s oblateness. In fact, small errors in the initial mean state estimation – due to the use of a first-order contact transformation – are mapped into errors in the coefficient $C_u = C_u(\bar{a}, \bar{e}, r_{eq}, J_2)$, which, in turn, modifies the mean orbital period (Equation (4.12d)) and results in a linear drift of the mean anomaly.

In [Martinusi et al., 2015], we carry out a MC analysis aimed at comparing the drift of our propagator with and without the atmosphere. The errors in the two cases have a correlation of 99.8%, which proves our conjecture on the nature of the drift.

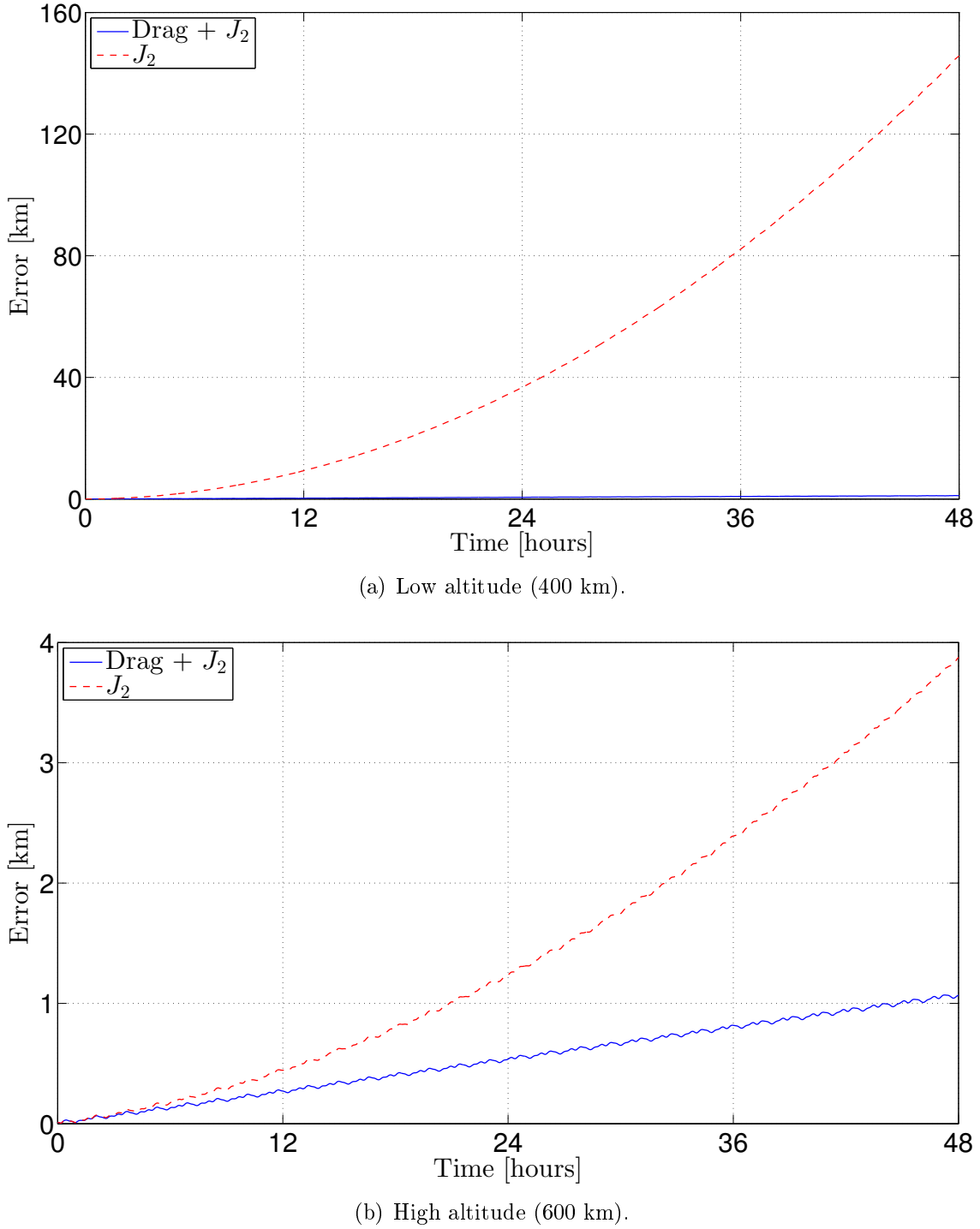


Figure 4.2: Numerical simulations for the absolute motion. The blue-solid curves depict the error of our analytical propagator. The red-dashed curves are the error made by neglecting drag.

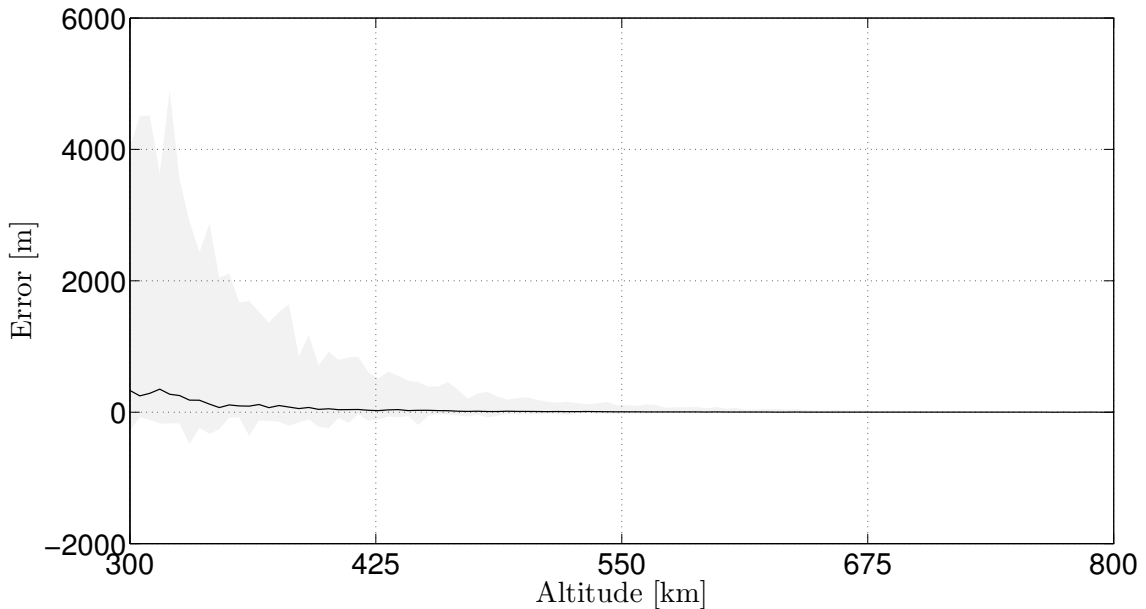


Figure 4.3: Comparison of the drift of our propagator when the simulation environment accounts for or neglects the atmospheric drag. The black line is the median of the Monte Carlo samples. The grey region indicates 90% confidence bounds.

Figure 4.3 illustrates the difference between the drift with and without atmosphere as a function of altitude.

4.5.2 Relative motion

Two case studies are considered for the validation of the relative motion propagator, i.e., at 400 and 600 kilometers altitude. The inputs for the absolute states and ballistic properties of the chief are the same as in Table 4.1. Table 4.2 lists the inputs for the initial relative states and ballistic properties of the deputy.

Figure 4.4 depicts the norm of the relative position between the two spacecraft

Table 4.2: Input parameters for the deputy.

Relative conditions		
Altitude	20	m
Eccentricity	0.0003	
Inclination	0	deg
AoP	0.001	deg
RAAN	0.0001	deg
True anomaly	0.0011	deg

Drag model		
Ballistic coefficient	0.044	$\text{m}^2 \text{ kg}$

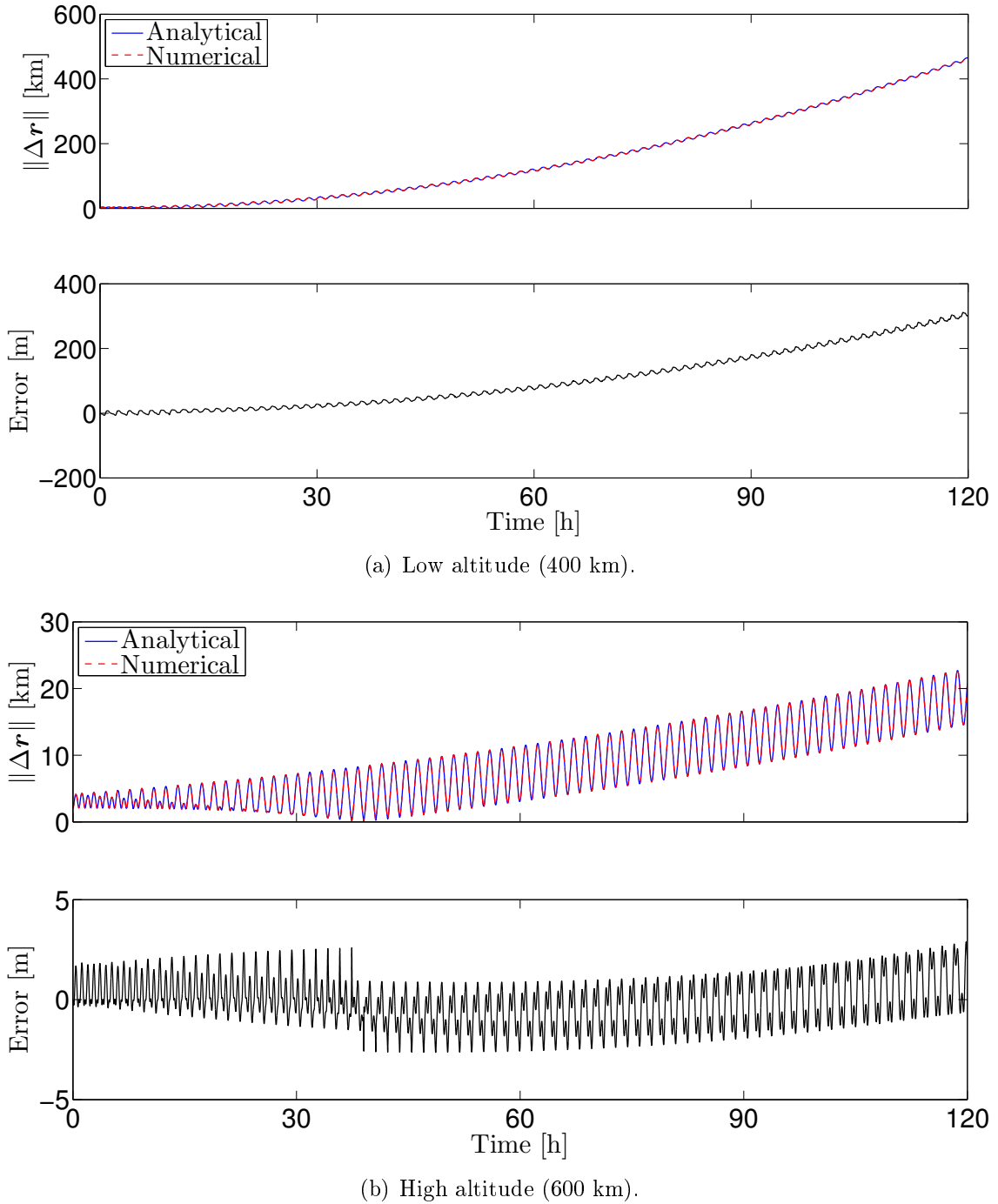


Figure 4.4: Numerical simulations for the relative motion. The blue-solid curves depict the relative distance estimated by our analytical propagator. The red-dashed curves – essentially superimposed – are the true relative distance. The norm of the position error is depicted in the bottom plots.

and the error made by our analytical propagator. Because no assumption on the relative dynamics was introduced to develop the propagator, the error is extremely modest even when the two satellites are separated by several tens of kilometers.

The error is considerably smaller than the one obtained for the absolute motion in Figure 4.2. This enhanced accuracy is due to the fact that the chief and deputy are in close proximity, so that the error injected by the contact transformation is similar for the two satellites and it is almost fully compensated when considering relative states.

Because most errors due to J_2 are compensated, the drift of the relative propagator is dominated by the drag, as shown by the nonlinear trend of the error at 400 km altitude.

4.6 Conclusion

Time-explicit solution of the equations of motion for a satellite moving in the atmosphere of an oblate planet was derived and validated. The propagator is able to run on a processor with very limited capabilities, such as those on-board small satellites. In addition, a closed-form solution for the relative motion was developed based on the aforementioned propagator of the absolute motion. The equations of the relative motion are expressed in the LVLH frame and no simplifying assumption on the relative distance between the two satellites is made.

The solutions were developed in two cases, namely small and very small initial osculating eccentricities. Numerical simulations show that most errors are inherited from Brouwer's first-order model, through the truncation of the development in Fourier series of the J_2 potential, and to a lesser amount by the Brouwer-Lyddane contact transformation.

In Chapters 5 and 6, the propagator of the inertial motion is integrated in the control plant we use to plan and execute differential-drag-based maneuvers.

Chapter 5

Differential Drag: an Optimal Control Approach

Abstract

Optimization of fuel consumption is a key driver in the design of spacecraft maneuvers. For this reason, growing interest in propellant-free maneuvers is observed in the literature. Because it allows to turn the often-undesired drag perturbation into a control force for relative motion, differential drag is among the most promising propellantless techniques for low-Earth orbiting satellites. An optimal control approach to the problem of orbital rendez-vous using differential drag is proposed in this chapter. Thanks to a direct transcription of the optimal control problem resulting in the scheduling of a reference maneuver, the method is flexible in terms of cost function and can easily account for constraints of various nature. Considerations on the practical realization of differential-drag-based maneuvers are also provided. The developments are illustrated by means of high-fidelity simulations including a coupled 6-degree-of-freedom model with advanced aerodynamics

5.1 Introduction

Optimization is a key factor in mission design, especially when dealing with formation flying, where severe size and weight constraints may strongly limit the performance of the propulsive system. Nowadays, propellantless techniques for formation flying, e.g., solar sail [Williams and Wang, 2002], geomagnetic [Peck et al., 2007], and Coulomb formation flying [King et al., 2002], are envisaged as possible solutions to either reduce or even remove the need for on-board propellant.

This chapter focuses on the use of differential drag as a means of controlling relative motion. By modifying the surface exposed to the residual atmosphere, it is possible to change the magnitude of the atmospheric drag to obtain a differential force between the deputy and either the chief or a desired target point.

The idea of exploiting differential drag for relative maneuvers dates back to a couple of decades with the pioneering research of Leonard [Leonard et al., 1989], who developed a strategy for controlling the cross section aimed at achieving a rendez-vous within the linear dynamics equations of Hill-Clohessy-Wiltshire. The relative motion was decomposed into a mean and a harmonic component, yielding insight into the physical behavior of the problem. However, the methodology relied upon several restrictive assumptions, including circular orbits, spherical Earth, and uniform atmosphere. Motivated by the desire to consider more representative scenarios, Bevilacqua *et al.* included the secular perturbations of the Earth's oblateness in Leonard's method [Bevilacqua and Romano, 2008]. They also proposed a hybrid approach combining differential drag and continuous low-thrust [Bevilacqua et al., 2009] aimed at enhancing out-of-plane controllability. Finally, a novel approach for bang-bang control based on an adaptive Lyapunov control strategy was developed to account for nonlinear orbital dynamics [Pérez and Bevilacqua, 2013]. Kumar *et al.* implemented the solution in a high-precision propagator [Kumar and Ng, 2008], and they highlighted the importance of accurate relative states estimation in order to prevent the solution from drastic deterioration. Lambert *et al.* [Lambert et al., 2012] overcame this issue by exploiting a conversion from osculating to mean orbital elements of both the target and the chaser. Targeting long-term cluster keeping and collision avoidance using differential drag, Ben-Yaakov *et al.* [Ben-Yaakov and Gurfil, 2013, 2014] proposed a nonlinear control approach based on mean and osculating ROE, respectively. Differently from the other references, the feedback loop relies on the geometry of the relative trajectory only, i.e., it does not require to estimate the magnitude of the differential drag. In addition, the use of ROE yielded the advantages discussed in Section 1.4.

Several forthcoming missions highlight the overall interest in this technique and the opportunities it enables, e.g., JC2sat [Ng, 2010], SAMSON [Gurfil et al., 2012], and CYGNSS [Ruf et al., 2013] plan to use differential drag for orbital rendez-vous, cluster keeping, and constellation deployment, respectively. Nonetheless, the ORB-COMM constellation is currently the only application of the differential drag technique in space and it is only limited to support station-keeping maneuvers [Lewin, 1998]. The reason for this shortage of real missions is that most existing theoret-

ical works on differential drag rely on several restrictive hypotheses, e.g., constant atmosphere and linear relative dynamics equations, while relevant uncertainties in satellite aerodynamic modeling make the practical realization of differential-drag-based maneuvers a challenge.

In this chapter we focus on the initial phase of a rendez-vous maneuver. Starting from a distance of tens-to-hundred kilometers, the maneuver is aimed at driving two satellites in close proximity. Docking is not considered because the maneuver is performed without any propulsive means but differential drag, which has limitations, as discussed in Section 5.2. The chapter has a twofold objective:

- First, a novel formulation of the rendez-vous maneuver using differential drag is proposed. This is an improved version of the optimal control approach developed in [Dell'Elce and Kerschen, 2013, 2015]. The method consists of three main blocks, namely the drag estimator, the maneuver planner, and the on-line compensator. The drag estimation is carried out by means of a simple density model which, nonetheless, is able to detect the main features of the upper atmosphere. The planner is then in charge of the scheduling of an optimal reference path. For this purpose, the problem is formulated as a two-point boundary value problem (TPBVP). The dynamics equations are formulated in terms of mean equinoctial ROE and they use the analytical propagator developed in Chapter 4 to estimate the dynamics of the chief. The proposed formulation results in time-continuous control of the cross section, as in [Ben-Yaacov and Gurfil, 2013, Kumar and Ng, 2009]. On the contrary, most of the literature on differential drag considers the bang-bang control of the cross section. When the relative ballistic coefficient is imposed through attitude control, the assumption of bang-bang control is restrictive, especially for small satellites with limited power available. Finally, on-line compensation relying on a MPC algorithm is implemented to account for uncertainties and unmodeled dynamics.
- Second, some practical challenges intimately related to the exploitation of differential drag in a realistic scenario are addressed. For this purpose, high-fidelity 6-degree-of-freedom (DoF) propagation including advanced drag modeling and detailed space environment is exploited to validate the algorithm. We note, for instance, that the entire literature on differential drag assumes that drag is proportional to the cross-section of the spacecraft and that it is the only component of the aerodynamic force. In addition, the present chapter assumes that the two satellites have different geometries, which result in different ballistic properties, as discussed in Section 1.5.3.

The chapter is organized as follows. The modeling assumptions of the control plant are discussed in Section 5.2. Section 5.3 describes the different building blocks of the proposed optimal control strategy. Finally, numerical simulations based on the QARMAN mission are detailed in Section 5.4.

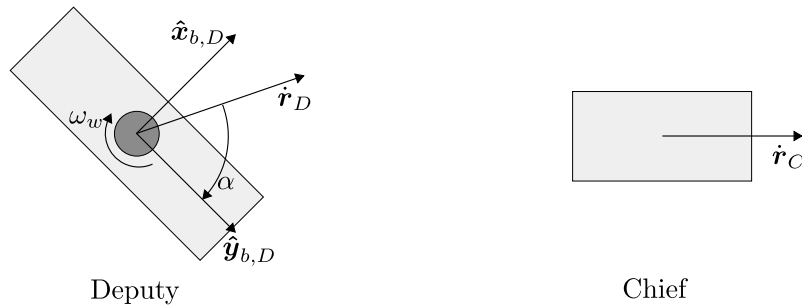


Figure 5.1: Nominal attitude of deputy (left) and chief (right).

5.2 Modeling assumptions

This study focuses on the rendez-vous problem between two satellites, namely the chief and the deputy, using differential drag as the only control force. The chief can also be a fictitious target point. It is assumed that the orbits of the satellites are nearly circular and quasi coplanar. Though the former assumption could be removed, it is not the case for the latter, which comes from the extremely modest authority of the differential drag in the out-of-plane direction. Specifically, Ben-Yaacov *et al.* showed that the controllability is two orders of magnitude smaller in this direction even for highly inclined orbits [Ben-Yaacov and Gurfil, 2014]. For this reason, *only the in-plane position and velocity of the relative dynamics are controlled herein*.

Differential drag is imposed by changing the ballistic coefficient of the deputy. This can be achieved either by reorienting solar panels or through attitude control. The second option is considered herein, so that rotational and translational degrees of freedom are coupled. Depending on the specific actuators considered, attitude constraints of various nature are introduced into the problem. In this chapter, the combination of three reaction wheels and 3-axis magnetotorquers is exploited.

The chief is assumed to be passive, i.e., its ballistic coefficient cannot be controlled. *The proposed methodology is only applicable if the attitude of the chief is predictable*. This includes not only fully-stabilized configurations, but also spinning and tumbling satellites. Scheduled maneuvers can be included, as well. On the contrary, the method fails if the chief performs, for example, attitude and orbital maneuvers or solar panel reconfigurations which were not expected before the beginning of the rendez-vous maneuver. The same methodology applies for spinning and tumbling targets, while minor modifications should be included to account for prescribed maneuvers of the chief.

Because the case study in Section 5.4 considers CubeSats without deployable panels, the two satellites are modeled with a parallelepiped shape and the principal axes are assumed to be aligned with the symmetry axes of the parallelepiped. However, the proposed formulation is *independent from the specific geometry*, provided that minimum and maximum drag configurations of the deputy are identified.

Considering Figure 5.1 and the notations of Section 1.3, the reference attitude of

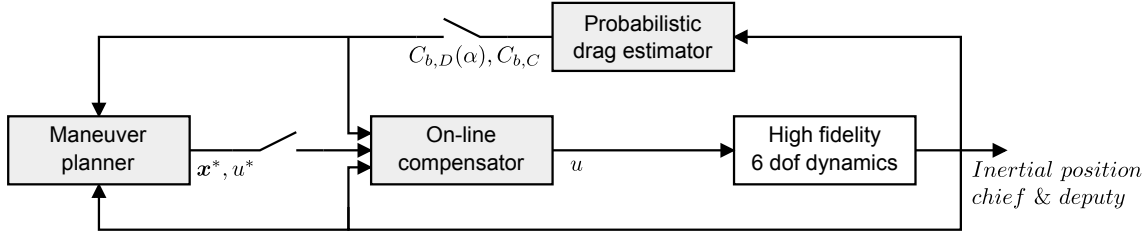


Figure 5.2: High-level optimal control strategy. The asterisk denotes the reference trajectory and control.

the two satellites is such that:

- the chief is in its minimum-drag configuration, which here is assumed to be such that its long axis is toward its orbital velocity direction, $\hat{\mathbf{r}}_C$. The $\hat{\mathbf{z}}_{b,C}$ axis is toward $\hat{\mathbf{h}}_C$;
- the deputy's $\hat{\mathbf{z}}_{b,D}$ axis is toward $\hat{\mathbf{h}}_D \approx \hat{\mathbf{h}}_C$. The magnitude of the differential drag is changed by pitching the deputy about $\hat{\mathbf{z}}_{b,D}$. The pitch angle is given by

$$\alpha = \cos^{-1} \left(\frac{\dot{\mathbf{r}}_D}{\|\dot{\mathbf{r}}_D\|} \cdot \hat{\mathbf{y}}_{b,D} \right) \operatorname{sign} (\dot{\mathbf{r}}_D \cdot \hat{\mathbf{x}}_{b,D}), \quad (5.1)$$

where $\hat{\mathbf{y}}_{b,D}$ is toward the long axis of the deputy. We note that differential drag can also be controlled by yawing rather than pitching. However, for highly-inclined orbits, pitching is preferred because it enhances the de-saturation capabilities of the magnetotorquers.

5.3 Optimal maneuvers using differential drag

The proposed optimal control strategy consists of three modules: i) the drag estimator evaluates the ballistic coefficient of the two satellites, ii) the maneuver planner schedules an optimal reference trajectory, iii) the on-line compensator corrects the deviations from the reference path due to unmodeled dynamics and uncertainties. The high-level control strategy is schematized in Figure 5.2.

The drag estimator and the maneuver planner are activated only a few times during the whole maneuver, e.g., they can be executed either when the divergence between the real and the planned path is beyond a given threshold or after a fixed period of one-to-few days¹. In this work, we execute these two modules only once at the beginning of the maneuver.

¹In our experience, the maximum update rate of the reference path should exceed 5 days.

5.3.1 Drag estimator

This module is in charge of the estimation of the ballistic properties of the satellites. The estimation using particle filtering is not considered in this chapter because it was developed only at the very end of the thesis.

The estimator requires that the position of the two spacecraft is monitored during an observation time t_{obs} . Their attitude is imposed throughout this period. If a single pose is sufficient for the determination of the ballistic coefficient of the chief, this is not the case for the deputy: because thermal flow is assumed in the simulation environment, the ballistic coefficient is not proportional to the cross section. Minimum and maximum drag configurations must be observed. Each pose is monitored for a time equal to $\frac{t_{obs}}{2}$.

The ballistic coefficient is estimated by minimizing the drift between observed and simulated inertial positions. Simulated data are generated on-board through a low-precision propagation including J_2 gravitational effect and drag perturbation only. The aerodynamic force of the simulated data is given by:

$$\mathbf{f}_{drag} = -\frac{1}{2}\rho C_b \|\mathbf{v}_{TAS}\| \mathbf{v}_{TAS} \quad (5.2)$$

where $\mathbf{v}_{TAS} = \mathbf{v} - \boldsymbol{\Omega}_e \times \mathbf{r}$, C_b , ρ , \mathbf{r} , \mathbf{v} , and $\boldsymbol{\Omega}_e$ are the airspeed, the ballistic coefficient, the atmospheric density, the inertial position and velocity, and the Earth's angular velocity, respectively. A basic analytical model is exploited to estimate the density:

$$\rho(r, \theta, i; A, B, C, D) = A(1 + B \cos(\theta - C)) \exp\left(\frac{r - r_{eq}\sqrt{1 - e_{eq}^2 \sin^2 i \sin^2 \theta}}{D}\right) \quad (5.3)$$

where θ , i , (A, B, C, D) , r_{eq} , and e_{eq} , are the argument of latitude and orbital inclination, the calibration coefficients of the model, and the Earth's equatorial radius and eccentricity, respectively. Though relatively simple, this model is able to outline the most relevant characteristics of the upper atmosphere, namely the exponential vertical structure, the day-night bulge, and the Earth's oblateness. Neglecting these contributions results in inconsistent predictions of the short-term evolution of the density, e.g., the day-night bulge is responsible for variations of approximatively a factor 5 at 500 km according to [Doornbos, 2012], which lead to the generation of an unreliable reference path.

The coefficients of the model are orbit-dependent and they are tuned using a more advanced model, i.e., Jacchia 71 in this work, by minimizing the root mean square error between the density provided by Equation (5.3) and the advanced model during one orbit.

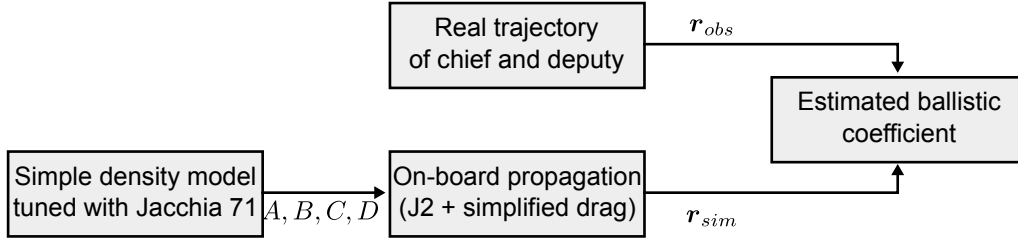


Figure 5.3: Schematic representation of the estimation of the ballistic coefficient.

The estimation is then performed by solving:

$$\begin{aligned} C_{b,C} &= \arg \left[\min_{C_b} \left(\int_0^{t_{obs}} (\mathbf{r}_{obs,C} - \mathbf{r}_{sim,C}(C_b))^2 dt \right) \right] \\ C_{b,D}(\alpha_i) &= \arg \left[\min_{C_b} \left(\int_{\frac{t_{obs}}{2}(i-1)}^{\frac{t_{obs}}{2}i} (\mathbf{r}_{obs,D} - \mathbf{r}_{sim,D}(C_b))^2 dt \right) \right] \quad i = 1, 2 \end{aligned} \quad (5.4)$$

Here, \mathbf{r}_{obs} and \mathbf{r}_{sim} are the observed and simulated inertial position, respectively. The subscripts C and D indicate chief and deputy, respectively. The pitch angles α_1 and α_2 correspond to the minimum and maximum drag configuration of the deputy, respectively. The computation of the ballistic coefficient is illustrated in Figure 5.3.

The necessary condition for the exploitation of the differential drag is that the estimated ballistic coefficient of the chief must lie between the minimum and maximum ballistic coefficients of the deputy, i.e., $C_{b,D}(\alpha_1) < C_{b,C} < C_{b,D}(\alpha_2)$. In this case, the target point is feasible.

Finally, the ballistic coefficient of the deputy is fitted with a linear interpolation as a function of the exposed cross section, S . The simple geometry considered in this study yields:

$$S = S_x |\sin \alpha| + S_y |\cos \alpha|, \quad \alpha_1 = 0, \quad \alpha_2 = \tan^{-1} \frac{S_x}{S_y}, \quad (5.5)$$

where S_x and S_y are the surface of the faces of the deputy with normal $\hat{\mathbf{x}}_{b,D}$ and $\hat{\mathbf{y}}_{b,D}$, respectively.

The outputs of the drag estimator are the fitted ballistic coefficient of the deputy, $C_{b,D}(\alpha)$, and the constant ballistic coefficient of the chief, $C_{b,C}$.

5.3.2 Maneuver planner

The maneuver planner schedules an optimal reference trajectory for the rendez-vous maneuver. An optimal control formulation of the maneuver planning problem is envisaged.

Let $\dot{\mathbf{x}} = \mathbf{f}(\mathbf{x}, \mathbf{u}, t)$ be a dynamical system with $\mathbf{x} \in \mathbb{R}^{n_x}$ and $\mathbf{u} \in \mathbb{R}^{n_u}$ states and control variables, respectively. Optimal control in this chapter is aimed at

driving the system from its initial state, $\mathbf{x}(0) = \mathbf{x}_0$, to a desired state, $\mathbf{x}(t_f) = \mathbf{x}_f$, where t_f is the maneuvering time. The trajectory is required to minimize a cost function $\mathcal{J}(\mathbf{x}, \mathbf{u}, t_f) = \mathcal{M}(t_f) + \int_0^{t_f} \mathcal{L}(\mathbf{x}, \mathbf{u}, t) dt$. The trajectory must also satisfy the inequality constraints, $\mathbf{g}(\mathbf{x}, \mathbf{u}, t) \leq \mathbf{0}$. Here $\mathbf{g} : \mathbb{R}^{n_x} \times \mathbb{R}^{n_u} \times \mathbb{R} \rightarrow \mathbb{R}^{n_g}$ is a n_g -dimensional vectorial function of path constraints which need to be enforced continuously in time.

This set of constraints yields the *Bolza* problem:

$$\begin{aligned} [\mathbf{x}^*, \mathbf{u}^*] &= \arg \left[\min_{\mathbf{x}(t), \mathbf{u}(t), t \in [0, t_f]} \mathcal{J}(\mathbf{x}, \mathbf{u}, t_f) \right] \text{ s.t.} \\ \dot{\mathbf{x}} &= \mathbf{f}(\mathbf{x}, \mathbf{u}, t) \quad \forall t \in [0, t_f], \\ \mathbf{g}(\mathbf{x}, \mathbf{u}, t) &\leq \mathbf{0} \quad \forall t \in [0, t_f], \\ \mathbf{x}(0) &= \mathbf{x}_0, \\ \mathbf{x}(t_f) &= \mathbf{x}_f. \end{aligned} \tag{5.6}$$

In our study, the different quantities of Problem (5.6) are:

Cost function, $\mathcal{J}(\mathbf{x}, u, t_f)$

The performance index is aimed at minimizing a desired convex functional,

$$\int_0^{t_f} \mathcal{L}(\mathbf{x}, u, t) dt,$$

chosen according to the needs of the mission. It can for instance include the dissipated to collected power ratio, i.e., the consumption of the attitude control system over the incoming solar power, the mean squared differential drag (as in Section 5.4.2), the optimization of a geometrical feature of the trajectory (as shown later in Equation (6.53)).

Although time optimality could be included in the cost function, i.e., $\mathcal{M}(t_f) = t_f$, we observed that the maneuvering time is highly determined by the initial guess provided to the optimal control solver. For this reason, time optimal maneuvers are not considered in this work.

Dynamical system, $\dot{\mathbf{x}} = \mathbf{f}(\mathbf{x}, u, t)$

The proper choice of the differential equations is the core of the trade-off between accuracy and computational efficiency of the planner:

- the planner is required to be consistent with the real dynamics. Consistency implies that *all* the dominant effects are modeled. This includes short-period and altitude-dependent variations of the drag. When propagating the open-loop control, we observed that neglecting short-period variations results in inconsistent predictions of the oscillatory movement, while neglecting altitude dependency results in greater in-track errors at the end of the maneuver.

- targeting computational efficiency, we want that *only* the dominant effects are modeled in the planner. This excludes all the orbital perturbations but the drag and secular J_2 effects. The same simplified drag modeling of the drag estimation module is used, i.e., Equations (5.2) and (5.3).

Further efficiency is achieved by considering only a reduced set of equations of motion in the control plant. This includes only the pitch of the deputy for attitude dynamics, and only the in-plane motion for translational dynamics. For the latter, we use mean equinoctial ROE – which evolve in a “smoother” way than Cartesian or curvilinear relative states – so that the state of the control plant is:

$$\boldsymbol{x} = \begin{bmatrix} \Delta\bar{\mathcal{E}}_{eq,pl} \\ \alpha \\ \dot{\alpha} \\ \omega_w \end{bmatrix} \quad (5.7)$$

where ω_w and $\Delta\bar{\mathcal{E}}_{eq,pl}$ are the angular velocity of the reaction wheel controlling the pitch and the subset of equinoctial ROE describing the in-plane motion, i.e., $\Delta\bar{\mathcal{E}}_{eq,pl} = [\Delta\bar{a}, \Delta\bar{P}_1, \Delta\bar{P}_2, \Delta\bar{l}]$.

Attitude dynamics about the $\hat{\mathbf{z}}_{b,D}$ axis is expressed as:

$$\begin{aligned} \ddot{\alpha} &= I_{zz}^{-1} ((\mathbf{r}_{cg} \times \mathbf{f}_{drag,D}) \cdot \hat{\mathbf{z}}_b - M_{mag}(\omega_w, t) - u) \\ \dot{\omega}_w &= (I_w^{-1} + I_{zz}^{-1}) u - I_{zz}^{-1} ((\mathbf{r}_{cg} \times \mathbf{f}_{drag,D}) \cdot \hat{\mathbf{z}}_{b,D} - M_{mag}(\omega_w, t)) \end{aligned} \quad (5.8)$$

where I_w , I_{zz} , \mathbf{r}_{cg} , and M_{mag} are the rotational inertia of the reaction wheel and of the deputy about the $\hat{\mathbf{z}}_{b,D}$ direction, the position of the center of mass of the deputy with respect to its geometric center, and the torque provided by the magnetotorquers, respectively.

Concerning the relative motion, linearized equations for the mean equinoctial ROE are computed by differentiating the averaged equinoctial GVE Equation (1.10) with respect to the equinoctial elements and perturbing force:

$$\dot{\Delta\bar{\mathcal{E}}}_{eq,pl} = \mathbf{A}(\bar{\mathcal{E}}_{eq,C}, \mathbf{f}_{drag,C}) \Delta\bar{\mathcal{E}}_{eq,pl} + \mathbf{B}(\bar{\mathcal{E}}_{eq,C}, \mathbf{f}_{drag,C}) \Delta f_{drag} \quad (5.9)$$

where $\mathbf{A}(\bar{\mathcal{E}}_{eq,C}, \mathbf{f}_{drag,C})$ and $\mathbf{B}(\bar{\mathcal{E}}_{eq,C}, \mathbf{f}_{drag,C})$ are the Jacobian of the GVE with respect to $\bar{\mathcal{E}}_{eq,pl}$ and to the tangential perturbing force, respectively. The effect of Earth’s oblateness is introduced by means of Equations 4.5 and, as such, it is accommodated in $\mathbf{A}(\bar{\mathcal{E}}_{eq,C}, \mathbf{f}_{drag,C})$ and $\mathbf{B}(\bar{\mathcal{E}}_{eq,C}, \mathbf{f}_{drag,C})$. This approach was proposed in [Schaub, 2003], but Keplerian elements were used. To the best of our knowledge, an analytical expression of the linearized equations of mean equinoctial ROE is not available in the literature, so that it is provided in Appendix B.

Equations (5.9) assume that the differential relative orbital elements are small enough, but no assumption is introduced on the dynamics of the chief. This is why these equations are superior to popular linearized models assuming circular orbits, e.g., [Clohessy and Wiltshire, 1960, Schweighart and Sedwick, 2002]. Although

Equation (5.9) is expressed in terms of mean elements, the instantaneous differential drag is used. The underlying assumption is that the differential perturbing force acting on the mean elements has the same effect on the osculating ones. This approximation is justified in [Schaub et al., 2000] by noting that the gradient of the contact transformation, \mathbf{T} is close to the identity matrix.

The computation of the matrices \mathbf{A} and \mathbf{B} requires that the absolute motion of the chief is integrated, too. *We avoid this task by using the analytical model developed in Chapter 4, which yields a time explicit analytical expression for the two matrices.*

Because the only in-plane motion is modeled in the planner, differential drag is defined as:

$$\Delta f_{drag}(\mathcal{E}_{eq,C}, \Delta\mathcal{E}_{eq}, \alpha) = \frac{\dot{\mathbf{r}}_D}{\dot{r}_D} \cdot \mathbf{f}_{drag,D} - \frac{\dot{\mathbf{r}}_C}{\dot{r}_C} \cdot \mathbf{f}_{drag,C}. \quad (5.10)$$

Rendez-vous conditions, $\mathbf{x}(t_f) = \mathbf{x}_f$

At the end of the maneuver the deputy should be in close proximity of the target. This constraint is imposed as:

$$\Delta \bar{a}(t_f) = \Delta \bar{P}_1(t_f) = \Delta \bar{P}_2(t_f) = \Delta \bar{l}(t_f) = 0. \quad (5.11)$$

Path constraints, $\mathbf{g}(\mathbf{x}, u, t)$

Physical constraints include the maximum available torque, T_w , and operating range of the wheel, $[\omega_{w,l}, \omega_{w,u}]$, and the saturation of the magnetic coils, i.e.,

$$\omega_w \in [\omega_{w,l}, \omega_{w,u}], |u| \leq T_w, |M_{mag}(\omega_w, t)| \leq M_{mag,max}(t) \quad \forall t \in [0, t_f] \quad (5.12)$$

where $M_{mag,max}(t)$ is the maximum available torque of the magnetotorquers in the direction $\hat{\mathbf{z}}_{b,D}$.

Direct transcription of the optimal control problem

The *Pontryagin minimum principle* [Pontryagin, 1987] provides first-order optimality conditions of Problem (5.6) consisting of an unconstrained TPBVP, i.e., without path and dynamics constraints, with the $2n_x$ -dimensional state vector given by the initial states \mathbf{x} plus a set of so-called *co-states*. Indirect techniques attempt to solve Problem (5.6) by enforcing optimality conditions. Such an approach requires a guess of the initial co-states. Unfortunately, these variables usually have no physical interpretation, which complicates the exploitation of indirect approaches.

Direct techniques are a valuable alternative aimed at directly tackling Problem (5.6) via the paradigm *discretize and then optimize* [Betts, 1998, 2010, Conway, 2010, Yan et al., 2011]. The optimal control problem is recast into a finite-dimensional non-linear programming (NLP) optimization problem by expressing the

state and control variables with a finite-dimensional basis and by enforcing path and dynamics equations on a temporal grid. Analogously, the cost function is approximated with a quadrature rule. Direct methods comprise four main blocks, namely the function generator (i.e., dynamics equations), discretization, optimization, and convergence analysis.

Although direct techniques yield large dimensional NLP, they are flexible because constraints of various nature can be naturally included in the formulation. In addition, direct approaches are more robust than indirect ones which suffer from dramatic sensitivity with respect to the initial guess.

The direct approach used in this chapter belongs to the *pseudospectral* family [Fahroo and Ross, 2002, 2008], which provides efficient approximation of the cost function, state dynamics, and path constraints by means of orthogonal polynomial bases and carefully selected nodes. Specifically, we use a *hp*-adaptive Radau pseudospectral transcription [Garg et al., 2010] using the software GPOPS, which tackles the discretization by means of an implicit Gaussian quadrature based on the *Legendre-Gauss-Radau* collocation points. This approach lends to an *hp*-adaptive strategy for the convergence analysis and mesh refinement. The optimization is carried out by means of the sparse solver SNOPT.

The initial guess for the NLP is provided by the analytical solution of Bevilacqua *et al.* [Bevilacqua and Romano, 2008], which relies on the linearized Schweighart-Sedwick equations of relative motion [Schweighart and Sedwick, 2002], and it provides a bang-bang control for the differential drag, whose magnitude is assumed to be constant. This model yields a non-feasible solution to Problem (5.6). However, this is not a crucial issue for pseudospectral techniques which, as discussed in the previous paragraph, exhibit a modest sensitivity to the initial guess compared to indirect approaches.

We stress that the *only* inputs to the planner are the initial conditions and the outputs of the drag estimator.

The outputs of the planner are the reference control and states as a function of time, namely u^ and \mathbf{x}^* .*

5.3.3 On-line compensator

On-line compensation is mandatory to account for unmodeled dynamics and uncertainties. The former issue arises from the assumptions introduced in the definition of the control plant. In addition, the density model of the drag estimator is another source of unmodeled dynamics, because different atmospheric models generate different outputs given the same inputs. The latter issue reflects the practical difficulties in the prediction of stochastic processes like the solar and geomagnetic activity proxies and thermospheric winds.

No matter the origin, the effect of all these perturbations is the deviation of the observed trajectory from the scheduled path. A model predictive control algorithm is developed to cope with such deviations.

At each evaluation, the on-line compensator solves a problem analogous to the maneuver planner. The only differences are the boundary conditions, the fixed horizon, and the performance index.

Initial conditions are provided by the current states at the beginning of the evaluation at time t . MPC is based upon the receding horizon principle, i.e., the final time is fixed to $t + t_h$, where t_h is the horizon. The computed corrected control is then applied to the plant for a time $t_c \leq t_h$.

The performance index is aimed at minimizing the divergence from the reference path

$$\int_t^{t+t_h} \sum_{j=1}^{n_x} W_{x_j} (x_j - x_j^*)^2 d\tau \quad (5.13)$$

where $W_{(.)}$ are user-defined weights. A direct contribution of the controlled variable is not included, because its variation is dominated by the variations of α . The proper selection of the weights is not trivial, and stability issues may arise. Large W_α means high confidence in the reference path, but a less efficient tracking of the reference trajectory itself. Ideally, a large W_α is more suitable for the first phase of the maneuver. We tested different setups with initial in-track distances ranging up to 300km. Setting coefficients such that the three contributions have the same order of magnitude resulted in a stable controller within this range. However, a robust and automatic procedure for tuning the coefficients would be a relevant contribution.

5.4 Rendez-vous between two satellites of the QB50 constellation

The proposed case study consists of the rendez-vous between QARMAN and another CubeSat of the QB50 constellation [Muylaert et al., 2009]. QB50 will be a constellation of 40 double and 10 triple CubeSats [Heidt et al., 2000]. The QB50 requirements for the ‘standard 2U CubeSats’ [Muylaert, 2012] impose that the long axis of the CubeSat must be aligned with the orbital velocity. One of these standard CubeSats is considered to be the chief. QARMAN, a 3U CubeSat, will be the deputy. Both satellites are assumed to be equipped with 3-axis magnetotorquers and 3 reaction wheels with spin axes aligned with the geometric axes of the CubeSat. Quaternion feedback algorithm [Wie, 2008] is exploited to follow the required attitude of the two satellites. Table 5.1 lists the input parameters of the numerical simulations.

Numerical simulations are carried out in a highly-detailed environment. Both attitude and orbit are propagated. Table 5.2 summarizes the main features of the simulation environment and compares them to those of the control plant. As discussed in Section 1.6, the aerodynamic model of the propagator assumes thermal flow, variable accommodation of the energy, and non-zero re-emission velocity. We will show that exploiting this aerodynamic model affects the accuracy of the maneuver.

Table 5.1: Simulation parameters.

Mean elements of the target	semi-major axis	$6758 \cdot 10^3$	m
	eccentricity	0.001	
	inclination	98	deg
	RAAN	45	deg
	argument of perigee	0	deg
	true anomaly	0	deg
Initial curvilinear states	Julian date	2455287.5	days
	in-track position, i.e., \tilde{y}	$50 \cdot 10^3$	m
	radial position, i.e., \tilde{x}	100	m
	out-of-plane position, i.e., \tilde{z}	20	m
	in-track velocity, i.e., \tilde{v}_y	0	m s^{-1}
	radial velocity, i.e., \tilde{v}_x	0	m s^{-1}
Initial target's attitude (LVLH)	out-of-plane velocity, i.e., v_z	0	m s^{-1}
	pitch, roll, yaw	0	deg
	pitch, roll, yaw	0	deg
Space weather	Daily solar flux	200	sfu
	81-day averaged flux	155	sfu
	geomagnetic index K_p	4	
Chief's properties	mass	2	kg
	dimensions	$0.1 \times 0.2 \times 0.1$	m^3
	inertia	$I_y = 8 \cdot 10^{-3}$ kg	$\text{m}^2,$
Deputy's properties		$I_x = I_z = 3 \cdot 10^{-3}$	kg m^2
	offset of the center of mass	$0.01\mathbf{y}_b$	m
	mass	4	kg
Attitude actuators	dimensions	$0.1 \times 0.3 \times 0.1$	m^3
	inertia	$I_y = 25 \cdot 10^{-3}$	$\text{kg m}^2,$
		$I_x = I_z = 5 \cdot 10^{-3}$	kg m^2
On-line compensator's weights	offset of the center of mass	$0.01\mathbf{y}_b$	m
	wheels' maximum torque	$0.03 \cdot 10^{-3}$	N m
	wheels' operating range	[-6000, 6000]	rpm
	wheels' inertia	$0.25 \cdot 10^{-6}$ kg	m^2
	Magnetic rods' dipole	0.2	A m^2
	$W_{\Delta\bar{\alpha}}$	1 m^{-2}	
	$W_{\Delta\bar{P}_1}, W_{\Delta\bar{P}_2}$	10^6	
	W_α	10^4	rad^{-2}
	$W_{\dot{\alpha}}$	10^8	$\text{s}^2 \text{ rad}^{-2}$

Table 5.2: Differences between the simulation environment and the plant of the controller.

	Simulation environment	Control plant
Orbital dynamics	Full nonlinear osculating relative dynamics.	Linearized equations for mean equinoctial ROE.
Attitude dynamics	3 DoF Euler equations.	Single DoF dynamics about the pitch axis.
Atmospheric model	NRLMSISE-00 with short-term stochastic variations. Geodetic altitude from the reference ellipsoid.	Exponential vertical structure and sinusoidal periodic variations (day-night). Geocentric altitude from the reference ellipsoid.
Aerodynamic force	Sentman's model with more recent updates.	Drag force only. Cubic polynomial fitting of the estimated ballistic coefficients with the different poses.
Gravitational model	Harmonics up to order and degree 10.	J_2 secular effect.
Other perturbations	Luni-solar third-body perturbations, solar radiation pressure. Nutation, precession and polar wandering.	None.
External torques	Gravity gradient and aerodynamic torque computed with Sentman's model and more recent updates.	Simplified aerodynamic torque consisting of the cross product between the drag and the aerodynamic-to-gravity center distance vector.
Attitude control	Three-axis magnetic coils and three reaction wheels. Quaternion feedback control algorithm. Magnetic coils desaturate wheels in permanence.	Single reaction wheel about the pitch angle. Magnetic coils desaturate the wheel in permanence. The control torque is determined by the planner and on-line compensator.

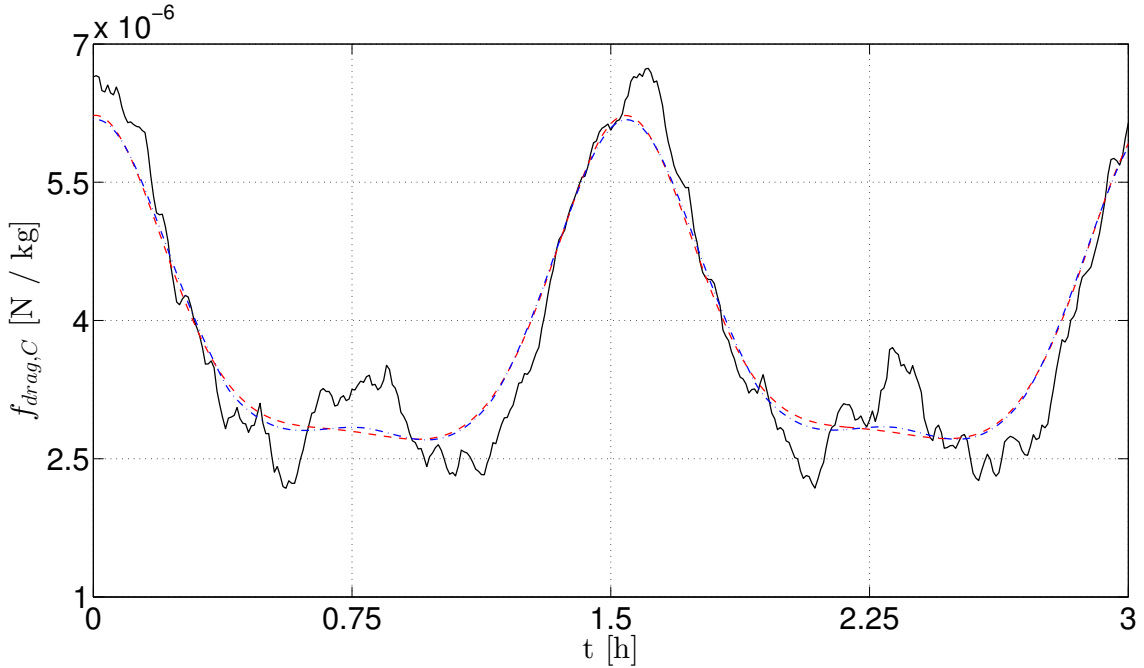


Figure 5.4: Drag force of the chief. The solid line is the real drag. The dashed line is the estimated drag with the simple atmospheric model. The dash-dot line is the estimated drag with the Jacchia 71 model.

We note that the calibration of the simple model defined in Equation (5.3) was not performed with the same model exploited for the high-fidelity simulations, i.e., Jacchia 71 and NRLMSISE-00, respectively. This is motivated by the scope of the chapter to consider a realistic scenario. In this way, the controller does not know the exact structure of the atmosphere. Nonetheless, uncertainty in the space weather is not considered here. Its impact on the maneuver is assessed in Chapter 6.

For the sake of clarity, in the remainder of the paper we will refer to high-precision propagation with the adjectives ‘observed’ or ‘real’. This will avoid confusion with data generated by the control plant, which we will refer to as ‘simulated’.

5.4.1 Drag estimator

We selected $t_{obs} = 8 t_{orb}$, where t_{orb} is the orbital period of the chief, so that we observed each pose of the deputy during 4 orbits.

Figure 5.4 compares the real drag force of the chief with the one estimated with the identified $C_{b,C}$ and the simplified density model of the drag estimator (Equation (5.3)). Because the controller does not know the exact structure of the atmosphere, there is an important difference between the estimated and real drag forces. Nonetheless, the good match between the simple and the largely more advanced Jacchia 71 model validates our claim that the former model is able to detect the main features of the structure of the upper atmosphere.

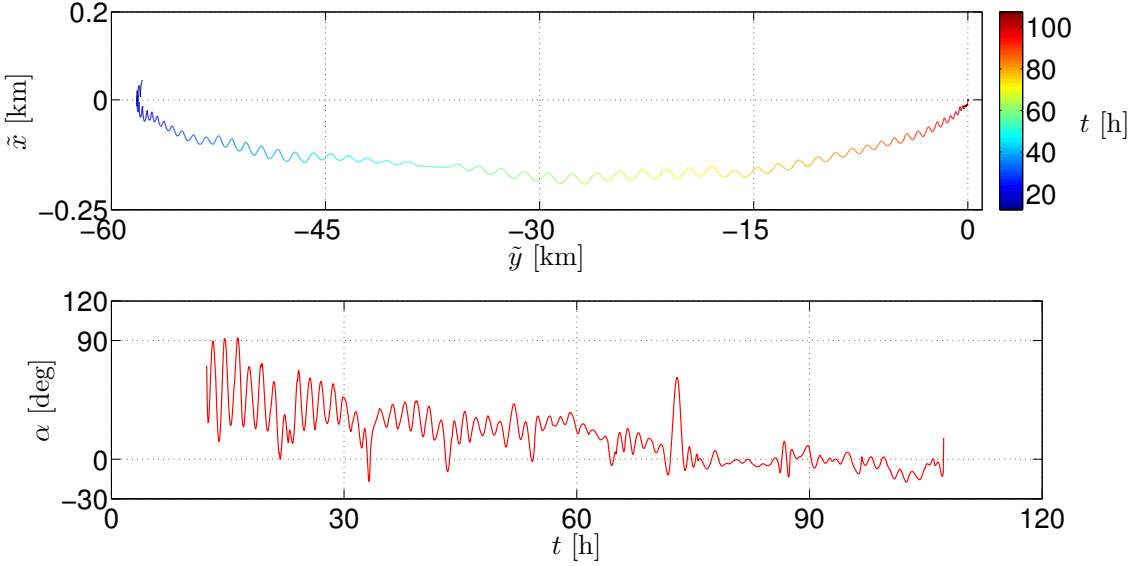


Figure 5.5: Minimum-differential-drag off-line (i.e., scheduled) maneuver. In the upper figure, the color indicates the elapsed time since the beginning of the maneuver, including the drag estimation time. The trajectory is illustrated with relative curvilinear states (defined in Section 1.4).

5.4.2 Maneuver planner

The first cost function considered consists of the mean-squared differential drag:

$$\frac{1}{t_f} \int_{t_{obs}}^{t_{obs}+t_f} \Delta f_{drag}^2(\mathcal{E}_{eq,C}, \Delta\mathcal{E}_{eq}, \alpha) dt. \quad (5.14)$$

The objective is to achieve a trajectory that can be robustly followed: minimizing the differential drag used by the planner results in the maximization of the remaining differential drag that can be exploited to compensate for deviations from the reference path. In other words, this objective function avoids bang-bang-like solutions. In fact, this latter strategy is such that differential drag is for most of the time at its extreme values, so that on-line compensation cannot provide two-sided maneuverability.

Figure 5.5 displays the scheduled trajectory generated by the planner. The reference pitch exhibits a gradual transition from a maximum to a minimum differential drag configuration. This is consistent with the above explanation on the purpose of the cost function.

The pseudospectral solver is able to converge to a feasible solution, so that, at the end of the planned maneuver, rendez-vous conditions are satisfied.

The interest in the proposed approach is its flexibility, i.e., the trajectory can be optimized according to the needs of the mission. Assume, for example, that a smooth relative trajectory is envisaged. The objective function of the planner can

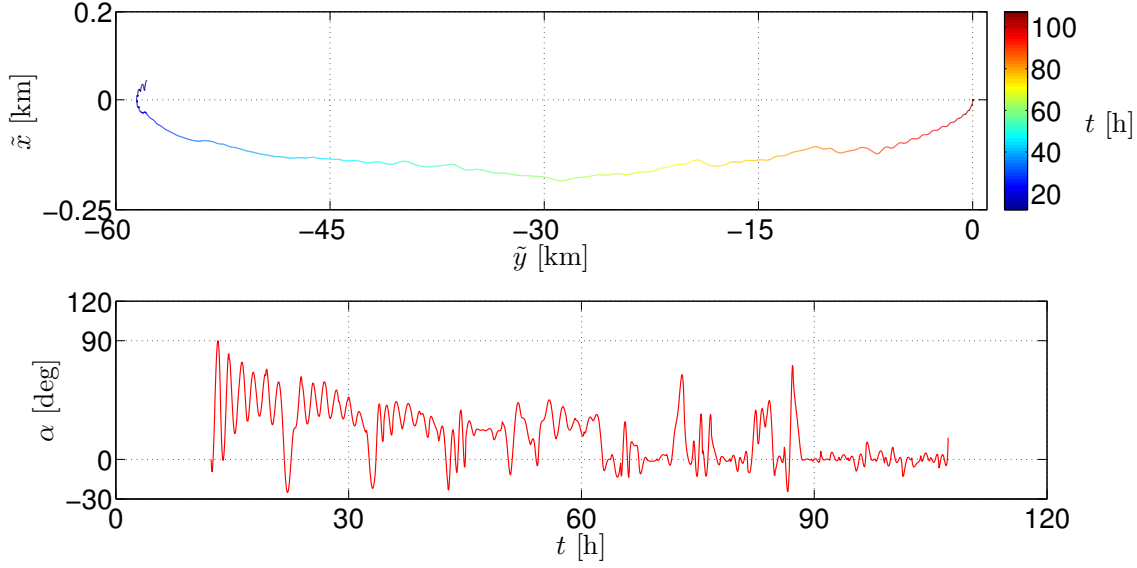


Figure 5.6: ‘Flattest trajectory’ off-line maneuver (i.e., scheduled). In the upper figure, the color indicates the elapsed time since the beginning of the maneuver, including the drag estimation time. The trajectory is illustrated with relative curvilinear states (defined in Section 1.4).

then be selected as follows

$$\frac{1}{t_f - t_{obs}} \int_{t_{obs}}^{t_{obs} + t_f} (\dot{r}_D - \dot{r}_C)^2 dt \quad (5.15)$$

Figure 5.6 illustrates the solution obtained by considering this cost function. The benefit of the optimization process is evident. Achieving this trajectory with other approaches would be at best challenging.

5.4.3 On-line compensator

The horizon and the control time of the on-line compensator are set to $t_h = 2t_c = 2t_{orb}$. This combination allows for an adequate averaging of short period variations that are the most critical to predict. The on-line controller is thus activated once per orbit, and it computes an open loop control with two-orbit horizon.

Figure 5.7 illustrates the trajectory obtained in the high-fidelity simulations and the corrected pitch angle. The overshoot in the \hat{y} direction at the end of the scheduled maneuver, $t_f + t_{obs}$, is of the order of 20 m, as shown in the close-up of the terminal phase in Figure 5.8. The on-line compensator is able to track the reference path with an adequate accuracy, given the limitations and the uncertainties inherent to differential drag. We note that this result outperforms the one obtained in [Dell’Elce and Kerschen, 2015] where Sedwick-Schweighart equations were used in the control plant.

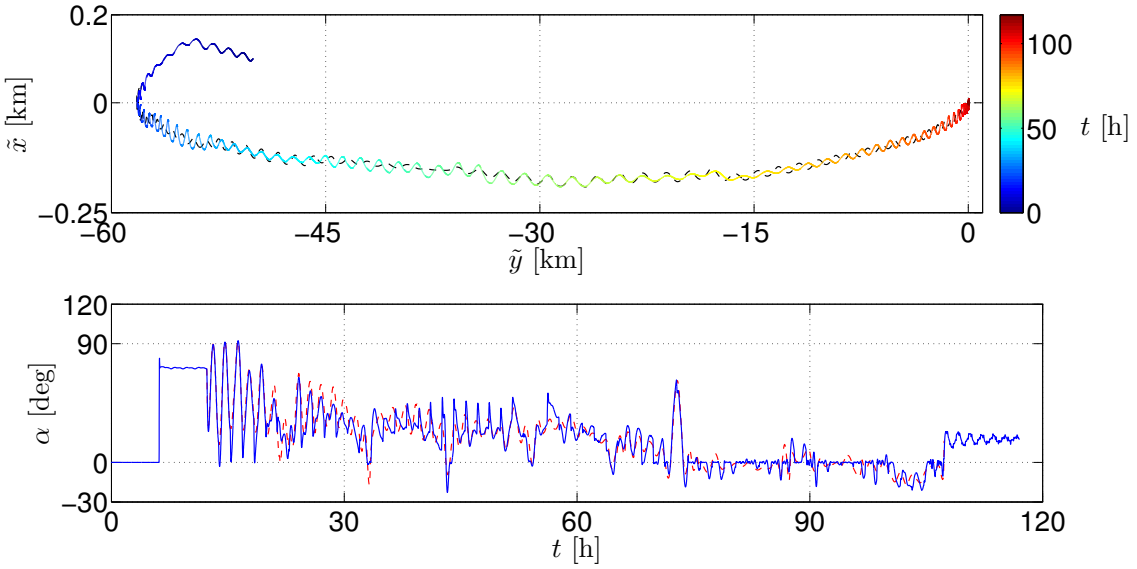


Figure 5.7: Minimum-differential-drag on-line maneuver. In the upper figure, the black-dotted and the colored line are the planned and the on-line trajectories, respectively. The color indicates the elapsed time since the beginning of the maneuver, including the drag estimation time. In the bottom figure, the dashed and the solid lines are the scheduled and the on-line pitch angles, respectively. The trajectory is illustrated with relative curvilinear states (defined in Section 1.4).

The accuracy of the maneuver is affected by the assumptions used in the development of the control plant. As said, the rendez-vous conditions are met with an accuracy of the order of 20 m, which is worse than the accuracy shown in previous works where a simpler aerodynamic model is considered in the simulations, e.g., [Dell'Elce and Kerschen, 2013]. This loss of accuracy needs to be considered when including collision avoidance constraints. The reason why it is not possible to improve the accuracy further is that the satellites have different geometries and masses. Recalling that the aerodynamic coefficients are computed on the actual geometry at every time step of the high-fidelity simulations and that drag is not proportional to the exposed surface, it follows that the real zero-differential drag configuration is unknown. In addition, the MPC algorithm is open-loop over the control horizon.

However, in our opinion, it is not the scope of differential-drag maneuvers to achieve the highest accuracy, especially given the limited out-of-plane controllability. In the numerical simulations, in fact, out-of-plane oscillations are of the same order as the accuracy of the terminal phase.

The importance of the weights of the reference pitch angle and its derivative in the cost function of the on-line compensator is given in Figure 5.9. Here, the weights related to the tracking and the derivative of the pitch are removed from the objective function of the MPC algorithm, i.e., $W_\alpha = W_{\dot{\alpha}} = 0$. In this case, the quality of the tracking of the reference path is slightly improved, but the corrected pitch exhibits spurious oscillations. This time history of the pitch is more demanding for the

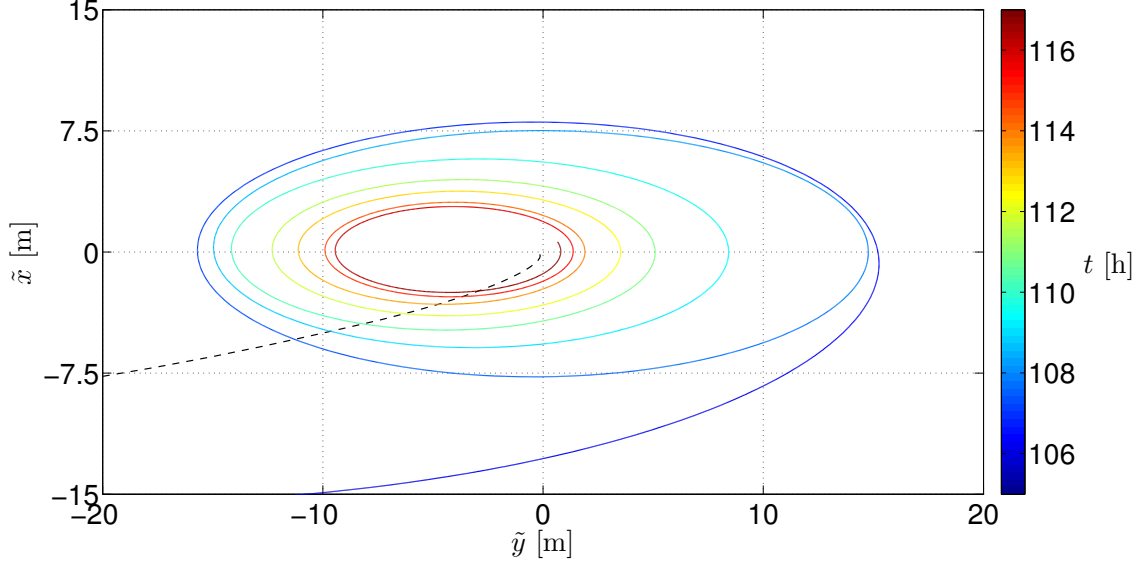


Figure 5.8: Minimum-differential-drag on-line maneuver. Zoom of the terminal phase. The black-dotted and the colored line are the planned and the on-line trajectories, respectively. The color indicates the time since the beginning of the maneuver.

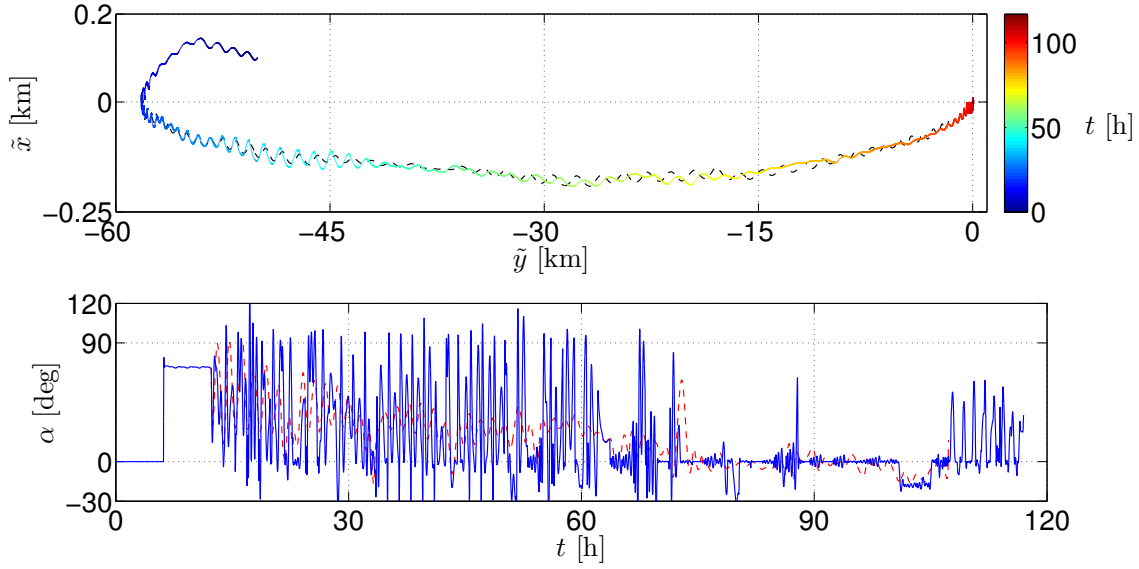


Figure 5.9: Minimum-differential-drag on-line maneuver without tracking of the reference pitch angle. In the upper figure, the black-dotted and the colored line are the planned and the on-line trajectories, respectively. The color indicates the elapsed time since the beginning of the maneuver, including the drag estimation time. In the bottom figure, the dashed and the solid lines are the scheduled and the on-line pitch angles, respectively.

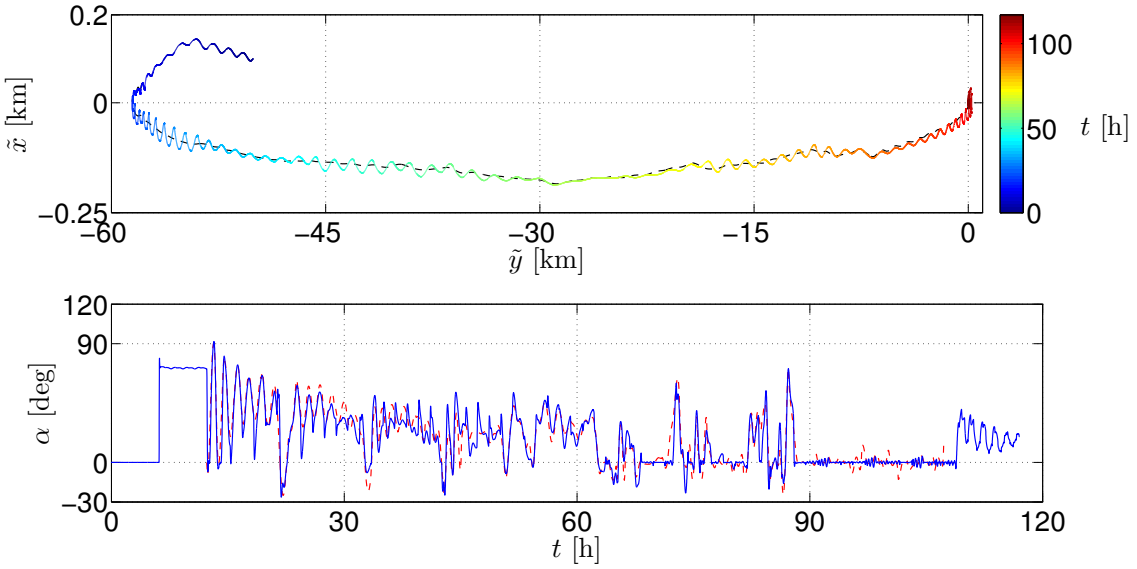


Figure 5.10: ‘Flattest trajectory’ maneuver. In the upper figure, the black-dotted and the colored line are the planned and the on-line trajectories, respectively. The color indicates the elapsed time since the beginning of the maneuver, including the drag estimation time. In the bottom figure, the dashed and the solid lines are the scheduled and the on-line pitch angles, respectively. The trajectory is illustrated with relative curvilinear states (defined in Section 1.4).

attitude control system and results in larger power consumption.

For completeness, Figure 5.10 depicts the on-line solution for the ‘flat’ trajectory.

5.5 Conclusion

This chapter proposed a three-step optimal control approach for differential-drag-based maneuvers. The maneuver planning is solved by means of a direct transcription of the optimal control problem, which enhances the flexibility for the choice of the cost function and allows us to naturally include constraints of various nature. For these reasons, the proposed approach *enables the possibility to accomplish complex and realistic maneuvers using differential drag*.

The formulation of the control plant in terms of mean ROE and the exploitation of the analytical propagator developed in Chapter 4 enhanced the accuracy of the maneuver with respect to previous results based on the linearized Sedwick-Schweighart equations.

The method was validated with high-fidelity simulations of a rendez-vous maneuver between satellites with different masses and geometries and advanced drag modeling.

This chapter raises two open questions: how can we improve drag estimation and

prediction? How can we plan trajectories that can account for the uncertainty in the atmospheric force?

The first question is addressed by replacing the drag estimation module with the particle filter developed in Chapter 3. Concerning the second question, a general-purpose methodology for the planning of robust maneuvers is proposed in Chapter 6.

Chapter 6

Robust Maneuver Planning

Abstract

The maneuver planning of a dynamical system subject to uncertain constraints and dynamics can be formulated as an infinite-dimensional optimization problem: the design variables are continuous functions of time and dynamics and path constraints must be enforced for every time instant and for every occurrence of the generally-dense uncertain set. Starting from such an infinite-dimensional formulation and assuming that the system is differentially flat, this chapter proposes a discretization of the problem which guarantees the feasibility of the trajectory over an arbitrary user-defined portion of the uncertain set. Taking advantage of the formalism of squared functional systems and of the scenario approach, the methodology does not require a temporal grid and it is able to include uncertainty sources of various nature. The methodology is applied to the differential-drag-based rendez-vous maneuver. It also integrates the outcomes of Chapters 3 and 4: both the analytical propagator and the particle filter are used to accomplish the robust rendez-vous maneuver.

6.1 Introduction

The optimal control methodology developed in Chapter 5 is in principle able to cope with unmodeled dynamics and uncertainties. However, the feasibility of the planned trajectory cannot be guaranteed. For instance, it could happen that there is not enough differential drag for a specific realization of the solar and geomagnetic activities.

This is why the present Chapter proposes a general methodology for the robust planning of constrained trajectories. We consider a two-point boundary value problem with both uncertainties in the dynamics equations and in the path constraints, e.g., saturation of the actuators or collision avoidance. The feasibility of the solution of the problem must be guaranteed for a prescribed portion of the possible outcomes of the uncertain set.

The study is focused on the class of differentially flat systems theorized by Fliess *et al.* [Fliess et al., 1995]. Differential flatness is an attractive property for control purposes because it establishes an equivalence between the original and a trivial algebraic and invertible system. This facilitates the problem of maneuver planning by removing the need for the explicit enforcement of the dynamics equations. For this reason, a large body of literature exists on the deterministic counterpart of the problem tackled herein [Lévine, 2009, Ross and Fahroo, 2004, Faulwasser et al., 2014]. Algorithms suitable for the real-time generation of both constrained and unconstrained trajectories of flat systems were also proposed by Faiz *et al.* [Faiz et al., 2001] and by van Nieuwstadt *et al.* [Van Nieuwstadt and Murray, 1998], respectively. Henrion *et al.* [Henrion and Lasserre, 2004] and Louembet *et al.* [Louembet et al., 2010, Louembet and Deaconu, 2011] offered methodologies which guarantee the feasibility of the trajectory continuously in time. These latter contributions inspired the present work.

The generation of robust trajectories is also a problem of great timeliness in the control community [Svestka and Overmars, 1998]. The tradeoff between computational efficiency and generality led to the development of both sampling-less and randomized methodologies. In the former case, the computation of the robust reference maneuver is performed by solving a single optimization problem [Ono and Williams, 2008, Blackmore, 2008, Blackmore and Ono, 2009, Blackmore et al., 2011], but these methodologies are often limited to a small class of dynamical systems and perturbations, e.g., linear time invariant system and Gaussian random variables. In the latter case, the identification of the feasible maneuvers is achieved by constructing a random tree of possible trajectories [Marti, 1999, Kewlani et al., 2009, Kothari and Postlethwaite, 2012, van den Berg et al., 2011]. Finally, Ross *et al.* [Ross et al., 2014] proposed to approximate the probability distribution of the uncertain quantities by means of the unscented transform and to solve a single classical optimal control problem for the augmented dynamical system defined by the sigma points of the transform and a single common control signal.

Most approaches cited in the previous paragraph lead to the determination of a deterministic control action associated with a probabilistic description of the refer-

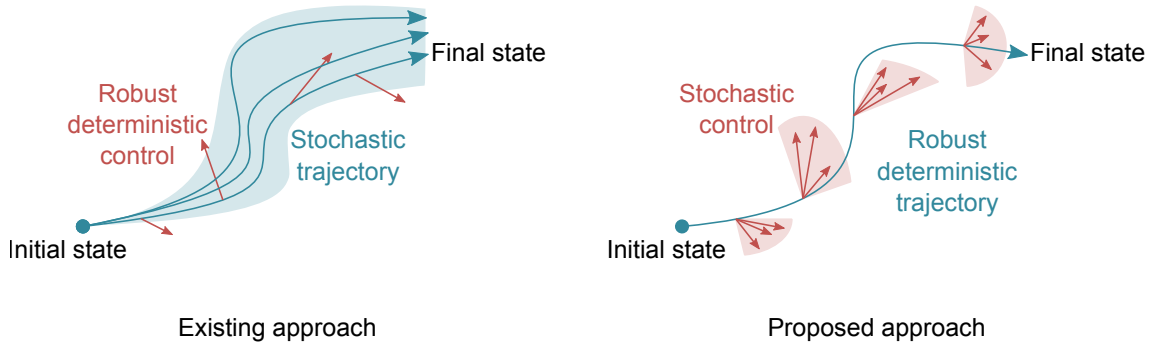


Figure 6.1: Conceptual difference between the existing and the proposed approaches to robust maneuver planning.

ence path. When the dynamics of the system is extremely sensitive to the outcome of the uncertain environment, e.g., like in the drag-assisted rendez-vous, the confidence bounds of the trajectory might be too large to make it of practical interest. For this reason, we propose a different paradigm in this Chapter, as illustrated in Figure 6.1. The idea is to find a *deterministic reference trajectory which is feasible for most of the outcomes of the uncertain set*. In this case, the control action required for the execution of this maneuver depends on the uncertain set and, as such, it is stochastic. The proposed methodology is unaware of the feedback loop implemented for tracking the reference trajectory. However, the feasibility of the on-line maneuver can be guaranteed within a prescribed convex set in the tracking error's space. A similar “reference-trajectory-oriented” perspective was proposed by Graettinger and Krogh [Graettinger and Krogh, 1992] in the framework of linear time-varying systems. However, such approach is still missing in the literature on robust maneuver planning.

The resulting formulation consists of an *infinite-dimensional* optimization problem. Two fundamental results existing in the literature are combined to achieve a finite-dimensional tractable form with guaranteed feasibility both in time and in the uncertain set:

- after generating an inner polytopic approximation of the feasible set, the theory of positive functional systems developed by Nesterov [Nesterov, 2000] is used to *guarantee the feasibility continuously in time*. As anticipated, this approach is analogous to the one developed in [Henrion and Lasserre, 2004, Louembet et al., 2010]. A less conservative implementation is proposed herein in order to improve the performance of the maneuver in the presence of affine exogenous perturbations sufficiently smooth in time;
- the scenario approach developed by Calafiore and Campi [Calafiore and Campi, 2004, 2006] is then exploited to *guarantee that the solution is feasible for a desired portion of the event space of the uncertain set*. Although few simplifying assumptions are introduced, the use of the scenario approach yields a methodology applicable to a wide class of dynamical systems and of exogenous per-

turbations, e.g., non-Gaussian random variables or non-stationary stochastic processes. In addition, the scenario approach does not require the constraints to be convex with respect to the uncertain parameters.

The chapter is organized as follows. Section 6.2 introduces the concept of *robust deterministic trajectory* as the solution of an infinite-dimensional worst-case optimization problem. After recalling the notion of differentially flat system, sufficient conditions for the existence of the solution of the problem are derived. Semi-infinite and discrete approximations are then developed in Section 6.3 by using positive polynomials and the scenario approach. A simple example consisting of a steering maneuver of a car is proposed to illustrate the methodology step-by-step. Finally, the rendez-vous using differential drag is tackled in Section 6.5.

6.2 Robust maneuver planning

This Section details our proposed maneuver planning approach. The concept of robust deterministic trajectory is firstly introduced as being the solution of a worst-case optimization problem. Such notation is used to emphasize the fact that we seek a trajectory which is independent from the specific outcome of the uncertain set. Sufficient conditions for the existence of the solution are outlined. Finally, the inclusion of tracking error constraints is discussed yielding the formulation which is tackled in Section 6.3.

6.2.1 The robust deterministic trajectory

Consider the dynamical system $\dot{\mathbf{x}} = \mathbf{f}(\mathbf{x}, \mathbf{u}, \delta)$. Here $\mathbf{x} \in \mathbb{R}^{n_x}$, $\mathbf{u} \in \mathbb{R}^{n_u}$ are the state and control variables, respectively. The variable $\delta \in \Delta$ indicates a generic exogenous perturbation defined on the uncertain environment Δ and provided with probability distribution Pr_Δ . The perturbation can be any generic random quantity provided with a probabilistic description, e.g., a set of random variables, a non-stationary stochastic process indexed by the time, t , a n_x -valued random field, or any of their combinations. For the sake of conciseness, $\delta(\mathbf{x}, t)$ is only referred to as δ in the following.

The objective of this study is to determine a reference path driving the state vector from its initial condition \mathbf{x}_0 to a desired final state \mathbf{x}_f after a prescribed maneuvering time t_f . The reference trajectory is required to be globally feasible and to minimize a cost function $\mathcal{J}(\mathbf{x}, \mathbf{u}, \delta)$ with respect to \mathbf{x} and \mathbf{u} . The trajectory must also satisfy the inequality constraints $\mathbf{g}(\mathbf{x}, \mathbf{u}, t, \delta) \leq \mathbf{0}$. Here $\mathbf{g} : \mathbb{R}^{n_x} \times \mathbb{R}^{n_u} \times \mathbb{R} \times \Delta \rightarrow \mathbb{R}^{n_g}$ is a n_g -dimensional vectorial function of path constraints which needs to be enforced continuously in time and for every possible realization of the uncertain quantities.

By globally feasible, we mean that the feasibility of the trajectory must be ensured for all realization of the uncertain set, i.e., we are looking for a deterministic trajectory \mathbf{x}^* such that, $\forall \delta \in \Delta$, a control input \mathbf{u}_δ exists which exactly steers the

system along \mathbf{x}^* :

$$\begin{aligned} \mathbf{x}^* &= \arg \left[\min_{\mathbf{x}(t), t \in [0, t_f]} \left(\max_{\delta \in \Delta} \mathcal{J}(\mathbf{x}, \mathbf{u}_\delta, \delta) \right) \right] \text{ s.t.} \\ \forall t \in [0, t_f], \delta \in \Delta \quad &\exists \mathbf{u}_\delta(t) = \mathbf{u}(t, \delta) \text{ s.t.} \\ \dot{\mathbf{x}} &= \mathbf{f}(\mathbf{x}, \mathbf{u}_\delta, \delta), \\ \mathbf{g}(\mathbf{x}, \mathbf{u}_\delta, t, \delta) &\leq \mathbf{0}, \\ \mathbf{x}(0) &= \mathbf{x}_0, \\ \mathbf{x}(t_f) &= \mathbf{x}_f. \end{aligned} \tag{6.1}$$

The solution \mathbf{x}^* is referred to as *robust deterministic trajectory*. This terminology is used to emphasize that the temporal evolution of the states is always the same, regardless of the outcome of the uncertain set, as indicated by the second equation of Problem (6.1).

The distinction between δ and δ_w indicates that the trajectory \mathbf{x}^* is feasible for all outcomes of Δ and not only for the one which maximizes the cost function \mathcal{J} .

Remark 1. The robust deterministic trajectory is *executable* for all possible realizations of the uncertain quantity, i.e., for any $\delta \in \Delta$ a control $\mathbf{u}_\delta(t)$ exists such that $\dot{\mathbf{x}}^*(t) = \mathbf{f}(\mathbf{x}^*, \mathbf{u}_\delta, \delta)$, $\forall t \in [0, t_f]$. Nonetheless, $\mathbf{u}_\delta(t)$ is generally unknown for real-life problems because it requires the knowledge of the actual value of the uncertain quantity and of the states. This is why tracking error constraints are introduced in Paragraph 6.2.2.

Problem (6.1) does not necessarily admit a solution even in its simple unconstrained TPBVP form, i.e., without path constraints \mathbf{g} . In this Section, we provide sufficient conditions for the existence of a solution. For this purpose, we firstly recall the concept of differential flatness for a deterministic system.

Definition 1 (Differential flatness [Fliess et al., 1995]). The system $\dot{\mathbf{x}} = \mathbf{f}(\mathbf{x}, \mathbf{u})$ with n_x states, $\mathbf{x} \in \mathbb{R}^{n_x}$, and $n_u \leq n_x$ inputs, $\mathbf{u} \in \mathbb{R}^{n_u}$, is differentially flat if a set of n_u variables

$$\mathbf{q} = \mathcal{Q}(\mathbf{x}, \mathbf{u}, \dot{\mathbf{u}}, \ddot{\mathbf{u}}, \dots, \mathbf{u}^{(c)}), \tag{6.2}$$

exists such that

$$\begin{aligned} \mathbf{x} &= \mathcal{X}(\mathbf{q}, \dot{\mathbf{q}}, \ddot{\mathbf{q}}, \dots, \mathbf{q}^{(d)}), \\ \mathbf{u} &= \mathcal{U}(\mathbf{q}, \dot{\mathbf{q}}, \ddot{\mathbf{q}}, \dots, \mathbf{q}^{(d)}). \end{aligned} \tag{6.3}$$

The variables $\mathbf{q} \in \mathbb{R}^{n_u}$ are referred to as *flat outputs*. Here the superscripts (c) and (d) indicate the c -th and d -th order derivatives, respectively. Differential flatness is a property of the system.

In the remaining of the chapter, the compact notation $\mathbf{q}^{(0-d)}$ is exploited to indicate the column vector $\{\mathbf{q}^T, \dots, \mathbf{q}^{(d),T}\}^T$.

When uncertainties are accounted for, the three mappings can also be non-deterministic, i.e., $\mathbf{q} = \mathcal{Q}(\mathbf{x}, \mathbf{u}^{(0-c)}, \delta)$, $\mathbf{x} = \mathcal{X}(\mathbf{q}^{(0-d)}, \delta)$, and $\mathbf{u} = \mathcal{U}(\mathbf{q}^{(0-d)}, \delta)$.

Sufficient conditions for the existence of the robust deterministic trajectory are now discussed. The unconstrained TPBVP case is firstly addressed. Path constraints are then included.

Lemma 1. *Consider the TPBVP*

$$\begin{aligned} \mathbf{x}^* &= \arg \left[\min_{\mathbf{x}(t), t \in [0, t_f]} \left(\max_{\delta \in \Delta} \mathcal{J}(\mathbf{x}, \mathbf{u}_\delta, \delta) \right) \right] \text{ s.t.} \\ \forall t \in [0, t_f], \delta \in \Delta \quad &\exists \mathbf{u}_\delta(t) = \mathbf{u}(t, \delta) \text{ s.t.} \\ \dot{\mathbf{x}} &= \mathbf{f}(\mathbf{x}, \mathbf{u}_\delta, \delta), \\ \mathbf{x}(0) &= \mathbf{x}_0, \\ \mathbf{x}(t_f) &= \mathbf{x}_f. \end{aligned} \tag{6.4}$$

Let system $\mathbf{f}(\mathbf{x}, \mathbf{u}, \delta)$ be differentially flat and the mapping between flat outputs and states be deterministic, i.e., $\mathbf{x} = \mathcal{X}(\mathbf{q}^{(0-d)})$, and let \mathbf{x}_0 and \mathbf{x}_f belong to the same connected component of $\mathbb{R}^{n_x} \times \mathbb{R}^{n_u}$ that does not contain singularities of the Lie-Bäcklund isomorphism $(\mathcal{X}, \mathcal{U})$, then Problem (6.4) admits solutions.

Proof. Differential flatness implies that the system is controllable; in addition, because the isomorphism $(\mathcal{X}, \mathcal{U})$ has no singularities on the connected component of $\mathbb{R}^{n_x} \times \mathbb{R}^{n_u}$ including \mathbf{x}_0 and \mathbf{x}_f , it is always possible to find a path that satisfies boundary conditions, i.e., for any possible realization of the uncertain quantity $\delta \in \Delta$, the set

$$\mathcal{B}_\delta = \{ \mathbf{q}(t) \in C^d : \mathcal{X}(\mathbf{q}^{(0-d)}(0), \delta) = \mathbf{x}_0, \mathcal{X}(\mathbf{q}^{(0-d)}(t_f), \delta) = \mathbf{x}_f \} \tag{6.5}$$

is not empty.

In addition, because the mapping \mathcal{X} is deterministic, there exists a strict one-to-one relationship between the trajectory in the state and in the flat output spaces, so that \mathcal{B}_δ can be replaced by its deterministic counterpart

$$\mathcal{B} = \{ \mathbf{q}(t) \in C^d : \mathcal{X}(\mathbf{q}^{(0-d)}(0)) = \mathbf{x}_0, \mathcal{X}(\mathbf{q}^{(0-d)}(t_f)) = \mathbf{x}_f \} \tag{6.6}$$

which is still not empty and valuable for all the possible realizations of Δ .

Problem (6.4) can thus be recast into the flat formulation

$$\mathbf{q}^*(t) = \arg \left[\min_{\mathbf{q}(t) \in \mathcal{B}} \left(\max_{\delta \in \Delta} \tilde{\mathcal{J}}(\mathbf{q}^{(0-d)}, \delta) \right) \right]. \tag{6.7}$$

Here $\tilde{\mathcal{J}}(\mathbf{q}^{(0-d)}, \delta) = \mathcal{J}(\mathcal{X}(\mathbf{q}^{(0-d)}), \mathcal{U}(\mathbf{q}^{(0-d)}, \delta), \delta)$ and \mathbf{q}^* is such that $\mathbf{x}^* = \mathcal{X}(\mathbf{q}^{*(0-d)})$.

Because $\mathcal{B} \neq \emptyset$, Problem (6.7) admits deterministic solutions $\mathbf{x}^*(t)$. □

Sufficient conditions of Lemma 1 guarantee that the control \mathbf{u}_δ actually exists for

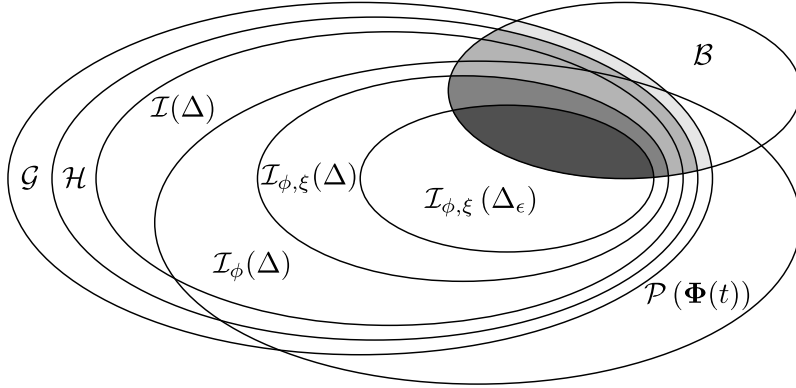


Figure 6.2: Schematic representation of the sets. From the lightest to the darkest, the gray regions indicate the feasible sets of Problems (6.1), (6.12), (6.27), and (6.29), respectively. The notation $\mathcal{I}(\Delta)$ is used to indicate $\bigcap_{\delta \in \Delta} \mathcal{I}(\delta)$.

all $\delta \in \Delta$. The uniqueness of the solution can only be guaranteed if $\tilde{\mathcal{J}}(\mathbf{q}^{(0-d)}, \delta)$ is convex with respect to $\mathbf{q}^{(0-d)}$.

Compared to Problem (6.4), the corresponding flat formulation (Problem (6.7)) does not require dynamics equations to be enforced as equality constraints of the optimization problem.

Theorem 1. *Problem (6.1) admits solutions if the conditions of Lemma 1 are satisfied and if $\mathcal{G} \cap \mathcal{B} \neq \emptyset$, where*

$$\mathcal{G} = \left\{ \mathbf{q}(t) \in C^d : \tilde{\mathbf{g}}(\mathbf{q}^{(0-d)}, t, \delta) \leq \mathbf{0}, \forall t \in [0, t_f], \delta \in \Delta \right\}, \quad (6.8)$$

and $\tilde{\mathbf{g}}$ is defined as

$$\tilde{\mathbf{g}}(\mathbf{q}^{(0-d)}, t, \delta) = \mathbf{g}(\mathcal{X}(\mathbf{q}^{(0-d)}), \mathcal{U}(\mathbf{q}^{(0-d)}, \delta), t, \delta). \quad (6.9)$$

Given Lemma 1, the proof of Theorem 1 is straightforward. Problem (6.1) can now be recast into its flat formulation

$$\mathbf{q}^*(t) = \arg \left[\min_{\mathbf{q}(t) \in (\mathcal{B} \cap \mathcal{G})} \left(\max_{\delta \in \Delta} \tilde{\mathcal{J}}(\mathbf{q}^{(0-d)}, \delta) \right) \right]. \quad (6.10)$$

We note that a large class of problems falls in the assumption of a deterministic mapping, e.g., fully-actuated manipulators. Specifically, the methodology is applicable whenever the nonholonomic constraints are not subject to uncertainty. This assertion is further clarified with the example in Section 6.4).

Different sets are introduced in the next sections. In order to facilitate the lecture, Figure 6.2 provides a graphical representation of these sets.

6.2.2 Inclusion of the tracking error

Remark 1 offers a theoretical interpretation of the robust deterministic trajectory. In most real-life applications, the available information on the uncertain quantity and on the state estimation is incomplete, so that the control action required for the exact execution of the reference trajectory is unknown and the implementation of a feedback loop on the tracking error is mandatory. Because the feasibility of the trajectory is only guaranteed on the trajectory itself, Problem (6.10) lacks practical interest. For this reason, conditions on the tracking error are introduced herein in order to extend the feasibility of the solution within a prescribed region close to the robust reference trajectory.

Specifically, it is required that the executed maneuver $\mathbf{q}(t)$ is feasible whenever the tracking error $\mathbf{e}(t) = \mathbf{q}(t) - \mathbf{q}^*(t)$ is such that $\mathbf{h}(\mathbf{e}^{(0-d)}) \leq \mathbf{0}$, where $\mathbf{h}(\mathbf{e}^{(0-d)})$ is a convex closed set of constraints defining the desired feasible region in the neighborhood of the reference path. This function is chosen by the user according to the performance of the on-line control algorithm implemented to track the reference path. A smaller region delimited by \mathbf{h} generally improves the cost function, $\tilde{\mathcal{J}}$, but it requires a more accurate on-line controller.

In order to avoid unnecessary notations, the set delimited by \mathbf{h} is assumed to be a polyhedron in the $n_u(d+1)$ dimensional phase space, i.e., the constraints \mathbf{h} are linear combinations of $\mathbf{e}^{(0-d)}$. We note that this assumption is not affecting the generality of the methodology because an outer polyhedral approximation of a generic convex and closed set can be found, for example, with the methodology proposed in [Cerone et al., 2012].

Including these constraints is equivalent to guaranteeing that the solution remains feasible whenever the tracking error stays in the set

$$\mathcal{E} = \{\mathbf{e}(t) \in C^d : \mathbf{h}(\mathbf{e}^{(0-d)}) \leq \mathbf{0}, \forall t \in [0, t_f]\}. \quad (6.11)$$

Accounting for these constraints yields the flat formulation of the problem

$$\mathbf{q}^*(t) = \arg \left[\min_{\mathbf{q}(t) \in (\mathcal{B} \cap \mathcal{H})} \left(\max_{\delta \in \Delta} \tilde{\mathcal{J}}(\mathbf{q}^{(0-d)}, \delta) \right) \right]. \quad (6.12)$$

Here, the set \mathcal{H} is such that

$$\mathcal{H} = \left\{ \mathbf{q}(t) \in C^d : \tilde{\mathbf{g}}(\mathbf{q}^{(0-d)} + \mathbf{e}^{(0-d)}, t, \delta) \leq \mathbf{0}, \forall t \in [0, t_f], \delta \in \Delta, \mathbf{e}(t) \in \mathcal{E} \right\}. \quad (6.13)$$

All trajectories $\mathbf{q}^*(t) + \mathbf{e}(t)$ are *executable* for all possible realizations of the tracking error $\mathbf{e}(t) \in \mathcal{E}$.

The corresponding sufficient conditions for the existence of the solution of Problem (6.12) are:

Corollary 1. *Problem (6.12) admits solutions if the conditions of Theorem 1 are satisfied and if $\mathcal{H} \cap \mathcal{B} \neq \emptyset$.*

From now, it is assumed that the conditions required by Corollary 1 are satisfied.

6.3 Discretization of the problem

This Section offers a methodology for the solution of Problem (6.12). First, the problem is recast into a semi-infinite approximation by using a polytopic inner approximation of the set \mathcal{G} , a truncated polynomial expansion of the flat outputs, and basic properties of the convex sets. Second, the finite dimensional formulation of the problem is achieved by sampling from the uncertain set according to the theory of the scenario approach.

On top of the conditions required by Corollary 1, additional simplifying assumptions are introduced herein.

Assumption 1. At any time instant $t \in [0, t_f]$ and for any outcome of the uncertain set $\delta \in \Delta$, the set defined as

$$\mathcal{G}(t, \delta) = \{\mathbf{c} \in \mathbb{R}^{n_u(d+1)} : \tilde{\mathbf{g}}(\mathbf{c}, t, \delta) \leq \mathbf{0}\} \quad (6.14)$$

is either a polytope or it can be replaced by an inner polytopic approximation, $\mathcal{I}(t, \delta) \subseteq \mathcal{G}(t, \delta)$.

Going into the details of inner approximations techniques is beyond the scope of the chapter. We suggest these references on the topic: Henrion *et al.* [Henrion and Louembet, 2012] proposed a methodology for the semi-algebraic convex approximation of semi-algebraic sets. Based on the local reduction technique for semi-infinite programming [Hettich and Kortanek, 1993], Faiz *et al.* [Faiz et al., 2001] developed a maximum-volume approach for the computation of the inner approximation. Finally, Louembet *et al.* [Louembet and Deaconu, 2011] proposed a basic strategy to treat multiply-connected domains, e.g., collision avoidance constraints.

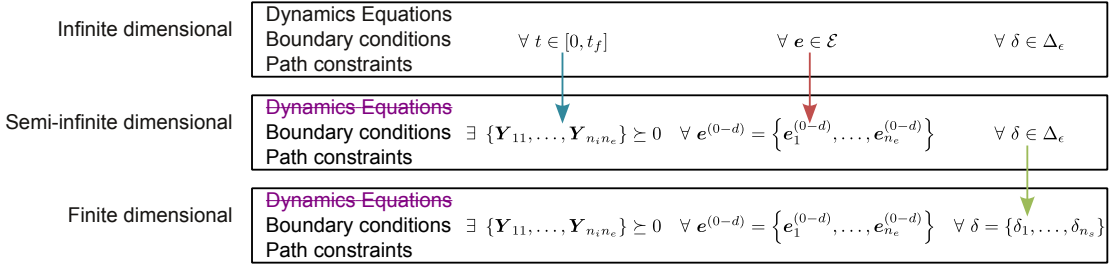
Assumption 2. The mapping between $\mathcal{G}(t_1, \delta)$ and $\mathcal{G}(t_2, \delta)$ is affine for all $t_1, t_2 \in [0, t_f]$ and for all $\delta \in \Delta$.

Assumption 3. The path constraints are assumed to be sufficiently smooth functions with respect to the time variable, i.e., $\tilde{\mathbf{g}}(\mathbf{q}^{(0-d)}, t, \delta) \in C^d$, $\forall \mathbf{q}(t) \in C^d, \delta \in \Delta$.

Specifically, it is supposed that they can be modeled with a n_ψ -dimensional polynomial basis, $\Psi(t) = [\psi_1(t), \dots, \psi_{n_\psi}(t)]^T$.

When the problem does not encompass Assumptions 2 or 3, the method is still valuable if at any time the instantaneous stochastic feasible sets, $\mathcal{G}(t, \delta)$, are replaced by their intersection for all $t \in [0, t_f]$. In this case, the solution will be more conservative.

Figure 6.3 summarizes the theoretical framework we exploited in our methodology.



Theoretical tools exploited: differential flatness, positive polynomials, properties of convex sets, scenario approach

Figure 6.3: Theoretical framework of the proposed methodology.

6.3.1 Semi-infinite formulation

The discretization of the design variables is achieved by expanding the flat outputs' trajectories through a finite dimensional (possibly complex-valued) polynomial basis, $\Phi(t) = [\phi_1(t), \dots, \phi_{n_\phi}(t)]^T \subseteq \Psi(t)$, i.e.,

$$q_j(t) = \langle c_j, \Phi(t) \rangle_H, \quad j = 1, \dots, n_u. \quad (6.15)$$

Here $\langle \cdot, \cdot \rangle_H$ and $c_j \in \mathbb{C}^{n_\phi}$ denote the Hermitian inner product and a vector of n_ϕ coefficients, respectively. The notation $\mathbf{q}(t) \in \mathcal{P}(\Phi(t))$ is exploited to indicate that the vectorial function $\mathbf{q}(t)$ has a polynomial representation in the base $\Phi(t)$.

By virtue of Assumptions 1 and 2, the matrices $\mathbf{A}(t, \delta) \in \mathbb{R}^{n_i \times n_u(d+1)}$ and $\mathbf{b}(t, \delta) \in \mathbb{R}^{n_i}$ exist such that

$$\begin{aligned} \mathcal{I}(t, \delta) &= \{c \in R^{n_u(d+1)} : \mathbf{A}(t, \delta)c \geq \mathbf{b}(t, \delta)\} \subseteq \mathcal{G}(t, \delta) \\ &\quad \forall t \in [0, t_f], \delta \in \Delta, \end{aligned} \quad (6.16)$$

i.e., $\mathbf{A}(t, \delta)$ and $\mathbf{b}(t, \delta)$ define the H-representation (n_i half spaces), of $\mathcal{I}(t, \delta)$. Thus, given an outcome $\delta \in \Delta$, the set of feasible flat outputs defined by the temporal sequence of $\mathcal{I}(t, \delta)$ is

$$\begin{aligned} \mathcal{I}(\delta) &= \left\{ \mathbf{q}(t) \in C^d : (\mathbf{q}(t) + \mathbf{e}(t)) \in \mathcal{I}(t, \delta), \right. \\ &\quad \forall t \in [0, t_f], \mathbf{e}(t) \in \mathcal{E} \Big\} \\ &= \left\{ \mathbf{q}(t) \in C^d : \mathbf{A}(t, \delta)(\mathbf{q}^{(0-d)} + \mathbf{e}^{(0-d)}) \geq \mathbf{b}(t, \delta), \right. \\ &\quad \forall t \in [0, t_f], \mathbf{e}(t) \in \mathcal{E} \Big\}, \end{aligned} \quad (6.17)$$

Limiting the variety of the flat outputs to the curves expressed by Equation (6.15) yields the subset of $\mathcal{I}(\delta)$:

$$\mathcal{I}_\phi(\delta) = \{\mathbf{q}(t) \in [\mathcal{P}(\Phi(t)) \cap \mathcal{I}(\delta)]\}. \quad (6.18)$$

Assumption 3 allows to recast the set $\mathcal{I}_\phi(\delta)$ into:

$$\begin{aligned} \mathcal{I}_\phi(\delta) = & \left\{ \mathbf{q}(t) \in \mathcal{P}(\Phi(t)) : \right. \\ & q_j(t) = \langle \mathbf{c}_j, \Phi(t) \rangle_H, j = 1, \dots, n_u; \\ & \left\langle \Psi(t), \sum_{j=1}^{n_u} \boldsymbol{\alpha}_{jk}(\delta) \mathbf{c}_j + \boldsymbol{\gamma}_k(\delta) \mathbf{e}^{(0-d)} - \boldsymbol{\beta}_k(\delta) \right\rangle_H \geq 0, \\ & \forall t \in [0, t_f], \mathbf{e} \in \mathcal{E}, k = 1, \dots, n_i \Big\}, \end{aligned} \quad (6.19)$$

where $\boldsymbol{\alpha}_{ik}(\delta) \in \mathbb{C}^{n_\psi \times n_\phi}$, $\boldsymbol{\gamma}_k(\delta) \in \mathbb{C}^{n_\psi \times (d+1)n_u}$, and $\boldsymbol{\beta}_k(\delta) \in \mathbb{C}^{n_\psi}$ are such that

$$\begin{aligned} \Psi^\#(t) \boldsymbol{\alpha}_{jk}(\delta) &= \sum_{l=0}^d \left(a_{k,n_u l+j}(t, \delta) \Phi^{(l)}(t) \right)^\#, \\ \operatorname{Re}(\Psi^\#(t) \boldsymbol{\gamma}_k(\delta)) &= \mathbf{a}_k(t, \delta), \\ \operatorname{Re}(\Psi^\#(t) \boldsymbol{\beta}_k(\delta)) &= b_k(t, \delta), \end{aligned} \quad (6.20)$$

$a_{k,l}(t, \delta)$, $\mathbf{a}_k(t, \delta)$, and $b_k(t, \delta)$ being the element of $\mathbf{A}(t, \delta)$ located at the k -th row and l -th column, the k -th row of $\mathbf{A}(t, \delta)$, and the k -th element of $\mathbf{b}(t, \delta)$, respectively. The superscript $\#$ indicates the complex adjoint operator.

The inclusion in $\mathcal{I}_\phi(\delta)$ requires the enforcement of the constraints on the dense sets $[0, t_f]$ and \mathcal{E} . Thanks to the fundamental theory of positive polynomials postulated by Nesterov [Nesterov, 2000] and to few other basic properties of convex sets, the inclusion can be recast into a set of linear matrix inequalities (LMI). In what follows, we show that this reformulation has the effect of canceling the density of the problem without the need for other trade-offs than Assumptions 1-3. Specifically, *the enforcement of the constraints is not relaxed on subsets of $[0, t_f]$ and \mathcal{E} .*

Let $\boldsymbol{\Xi}(t) = [\xi_1(t), \dots, \xi_{n_\xi}(t)]^T$ be a polynomial basis such that its corresponding squared functional system $\boldsymbol{\Xi}^2(t) = \boldsymbol{\Xi}(t)\boldsymbol{\Xi}^\#(t)$ is covered by $\Psi(t)$, i.e., the linear operator $\Lambda_H : \mathbb{C}^{n_\psi} \rightarrow \mathbb{C}^{n_\xi \times n_\xi}$ exists such that

$$\Lambda_H(\Psi(t)) = \boldsymbol{\Xi}(t)\boldsymbol{\Xi}^\#(t), \quad (6.21)$$

and let the adjoint operator $\Lambda_H^* : \mathbb{C}^{n_\xi \times n_\xi} \rightarrow \mathbb{C}^{n_\psi}$ be defined as

$$\langle \Lambda_H^*(\mathbf{Y}), \mathbf{y} \rangle_H = \langle \mathbf{Y}, \Lambda_H(\mathbf{y}) \rangle_H, \quad \forall \mathbf{Y} \in \mathbb{C}^{n_\xi \times n_\xi}, \mathbf{y} \in \mathbb{C}^{n_\psi}. \quad (6.22)$$

Let $\left\{ \mathbf{e}_1^{(0-d)}, \mathbf{e}_2^{(0-d)}, \dots, \mathbf{e}_{n_e}^{(0-d)} \right\}$ be the V-representation, i.e., the n_e vertexes of the polyhedron, of the set delimited by $\left\{ \mathbf{c} \in \mathbb{R}^{n_u(d+1)} : \mathbf{h}(\mathbf{c}) \leq \mathbf{0} \right\}$.

Lemma 2. *The inclusion in the set*

$$\begin{aligned} \mathcal{I}_{\phi,\xi}(\delta) = & \left\{ \mathbf{q}(t) \in \mathcal{P}(\Phi(t)) : \right. \\ & \mathbf{q}(t) = \operatorname{Re} \left([\mathbf{c}_1, \dots, \mathbf{c}_{n_u}]^\# \boldsymbol{\Phi}(t) \right), \\ & \exists \mathbf{Y}_{kl}(\delta) \succeq 0, \\ & \sum_{j=1}^{n_u} \boldsymbol{\alpha}_{jk}(\delta) \mathbf{c}_j + \boldsymbol{\gamma}_k(\delta) \mathbf{e}_l^{(0-d)} - \boldsymbol{\beta}_k(\delta) = \Lambda_H^*(\mathbf{Y}_{kl}(\delta)), \\ & k = 1, \dots, n_i, l = 1, \dots, n_e \left. \right\}. \end{aligned} \quad (6.23)$$

implies the inclusion in $\mathcal{I}_\phi(\delta)$.

Proof. Let $\mathbf{p}_{kl} = \sum_{j=1}^{n_u} \boldsymbol{\alpha}_{jk}(\delta) \mathbf{c}_j + \boldsymbol{\gamma}_k(\delta) \mathbf{e}_l^{(0-d)} - \boldsymbol{\beta}_k$. According to Theorem 18.7 in [Nesterov, 2000], the conditions expressed in Equation (6.23) guarantee that the polynomial $p_{kl}(t) = \langle \mathbf{p}_{kl}, \boldsymbol{\Psi}(t) \rangle_H$ is nonnegative for any $t \in [0, t_f]$. In fact:

$$\begin{aligned} p_{kl}(t) &= \langle \mathbf{p}_{kl}, \boldsymbol{\Psi}(t) \rangle_H = \langle \Lambda_H^*(\mathbf{Y}_{kl}), \boldsymbol{\Psi}(t) \rangle_H \\ &= \langle \mathbf{Y}_{kl}, \Lambda_H(\boldsymbol{\Psi}(t)) \rangle_H = \langle \mathbf{Y}_{kl}, \boldsymbol{\Xi}(t) \boldsymbol{\Xi}^\#(t) \rangle_H \\ &= \underbrace{\boldsymbol{\Xi}^\#(t) \mathbf{Y}_{kl} \boldsymbol{\Xi}(t)}_{\geq 0 \text{ given } \mathbf{Y}_{kl} \succeq 0} \geq 0. \end{aligned} \quad (6.24)$$

As such, the constraints are satisfied continuously in time for each vertex of the tracking error set, $\{\mathbf{e}_1^{(0-d)}, \mathbf{e}_2^{(0-d)}, \dots, \mathbf{e}_{n_e}^{(0-d)}\}$, i.e.,

$$\mathbf{A}(t, \delta) \left(\mathbf{q}^{(0-d)} + \mathbf{e}_l^{(0-d)} \right) - \mathbf{b}(t, \delta) = \begin{Bmatrix} p_{1l}(t) \\ \vdots \\ p_{n_il}(t) \end{Bmatrix} \geq 0, \quad (6.25)$$

$l = 1, \dots, n_e, \forall t \in [0, t_f].$

Because $\mathcal{I}(t, \delta)$ and the tracking error set are polytopes, the enforcement of the path constraints at the vertexes $\{\mathbf{e}_1^{(0-d)}, \mathbf{e}_2^{(0-d)}, \dots, \mathbf{e}_{n_e}^{(0-d)}\}$ is necessary and sufficient condition for the satisfaction in all the interior points of \mathcal{E} . In fact, according to the theory of convex polytopic sets, for every $\mathbf{e}(t) \in \mathcal{E}$, a set of coefficients $\{\lambda_j(t) \geq 0, j = 1, \dots, n_e : \sum_{j=1}^{n_e} \lambda_j(t) = 1 \forall t \in [0, t_f]\}$ exists such that $\mathbf{e}^{(0-d)}(t) =$

$\sum_{j=1}^{n_e} \lambda_j(t) e_j^{(0-d)}$. This yields:

$$\begin{aligned} \mathbf{A}(\mathbf{q}^{(0-d)} + \mathbf{e}^{(0-d)}) &= \mathbf{A}\left(\mathbf{q}^{(0-d)} + \sum_{j=1}^{n_e} \lambda_j \mathbf{e}_j^{(0-d)}\right) = \\ &= \sum_{j=1}^{n_e} \lambda_j \underbrace{\mathbf{A}(\mathbf{q}^{(0-d)} + \mathbf{e}_j^{(0-d)})}_{\geq \mathbf{b}} \geq \mathbf{b} \sum_{j=1}^{n_e} \lambda_j = \mathbf{b} \end{aligned} \quad (6.26)$$

where the dependencies on t and δ were omitted for the sake of conciseness.

□

The inner semi-infinite approximation of Problem (6.12) is thus:

$$\begin{aligned} \mathbf{q}^*(t) &= \arg \left[\min_{\mathbf{q}(t) \in \mathcal{P}(\Phi(t))} \left(\max_{\delta \in \Delta} \tilde{\mathcal{J}}(\mathbf{q}^{(0-d)}, \delta) \right) \right] \text{ s.t.} \\ \mathbf{q}(t) &\in \left[\mathcal{B} \cap \left(\bigcap_{\delta \in \Delta} \mathcal{I}_{\phi, \xi}(\delta) \right) \right]. \end{aligned} \quad (6.27)$$

The inclusion in the set $\mathcal{I}_{\phi, \xi}(\delta)$ does not require that constraints are satisfied for all elements of $[0, t_f]$ and \mathcal{E} , but it only requires the existence of $n_i n_e$ Hermitian semi-positive definite matrices. Thus, it consists of a set of LMI and, as such, it is a convex feasibility problem. Nowadays, solving LMI is achieved by means of efficient numerical techniques in polynomial time.

6.3.2 Discrete formulation

Solving the *min-max* optimization Problem (6.27) is challenging because the uncertain sets are generally dense and unbounded. When the enforcement of the path constraints does not strictly need to be guaranteed for all possible outcomes of the uncertain set, Problem (6.27) can be recast into the more relaxed *chance-constrained* formulation by replacing the set Δ with a subset Δ_ϵ such that $Pr_{\Delta}(\delta \in \Delta_\epsilon) \geq 1 - \epsilon$. Here, $\epsilon \in (0, 1]$ and Δ_ϵ are the risk parameter and a subset of Δ whose probability is no smaller than $1 - \epsilon$, respectively. The risk parameter represents the hazard that the user is willing to run. The higher the risk, the better the performance in terms of cost function.

The scenario approach is a general-purpose methodology aimed at solving chance-constrained problems. Specifically, given the convexity of the problem with respect to the design variables, it provides a guarantee that the solution obtained by enforcing the constraints for only a prescribed finite number of independent outcomes of the uncertain quantity is feasible on a prescribed portion of the uncertain set. This result was postulated by the seminal work of Campi *et al.* in [Campi et al., 2009].

Another appealing property of the scenario approach is that *it does not require a probabilistic characterization of the stochastic sources* of the problem. In fact, even

though it assumes the existence of a probability distribution Pr_{Δ} , it does not require its knowledge but only the realization of a certain number of samples. For this reason, the scenario approach facilitates the inclusion of uncertainty sources of arbitrary nature in the dynamics, e.g., non-Gaussian random variables, non-stationary stochastic processes, and random fields.

The results of Lemma 2 are now used in conjunction with the scenario approach to achieve the finite dimensional formulation of Problem (6.27).

Theorem 2. *Let $\beta \in (0, 1]$ and $\epsilon \in (0, 1]$ be the user-defined confidence and the risk parameters, respectively. Let $\delta_1, \delta_2, \dots, \delta_{n_s}$ be a set of n_s independent random samples of Δ distributed according to $Pr_{\Delta}(\delta)$ and such that*

$$n_s \geq \frac{2}{\epsilon} \left[1 + 2(n_u n_\phi - n_x) + \ln \frac{1}{\beta} \right]. \quad (6.28)$$

Then, with probability $1 - \beta$, the solution of the finite-dimensional problem

$$\begin{aligned} \mathbf{q}^*(t) &= \arg \left[\min_{\mathbf{q}(t) \in \mathcal{P}(\Phi(t))} \left(\max_{\delta=\{\delta_1, \dots, \delta_s\}} \tilde{\mathcal{J}}(\mathbf{q}^{(0-d)}, \delta) \right) \right] \text{ s.t.} \\ \mathbf{q}(t) &\in \left[\mathcal{B} \cap \left(\bigcap_{j=1}^{n_s} \mathcal{I}_{\phi, \xi}(\delta_j) \right) \right]. \end{aligned} \quad (6.29)$$

is guaranteed to be feasible on a subset $\Delta_\epsilon \subseteq \Delta$ such that $Pr_{\Delta}(\delta \in \Delta_\epsilon) \geq 1 - \epsilon$.

Remark 2. The confidence parameter, β , appears as the argument of a logarithm in Equation (6.28). When β approaches 0 its logarithm decreases slowly. For practical purposes, the confidence parameter can be chosen small enough to be neglected, e.g., $\beta = 10^{-7} \Rightarrow -\ln \beta \simeq 16$.

Proof. The demonstration is carried out by firstly reformulating Problem (6.29) according to the formalism exploited in [Formentin et al., 2014], i.e.,

$$\begin{aligned} \mathbf{y}^* &= \arg \left[\min_{\mathbf{y} \in \mathbb{R}^{n_y}; \zeta_1, \dots, \zeta_{n_s} \in Z} (\mathbf{j}^T \mathbf{y}) \right] \quad \text{s.t. :} \\ \boldsymbol{\rho}(\mathbf{y}, \zeta_m, \delta_m) &\leq \mathbf{0} \quad \delta_m \sim Pr_{\Delta}(\delta_m) \\ m &= 1, \dots, n_s, \end{aligned} \quad (6.30)$$

with

$$n_s \geq \frac{2}{\epsilon} \left(n_y + \ln \frac{1}{\beta} \right), \quad (6.31)$$

where $\boldsymbol{\rho}(\mathbf{y}, \delta) \leq \mathbf{0}$, $\zeta_m \in Z$, and $\mathbf{j} \in \mathbb{R}^{n_y}$ are a generic constraint convex with respect to \mathbf{y} , a set of so-called *certificate* variables and a constant vector, respectively. According to Theorem 1 in [Formentin et al., 2014] and Proposition 2.1 in [Calafiore, 2009], with probability $1 - \beta$, the solution \mathbf{y}^* of Problem (6.30) satisfies

$$\forall \delta \in \Delta_\epsilon \subseteq \Delta \quad \exists \zeta \in Z \quad \text{s.t.} \quad \boldsymbol{\rho}(\mathbf{y}^*, \zeta, \delta) \leq \mathbf{0}, \quad (6.32)$$

where Δ_ϵ is a subset of Δ such that $Pr_\Delta(\delta \in \Delta_\epsilon) \geq 1 - \epsilon$. Then, the results of Lemma 2 are exploited yielding the finite-dimensional formulation (Problem (6.29)).

Let $\mathbf{Q} = [\mathbf{c}_1, \dots, \mathbf{c}_{n_u}]^T$. In order to remove the constraints which impose the inclusion in \mathcal{B} in Problem (6.27), the basis $\Phi(t)$ is projected into a self-boundary-compliant subspace. For this purpose, $\Phi(t)$ is partitioned into $n_\phi - n_x$ independent¹ and n_x dependent elements² $\Phi(t) = \begin{bmatrix} \Phi_{ind}(t) \\ \Phi_{dep}(t) \end{bmatrix}$. An analogous partition is performed for the corresponding columns of \mathbf{Q} , which is rearranged as $\mathbf{Q} = [\mathbf{Q}_{ind}, \mathbf{Q}_{dep}]$. The discretized flat output becomes

$$\mathbf{q}(t) = \mathbf{q}(t, \mathbf{Q}_{ind}) = [\operatorname{Re}(\mathbf{Q}_{ind}), \operatorname{Im}(\mathbf{Q}_{ind})] \Phi_q(t) + \Phi_0(t) \quad (6.33)$$

where

$$\begin{aligned} \Phi_q(t) &= \begin{bmatrix} \operatorname{Re}(\Phi_{ind}(t)) \\ \operatorname{Im}(\Phi_{ind}(t)) \end{bmatrix} - \mathbf{B}_{ind} \mathbf{B}_{dep}^{-1} \begin{bmatrix} \operatorname{Re}(\Phi_{dep}(t)) \\ \operatorname{Im}(\Phi_{dep}(t)) \end{bmatrix}, \\ \Phi_0(t) &= [\mathbf{q}^{(0|d)}(0), \mathbf{q}^{(0|d)}(t_f)] \mathbf{B}_{dep}^{-1} \begin{bmatrix} \operatorname{Re}(\Phi_{dep}(t)) \\ \operatorname{Im}(\Phi_{dep}(t)) \end{bmatrix}, \\ \mathbf{B}_{(\cdot)} &= \begin{bmatrix} \operatorname{Re}(\Phi_{(\cdot)}^{(0|d)}(0)), & \operatorname{Re}(\Phi_{(\cdot)}^{(0|d)}(t_f)) \\ \operatorname{Im}(\Phi_{(\cdot)}^{(0|d)}(0)), & \operatorname{Im}(\Phi_{(\cdot)}^{(0|d)}(t_f)) \end{bmatrix}; \end{aligned} \quad (6.34)$$

here, the notation $\mathbf{a}^{(0|d)} = [\mathbf{a}, \dots, \mathbf{a}^{(d)}]$ is exploited. In practice, given any $\mathbf{Q}_{ind} \in \mathbb{C}^{n_u \times (n_\phi - n_x)}$, the n_x dependent complex coefficients are imposed such that boundary conditions are satisfied.

Problem (6.29) is recast into

$$\begin{aligned} [\mathbf{Q}_{ind}^*, J^*] &= \arg \left[\min_{\mathbf{Q}_{ind}, J, \mathbf{Y}_{1,1}^{(1)}, \dots, \mathbf{Y}_{n_i n_e}^{(n_s)}} J \right] \text{ s.t. :} \\ \tilde{\mathcal{J}}(\mathbf{q}(t, \mathbf{Q}_{ind}), \delta_m) &\leq J, \\ \mathbf{Y}_{kl}^{(m)} &\succeq 0, \\ \sum_{j=1}^{n_u} \boldsymbol{\alpha}_{jk}(\delta_m) \mathbf{c}_j(\mathbf{Q}_{ind}) + \boldsymbol{\gamma}_k(\delta_m) \mathbf{e}_l^{(0-d)} - \boldsymbol{\beta}_k(\delta_m) &= \Lambda_H^* \left(\mathbf{Y}_{kl}^{(m)} \right), \\ k &= 1, \dots, n_i, \quad l = 1, \dots, n_e, \quad m = 1, \dots, n_s, \end{aligned} \quad (6.35)$$

where the slack variable J is introduced to have a linear objective function as in Problem (6.30), and $\mathbf{q}(t, \mathbf{Q}_{ind})$ is given by Equation (6.33), so that the inclusion in \mathcal{B} is guaranteed. Matrices $\mathbf{Y}_{kl}^{(m)}$ serve as certificate variables.

Problem (6.35) has $1 + 2(n_u n_\phi - n_x)$ design variables. The assumption in Equa-

¹We note that only n_x dependent elements are required to cope with the $2n_x$ boundary conditions because Q is a complex-valued matrix.

²The choice of dependent functions is arbitrary provided that B_{dep} as defined in Equation (6.34) is not singular.

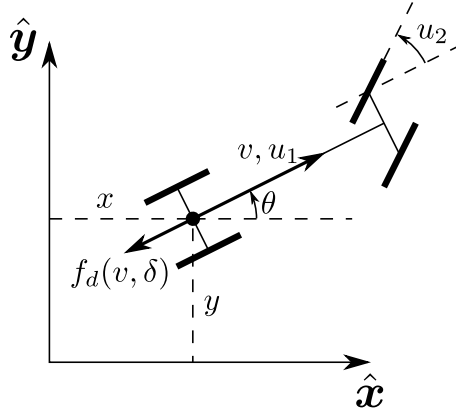


Figure 6.4: Notation of the car steering example.

tion (6.28) is thus equivalent to the condition in Equation (6.31). This latter can be invoked to solve Problem (6.35), i.e., the enforcement on the constraints on Δ_ϵ is replaced by the enforcement on the only n_s independent samples of Δ , such that n_s satisfies Equation (6.28).

□

Remark 3. Problem (6.29) requires the enforcement of $n_s n_e n_i$ LMI of $n_\xi \times n_\xi$ matrices. In Section 6.4, we will show that this number can be drastically reduced *a priori* in several problems. Specifically, if the feasible domain is stationary or if the matrix $\mathbf{A}(t, \delta)$ is deterministic, the number of LMI can be reduced by a factor ranging between n_e and $n_e n_s$.

6.4 Step-by-step implementation

The proposed methodology is now illustrated by means of a simple example involving the steering maneuver of a car. It serves as a guidance for the practical implementation of the methodology, so that all the necessary steps are detailed. The possibility to reduce *a priori* the number of inequality constraints of Problem (6.29) is investigated as well.

Consider the steering maneuver of the car illustrated in Figure 6.4. The dynamics of the car is approximated by means of a bicycle model. The states $\mathbf{x} = [x, y, v, \theta]^T$ are the position of the center of the rear axis, the norm of the velocity, and the angle between the $\hat{\mathbf{x}}$ axis and the longitudinal axis of the car. The control variables $\mathbf{u} = [u_1, u_2]^T$ are the force transmitted by the rear wheels on the ground and the steering angle, respectively. The dynamics equations assume perfect rolling of the wheels.

Table 6.1: Steering a car. Simulation parameters.

Mass of the car, M	1000 kg
Length of the car, L	3 m
Terminal states, \mathbf{x}_f	$[1500\text{m}, 500\text{m}, 0, 0\text{m s}^{-1}]^T$
Maximum power, W_{max}	100 kW
Maximum traction force, $u_{1,max}$	5.55 kN
Atmospheric density, ρ	1.225 kg m^{-3}
Cross section, S	1.5 m^2
Maneuvering time	60 s
Targeted trajectory, \mathbf{r}_{obj}	$(25t, 500 \cos(\pi t/t_f)) \text{ m}$
Probability distribution of C_d , $P_{C_d}(C_d)$	$0.5[1 + \tanh(50(C_d - 0.3))]$

The formulation of the robust maneuver planning problem is:

$$\begin{aligned}
 \mathbf{x}^* = \arg \left[\min_{\mathbf{x}} \sqrt{\frac{1}{t_f} \int_0^{t_f} ((x - x_{obj})^2 + (y - y_{obj})^2) dt} \right] \\
 \forall t \in [0, t_f], \quad \delta \in \Delta \quad \exists u_1(t, \delta), u_2(t, \delta) \text{ s.t.} \\
 \frac{d}{dt} \begin{Bmatrix} x \\ y \\ \theta \\ v \end{Bmatrix} = \begin{Bmatrix} v \cos \theta \\ v \sin \theta \\ \frac{v}{L} \tan u_2 \\ \frac{1}{M} (u_1 - f_d(v, \delta)) \end{Bmatrix}, \tag{6.36} \\
 |u_1 v| \leq W_{max}, \quad |u_1| \leq u_{1,max}, \quad |u_2| \leq 0.5\pi, \\
 \mathbf{x}(0) = \mathbf{0}, \quad \mathbf{x}(t_f) = \mathbf{x}_f,
 \end{aligned}$$

where $f_d(v, \delta)$, M , L , and W_{max} are the drag force, the mass and the length of the car, and the maximum available power, respectively. The drag force is given by $f_d(v, \delta) = 0.5\rho S C_d(\delta) v^2$ where ρ , S , and C_d are the atmospheric density, the cross section, and the drag coefficient, respectively. This latter is uncertain and provided with a known probability distribution $P_{C_d}(C_d)$.

The objective function, \mathcal{J} , is aimed at minimizing the distance between a desired trajectory, $\mathbf{r}_{obj} = [x_{obj}, y_{obj}]^T$, and the robust one.

Table 6.1 summarizes the numerical values of the parameters.

6.4.1 Flat formulation

System (6.36) is differentially flat and it admits the position of the center of the rear axis as flat outputs, i.e., $\mathbf{q} = [x, y]^T$, as discussed in the catalog of differentially flat system proposed by Martin *et al.* in [Martin et al., 2003]. In more general applications, proving that a system is differentially flat can be a difficult task. Necessary and sufficient condition for differential flatness are proposed by Antritter *et al.* in [Antritter and Lévine, 2010].

The mapping between the flat outputs and the state and control variables is

$$\begin{aligned} \mathbf{x} &= \left\{ \begin{array}{c} q_1 \\ q_2 \\ \frac{\dot{q}_2}{|\dot{q}_2|} \cos^{-1} \frac{\dot{q}_1}{\sqrt{\dot{q}_1^2 + \dot{q}_2^2}} \end{array} \right\} \\ \mathbf{u} &= \left\{ \begin{array}{c} M \left(\frac{\dot{q}_1 \ddot{q}_2 + \dot{q}_2 \ddot{q}_1}{\sqrt{\dot{q}_1^2 + \dot{q}_2^2}} \right) + 0.5\rho SC_d(\delta) (\dot{q}_1^2 + \dot{q}_2^2) \\ \tan^{-1} L \frac{\ddot{q}_1 \dot{q}_2 - \ddot{q}_2 \dot{q}_1}{(\dot{q}_1^2 + \dot{q}_2^2)^{3/2}} \end{array} \right\} \end{aligned} \quad (6.37)$$

By means of this mapping, the path constraints are recast into

$$\begin{aligned} \left| M (\dot{q}_1 \ddot{q}_2 + \dot{q}_2 \ddot{q}_1) + 0.5\rho SC_d(\delta) (\dot{q}_1^2 + \dot{q}_2^2)^{3/2} \right| &\leq W_{max} \\ \left| M \left(\frac{\dot{q}_1 \ddot{q}_2 + \dot{q}_2 \ddot{q}_1}{\sqrt{\dot{q}_1^2 + \dot{q}_2^2}} \right) + 0.5\rho SC_d(\delta) (\dot{q}_1^2 + \dot{q}_2^2) \right| &\leq u_{1,max} \\ \left| L \frac{\ddot{q}_1 \dot{q}_2 - \ddot{q}_2 \dot{q}_1}{(\dot{q}_1^2 + \dot{q}_2^2)^{3/2}} \right| &\leq \infty \end{aligned} \quad (6.38)$$

Because it is assumed that there is no side slip of the rear wheel, the mapping is deterministic and the conditions for Theorem 1 are satisfied.

Tracking error constraints are now included. We note that all the constraints are expressed in terms of $\dot{\mathbf{q}}$ and $\ddot{\mathbf{q}}$ only. For this reason, tracking error constraints on \mathbf{q} would not affect the solution of the problem. In this example, we want the solution to be feasible for all the $\mathbf{e}^{(1)} \leq [1, 1]^T \text{ m s}^{-1}$.

6.4.2 Choice of the polynomial basis

The polynomial expansion of the flat outputs is performed by means of a trigonometric polynomial basis $\Phi(t)$ such that

$$\phi_k(t) = \exp \left(\pi \frac{t}{t_f} (k-1)i \right), \quad k = 1, \dots, n_\phi, \quad i = \sqrt{-1}, \quad (6.39)$$

Because the path constraints do not have explicit dependency on time, it holds that $\Psi(t) \equiv \Phi(t)$.

As detailed in [Nesterov, 2000], all the positive polynomials in the basis $\Phi(t)$, $t \in [0, 2t_f]$ admit a sum of square representation in the same basis, i.e., $\Xi(t) \equiv \Phi(t)$. By

noting that $\xi_j \xi_k^\# = \phi_{j-k}$, the operators Λ_H and Λ_H^* are straightforwardly deduced:

$$\begin{aligned}\Lambda_H(\mathbf{p}) &= \frac{1}{2} \sum_{j=1}^{n_\phi} (\mathbf{T}_j p_j + \mathbf{T}_j^T \bar{p}_j) \\ \Lambda_H^*(\mathbf{Y}) &= [\langle \mathbf{Y}, \mathbf{T}_1 \rangle_C, \dots, \langle \mathbf{Y}, \mathbf{T}_{n_\phi} \rangle_C]^T\end{aligned}\quad (6.40)$$

where $\mathbf{p} \in \mathbb{C}^{n_\phi}$, $\mathbf{Y} \in \mathbf{C}^{n_\phi \times n_\phi}$. The matrices $\mathbf{T}_j \in \mathbb{R}^{n_\phi \times n_\phi}$ are such that

$$\mathbf{T}_1 = \mathbf{I}, \quad T_{j,(k,l)} = 2 \operatorname{kron}(k-l, j-1), \quad j = 2, \dots, n_\phi. \quad (6.41)$$

here $\operatorname{kron}(\cdot, \cdot)$ denotes the Kronecker's delta operator.

In this work we chose $n_\phi = 11$.

6.4.3 Discretization of the path constraints

We start by generating n_s independent samples of C_d according to its probability distribution (see Table 6.1). By choosing the risk parameter $\epsilon = 0.1$ and the confidence parameter small enough to be considered zero in practice, $\beta = 10^{-6}$, the minimum number of samples according to Equation (6.28) is $n_s = 937$.

The inner approximation of the feasible set of each outcome of the uncertain variable is generated by means of the methodology proposed by Faiz *et al.* which is aimed at maximizing the volume of the polytope. Here, $n_i = 24$ half-spaces were exploited. Figure 6.5 illustrates the obtained feasible sets associated with the minimum and maximum drag coefficients among the samples.

Finally, by noting that

$$\Phi^{(l)}(t) = \operatorname{diag} \left(\frac{\pi}{t_f} i [0, 1, \dots, n_\phi - 1] \right)^l \Phi(t),$$

the matrices defined in Equation (6.20) are

$$\begin{aligned}\boldsymbol{\alpha}_{jk}(\delta_m) &= \sum_{l=0}^d a_{k,n_u l+j}(\delta) \left[\operatorname{diag} \left(\frac{\pi}{t_f} i [0, 1, \dots, n_\phi - 1] \right)^l \right]^\# , \\ \boldsymbol{\gamma}_k(\delta_m) &= [1, 0, 0, \dots, 0]^T \mathbf{a}_k(\delta), \\ \boldsymbol{\beta}_k(\delta_m) &= [1, 0, 0, \dots, 0]^T b_k(\delta).\end{aligned}\quad (6.42)$$

6.4.4 Solution of the problem

Before proceeding with the numerical solution of the problem, few considerations are proposed in order to reduce the number of constraints that need to be enforced:

- The feasible set of each outcome is stationary, i.e., $[\mathbf{A}, \mathbf{b}](t, \delta) = [\mathbf{A}, \mathbf{b}](\delta)$, $\forall t \in [0, t_f], \delta \in \Delta$. For this reason, the outward normal vector to the half-spaces

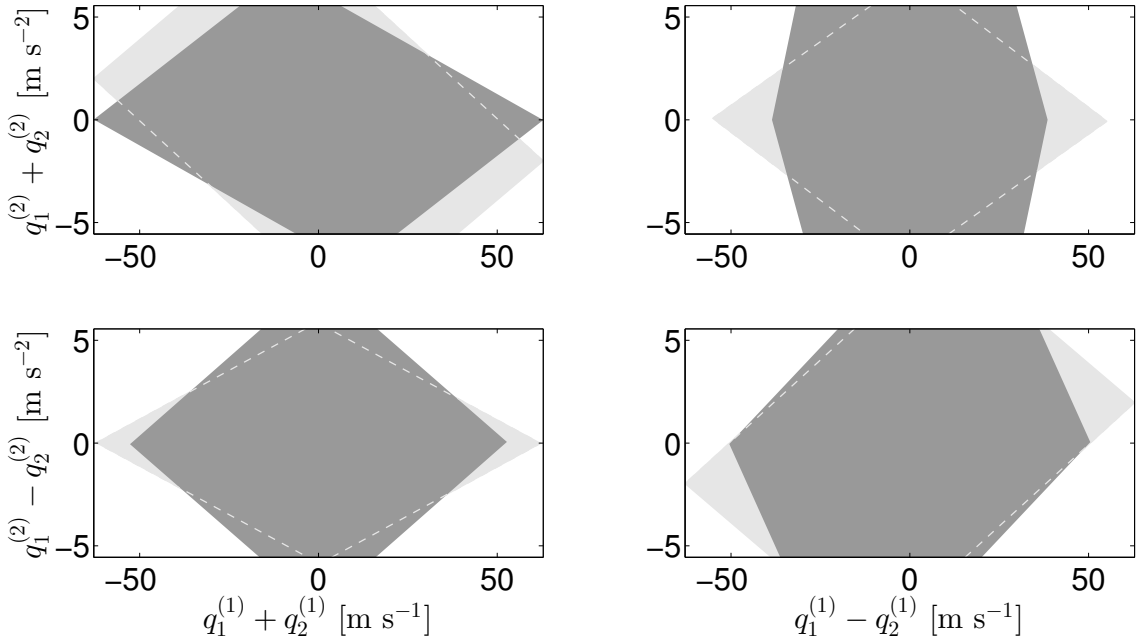


Figure 6.5: Steering a car. Inner approximation of the feasible set. The dark and light grey regions are related to the maximum and minimum samples of the drag coefficient, respectively. The dashed lines are the hidden edges of the light-grey regions.

defining the feasible set, $\mathbf{n}_k, k = 1, \dots, n_i$, does not change in time. In this case, every constraint needs only to be enforced for the vertex $\mathbf{e}_l^{(0-d)}$ such that $\mathbf{e}_l^{(0-d)} = \max_{\mathbf{e}_j^{(0-d)}, j=1, \dots, n_e} (\mathbf{e}_j^{(0-d)} \cdot \mathbf{n}_k)$. The number of constraints is thus reduced of a factor n_e .

- Because the constraints are linear in the drag coefficient, the intersection of the feasible sets of all the samples is equal to the intersection of the ones delimited by the extreme values $\min_{\delta \in \{\delta_1, \dots, \delta_{n_s}\}} C_d(\delta)$ and $\max_{\delta \in \{\delta_1, \dots, \delta_{n_s}\}} C_d(\delta)$. Their intersection yields the feasible set for the chance constrained maneuver. The number of LMI to be enforced is thus further reduced of a factor $0.5n_s$.

Thanks to the above considerations, only $2n_i = 48$ LMI and the boundary conditions need to be enforced. CVX, a package for specifying and solving convex programs [Grant and Boyd, 2014, 2008], is exploited to solve the optimization problem. Figure 6.6(a) illustrates the obtained solution in the phase space of the flat outputs. The dark-gray region delimits the tolerated tracking error. If the real state vector happens to be in that region the trajectory remains still feasible. More severe requirements on the tracking error would allow $\mathbf{q}^*(t)$ to be further pushed toward the boundaries this resulting in potential improvements of the cost function at the price of a more accurate on-line tracking.

The close up zoom of Figure 6.6(b) emphasizes that the path constraints are enforced with continuity in time. The trajectory of the rear wheel of the car is

illustrated in Figure 6.6(c).

Figure 6.7(a) illustrates the performance index, \tilde{J} , obtained by sweeping the risk parameter. By reducing ϵ , the number of required samples increases, this resulting into a reduction of the size of the feasible set. In fact, the more samples, the higher the probability to obtain samples in the tails of the distribution, as shown by the min-max values of the sampled C_d . The analysis of the performance-risk diagram allows to spot a good trade-off between the gain obtained by accepting larger risks and the risk itself. For example, little gain is obtained by choosing $\epsilon > 0.2$ in this example. The trajectories corresponding to three different levels of ϵ are shown in Figure 6.7(b). The more relaxed feasible domain allows higher absolute values of the accelerations in the initial and terminal phase of the maneuver, yielding the increase in the maneuverability of the car and the consequent improvement of the cost function.

6.5 Orbital rendez-vous using differential drag

We consider the maneuver orbital rendez-vous via differential drag discussed in Chapter 5. The maneuver is accomplished in three steps, namely drag estimation, maneuver planning, and on-line compensation, as illustrated in Figure 5.2.

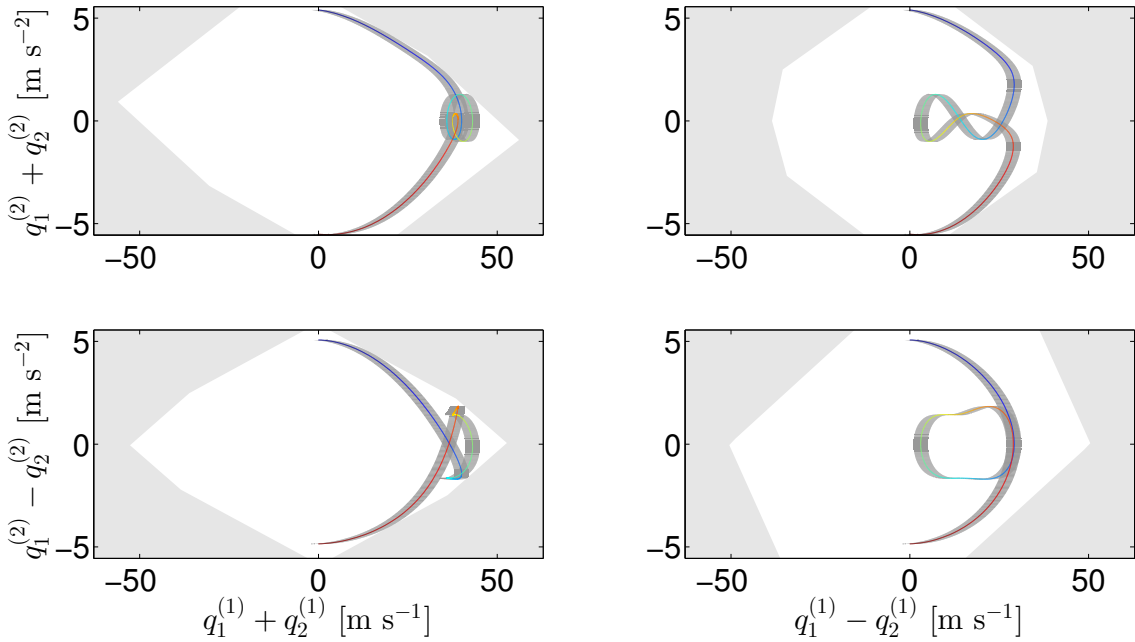
Because the aim of this section is to point out the benefits of the robust deterministic trajectory, attitude dynamics and constraints are removed from the planner for the sake of simplicity, so that $\mathbf{x} = [\Delta\bar{a}, \Delta\bar{P}_1, \Delta\bar{P}_2, \Delta\bar{L}]$. Differential drag is now the controlled variable, $u = \Delta f_{drag}$. Equations (5.9) and the saturation of the differential drag are thus the only constraints for the planner.

Uncertainty in the differential drag bounds is considered, i.e., $\Delta f_{drag}^{(max)}(t, \delta) = f_{drag,D}(t, \alpha_1, \delta) - f_{drag,C}(t, \delta)$ and $\Delta f_{drag}^{(min)}(t, \delta) = f_{drag,D}(t, \alpha_2, \delta) - f_{drag,C}(t, \delta)$, where α_1 and α_2 are the pitch angles corresponding to the minimum and maximum drag configurations of the deputy, respectively. We note that these bounds should also depend on the position of the chief and on the state \mathbf{x} . Because the former is provided by the propagator presented in Chapter 4 and small displacements are assumed, we neglect this dependency.

According to these assumptions, the problem becomes:

$$\begin{aligned} \mathbf{x}^* = \arg \left[\min_{\mathbf{x}(t), t \in [0, t_f]} \mathcal{J}(\mathbf{x}, u_\delta, t_f) \right] \quad & s.t. \\ \forall t \in [0, t_f], \delta \in \Delta \quad & \exists u_\delta = u(t, \delta) \quad s.t. \\ \dot{\mathbf{x}} = \mathbf{A}(t) \mathbf{x} + \mathbf{B}(t) u_\delta \quad & \\ \Delta f_{drag}^{(min)}(t, \delta) \leq u_\delta \leq \Delta f_{drag}^{(max)}(t, \delta) \quad & \\ \mathbf{x}(0) = \mathbf{x}_0, \quad & \\ \mathbf{x}(t_f) = \mathbf{0}. \quad & \end{aligned} \tag{6.43}$$

where $\mathbf{A}(t) = \mathbf{A}(\bar{\mathcal{E}}_{eq,C}(t), \mathbf{f}_{drag,C}(t))$ and $\mathbf{B}(t) = \mathbf{B}(\bar{\mathcal{E}}_{eq,C}(t), \mathbf{f}_{drag,C}(t))$ and the



(a) Trajectories in the $(\mathbf{q}^{(1)}, \mathbf{q}^{(2)})$ space. The light and dark grey regions indicate the infeasible and the tracking error set, respectively.

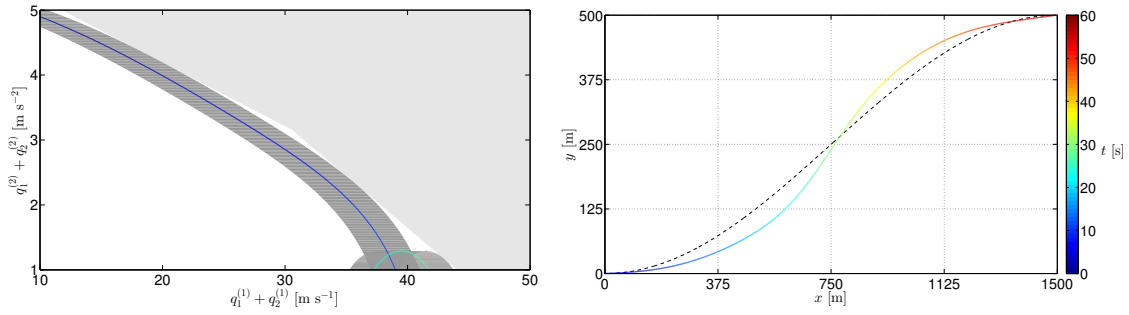
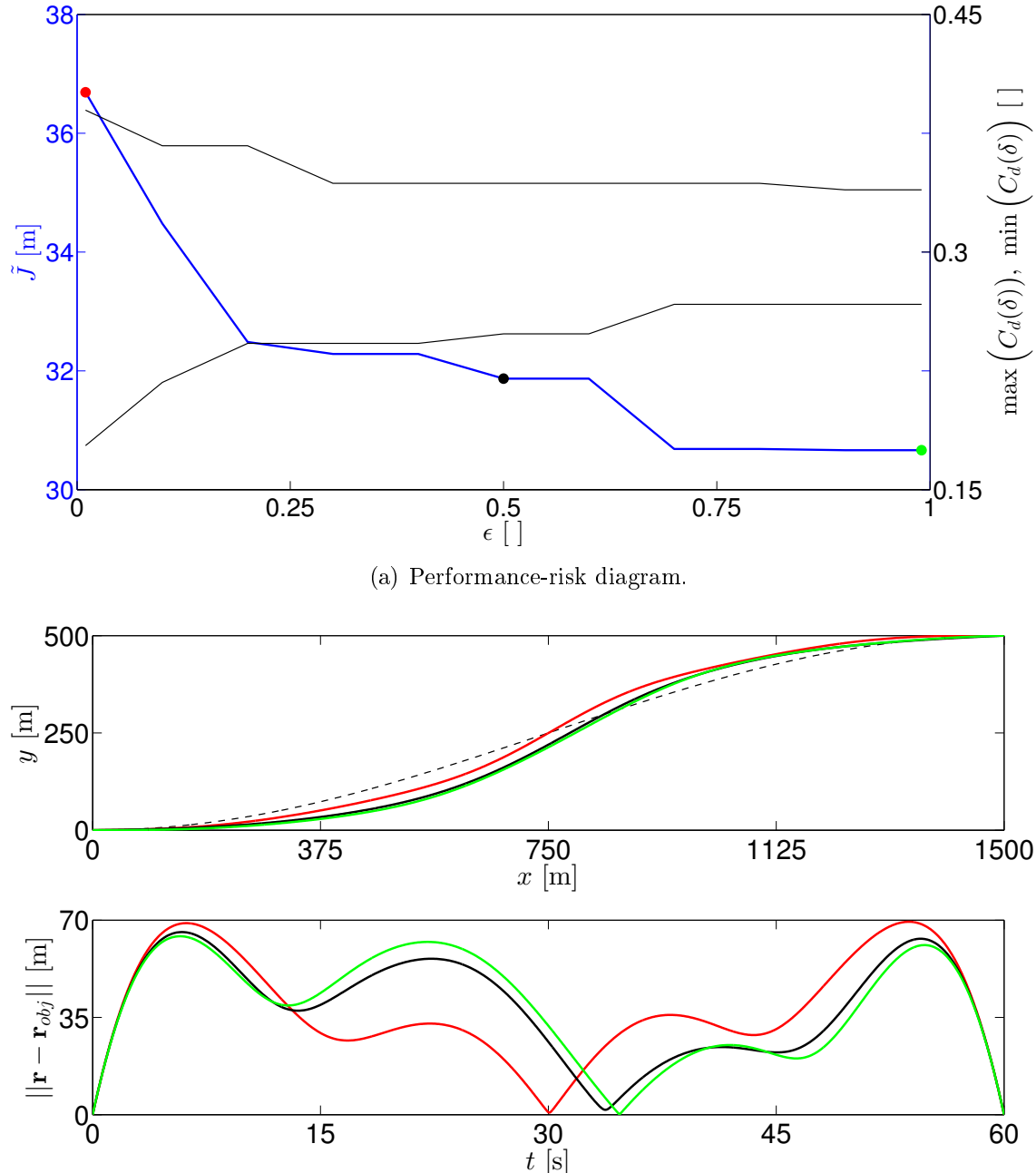


Figure 6.6: Steering a car. Solution of the chance constrained optimization problem.



(b) Trajectory and distance from the desired path. The red, black, and green curves correspond to the risk levels 0.01, 0.5, and 0.99, respectively.

Figure 6.7: Steering a car. Influence of the risk parameter on the performance index.

evolution of the vector $\bar{\mathcal{E}}_{eq,C}$ is modeled with the time-explicit solution developed in Chapter 4.

6.5.1 Flat formulation

Linear time-varying systems are differentially flat if and only if they are uniformly controllable. According to [Silverman, 1966], the couple $(\mathbf{A}(t), \mathbf{B}(t))$ is uniformly controllable if the controllable matrix $\mathbf{K}(t)$ has full rank in the interval $[0, t_f]$. For a single-input system it holds

$$\mathbf{K}(t) = [\mathbf{k}_0(t), \mathbf{k}_1(t), \dots, \mathbf{k}_{n_x}(t)], \quad (6.44)$$

where

$$\mathbf{k}_0(t) = \mathbf{B}(t), \quad \mathbf{k}_j(t) = \dot{\mathbf{k}}_{j-1}(t) - \mathbf{A}(t)\mathbf{k}_{j-1} \text{ for } j = 1, \dots, n_x. \quad (6.45)$$

The canonical control form yields the mappings \mathcal{X} and \mathcal{U} , i.e.,

$$\begin{aligned} \mathbf{x} = & \mathcal{X}(q^{(0-(n_x-1))}) = \mathbf{P}(t)q^{(0-(n_x-1))} \\ u = & \mathcal{U}(q^{(0-(n_x-1))}) = q^{n_x} + \sum_{j=0}^{n_x-1} a_j(t)q^{(j)} \end{aligned} \quad (6.46)$$

where $a_j(t)$ are the instantaneous coefficients of the canonical form of the couple $(\mathbf{A}(t), \mathbf{B}(t))$ and $\mathbf{P}(t) = \hat{\mathbf{K}}(t) \mathbf{K}^{-1}(t)$ defines the instantaneous transformation in canonical form

$$\hat{\mathbf{A}}(t) = \mathbf{P}(t)\mathbf{A}(t)\mathbf{P}^{-1}(t) + \dot{\mathbf{P}}(t)\mathbf{P}(t), \quad \hat{\mathbf{B}} = \mathbf{P}(t)\mathbf{B}(t) \quad (6.47)$$

with

$$\hat{\mathbf{A}}(t) = \begin{bmatrix} 0 & 1 & 0 & \cdots & 0 \\ 0 & 0 & 1 & \cdots & 0 \\ \vdots & & & \ddots & \vdots \\ 0 & 0 & \cdots & 0 & 1 \\ -a_0(t) & -a_1(t) & -a_2(t) & \cdots & -a_{n_x-1}(t) \end{bmatrix}, \quad \hat{\mathbf{B}} = \begin{bmatrix} 0 \\ 0 \\ \vdots \\ 0 \\ 1 \end{bmatrix}. \quad (6.48)$$

The conditions of Theorem 1 are satisfied if the matrix $\mathbf{P}(t)$ is deterministic. Although this requirement does not necessarily preclude any uncertainty in $\mathbf{A}(t)$ and $\mathbf{B}(t)$, we have not yet been able to obtain an analytical expression for $\mathbf{P}(t)$. For this reason, we have to assume that $\mathbf{A}(t)$ and $\mathbf{B}(t)$ are deterministic. Specifically, this means that we cannot introduce the uncertainty in the dynamics of the chief.

6.5.2 Choice of the polynomial basis

The same polynomial basis of the previous example is exploited both to expand the flat outputs and the coefficients $a_j(t)$. By noting that $\phi_k \phi_l = \phi_{k+l-1}$, the basis $\Psi(t)$ becomes

$$\Psi = \begin{bmatrix} \Phi(t) \\ \exp\left(\pi \frac{t}{t_f} n_\phi i\right) \Phi(t) \end{bmatrix}. \quad (6.49)$$

6.5.3 Discretization of the path constraints

According to Equation (6.46), the path constraints are:

$$\Delta f_{drag}^{(min)}(t, \delta_l) \leq q^{(4)} + \sum_{j=0}^3 a_j(t) q^{(j)} \leq \Delta f_{drag}^{(max)}(t, \delta_l), \quad l = 1, \dots, n_s. \quad (6.50)$$

The samples $\Delta f_{drag}^{min}(t, \delta_l)$ and $\Delta f_{drag}^{max}(t, \delta_l)$, $l = 1, \dots, n_s$, are generated by means of the *medium-period predictor* discussed in Section 3.3.1. In this way, the samples are provided both with short-period variations due to the posterior distribution of the particle filter and with medium-period variations due to the stochastic evolution of the space weather proxies. The samples of Δf_{drag}^{min} and Δf_{drag}^{max} are expanded on the basis $\Psi(t)$.

Because the coefficients $a_j(t)$ are deterministic, it is possible to replace all the samples by only two inner barriers $\Delta f_{drag}^{(MIN)}(t)$ and $\Delta f_{drag}^{(MAX)}(t)$ such that

$$\begin{aligned} \Delta f_{drag}^{(MIN)}(t) &\geq \Delta f_{drag}^{(min)}(t, \delta_l) \\ \Delta f_{drag}^{(MAX)}(t) &\leq \Delta f_{drag}^{(max)}(t, \delta_l) \end{aligned} \quad l = 1, \dots, n_s. \quad (6.51)$$

The theory of positive polynomials can be used to compute these barriers.

Based on these considerations, only two LMI have to be enforced in the optimization problem, i.e.,

$$\begin{aligned} q^{(4)} + \sum_{j=0}^3 a_j(t) q^{(j)} &\leq \Delta f_{drag}^{(MAX)}(t) \\ q^{(4)} + \sum_{j=0}^3 a_j(t) q^{(j)} &\geq \Delta f_{drag}^{(MIN)}(t) \end{aligned} \quad (6.52)$$

6.5.4 Results

The main purpose of these simulations is to assess the benefit of using the robust reference trajectory against a non-robust one. For this reason, a MC analysis is carried out as follows:

- a single propagation is performed from $t = 0$ to $t = t_{obs}$. The parameters of the particle filter are trained;

Table 6.2: Initial space weather proxies.

Initial daily solar activity	150 sfu
Initial 81-day averaged solar activity	130 sfu
Initial geomagnetic activity, A_p	27

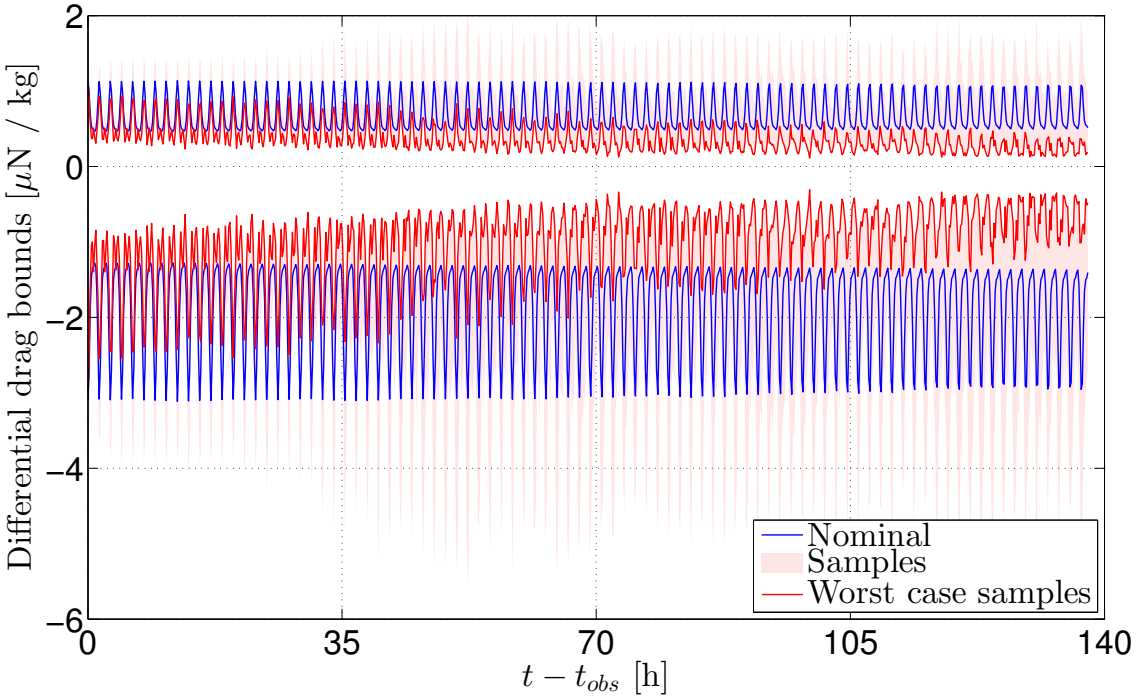


Figure 6.8: Differential drag bounds. The colored region is the envelop of the samples required by the scenario approach. Solid red lines are the worst case of these samples.

- a *nominal* and a *robust* reference trajectories are generated. The nominal one is generated without the scenario approach by using the mean prediction of the particle filter. The robust trajectory is computed by setting the risk and confidence parameters of the scenario approach to $\epsilon = 0.1$, and $\beta = 10^{-3}$, respectively;
- starting from $t = t_{obs}$, 1000 realizations of the stochastic processes related to the space weather proxies are generated by exploiting the conditional probability of the Gaussian copula defined in Equation (2.11) given the values of the proxies for $t < t_{obs}$. The on-line propagation is performed for each realization.

The simulation parameters of Chapter 5 are exploited (see Table 5.1). Only the space weather proxies are changed: their values at the beginning of the simulation are listed in Table 6.2.

The objective function is the amplitude of the oscillations of the relative trajec-

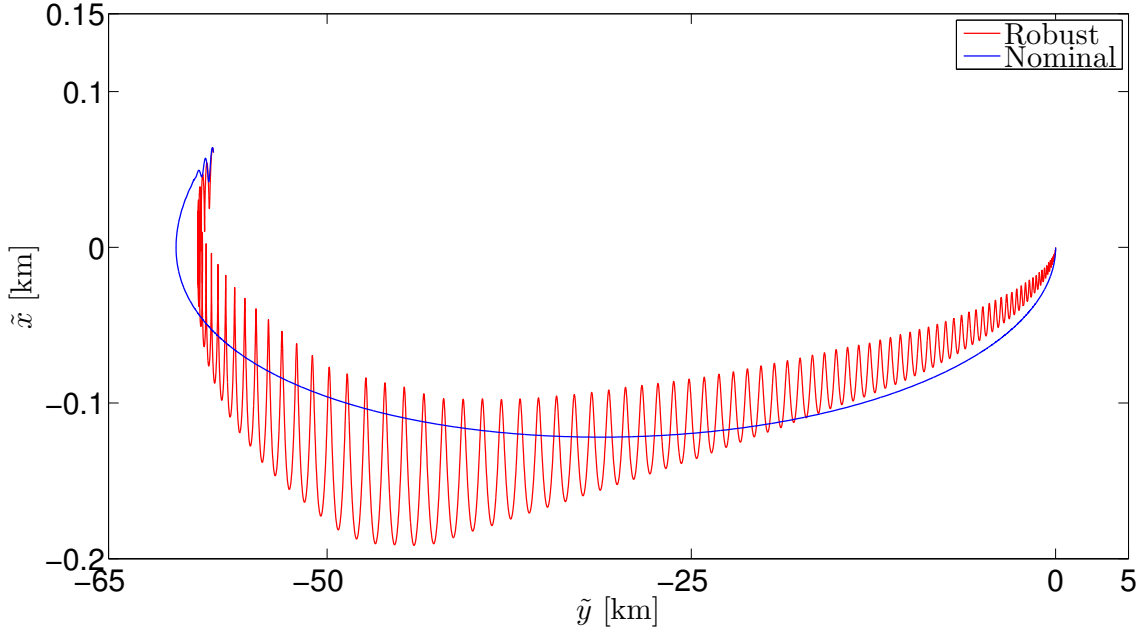


Figure 6.9: Scheduled reference trajectory in curvilinear coordinates.

tory, i.e.,

$$\mathcal{J} = \frac{1}{t_f} \int_0^{t_f} (\dot{r}_D - \dot{r}_C)^2 dt \quad (6.53)$$

The blue curve in Figure 6.8 illustrates the bounds imposed to the differential drag by the mean drag estimated by the particle filter. The region shaded in light red is the envelop of the samples required by the scenario approach generated by the medium-period predictor. The inner barriers, $\Delta f_{drag}^{(MIN)}$ and $\Delta f_{drag}^{(MAX)}$, are outlined by the red solid lines. These bounds become closer and closer as time passes. This is due to the fact that variations of the space weather proxies yield much lower values of the atmospheric density at the end of the maneuver compared to the initial value (which is used to fit the deterministic component of the drag model). In addition, the robust bounds are also narrower than the nominal ones at the very beginning because of the posterior distribution of the parameters of the particle filter.

The robust and nominal reference paths are illustrated in Figure 6.9. As expected, because of the larger control bounds, the nominal solution is ‘smoother’, i.e., it is more optimal than the robust one. Nonetheless, the solution obtained in the nominal case is infeasible for the bounds imposed in the robust case. This is emphasized in Figure 6.10 (bottom), where the robust bounds are superimposed to the differential drag required for the realization of the nominal solution. Most violation of the bounds occurs during the final phase of the maneuver.

The satisfaction of the rendez-vous conditions for the two cases is plotted in Figure 6.11. The confidence regions in the robust case are smaller and closer to the origin than in the nominal case.

The probability distribution of the root mean square distance between the planned

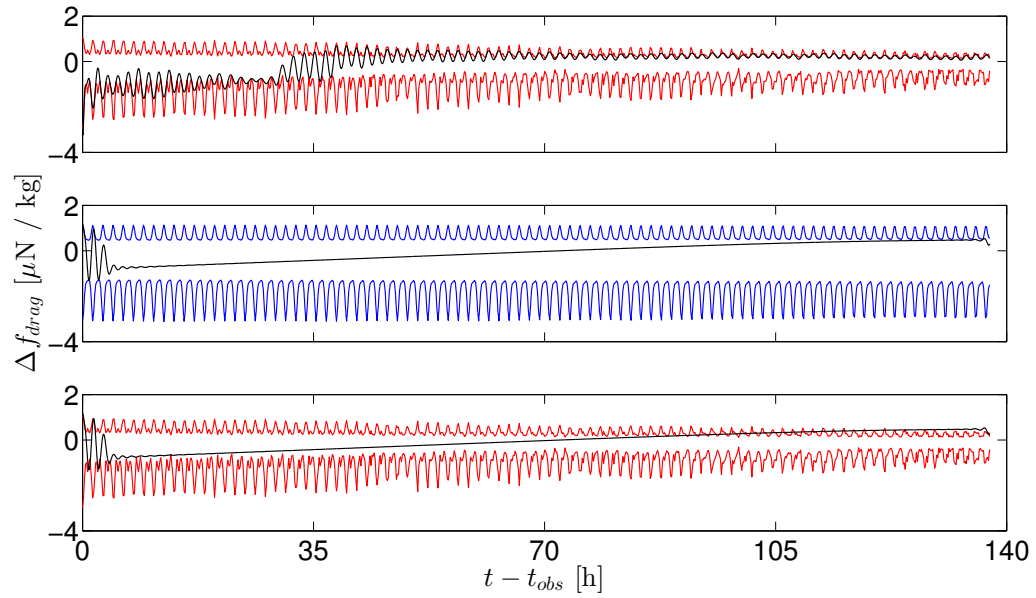


Figure 6.10: Planned differential drag. The red and blue curves depict the robust and nominal feasible regions. The black curve in the first and second plots depicts the differential drag required to accomplish the robust and nominal trajectory, respectively. The third plot superimposes the robust bounds to the planned differential drag in the nominal case.

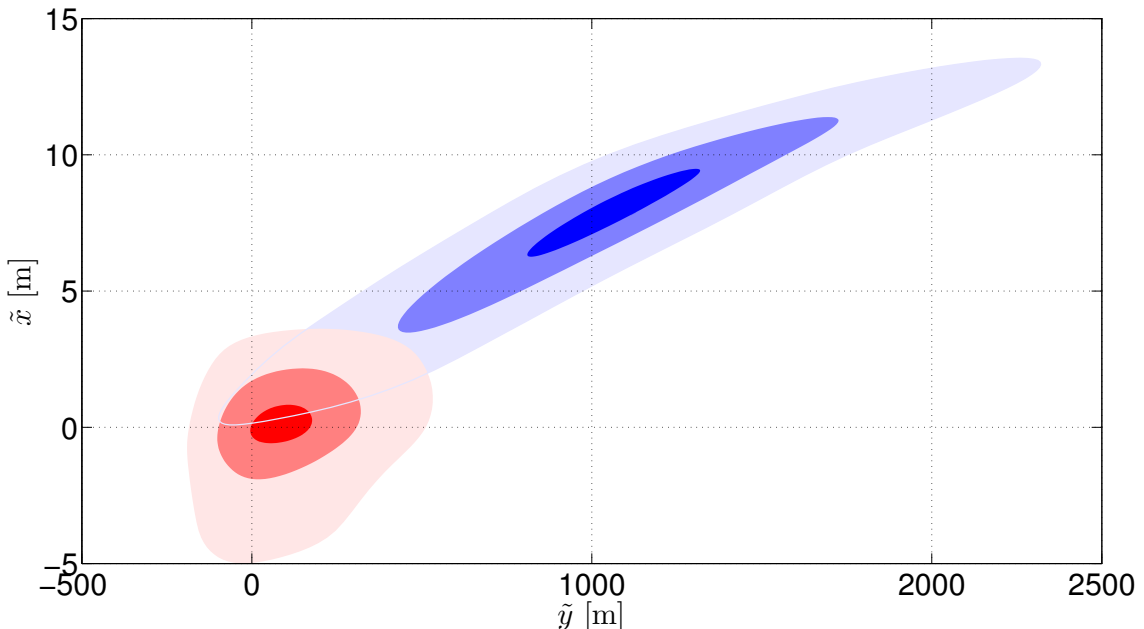
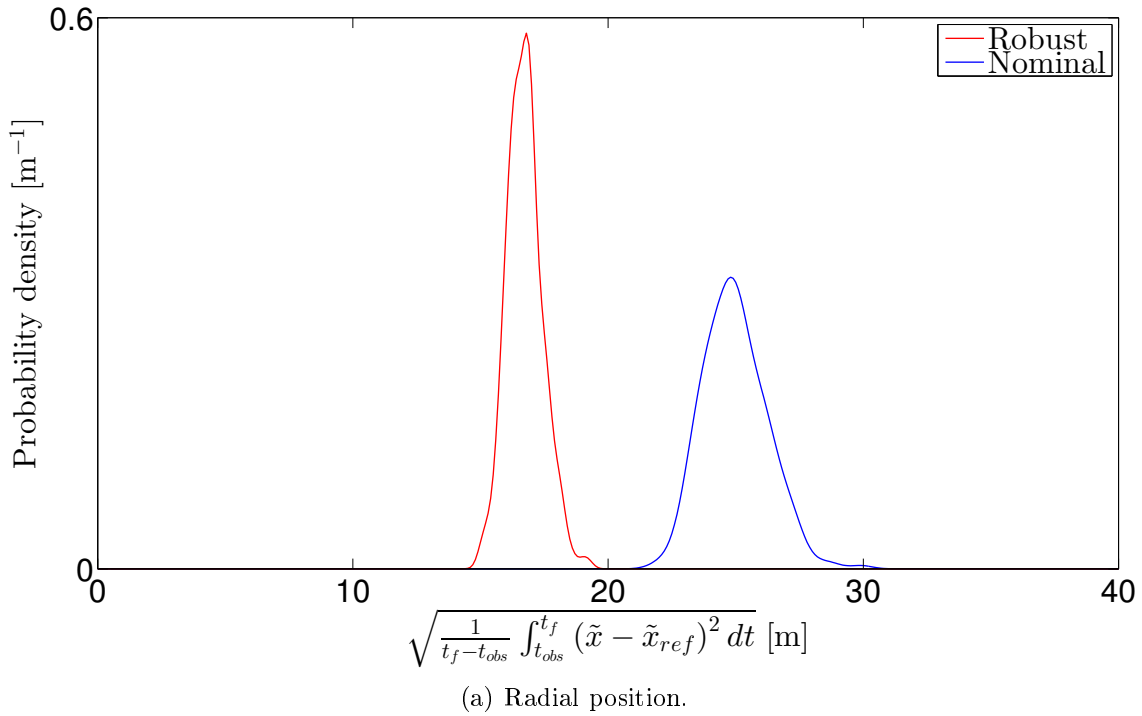
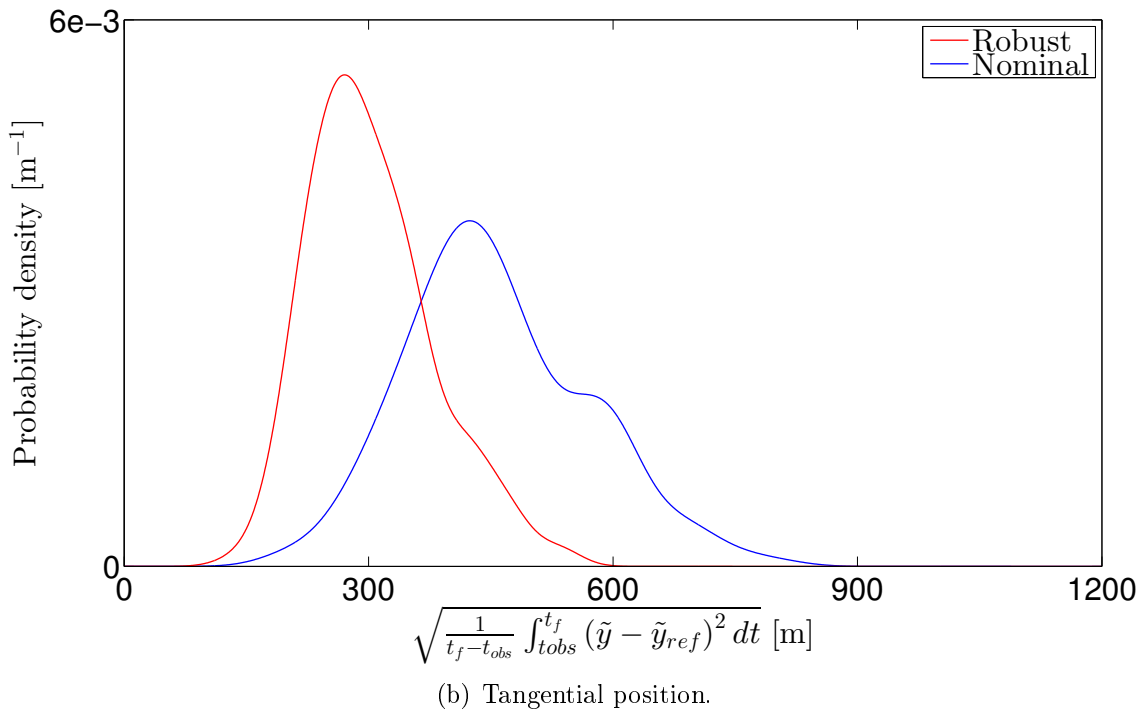


Figure 6.11: Satisfaction of the rendez-vous conditions. From the lighter to the darker, the colored regions indicate 90%, 50%, and 10% confidence bounds. Red regions refer to the robust trajectory. The blue regions are related to the nominal one.



(a) Radial position.



(b) Tangential position.

Figure 6.12: Probability density distribution of the root mean square distance between planned and on-line trajectory. Red and blue are related to the tracking of the robust and of the nominal reference path, respectively.

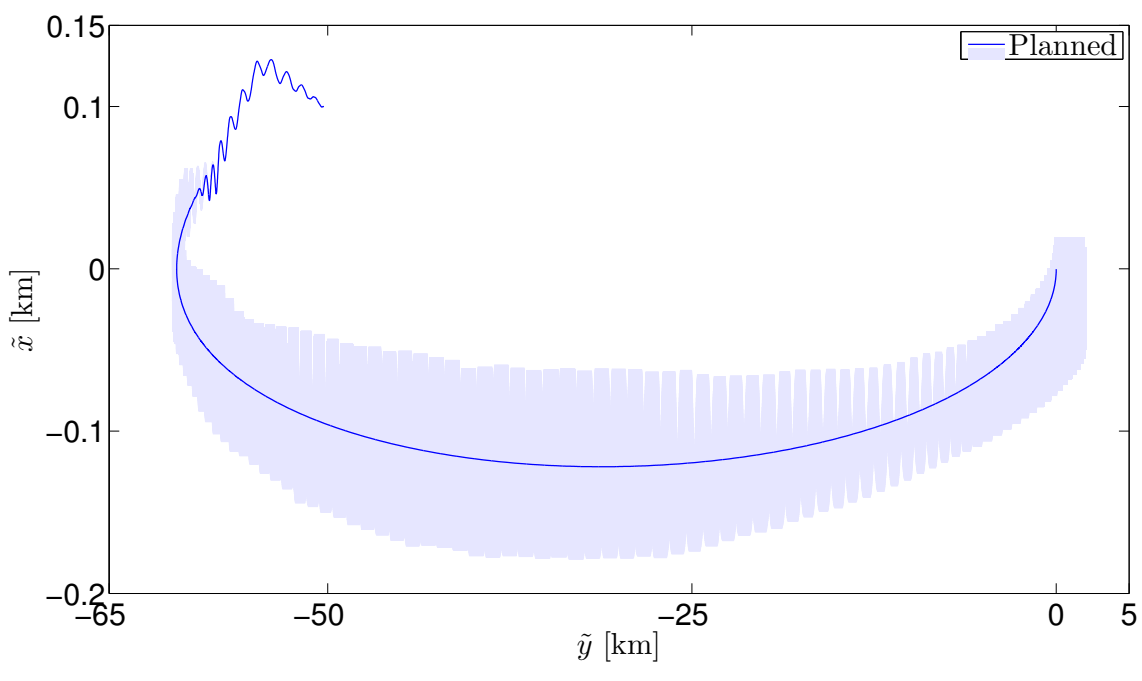
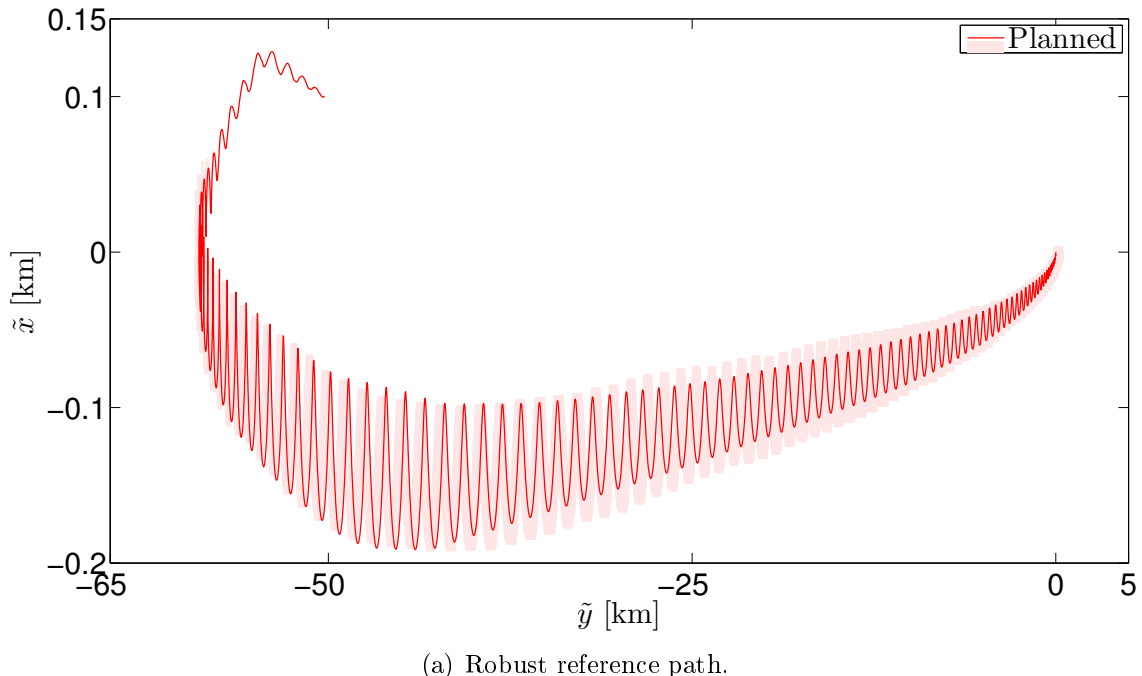


Figure 6.13: Comparison between the reference trajectories and the Monte Carlo samples. The colored regions indicate 99% confidence bounds on the trajectory of the samples. The tracking of the reference path is better with the robust reference path.

and the real curvilinear states is illustrated in Figure 6.12. The robust solution performs systematically better than the nominal one. In addition, not only the peaks of the distributions in the robust case are shifted to the left, but they are also higher, i.e., with a narrower distribution.

The enhanced performance of the tracking in the robust case can also be appreciated in Figure 6.13, where 99% percentiles of the on-line trajectories are superimposed to the reference path. At the end of the maneuver, these bounds are much closer to the origin when using the robust reference trajectory.

Appendix C provides a statistical validation of the controller and it shows that the method performs well for a broad set of initial relative states.

6.6 Conclusion

This chapter introduces the novel concept of robust deterministic trajectory for maneuver planning under uncertainties and proposes a numerical method to compute this trajectory based on a limited number of assumptions. The feasibility of the solution is guaranteed both continuously in time and for a desired portion of the uncertain set. The theory of positive polynomials and the scenario approach were exploited for these purposes, respectively. Targeting a practical exploitation of the trajectory, the feasibility of the solution can be further extended for a desired set of tracking errors.

Eventually, the initial infinite-dimensional NLP is recast into a LMI problem. Although the number of matrix inequalities could be large enough to be considered as a limitation of the methodology, we showed in two applications that this number can be drastically reduced by means of simple considerations on the nature of the problem at hand.

The methodology was implemented to accomplish differential-drag based rendezvous and integrates the contributions of Chapters 3 and 4. The combination of these contributions yields a remarkable enhancement of the accuracy of differential-drag-based maneuvers.

Conclusions

This thesis is an attempt to combine uncertainty quantification, analytical propagation, and optimal control of satellite trajectories in the atmosphere to effectively and robustly exploit the aerodynamic force. Specifically, by means of a probabilistic estimation and prediction of the aerodynamic force and an efficient and consistent propagation of LEO orbits, a robust reference trajectory for the realization of relative maneuvers between two satellites in a realistic environment can be generated. The main outcome of this work is presented schematically in Figure 1.

Contributions

The objective of the thesis was formulated using three fundamental questions in the introduction. Addressing them led to the following contributions:

How can we characterize the uncertainty sources affecting the evolution of satellite orbits in the atmosphere by using physical considerations and available experimental data?

We proposed a *probabilistic characterization* of the dominant sources of uncertainty affecting drag modeling. Mathematical statistics methods, i.e., maximum entropy and MLE, in conjunction with mechanical modeling considerations were used to infer the probabilistic characterization of these uncertainties from experimental data and atmospheric density models. This characterization facilitates the application of uncertainty propagation and sensitivity analysis methods, which, in turn, allows us

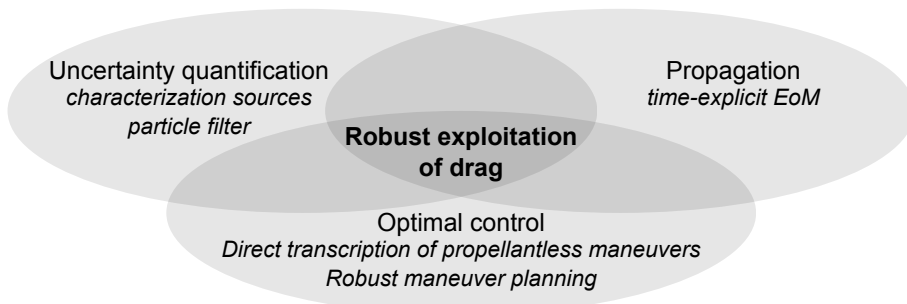


Figure 1: Contributions of the thesis.

to gain insight into the impact that these uncertainties have on absolute and relative satellite dynamics. Based on the same uncertainty characterization, a particle filter for the recursive estimation and prediction of the aerodynamic force was developed. The filter provides accurate estimations even when only GPS data are available, i.e., when accelerometers aboard the satellite are not available.

How can we efficiently propagate the trajectory of a satellite in the atmosphere?

We developed an *analytical propagator* for the absolute and relative motion of LEO satellites. The model incorporates the two dominant perturbations, namely the atmospheric drag and the Earth's oblateness. Assuming constant atmospheric density and near-circular orbits, a time-explicit solution of the governing equations of motion was first obtained. Without further assumptions, a closed-form solution for the relative dynamics was also achieved. The resulting model is suitable to be incorporated in on-board propagators for short-term orbit predictions.

How can we exploit the aerodynamic force for accomplishing complex propellantless maneuvers?

We established a novel methodology for the realization of differential-drag-based maneuvers. The core of the control loop is the off-line planning of a so-called *robust deterministic trajectory* which is conceived to be “easily” tracked by an on-line controller. For this purpose, the problem is formulated as an infinite-dimensional nonlinear programming problem. We proposed a discretization of this problem that guarantees the feasibility of the trajectory continuously in time and over an arbitrary user-defined portion of the uncertain set.

Perspectives

This thesis paves the way for both application-oriented and methodological perspectives.

Potential applications of the methodology are:

Uncertainty quantification: the methodology for the characterization of the uncertainty sources can be extended to other perturbations, e.g., SRP and thermospheric winds, and could therefore be used in other missions, including interplanetary transfer.

Orbital propagation: more advanced atmospheric models can be included in the analytical propagator. We already obtained some results in this direction, i.e., an analytical solution for the case of exponential density [Martinusi et al., 2014]. An analytical solution for the “harmonic” density model used by the particle filter is currently under investigation.

Optimal control: the methodology developed in Chapter 6 can be applied to other problems where uncertainty plays a major role, i.e., whenever the trajectory is highly sensitive to the uncertainty sources. It is no surprise that most problems in astrodynamics fall into this category, e.g., interplanetary transfer and asteroid deflection.

Potential improvements of the methodology are:

Uncertainty quantification: efficient techniques can be exploited to speed up the uncertainty propagation step. They include both smart randomized approaches, e.g., Markov chain Monte Carlo, and stochastic expansion methods, e.g., polynomial chaos expansion. In our view, because of the great number of uncertainty sources we identified, the former techniques are more suitable for our problem since they are less affected by the curse of dimensionality than the latter techniques. In addition, the use of Gaussian process surrogate models could be investigated to obtain a rigorous probabilistic description of the total effect sensitivity indexes [Marrel et al., 2009].

Orbital propagation: the accuracy of the analytical propagator can be enhanced by developing a pseudo-contact transformation that accommodates the non-conservative effects of the drag. For this purpose, the use of the Lie transform method could be investigated.

Optimal control: the assumptions in the definition of the robust deterministic trajectory can be relaxed to accommodate uncertainties in non-holonomic constraints into the maneuver planning. The inclusion of non-convex path constraints could also be a major improvement of the methodology. This could be accomplished, for example, by means of fictitious dynamical variables whose introduction “convexifies” the path constraints. Finally, the possibility to optimize the maneuvering time of the robust deterministic trajectory can be investigated, for example, by means of the geometrical approach proposed in [Loock et al., 2014].

Appendix A

Maximum Entropy: a Numerical Approach

In this appendix, a numerical implementation of the principle based on piecewise linear shape functions is carried out. The support $\mathcal{I}_X = [x_{min}, x_{max}]$ is divided into M uniform intervals of width $\Delta x = \frac{x_{max} - x_{min}}{M}$ with nodes x_0, x_1, \dots, x_M ¹. The generic PDF is constructed using linear shape functions $\varphi_i(x)$

$$p_X(x) = \sum_{j=0}^M \varphi_j(x) \vartheta_j \quad (\text{A.1})$$

where ϑ_j is non-negative and represents the evaluation of the PDF at node x_j , whereas φ_j is such that

$$\begin{aligned} \varphi_0(x) &= \begin{cases} \frac{x_1 - x}{\Delta x} & \text{if } x_0 \leq x < x_1 \\ 0 & \text{otherwise} \end{cases} \\ \varphi_j(x) &= \begin{cases} \frac{x - x_{j-1}}{\Delta x} & \text{if } x_{j-1} \leq x < x_j \\ \frac{x_{j+1} - x}{\Delta x} & \text{if } x_j \leq x < x_{j+1} \\ 0 & \text{otherwise} \end{cases} \quad \text{for } j = 1, \dots, M-1 \\ \varphi_M(x) &= \begin{cases} \frac{x - x_{M-1}}{\Delta x} & \text{if } x_{M-1} \leq x \leq x_M \\ 0 & \text{otherwise} \end{cases} \end{aligned} \quad (\text{A.2})$$

According to Equation 2.4, the entropy of the synthesized PDF is:

$$S_X = -\frac{\Delta x^2}{4} \sum_{j=1}^M S_{X,j} \quad (\text{A.3})$$

¹If either x_{min} or x_{max} is unbounded, a finite x_{min} or x_{max} should be selected such the PDF value at this modified bound is practically zero.

where:

$$S_{X,j} = \begin{cases} 0 & \text{if } \vartheta_j = \vartheta_{j-1} = 0 \\ \frac{2\vartheta_j(3\log(\vartheta_j\Delta x) - 1)}{\vartheta_j^2(2\log(\vartheta_j\Delta x) - 1) - \vartheta_{j-1}^2(2\log(\vartheta_{j-1}\Delta x) - 1)} & \text{if } \vartheta_j = \vartheta_{j-1} \\ \frac{\vartheta_j^2(2\log(\vartheta_j\Delta x) - 1) - \vartheta_{j-1}^2(2\log(\vartheta_{j-1}\Delta x) - 1)}{\vartheta_j - \vartheta_{j-1}} & \text{otherwise} \end{cases} \quad (\text{A.4})$$

Equations 2.5 and 2.6 are therefore recast into

$$\max_{\vartheta_0, \dots, \vartheta_M} S_X(\vartheta_0, \dots, \vartheta_M) \quad \text{s.t.} \quad (\text{A.5a})$$

$$I_X = \int_{\mathcal{I}_X} p_X(x; \vartheta_0, \dots, \vartheta_M) dx = \Delta x \left(\frac{\vartheta_0}{2} + \sum_{j=1}^{M-1} \vartheta_j + \frac{\vartheta_M}{2} \right) = 1 \quad (\text{A.5b})$$

$$\vartheta_j \geq 0 \quad j = 0, \dots, M \quad (\text{A.5c})$$

$$\mathbf{z}(\vartheta_0, \dots, \vartheta_M) \geq \mathbf{0} \quad (\text{A.5d})$$

$$\mathbf{g}(\vartheta_0, \dots, \vartheta_M) = \mathbf{0} \quad (\text{A.5e})$$

Equations A.5b and A.5c impose that p_X satisfies the properties of a PDF, while the available information related to the specific problem is expressed by equations A.5d and A.5e. For instance, the moments of the distribution are often known and can be expressed in terms of the shape functions. For the second-order descriptors, it follows that

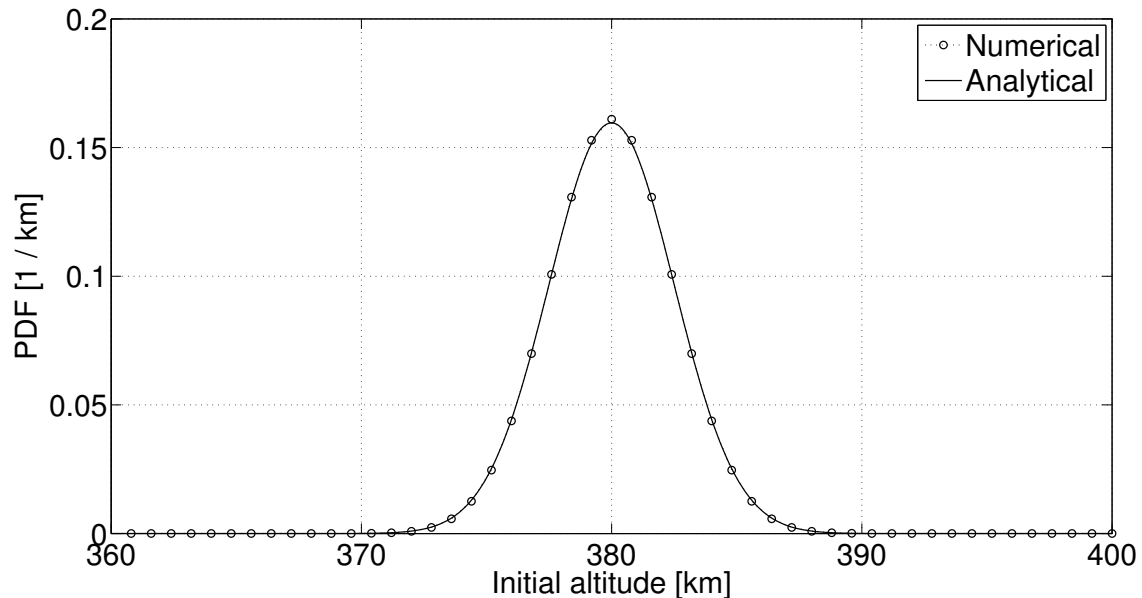
$$\mu_X = \frac{1}{\Delta x} \sum_{j=1}^M \left[\left(\frac{x_j^3}{6} - \frac{x_j x_{j-1}^2}{2} + \frac{x_{j-1}^3}{3} \right) \vartheta_{j-1} + \left(\frac{x_{j-1}^3}{6} - \frac{x_{j-1} x_j^2}{2} + \frac{x_j^3}{3} \right) \vartheta_j \right] \quad (\text{A.6a})$$

$$\sigma_X^2 = \frac{1}{\Delta x} \sum_{j=1}^M \left[\left(-\frac{1}{4} x_{j,j-1}^4 + \frac{2\mu_X + x_j}{3} x_{j,j-1}^3 - \frac{2\mu_X x_j - \mu_X^2}{2} x_{j,j-1}^2 + \mu_X^2 x_j x_{j,j-1}^1 \right) \vartheta_{j-1} + \left(\frac{1}{4} x_{j,j-1}^4 - \frac{2\mu_X + x_{j-1}}{3} x_{j,j-1}^3 + \frac{2\mu_X x_{j-1} - \mu_X^2}{2} x_{j,j-1}^2 - \mu_X^2 x_{j-1} x_{j,j-1}^1 \right) \vartheta_j \right] \quad (\text{A.6b})$$

where $x_{j,m}^k = x_j^k - x_m^k$. All the other constraints of the problem should also be expressed as a function of the design variables $\vartheta_0, \dots, \vartheta_M$.

This implementation through linear shape functions turned out to be computationally effective in our simulations, as discussed in Sections 2.4 and 2.5, but it can also be extended to any suitable family of shape functions.

Figure A.1 displays the application of the method to the initial altitude before



(a) Probability distribution for the initial altitude before ejection.

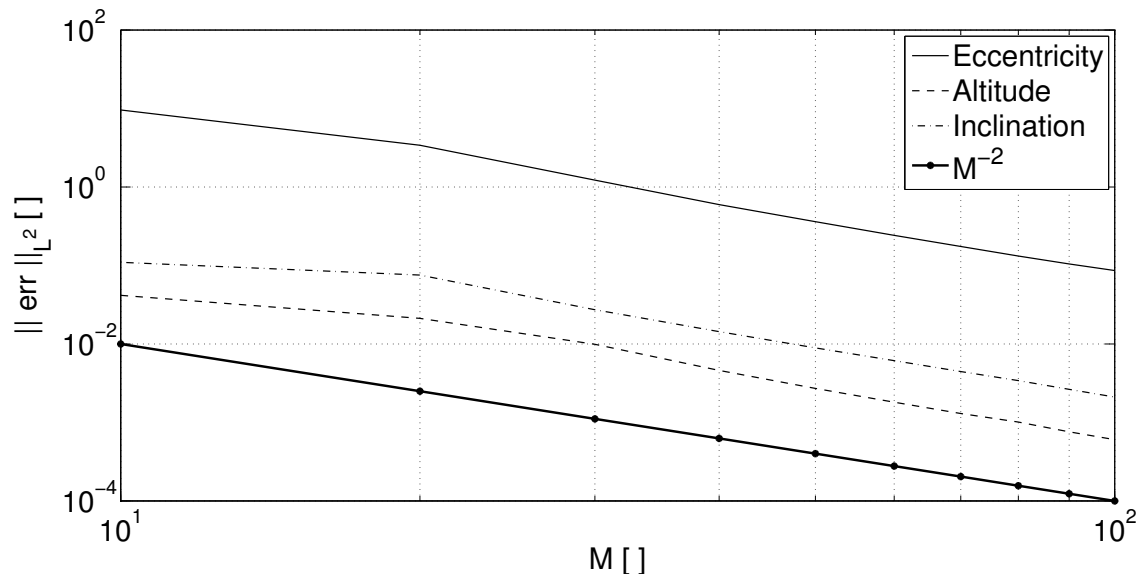
(b) Convergence of the PDFs identified with the numerical implementation of the maximum entropy method in function of the number of intervals, M .

Figure A.1: Numerical implementation of the maximum entropy principle.

ejection and the weighted divergence

$$\sqrt{\int_{\mathcal{R}} (p_{\bar{X}}(\bar{x}) - \tilde{p}_{\bar{X}}(\bar{x}))^2 \tilde{p}_{\bar{X}}(\bar{x}) d\bar{x}} \quad \text{with} \quad \bar{X} = \frac{X}{\sigma_X} \quad (\text{A.7})$$

between the discrete PDFs $p_{\bar{X}}(\bar{x})$ computed using the numerical implementation of the maximum entropy principle and the analytical solution $\tilde{p}_{\bar{X}}(\bar{x})$. We note that this norm attributes high weights to errors corresponding to high probabilities. The figure shows that the convergence rate is quadratic for the three cases. We note that the solution of the optimization problem showed no sensitivity to the initial guess.

Appendix B

Linearized equations of motion

Linearized equations for mean equinoctial ROE are written in the form¹:

$$\Delta \dot{\bar{\mathcal{E}}} = \mathbf{A}(\bar{\mathcal{E}}_{eq}) \Delta \dot{\bar{\mathcal{E}}} + \mathbf{B}(\bar{\mathcal{E}}_{eq}) \Delta \mathbf{f}_p \quad (\text{B.1})$$

where, neglecting the gradient of the contact transformation, [Schaub et al., 2000],

$$\mathbf{A}(\bar{\mathcal{E}}_{eq}) = \mathbf{A}^{(J_2)}(\bar{\mathcal{E}}_{eq}) + \nabla_{\boldsymbol{\varepsilon}_{eq}} \dot{\bar{\mathcal{E}}}_{eq} \quad (\text{B.2})$$

Because GVE are linear in the perturbing force, the matrix \mathbf{B} is straightforwardly deduced from Equations 1.10. The analytical expressions for the matrices $\mathbf{A}^{(J_2)}$ and $\nabla_{\boldsymbol{\varepsilon}_{eq}} \dot{\bar{\mathcal{E}}}_{eq}$ are provided in the following.

Secular effects of the Earth's oblateness

Define $K = nJ_2 \left(\frac{r_{eq}}{p} \right)^2$. The elements of the matrix $\mathbf{A}^{(J_2)}$ are:

$$A_{11}^{(J_2)} = 0;$$

$$A_{21}^{(J_2)} = -\frac{21}{8} \frac{KP_2}{a} (5c^2 - 2c - 1)$$

$$A_{31}^{(J_2)} = \frac{21}{8} \frac{KP_1}{a} (5c^2 - 2c - 1)$$

$$A_{41}^{(J_2)} = \frac{21}{4} \frac{KQ_2}{a} c$$

$$A_{51}^{(J_2)} = -\frac{21}{4} \frac{KQ_1}{a} c$$

$$A_{61}^{(J_2)} = -\frac{3n}{2a} - \frac{21K}{8a} \left[5c^2 - 2c - 1 + \frac{b}{a} (3c^2 - 1) \right]$$

$$A_{12}^{(J_2)} = 0;$$

$$A_{22}^{(J_2)} = \frac{3KP_1P_2a}{p} (5c^2 - 2c - 1)$$

¹Although a subset of these Equations is used in Chapter 5, we detail the complete form for completeness. In addition, the matrix \mathbf{B} is calculated for a generic perturbation here, while in chapter 5 the perturbation was assumed to be toward the velocity.

$$\begin{aligned}
A_{32}^{(J_2)} &= -\frac{3K}{2} \left(\frac{2P_1^2 a}{p} + \frac{1}{2} \right) (5c^2 - 2c - 1) \\
A_{42}^{(J_2)} &= -\frac{6KQ_2 P_1 a}{p} c \\
A_{52}^{(J_2)} &= \frac{6KQ_1 P_1 a}{p} c \\
A_{62}^{(J_2)} &= \frac{3KP_1 a}{p} \left[5c^2 - 2c - 1 + \frac{3b}{4a} (3c^2 - 1) \right] \\
A_{13}^{(J_2)} &= 0; \\
A_{23}^{(J_2)} &= \frac{3K}{2} \left(\frac{2P_2^2 a}{p} + \frac{1}{2} \right) (5c^2 - 2c - 1) \\
A_{33}^{(J_2)} &= \frac{-3K P_1 P_2 a}{p} (5c^2 - 2c - 1) \\
A_{43}^{(J_2)} &= \frac{-6KQ_2 P_2 a}{p} c \\
A_{53}^{(J_2)} &= \frac{6KQ_1 P_2 a}{p} c \\
A_{63}^{(J_2)} &= \frac{3KP_2 a}{p} \left[5c^2 - 2c - 1 + \frac{3b}{4a} (3c^2 - 1) \right] \\
A_{14}^{(J_2)} &= 0; \\
A_{24}^{(J_2)} &= \frac{3KQ_1 P_2}{2} (1 - 5c) (c + 1)^2 \\
A_{34}^{(J_2)} &= -\frac{3KQ_1 P_1}{2} (1 - 5c) (c + 1)^2 \\
A_{44}^{(J_2)} &= \frac{3KQ_1 Q_2}{2} (c + 1)^2 \\
A_{54}^{(J_2)} &= \frac{3K}{8} \left[(4Q_1^2 - 1) (c + 1)^2 + (1 - c)^2 \right] \\
A_{64}^{(J_2)} &= -\frac{3KQ_1}{2} (c + 1)^2 \left(5c - 1 + \frac{3b}{a} c \right) \\
A_{15}^{(J_2)} &= 0; \\
A_{25}^{(J_2)} &= \frac{3KQ_2 P_2}{2} (1 - 5c) (c + 1)^2 \\
A_{35}^{(J_2)} &= \frac{-3KQ_2 P_1}{2} (1 - 5c) (c + 1)^2 \\
A_{45}^{(J_2)} &= \frac{3K}{8} \left[(4Q_2^2 - 1) (c + 1)^2 + (1 - c)^2 \right] \\
A_{55}^{(J_2)} &= -\frac{3KQ_1 Q_2}{2} (c + 1)^2 \\
A_{65}^{(J_2)} &= -\frac{3KQ_2}{2} (c + 1)^2 \left(5c - 1 + \frac{3cb}{a} \right) \\
A_{16}^{(J_2)} &= 0; \\
A_{26}^{(J_2)} &= 0 \\
A_{36}^{(J_2)} &= 0 \\
A_{46}^{(J_2)} &= 0 \\
A_{56}^{(J_2)} &= 0 \\
A_{66}^{(J_2)} &= 0
\end{aligned}$$

Jacobian of the equinoctial GVE

Define:

$$\begin{aligned} P_1 \cos L - P_2 \sin L &= \kappa \\ Q_1 \cos L - Q_2 \sin L &= \lambda \\ Q_1 \sin L + Q_2 \cos L &= \zeta \\ 1 + Q_1^2 + Q_2^2 &= \xi \end{aligned}$$

Classical notations:

$$\begin{aligned} p &= a(1 - P_1^2 - P_2^2) \\ h &= \sqrt{\mu p} \\ b &= a\sqrt{1 - P_1^2 - P_2^2} \\ n &= \sqrt{\mu}a^{-3/2} \\ r &= \frac{p}{1 + P_1 \cos L + P_2 \sin L} \end{aligned}$$

Partial derivatives of L :

$$\begin{aligned} \frac{\partial L}{\partial P_1} &= -\frac{P_1 a}{p} \frac{\kappa}{P_1^2 + P_2^2} \left(\frac{p}{r} + 1 \right) \\ \frac{\partial L}{\partial P_2} &= -\frac{P_2 a}{p} \frac{\kappa}{P_1^2 + P_2^2} \left(\frac{p}{r} + 1 \right) \\ \frac{\partial L}{\partial l} &= \frac{ab}{r^2} \end{aligned}$$

The elements of the matrix $\nabla_{\boldsymbol{\varepsilon}_{eq}} \dot{\boldsymbol{\mathcal{E}}}_{eq}$ are:

$$\begin{aligned} \frac{\partial}{\partial \bar{a}} \left(\frac{d\bar{a}}{dt} \right)_{f_r} &= -\frac{3a\kappa}{h} \\ \frac{\partial}{\partial \bar{a}} \left(\frac{d\bar{a}}{dt} \right)_{f_t} &= \frac{3ap}{hr} \\ \frac{\partial}{\partial \bar{a}} \left(\frac{d\bar{a}}{dt} \right)_{f_h} &= 0 \\ \frac{\partial}{\partial \bar{a}} \left(\frac{d\bar{P}_1}{dt} \right)_{f_r} &= -\frac{b}{2na^3} \cos L \\ \frac{\partial}{\partial \bar{a}} \left(\frac{d\bar{P}_1}{dt} \right)_{f_t} &= -\frac{r}{2ha} (-2P_1 - 2 \sin L + \kappa \cos L) \\ \frac{\partial}{\partial \bar{a}} \left(\frac{d\bar{P}_1}{dt} \right)_{f_h} &= -\frac{rP_2}{2ha} \lambda \\ \frac{\partial}{\partial \bar{a}} \left(\frac{d\bar{P}_2}{dt} \right)_{f_r} &= -\frac{p \sin L}{2ha} \\ \frac{\partial}{\partial \bar{a}} \left(\frac{d\bar{P}_2}{dt} \right)_{f_t} &= \frac{r}{2ha} [P_2 + 2 \cos L + \left(\frac{p}{r} - 1 \right) \cos L] \end{aligned}$$

$$\begin{aligned}
\frac{\partial}{\partial \bar{a}} \left(\frac{d\bar{P}_2}{dt} \right)_{f_h} &= \frac{rP_1}{2ha} \lambda \\
\frac{\partial}{\partial \bar{a}} \left(\frac{d\bar{Q}_1}{dt} \right)_{f_r} &= 0 \\
\frac{\partial}{\partial \bar{a}} \left(\frac{d\bar{Q}_1}{dt} \right)_{f_t} &= 0 \\
\frac{\partial}{\partial \bar{a}} \left(\frac{d\bar{Q}_1}{dt} \right)_{f_h} &= \frac{r}{4ha} \xi \sin L \\
\frac{\partial}{\partial \bar{a}} \left(\frac{d\bar{Q}_2}{dt} \right)_{f_r} &= 0 \\
\frac{\partial}{\partial \bar{a}} \left(\frac{d\bar{Q}_2}{dt} \right)_{f_t} &= 0 \\
\frac{\partial}{\partial \bar{a}} \left(\frac{d\bar{Q}_2}{dt} \right)_{f_h} &= \frac{r}{4ha} \xi \cos L \\
\frac{\partial}{\partial \bar{a}} \left(\frac{d\bar{l}}{dt} \right)_{f_r} &= -\frac{1}{h} \left[\frac{br}{a^2} + \frac{p(p-r)}{2(a+b)r} \right] \\
\frac{\partial}{\partial \bar{a}} \left(\frac{d\bar{l}}{dt} \right)_{f_t} &= -\frac{(r+p)\kappa}{2h(a+b)} \\
\frac{\partial}{\partial \bar{a}} \left(\frac{d\bar{l}}{dt} \right)_{f_h} &= -\frac{br}{2pna^3} \lambda \\
\frac{\partial}{\partial \bar{P}_1} \left(\frac{d\bar{a}}{dt} \right)_{f_r} &= \frac{2a^2}{h} \left[\left(\frac{p}{r} - 1 \right) \frac{\partial L}{\partial \bar{P}_1} - \frac{aP_1}{p} \kappa - \cos L \right] \\
\frac{\partial}{\partial \bar{P}_1} \left(\frac{d\bar{a}}{dt} \right)_{f_t} &= \frac{2a^2}{h} \left[\kappa \frac{\partial L}{\partial \bar{P}_1} + \frac{aP_1}{r} + \sin L \right] \\
\frac{\partial}{\partial \bar{P}_1} \left(\frac{d\bar{a}}{dt} \right)_{f_h} &= 0 \\
\frac{\partial}{\partial \bar{P}_1} \left(\frac{d\bar{P}_1}{dt} \right)_{f_r} &= \frac{a}{h} \left[P_1 \cos L + \frac{p}{a} \sin L \frac{\partial L}{\partial \bar{P}_1} \right] \\
\frac{\partial}{\partial \bar{P}_1} \left(\frac{d\bar{P}_1}{dt} \right)_{f_t} &= \frac{f_r}{hp} \left\{ \frac{p}{a} \left[-\frac{r\kappa}{p} (P_1 + \sin L) \frac{\partial L}{\partial \bar{P}_1} + \left(1 + \frac{p}{r} \right) \cos L + 1 + \sin^2 L \right] \right. \\
&\quad \left. - \left[P_1 + \left(1 + \frac{p}{r} \right) \sin L \right] \left(P_1 + \frac{r}{a} \sin L \right) \right\} \\
\frac{\partial}{\partial \bar{P}_1} \left(\frac{d\bar{P}_1}{dt} \right)_{f_h} &= \frac{r^2 P_2}{hp} \left\{ \left[\lambda \kappa + \frac{p}{r} \zeta \right] \frac{\partial L}{\partial \bar{P}_1} + \left(\frac{aP_1}{r} + \sin L \right) \lambda \right\} \\
\frac{\partial}{\partial \bar{P}_1} \left(\frac{d\bar{P}_2}{dt} \right)_{f_r} &= \frac{p}{h} \cos L \frac{\partial L}{\partial \bar{P}_1} - \frac{aP_1}{h} \sin L \\
\frac{\partial}{\partial \bar{P}_1} \left(\frac{d\bar{P}_2}{dt} \right)_{f_t} &= -\frac{r}{h} \left[\frac{r}{p} (P_2 + \cos L) \kappa + \left(1 + \frac{p}{r} \right) \sin L \right] \frac{\partial L}{\partial \bar{P}_1} \\
&\quad + \frac{r}{hp} \left\{ - \left[P_2 + \left(1 + \frac{p}{r} \right) \cos L \right] (aP_1 + r \sin L) + p \sin L \cos L \right\} \\
\frac{\partial}{\partial \bar{P}_1} \left(\frac{d\bar{P}_2}{dt} \right)_{f_h} &= -\frac{rP_1}{h} \left[\frac{r}{p} \lambda \kappa + \zeta \right] \frac{\partial L}{\partial \bar{P}_1} + \frac{r\lambda}{h} \left[-\frac{aP_1}{p} \left(P_1 + \frac{r}{a} \sin L \right) + 1 \right] \\
\frac{\partial}{\partial \bar{P}_1} \left(\frac{d\bar{Q}_1}{dt} \right)_{f_r} &= 0 \\
\frac{\partial}{\partial \bar{P}_1} \left(\frac{d\bar{Q}_1}{dt} \right)_{f_t} &= 0 \\
\frac{\partial}{\partial \bar{P}_1} \left(\frac{d\bar{Q}_1}{dt} \right)_{f_h} &= \frac{r^2}{2hp} \xi \left[(P_2 + \cos L) \frac{\partial L}{\partial \bar{P}_1} - \frac{a}{p} (\kappa P_2 + P_1 + \sin L) \sin L \right]
\end{aligned}$$

$$\begin{aligned}
& \frac{\partial}{\partial \bar{P}_1} \left(\frac{d\bar{Q}_2}{dt} \right)_{f_r} = 0 \\
& \frac{\partial}{\partial \bar{P}_1} \left(\frac{d\bar{Q}_2}{dt} \right)_{f_t} = 0 \\
& \frac{\partial}{\partial \bar{P}_1} \left(\frac{d\bar{Q}_2}{dt} \right)_{f_h} = -\frac{r^2}{2hp} \xi \left[\kappa \cos L + \frac{p}{r} \sin L \right] \frac{\partial L}{\partial \bar{P}_1} - \frac{ar^2}{2hp^2} \xi [P_2 \kappa + P_1 + \sin L] \cos L \\
& \frac{\partial}{\partial \bar{P}_1} \left(\frac{d\bar{l}}{dt} \right)_{f_r} = \frac{r}{h} \left\{ \kappa \left[2 \frac{br}{ap} - \frac{ap}{(a+b)r} \right] \right\} \frac{\partial L}{\partial \bar{P}_1} \\
& \quad + \frac{r}{h} \left\{ \frac{aP_1}{p} \left[\frac{ap}{(a+b)r} \left(\frac{p}{r} - 1 \right) + 2 \frac{b}{a} \right] + \left[2 \frac{br}{ap} - \frac{ap}{(a+b)r} \right] \sin L \right. \\
& \quad \left. - \frac{aP_1}{b} \left[\frac{a^2 p}{(a+b)^2 r} \left(\frac{p}{r} - 1 \right) - 2 \right] \right\} \\
& \frac{\partial}{\partial \bar{P}_1} \left(\frac{d\bar{l}}{dt} \right)_{f_t} = \frac{ra}{h(a+b)} \left[\frac{p^2}{r^2} + \frac{r}{p} \kappa^2 - 1 \right] \\
& \quad + \frac{ra\kappa}{h(a+b)} \left[\left[\frac{1}{p} \left(1 + \frac{p}{r} \right) (aP_1 + r \sin L) - \frac{a^2 P_1}{b(a+b)} \left(1 + \frac{p}{r} \right) - \sin L \right] \right. \\
& \quad \left. - \left(1 + \frac{p}{r} \right) \cos L \right] \\
& \frac{\partial}{\partial \bar{P}_1} \left(\frac{d\bar{l}}{dt} \right)_{f_h} = \frac{r}{h} \left[\frac{r}{p} \lambda \kappa + \zeta \right] \frac{\partial L}{\partial \bar{P}_1} + \frac{r}{hp} \lambda (aP_1 + r \sin L) \\
& \frac{\partial}{\partial \bar{P}_2} \left(\frac{d\bar{a}}{dt} \right)_{f_r} = \frac{2a^2}{h} \left[\left(\frac{p}{r} - 1 \right) \frac{\partial L}{\partial \bar{P}_2} - \frac{aP_2}{p} \kappa + \sin L \right] \\
& \frac{\partial}{\partial \bar{P}_2} \left(\frac{d\bar{a}}{dt} \right)_{f_t} = \frac{2a^2}{h} \left[\kappa \frac{\partial L}{\partial \bar{P}_2} + \frac{aP_2}{r} + \cos L \right] \\
& \frac{\partial}{\partial \bar{P}_2} \left(\frac{d\bar{a}}{dt} \right)_{f_h} = 0 \\
& \frac{\partial}{\partial \bar{P}_2} \left(\frac{d\bar{P}_1}{dt} \right)_{f_r} = \frac{p}{h} \sin L \frac{\partial L}{\partial \bar{P}_2} + \frac{aP_2}{h} \cos L \\
& \frac{\partial}{\partial \bar{P}_2} \left(\frac{d\bar{P}_1}{dt} \right)_{f_t} = \frac{r}{h} \left[-\frac{r}{p} \kappa (P_1 + \sin L) + \left(1 + \frac{p}{r} \right) \cos L \right] \frac{\partial L}{\partial \bar{P}_2} \\
& \quad + \frac{r}{hp} \left\{ - \left[P_1 + \left(1 + \frac{p}{r} \right) \sin L \right] (aP_2 + r \cos L) + p \sin L \cos L \right\} \\
& \frac{\partial}{\partial \bar{P}_2} \left(\frac{d\bar{P}_1}{dt} \right)_{f_h} = \frac{rP_2}{h} \left[\frac{r}{p} \lambda \kappa + \zeta \right] \frac{\partial L}{\partial \bar{P}_2} + \frac{r}{h} \left[\frac{P_2}{p} (aP_2 + r \cos L) - 1 \right] \lambda \\
& \frac{\partial}{\partial \bar{P}_2} \left(\frac{d\bar{P}_2}{dt} \right)_{f_r} = \frac{p}{h} \cos L \frac{\partial L}{\partial \bar{P}_2} - \frac{aP_2}{h} \sin L \\
& \frac{\partial}{\partial \bar{P}_2} \left(\frac{d\bar{P}_2}{dt} \right)_{f_t} = \frac{r}{h} \left[-\frac{r}{p} \kappa (P_2 + \cos L) - \left(1 + \frac{p}{r} \right) \sin L \right] \frac{\partial L}{\partial \bar{P}_2} \\
& \quad + \frac{r}{h} \left\{ -\frac{ra}{p^2} (P_2 + \cos L - P_1 \kappa) \left[P_2 + \left(1 + \frac{p}{r} \right) \cos L \right] + 1 + \cos^2 L \right\} \\
& \frac{\partial}{\partial \bar{P}_2} \left(\frac{d\bar{P}_2}{dt} \right)_{f_h} = -\frac{r^2 P_1}{hp} (Q_1 P_1 + Q_2 P_2 + \zeta) \frac{\partial L}{\partial \bar{P}_2} - \lambda \frac{ar^2 P_1}{hp^2} (P_2 + \cos L - P_1 \kappa) \\
& \frac{\partial}{\partial \bar{P}_2} \left(\frac{d\bar{Q}_1}{dt} \right)_{f_r} = 0 \\
& \frac{\partial}{\partial \bar{P}_2} \left(\frac{d\bar{Q}_1}{dt} \right)_{f_t} = 0 \\
& \frac{\partial}{\partial \bar{P}_2} \left(\frac{d\bar{Q}_1}{dt} \right)_{f_h} = \frac{r^2}{2hp} \xi (P_2 + \cos L) \frac{\partial L}{\partial \bar{P}_2} - \frac{r\xi}{2hp} (aP_2 + r \cos L) \sin L \\
& \frac{\partial}{\partial \bar{P}_2} \left(\frac{d\bar{Q}_2}{dt} \right)_{f_r} = 0
\end{aligned}$$

$$\begin{aligned}
\frac{\partial}{\partial \bar{P}_2} \left(\frac{d\bar{Q}_1}{dt} \right)_{f_t} &= 0 \\
\frac{\partial}{\partial \bar{P}_2} \left(\frac{d\bar{Q}_1}{dt} \right)_{f_h} &= -\frac{r^2}{2hp} \xi (P_1 + \sin L) \frac{\partial L}{\partial \bar{P}_2} \\
&\quad + \frac{ar^2}{2hp^2} \xi (-P_2 - \cos L + P_1 \kappa) \cos L \\
\frac{\partial}{\partial \bar{P}_2} \left(\frac{d\bar{l}}{dt} \right)_{f_r} &= \frac{1}{h} \left(\frac{2br^2}{ap} - \frac{ap}{a+b} \right) \kappa \frac{\partial L}{\partial \bar{P}_2} \\
&\quad + \frac{r}{hp} \left[\frac{ap}{(a+b)r} \left(\frac{p}{r} - 1 \right) + \frac{2b}{a} \right] (aP_2 + r \cos L) \\
&\quad - \frac{ra}{h} \left[\frac{a^2 p P_2}{(a+b)^2 br} \left(\frac{p}{r} - 1 \right) + \frac{\cos L}{a+b} \left(\frac{2p}{r} - 1 \right) - \frac{2P_2}{b} \right] \\
\frac{\partial}{\partial \bar{P}_2} \left(\frac{d\bar{l}}{dt} \right)_{f_t} &= \frac{ra}{h(a+b)} \left[\frac{p^2}{r^2} + \frac{r}{p} \kappa^2 - 1 \right] \frac{\partial L}{\partial \bar{P}_2} \\
&\quad + \frac{ra}{h(a+b)} \left[\kappa \left(\frac{aP_2 + r \cos L}{p} \left(1 + \frac{p}{r} \right) - \frac{a^2 P_2}{(a+b)b} \left(1 + \frac{p}{r} \right) - \cos L \right) \right] \\
&\quad + \frac{ra}{h(a+b)} \left(1 + \frac{p}{r} \right) \sin L \\
\frac{\partial}{\partial \bar{P}_2} \left(\frac{d\bar{l}}{dt} \right)_{f_h} &= \frac{r}{h} \left[\frac{r}{p} \lambda \kappa + \zeta \right] \frac{\partial L}{\partial \bar{P}_2} + \frac{r}{hp} \lambda (aP_2 + r \cos L) \\
\frac{\partial}{\partial \bar{Q}_1} \left(\frac{d\bar{a}}{dt} \right)_{f_r} &= 0 \\
\frac{\partial}{\partial \bar{Q}_1} \left(\frac{d\bar{a}}{dt} \right)_{f_t} &= 0 \\
\frac{\partial}{\partial \bar{Q}_1} \left(\frac{d\bar{a}}{dt} \right)_{f_h} &= 0 \\
\frac{\partial}{\partial \bar{Q}_1} \left(\frac{d\bar{P}_1}{dt} \right)_{f_r} &= 0 \\
\frac{\partial}{\partial \bar{Q}_1} \left(\frac{d\bar{P}_1}{dt} \right)_{f_t} &= 0 \\
\frac{\partial}{\partial \bar{Q}_1} \left(\frac{d\bar{P}_1}{dt} \right)_{f_h} &= -\frac{rP_2}{h} \cos L \\
\frac{\partial}{\partial \bar{Q}_1} \left(\frac{d\bar{P}_2}{dt} \right)_{f_r} &= 0 \\
\frac{\partial}{\partial \bar{Q}_1} \left(\frac{d\bar{P}_2}{dt} \right)_{f_t} &= 0 \\
\frac{\partial}{\partial \bar{Q}_1} \left(\frac{d\bar{P}_2}{dt} \right)_{f_h} &= \frac{rP_1}{h} \cos L \\
\frac{\partial}{\partial \bar{Q}_1} \left(\frac{d\bar{Q}_1}{dt} \right)_{f_r} &= 0 \\
\frac{\partial}{\partial \bar{Q}_1} \left(\frac{d\bar{Q}_1}{dt} \right)_{f_t} &= 0 \\
\frac{\partial}{\partial \bar{Q}_1} \left(\frac{d\bar{Q}_1}{dt} \right)_{f_h} &= \frac{rQ_1}{h} \sin L \\
\frac{\partial}{\partial \bar{Q}_1} \left(\frac{d\bar{Q}_2}{dt} \right)_{f_r} &= 0 \\
\frac{\partial}{\partial \bar{Q}_1} \left(\frac{d\bar{Q}_2}{dt} \right)_{f_t} &= 0
\end{aligned}$$

$$\frac{\partial}{\partial \bar{Q}_1} \left(\frac{d\bar{Q}_2}{dt} \right)_{f_h} = \frac{rQ_1}{h} \cos L$$

$$\frac{\partial}{\partial \bar{Q}_1} \left(\frac{d\bar{l}}{dt} \right)_{f_r} = 0$$

$$\frac{\partial}{\partial \bar{Q}_1} \left(\frac{d\bar{l}}{dt} \right)_{f_t} = 0$$

$$\frac{\partial}{\partial \bar{Q}_1} \left(\frac{d\bar{l}}{dt} \right)_{f_r} = -\frac{r}{h} \cos L$$

$$\frac{\partial}{\partial \bar{Q}_2} \left(\frac{d\bar{a}}{dt} \right)_{f_r} = 0$$

$$\frac{\partial}{\partial \bar{Q}_2} \left(\frac{d\bar{a}}{dt} \right)_{f_t} = 0$$

$$\frac{\partial}{\partial \bar{Q}_2} \left(\frac{d\bar{a}}{dt} \right)_{f_h} = 0$$

$$\frac{\partial}{\partial \bar{Q}_2} \left(\frac{d\bar{P}_1}{dt} \right)_{f_r} = 0$$

$$\frac{\partial}{\partial \bar{Q}_2} \left(\frac{d\bar{P}_1}{dt} \right)_{f_t} = 0$$

$$\frac{\partial}{\partial \bar{Q}_2} \left(\frac{d\bar{P}_1}{dt} \right)_{f_h} = \frac{rP_2}{h} \sin L$$

$$\frac{\partial}{\partial \bar{Q}_2} \left(\frac{d\bar{P}_2}{dt} \right)_{f_r} = 0$$

$$\frac{\partial}{\partial \bar{Q}_2} \left(\frac{d\bar{P}_2}{dt} \right)_{f_t} = 0$$

$$\frac{\partial}{\partial \bar{Q}_2} \left(\frac{d\bar{P}_2}{dt} \right)_{f_h} = -\frac{rP_1}{h} \sin L$$

$$\frac{\partial}{\partial \bar{Q}_2} \left(\frac{d\bar{Q}_1}{dt} \right)_{f_r} = 0$$

$$\frac{\partial}{\partial \bar{Q}_2} \left(\frac{d\bar{Q}_1}{dt} \right)_{f_t} = 0$$

$$\frac{\partial}{\partial \bar{Q}_2} \left(\frac{d\bar{Q}_1}{dt} \right)_{f_h} = \frac{rQ_2}{h} \sin L$$

$$\frac{\partial}{\partial \bar{Q}_2} \left(\frac{d\bar{Q}_2}{dt} \right)_{f_r} = 0$$

$$\frac{\partial}{\partial \bar{Q}_2} \left(\frac{d\bar{Q}_2}{dt} \right)_{f_t} = 0$$

$$\frac{\partial}{\partial \bar{Q}_2} \left(\frac{d\bar{Q}_2}{dt} \right)_{f_h} = \frac{rQ_2}{h} \cos L$$

$$\frac{\partial}{\partial \bar{Q}_2} \left(\frac{d\bar{l}}{dt} \right)_{f_r} = 0$$

$$\frac{\partial}{\partial \bar{Q}_2} \left(\frac{d\bar{l}}{dt} \right)_{f_t} = 0$$

$$\frac{\partial}{\partial \bar{Q}_2} \left(\frac{d\bar{l}}{dt} \right)_{f_r} = \frac{r}{h} \sin L$$

$$\frac{\partial}{\partial \bar{l}} \left(\frac{d\bar{a}}{dt} \right)_{f_r} = \frac{2a^2}{h} \left(\frac{p}{r} - 1 \right) \frac{\partial L}{\partial \bar{l}}$$

$$\begin{aligned}
\frac{\partial}{\partial \bar{l}} \left(\frac{d\bar{a}}{dt} \right)_{fr} &= \frac{2a^2}{h} \kappa \frac{\partial L}{\partial \bar{l}} \\
\frac{\partial}{\partial \bar{l}} \left(\frac{d\bar{a}}{dt} \right)_{fr} &= 0 \\
\frac{\partial}{\partial \bar{l}} \left(\frac{d\bar{P}_1}{dt} \right)_{fr} &= \frac{p}{h} \sin L \frac{\partial L}{\partial \bar{l}} \\
\frac{\partial}{\partial \bar{l}} \left(\frac{d\bar{P}_1}{dt} \right)_{ft} &= \frac{r}{h} \left[-\frac{r}{p} \kappa (P_1 + \sin L) + \left(1 + \frac{p}{r} \right) \cos L \right] \frac{\partial L}{\partial \bar{l}} \\
\frac{\partial}{\partial \bar{l}} \left(\frac{d\bar{P}_1}{dt} \right)_{fh} &= \frac{r}{h} \left\{ \frac{rP_2}{p} \lambda \kappa + P_2 \zeta \right\} \frac{\partial L}{\partial \bar{l}} \\
\frac{\partial}{\partial \bar{l}} \left(\frac{d\bar{P}_2}{dt} \right)_{fr} &= \frac{p}{h} \cos L \frac{\partial L}{\partial \bar{l}} \\
\frac{\partial}{\partial \bar{l}} \left(\frac{d\bar{P}_2}{dt} \right)_{ft} &= -\frac{r}{h} \left[\frac{r}{p} (P_2 + \cos L) \kappa + \left(1 + \frac{p}{r} \right) \sin L \right] \frac{\partial L}{\partial \bar{l}} \\
\frac{\partial}{\partial \bar{l}} \left(\frac{d\bar{P}_2}{dt} \right)_{fh} &= -\frac{rP_1}{h} \left[\frac{r}{p} \lambda \kappa + \zeta \right] \frac{\partial L}{\partial \bar{l}} \\
\frac{\partial}{\partial \bar{l}} \left(\frac{d\bar{Q}_1}{dt} \right)_{fr} &= 0 \\
\frac{\partial}{\partial \bar{l}} \left(\frac{d\bar{Q}_1}{dt} \right)_{ft} &= 0 \\
\frac{\partial}{\partial \bar{l}} \left(\frac{d\bar{Q}_1}{dt} \right)_{fh} &= \frac{r}{2h} \xi \left[-\frac{r}{p} \kappa \sin L + \cos L \right] \frac{\partial L}{\partial \bar{l}} \\
\frac{\partial}{\partial \bar{l}} \left(\frac{d\bar{Q}_2}{dt} \right)_{fr} &= 0 \\
\frac{\partial}{\partial \bar{l}} \left(\frac{d\bar{Q}_2}{dt} \right)_{ft} &= 0 \\
\frac{\partial}{\partial \bar{l}} \left(\frac{d\bar{Q}_2}{dt} \right)_{fh} &= -\frac{r}{2h} \xi \left(\frac{r}{p} \kappa \cos L + \sin L \right) \frac{\partial L}{\partial \bar{l}} \\
\frac{\partial}{\partial \bar{l}} \left(\frac{d\bar{l}}{dt} \right)_{fr} &= \frac{r^2}{hp} \left[\frac{ap}{(a+b)r} \left(\frac{p}{r} - 1 \right) - \frac{a}{a+b} \left(\frac{2p}{r} - 1 \right) + \frac{2b}{a} \right] \kappa \frac{\partial L}{\partial \bar{l}} \\
\frac{\partial}{\partial \bar{l}} \left(\frac{d\bar{l}}{dt} \right)_{ft} &= \frac{ra}{h(a+b)} \left[\frac{p^2}{r^2} + \frac{r}{p} \kappa^2 - 1 \right] \frac{\partial L}{\partial \bar{l}} \\
\frac{\partial}{\partial \bar{l}} \left(\frac{d\bar{l}}{dt} \right)_{fh} &= \frac{r}{h} \left[\frac{r}{p} \lambda \kappa + \zeta \right] \frac{\partial L}{\partial \bar{l}}
\end{aligned}$$

Appendix C

QARMAN

This appendix provides additional results on the validation of the overall methodology proposed in this thesis. The inputs of Chapter 6 are used. The uncertainties in the initial absolute conditions of the chief and in the aerodynamic force are modeled according to the probabilistic characterization of Chapter 2. Ten percent uniformly distributed uncertainty in the deputy's mass is also considered.

The initial relative states are distributed over a large range of initial conditions in order to provide a “broadband” validation of the algorithm. Specifically, the initial position in the curvilinear states is uniformly distributed in:

$$\begin{aligned}\tilde{x} &\in [-0.5, 1.5] \text{ km} \\ \tilde{y} &\in [-200, 200] \text{ km}\end{aligned}\tag{C.1}$$

In addition, the relative orbital inclination is distributed in $[0, 0.1]$ deg. Out of these distributions, only the planned maneuvers that are such that $t_f \leq 15$ days are executed.

The results obtained with the controller proposed in Chapter 6 are compared to those of an earlier version of the controller proposed in Chapter 5 [Dell'Elce and Kerschen, 2014b], i.e., the control plant is based on the Schweighart-Sedwick equations [Schweighart and Sedwick, 2002].

Figure C.1 compares the CDF of the root-mean-squared distance between the planned and the executed trajectories. The satisfaction of the rendez-vous conditions is portrayed in Figure C.2. In both cases, the new controller outperforms the old controller. In addition, we note that the old algorithm exhibited an important correlation with the chief's orbital eccentricity, i.e., 31% and 29% for the root-mean squared error and rendez-vous conditions, respectively. This correlation is essentially canceled when ROE are used.

Figure C.3 depicts how rendez-vous conditions improve if additional maneuvering time is added. With the old algorithm, a relevant improvement is observed in the first hours. This improvement stabilizes as time passes by. The explanation for this result is that the satellites have different geometries and masses. Recalling that the aerodynamic coefficients are computed on the actual geometry at every time step

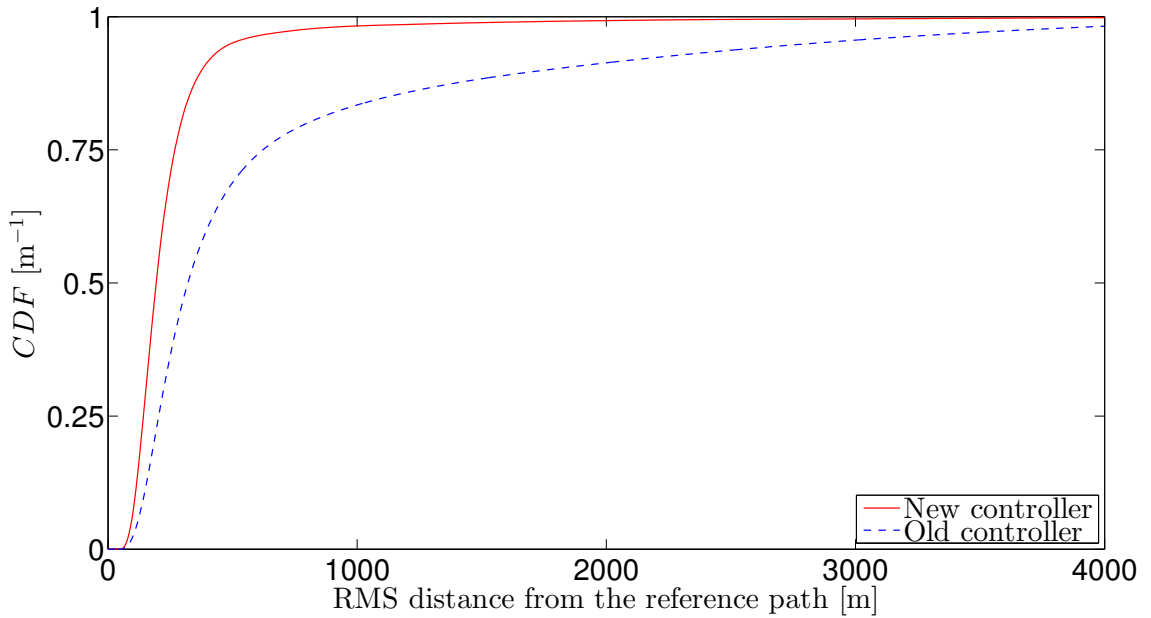


Figure C.1: CDF of the root-mean-squared distance between the reference and the executed trajectories.

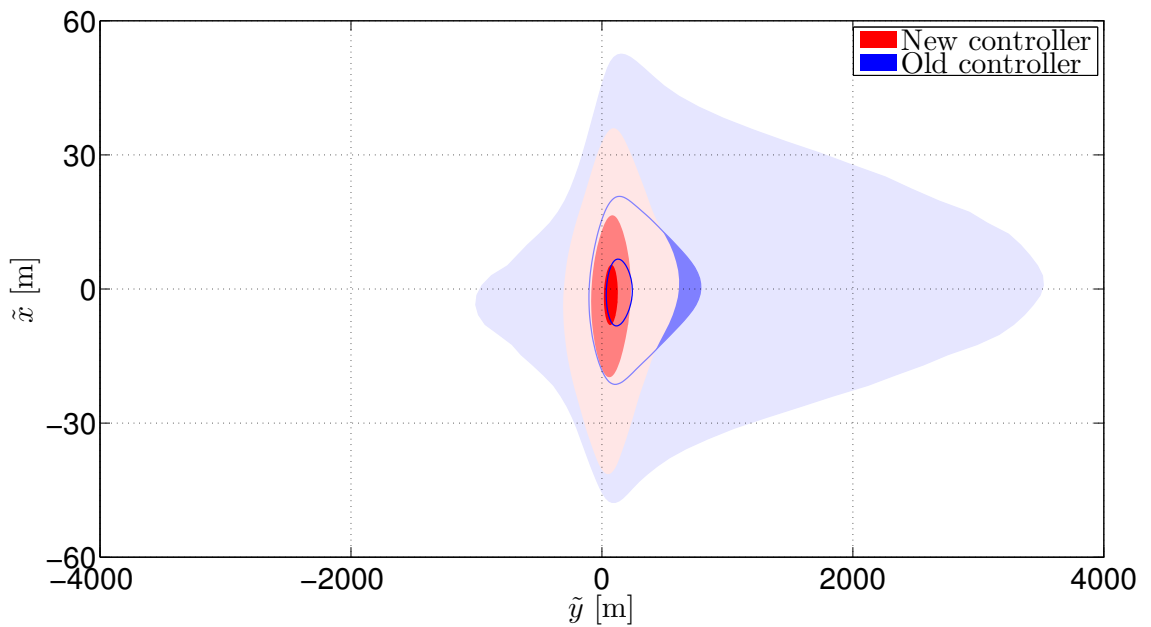
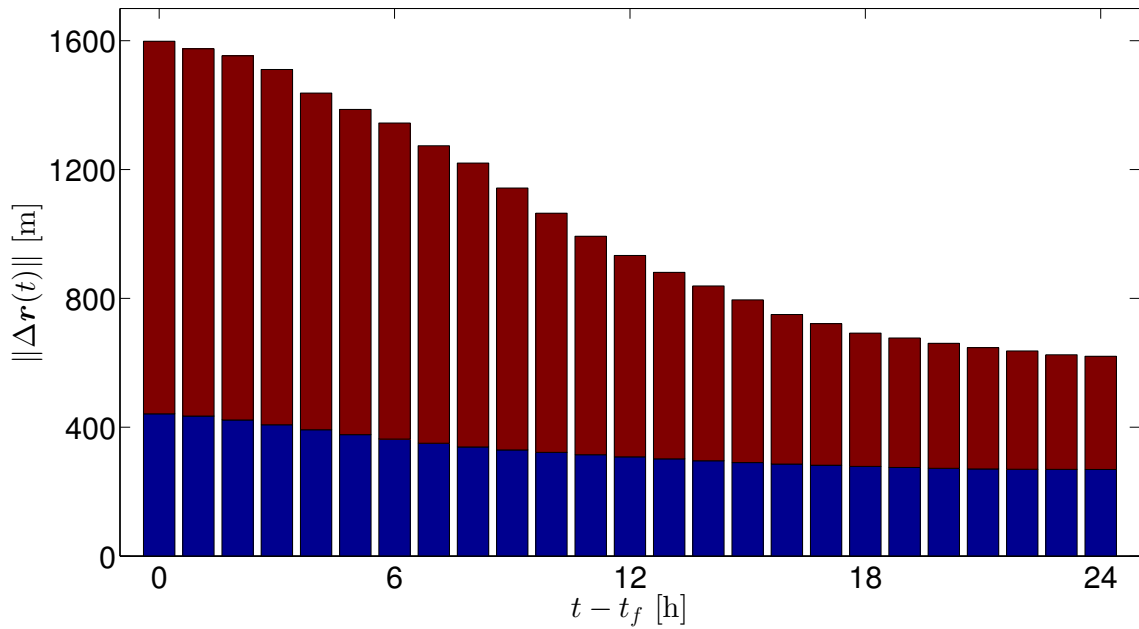
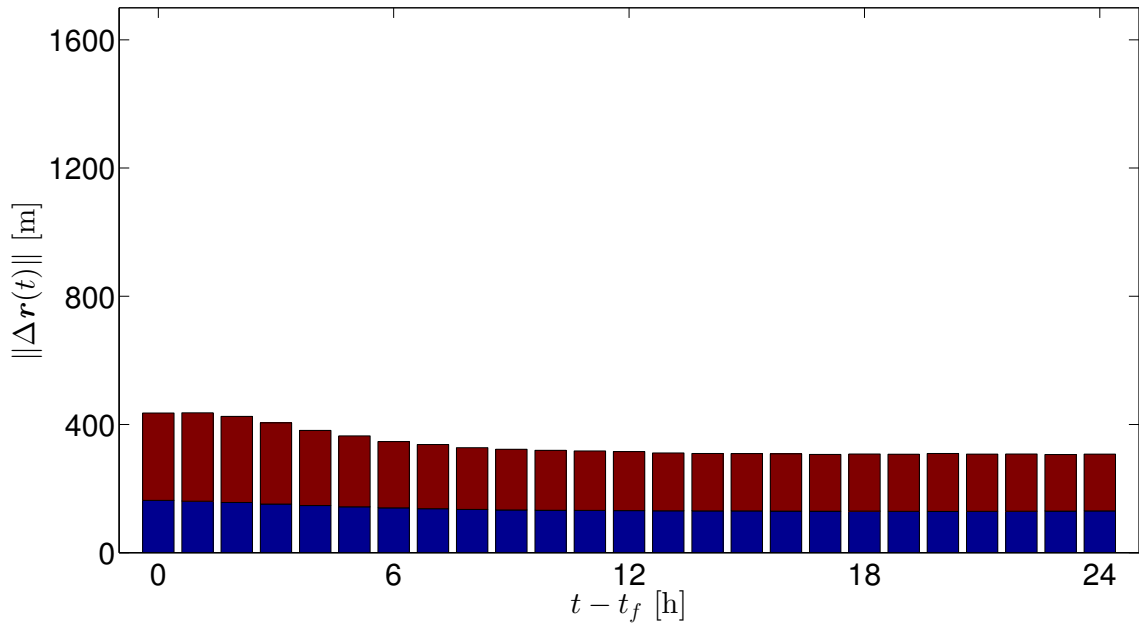


Figure C.2: Satisfaction of the rendez-vous conditions. From the lighter to the darker, the shaded regions indicate 90%, 50%, and 10% confidence regions.



(a) Old controller.



(b) New controller.

Figure C.3: Median (blue) and 90% confidence bounds (red) of the satisfaction of the rendez-vous conditions when additional time is added after the planned maneuvering time.

of the high-fidelity simulations and that drag is not proportional to the exposed surface, it follows that the real zero-differential drag configuration is unknown. The same result is observed for the new controller. However, in this case the magnitude of the error is smaller. The improvement of the enforcement of the rendez-vous conditions is less impressive than in the old results. This means that the trajectory is tracked in a more efficient way, thanks to the robust maneuver planning and to the recursive drag estimation.

Bibliography

- (iad, 2010). UN COPUOS space debris mitigation guidelines. In *Space Safety Regulations and Standards*, pages 475–479. Elsevier BV.
- (pos, 2006). Position paper on space debris mitigation. ESA SP-1301.
- Abramowitz, M. and Stegun, I. A. (1964). *Handbook of Mathematical Functions with Formulas, Graphs, and Mathematical Tables*. Dover, New York.
- Alfriend, K., Vadali, S. R., Gurfil, P., How, J., and Breger, L. (2009). *Spacecraft formation flying: Dynamics, control and navigation*, volume 2. Butterworth-Heinemann.
- Antritter, F. and Lévine, J. (2010). Flatness characterization: Two approaches. *Advances in the Theory of Control, Signals and Systems with Physical Modeling*, page 127–139.
- Ashrafi, S., Roszman, L., and Cooley, J. (1993). Nonlinear techniques for forecasting solar activity directly from its time series. In *Proceedings of the AAS/AIAA Space Flight Mechanics Conference*, pages 319–335.
- Battin, R. H. (1999). *An Introduction to the Mathematics and Methods of Astrodynamics*. AIAA, Reston, VA.
- Ben-Yaacov, O. and Gurfil, P. (2013). Long-term cluster flight of multiple satellites using differential drag. *Journal of Guidance, Control, and Dynamics*, 36(6):1731–1740.
- Ben-Yaacov, O. and Gurfil, P. (2014). Stability and performance of orbital elements feedback for cluster keeping using differential drag. *The Journal of the Astronautical Sciences*, pages 1–29.
- Betts, J. T. (1998). Survey of numerical methods for trajectory optimization. *Journal of Guidance, Control, and Dynamics*, 21(2):193–207.
- Betts, J. T. (2010). *Practical Methods for Optimal Control and Estimation Using Nonlinear Programming*. Society for Industrial & Applied Mathematics (SIAM).

- Bevilacqua, R., Hall, J. S., and Romano, M. (2009). Multiple spacecraft rendezvous maneuvers by differential drag and low thrust engines. *Celestial Mechanics and Dynamical Astronomy*, 106(1):69–88.
- Bevilacqua, R. and Romano, M. (2008). Rendezvous maneuvers of multiple space-craft using differential drag under j_2 perturbation. *Journal of Guidance, Control, and Dynamics*, 31(6):1595–1607.
- Blackmore, L. (2008). Robust path planning and feedback design under stochastic uncertainty. *AIAA Guidance, Navigation and Control Conference and Exhibit*.
- Blackmore, L. and Ono, M. (2009). Convex chance constrained predictive control without sampling. *AIAA Guidance, Navigation, and Control Conference*.
- Blackmore, L., Ono, M., and Williams, B. C. (2011). Chance-constrained optimal path planning with obstacles. *IEEE Trans. Robot.*, 27(6):1080–1094.
- Bombardelli, C., Zanotto, D., and Lorenzini, E. (2013). Deorbiting performance of bare electrodynamic tethers in inclined orbits. *Journal of Guidance, Control, and Dynamics*, 36(5):1550–1556.
- Bowman, B. R. and Hrncir, S. (2008). Drag coefficient variability at 100-300 km from the orbit decay analyses of rocket bodies (aas 07-262). *Advances in the Astronautical Sciences*, 129(1):207.
- Bowman, B. R. and Moe, K. (2005). Drag coefficient variability at 175–500 km from the orbit decay analyses of spheres. In *Advances in the Astronautical Sciences*, volume 123, pages 117–136.
- Broucke, R. A. and Cefola, P. J. (1972). On the equinoctial orbit elements. *Celestial Mechanics*, 5(3):303–310.
- Brouwer, D. (1959). Solution of the problem of artificial satellite theory without drag. *The Astronomical Journal*, 64:378.
- Brouwer, D. and Hori, G.-I. (1961). Theoretical evaluation of atmospheric drag effects in the motion of an artificial satellite. *The Astronomical Journal*, 66:193.
- Cain, B. J. (1962). Determination of mean elements for Brouwer's satellite theory. *Astronomical Journal*, 67:391.
- Calafiore, G. and Campi, M. (2004). Uncertain convex programs: randomized solutions and confidence levels. *Math. Program.*, 102(1):25–46.
- Calafiore, G. and Campi, M. (2006). The scenario approach to robust control design. *IEEE Trans. Automat. Contr.*, 51(5):742–753.

- Calafiore, G. C. (2009). On the expected probability of constraint violation in sampled convex programs. *Journal of Optimization Theory and Applications*, 143(2):405–412.
- Campi, M. C., Garatti, S., and Prandini, M. (2009). The scenario approach for systems and control design. *Annual Reviews in Control*, 33(2):149–157.
- Casella, R. C. and Casella, G. (2013). *Monte Carlo statistical methods*. Springer Science & Business Media.
- Cerone, V., Piga, D., and Regruto, D. (2012). Polytopic outer approximations of semialgebraic sets. *2012 IEEE 51st IEEE Conference on Decision and Control (CDC)*.
- Chao, C. and Platt, M. (1991). An accurate and efficient tool for orbit lifetime predictions. In *Spaceflight Mechanics 1991*, volume 1, pages 11–24.
- Clohessy, W. and Wiltshire, R. (1960). Terminal guidance system for satellite rendezvous. *Journal of the Astronautical Sciences*, 27(9):653–678.
- Condurache, D. and Martinusi, V. (2007a). Kepler’s problem in rotating reference frames part i: Prime integrals, vectorial regularization. *Journal of Guidance, Control, and Dynamics*, 30(1):192–200.
- Condurache, D. and Martinusi, V. (2007b). Kepler’s problem in rotating reference frames part ii: Relative orbital motion. *Journal of Guidance, Control, and Dynamics*, 30(1):201–213.
- Condurache, D. and Martinusi, V. (2007c). Relative spacecraft motion in a central force field. *Journal of Guidance, Control, and Dynamics*, 30(3):873–876.
- Condurache, D. and Martinusi, V. (2009). Analytic solution to the relative orbital motion around an oblate planet. In *AIAA Guidance, Navigation and Control Conference and Exhibit*, Chicago, IL.
- Condurache, D. and Martinusi, V. (2013). Analytical orbit propagator based on vectorial orbital elements. In *AIAA Guidance, Navigation and Control Conference*, number AIAA-2013-5188, Boston, MA.
- Conway, B., editor (2010). *Spacecraft Trajectory Optimization*. Cambridge University Press (CUP).
- Cook, G. (1965). Satellite drag coefficients. *Planetary and Space Science*, 13(10):929–946.
- Daum, F. (2005). Nonlinear filters: beyond the kalman filter. *IEEE Aerospace and Electronic Systems Magazine*, 20(8):57–69.

- Dell'Elce, L., Arnst, M., and Kerschen, G. (2014). Probabilistic assessment of the lifetime of low-earth-orbit spacecraft: Uncertainty characterization. *Journal of Guidance, Control, and Dynamics*, page 1–13.
- Dell'Elce, L. and Kerschen, G. (2013). Comparison between analytical and optimal control techniques in the differential drag based rendez-vous. In *Proceedings of the 5th International Conference on Spacecraft Formation Flying Missions & Technologies*, Munich, Germany.
- Dell'Elce, L. and Kerschen, G. (2014a). Probabilistic assessment of lifetime of low-earth-orbit spacecraft: Uncertainty propagation and sensitivity analysis. *Journal of Guidance, Control, and Dynamics*, pages 1–14.
- Dell'Elce, L. and Kerschen, G. (2014b). Validation of differential drag propellantless maneuvers using 6 dof simulations and stochastic dynamics. In *9th International ESA Conference on Guidance, Navigation & Control Systems*.
- Dell'Elce, L. and Kerschen, G. (2015). Optimal propellantless rendez-vous using differential drag. *Acta Astronautica*, 109:112–123.
- Deprit, A. (1969). Canonical Transformations Depending on A Small Parameter. *Celestial Mechanics*, 1:12–30.
- Deprit, A. (1981). The Elimination of The Parallax in Satellite Theory. *Celestial Mechanics*, 24:111–153.
- Doornbos, E. (2012). *Thermospheric density and wind determination from satellite dynamics*. Springer Science + Business Media.
- Doornbos, E. and Klinkrad, H. (2006). Modelling of space weather effects on satellite drag. *Advances in Space Research*, 37(6):1229 – 1239. Space weather prediction: Applications and validation.
- Doornbos, E., Klinkrad, H., and Visser, P. (2005). Atmospheric density calibration using satellite drag observations. *Advances in Space Research*, 36(3):515 – 521. Satellite Dynamics in the Era of Interdisciplinary Space Geodesy.
- Doucet, A., Freitas, N., and Gordon, N., editors (2001). *Sequential Monte Carlo Methods in Practice*. Springer Science + Business Media.
- Doucet, A., Godsill, S., and Andrieu, C. (2000). On sequential monte carlo sampling methods for bayesian filtering. *Statistics and computing*, 10(3):197–208.
- Emmert, J. T., Picone, J. M., and Meier, R. R. (2008). Thermospheric global average density trends, 1967–2007, derived from orbits of 5000 near-earth objects. *Geophysical Research Letters*, 35(5).

- Fahroo, F. and Ross, I. M. (2002). Direct trajectory optimization by a chebyshev pseudospectral method. *Journal of Guidance, Control, and Dynamics*, 25(1):160–166.
- Fahroo, F. and Ross, I. M. (2008). Advances in pseudospectral methods for optimal control. In *AIAA Guidance, Navigation and Control Conference and Exhibit*. American Institute of Aeronautics and Astronautics (AIAA).
- Faiz, N., Agrawal, S. K., and Murray, R. M. (2001). Trajectory planning of differentially flat systems with dynamics and inequalities. *Journal of Guidance, Control, and Dynamics*, 24(2):219–227.
- Faulwasser, T., Hagenmeyer, V., and Findeisen, R. (2014). Constrained reachability and trajectory generation for flat systems. *Automatica*, 50(4):1151–1159.
- Fliess, M., Lévine, J., Martin, P., and Rouchon, P. (1995). Flatness and defect of non-linear systems: introductory theory and examples. *International Journal of Control*, 61(6):1327–1361.
- Flohrer, T., Krag, H., and Klinkrad, H. (2008). Assessment and categorization of the orbit errors for the us ssn catalogue. In *Proceedings of the Advanced Maui Optical and Space Surveillance Technologies Conference*, Maui, US.
- Formentin, S., Dabbene, F., Tempo, R., Zaccarian, L., and Savaresi, S. M. (2014). Scenario optimization with certificates and applications to anti-windup design. *53rd IEEE Conference on Decision and Control*.
- Franco, J. M. (1991). An analytic solution for Deprit's radial intermediary with drag in the equatorial case. *Bulletin of the Astronomical Institutes of Czechoslovakia*, 42:219–224.
- Fraysse, H., Morand, V., Le Fevre, C., Deleflie, F., Wailliez, S., Lamy, A., Martin, T., and Perot, E. (2012). Long term orbit propagation techniques developed in the frame of the french space act. *Journal of Aerospace Engineering*, 4(4):2.
- Fujimoto, K., Scheeres, D. J., and Alfriend, K. T. (2012). Analytical nonlinear propagation of uncertainty in the two-body problem. *Journal of Guidance, Control, and Dynamics*, 35(2):497–509.
- Fuller, J. D. and Tolson, R. H. (2009). Improved method for the estimation of space-craft free-molecular aerodynamic properties. *Journal of Spacecraft and Rockets*, 46(5):938–948.
- Garfinkel, B. (1959). The orbit of a satellite of an oblate planet. *Astronomical Journal*, 64:353.
- Garg, D., Patterson, M., Hager, W. W., Rao, A. V., Benson, D. A., and Huntington, G. T. (2010). A unified framework for the numerical solution of optimal control problems using pseudospectral methods. *Automatica*, 46(11):1843–1851.

- Ghanem, R. G. and Spanos, P. D. (1991). *Stochastic Finite Elements: A Spectral Approach*. Springer Science + Business Media.
- Giza, D., Singla, P., and Jah, M. (2009). An approach for nonlinear uncertainty propagation: Application to orbital mechanics. In *AIAA Guidance, Navigation, and Control Conference*. American Institute of Aeronautics and Astronautics (AIAA).
- Gotlib, V. M., Evlanov, E. N., Zubkov, B. V., Linkin, V. M., Manukin, A. B., Podkolzin, S. N., and Rebrov, V. I. (2004). High-sensitivity quartz accelerometer for measurements of small accelerations of spacecraft. *Cosmic Research*, 42(1):54–59.
- Graettinger, T. J. and Krogh, B. H. (1992). On the computation of reference signal constraints for guaranteed tracking performance. *Automatica*, 28(6):1125–1141.
- Grant, M. and Boyd, S. (2008). Graph implementations for nonsmooth convex programs. In Blondel, V., Boyd, S., and Kimura, H., editors, *Recent Advances in Learning and Control*, Lecture Notes in Control and Information Sciences, pages 95–110. Springer-Verlag Limited.
- Grant, M. and Boyd, S. (2014). CVX: Matlab software for disciplined convex programming, version 2.1. <http://cvxr.com/cvx>.
- Gurfil, P., Herscovitz, J., and Pariente, M. (2012). The samson project—cluster flight and geolocation with three autonomous nano-satellites.
- Gurfil, P. and Kasdin, J. N. (2004). Nonlinear modeling of spacecraft relative motion in the configuration space. *Journal of Guidance, Control, and Dynamics*, 27(1):154–157.
- Häusler, K., Lühr, H., Rentz, S., and Köhler, W. (2007). A statistical analysis of longitudinal dependences of upper thermospheric zonal winds at dip equator latitudes derived from champ. *Journal of Atmospheric and Solar-Terrestrial Physics*, 69(12):1419–1430.
- Hedin, A. E. (1991). Extension of the msis thermosphere model into the middle and lower atmosphere. *Journal of Geophysical Research*, 96(A2):1159.
- Hedin, A. E., Spencer, N. W., and Killeen, T. L. (1988). Empirical global model of upper thermosphere winds based on atmosphere and dynamics explorer satellite data. *Journal of Geophysical Research*, 93(A9):9959.
- Heidt, H., Puig-Suari, J., Moore, A., Nakasuka, S., and Twiggs, R. (2000). Cubesat: A new generation of picosatellite for education and industry low-cost space experimentation.
- Henrion, D. and Lasserre, J.-B. (2004). LMIs for constrained polynomial interpolation with application in trajectory planning. *2004 IEEE International Conference on Robotics and Automation (IEEE Cat. No.04CH37508)*.

- Henrion, D. and Louembet, C. (2012). Convex inner approximations of nonconvex semialgebraic sets applied to fixed-order controller design. *International Journal of Control*, 85(8):1083–1092.
- Hestenes, D. (1999). *New Foundations for Classical Mechanics*. Kluwer.
- Hettich, R. and Kortanek, K. O. (1993). Semi-infinite programming: Theory, methods, and applications. *SIAM Review*, 35(3):380–429.
- Hughes, P. C. (2012). *Spacecraft attitude dynamics*. Courier Corporation.
- Hwang, S. S. and Speyer, J. L. (2011). Particle filters with adaptive resampling technique applied to relative positioning using GPS carrier-phase measurements. *IEEE Transactions on Control Systems Technology*, 19(6):1384–1396.
- Jacchia, L. G. (1965). Static diffusion models of the upper atmosphere with empirical temperature profiles. *Smithsonian Contributions to Astrophysics*, 8(9):213–257.
- Jacchia, L. G. (1971). Revised static models of the thermosphere and exosphere with empirical temperature profiles. Technical Report Special Rept. 332, 1971, Smithsonian Astrophysical Observatory.
- Johnson, L., Whorton, M., Heaton, A., Pinson, R., Laue, G., and Adams, C. (2011). Nanosail-d: A solar sail demonstration mission. *Acta Astronautica*, 68(5–6):571–575.
- Jones, B. A., Doostan, A., and Born, G. (2012). Conjunction assessment using polynomial chaos expansions. In *Proceedings of the 23rd International Symposium and Space Flight Dynamics*. Jet Propulsion Laboratory Pasadena.
- Jones, B. A., Doostan, A., and Born, G. H. (2013). Nonlinear propagation of orbit uncertainty using non-intrusive polynomial chaos. *Journal of Guidance, Control, and Dynamics*, 36(2):430–444.
- Junkins, J. L., Akella, M. R., and Alfrined, K. T. (1996). Non-gaussian error propagation in orbital mechanics. *Guidance and control 1996*, pages 283–298.
- Kahr, E., Montenbruck, O., and O’Keefe, K. P. G. (2013). Estimation and analysis of two-line elements for small satellites. *Journal of Spacecraft and Rockets*, 50(2):433–439.
- Kewlani, G., Ishigami, G., and Iagnemma, K. (2009). Stochastic mobility-based path planning in uncertain environments. *2009 IEEE/RSJ International Conference on Intelligent Robots and Systems*.
- Killeen, T., Roble, R., and Spencer, N. (1987). A computer model of global thermospheric winds and temperatures. *Advances in Space Research*, 7(10):207–215.

- Kim, Y. R., Park, S.-Y., Park, C., Park, E.-S., and Lim, H.-C. (2012). Precise orbit determination with satellite laser ranging observations using a batch filter based on particle filtering. In *AIAA/AAS Astrodynamics Specialist Conference*. American Institute of Aeronautics and Astronautics (AIAA).
- King, L. B., Parker, G. G., Deshmukh, S., and Chong, J.-H. (2002). Spacecraft formation-flying using inter-vehicle coulomb forces. *NASA/NIAC, Technical Report*.
- King-Hele, D. (1964). *Theory of Satellite Orbits in an Atmosphere*. Butterworths.
- Klinkrad, H. (2006). *Space Debris – Models and Risk Analysis*. Springer Verlag.
- Kothari, M. and Postlethwaite, I. (2012). A probabilistically robust path planning algorithm for UAVs using rapidly-exploring random trees. *J Intell Robot Syst*, 71(2):231–253.
- Kozai, Y. (1959). The Motion of a Close Earth Satellite. *Astronomical Journal*, 64:367–377.
- Kumar, B. S. and Ng, A. (2008). A bang-bang control approach to maneuver space-craft in a formation with differential drag. In *AIAA Guidance, Navigation and Control Conference and Exhibit*. American Institute of Aeronautics and Astronautics (AIAA).
- Kumar, B. S. and Ng, A. (2009). Time-optimal low-thrust formation maneuvering using a hybrid linear/nonlinear controller. *Journal of Guidance, Control, and Dynamics*, 32(1):343–347.
- Ladner, J. E. and Ragsdale, G. (1995). Earth orbital satellite lifetime. *NASA technical note NAKT Number D-1995*.
- Lambert, C., Kumar, B., Hamel, J.-F., and Ng, A. (2012). Implementation and performance of formation flying using differential drag. *Acta Astronautica*, 71:68–82.
- Lamy, A., Morand, V., Le Fèvre, C., and Fraysse, H. (2012). Resonance effects on lifetime of low earth orbit satellites. In *Proceedings of the 23rd International Symposium on Space Flight Dynamics*. Jet Propulsion Laboratory Pasadena.
- Lara, M. and Gurfil, P. (2012). Integrable approximation of j_2 -perturbed relative orbits. *Celestial Mechanics and Dynamical Astronomy*, 114(3):229–254.
- Le Maître, O. P. and Knio, O. M. (2010). *Spectral methods for uncertainty quantification: with applications to computational fluid dynamics*. Springer Science & Business Media.
- Leonard, C., Hollister, W., and Bergmann, E. (1989). Orbital formationkeeping with differential drag. *Journal of Guidance, Control, and Dynamics*, 12(1):108–113.

- Lewin, A. W. (1998). Low-cost operation of the orbcomm satellite constellation. *Journal of Reducing Space Mission Cost*, 1(1):105–117.
- Liu, H., Lühr, H., Watanabe, S., Köhler, W., Henize, V., and Visser, P. (2006). Zonal winds in the equatorial upper thermosphere: Decomposing the solar flux, geomagnetic activity, and seasonal dependencies. *J. Geophys. Res.*, 111(A7).
- Liu, J. and West, M. (2001). Combined parameter and state estimation in simulation-based filtering. In *Sequential Monte Carlo Methods in Practice*, pages 197–223. Springer Science + Business Media.
- Loock, W. V., Pipeleers, G., Diehl, M., Schutter, J. D., and Swevers, J. (2014). Optimal path following for differentially flat robotic systems through a geometric problem formulation. *IEEE Transactions on Robotics*, 30(4):980–985.
- Loskutov, A., Istomin, I., Kuzanyan, K., and Kotlyarov, O. (2001). Testing and forecasting the time series of the solar activity by singular spectrum analysis. *Nonlinear Phenomena in Complex Systems*, 4:47–57.
- Louembet, C., Cazaurang, F., and Zolghadri, A. (2010). Motion planning for flat systems using positive b-splines: An LMI approach. *Automatica*, 46(8):1305–1309.
- Louembet, C. and Deaconu, G. (2011). Collision avoidance in low thrust rendezvous guidance using flatness and positive b-splines. *Proceedings of the 2011 American Control Conference*.
- Lubey, D. P. and Scheeres, D. J. (2014). Identifying and estimating mismodeled dynamics via optimal control policies and distance metrics. *Journal of Guidance, Control, and Dynamics*, 37(5):1512–1523.
- Lyddane, R. H. (1963). Small eccentricities or inclinations in the Brouwer theory of the artificial satellite. *The Astronomical Journal*, 68:555 – 558.
- Lévine, J. (2009). Analysis and control of nonlinear systems.
- Marcos, F. (2006). New satellite drag modeling capabilities. In *44th AIAA Aerospace Sciences Meeting and Exhibit*. American Institute of Aeronautics and Astronautics (AIAA).
- Marrel, A., Iooss, B., Laurent, B., and Roustant, O. (2009). Calculations of sobol indices for the gaussian process metamodel. *Reliability Engineering & System Safety*, 94(3):742–751.
- Marriott, F. H. C. and Eaton, M. L. (1984). Multivariate statistics: A vector space approach. *Applied Statistics*, 33(3):319.
- Marti, K. (1999). Path planning for robots under stochastic uncertainty *. *Optimization*, 45(1-4):163–195.

- Martin, P., Murray, R. M., and Rouchon, P. (2003). Flat systems, equivalence and trajectory generation.
- Martinusi, V., Dell'Elce, L., and Kerschen, G. (2015). Analytical propagation for the near-circular satellite motion in the atmosphere of an oblate planet: The case of constant density. *Celestial Mechanics and Dynamical Astronomy*, (in review).
- Martinusi, V., Dell'Elce, L., and Kerschen, G. (2014). Analytic propagation for satellites in near-circular low-earth orbits. In *Proceedings of the AAS/AIAA Astrodynamics Specialist Conference*, San Diego, US.
- Mashiku, A., Garrison, J., and Carpenter, J. R. (2012). Statistical orbit determination using the particle filter for incorporating non-gaussian uncertainties. In *AIAA/AAS Astrodynamics Specialist Conference*. American Institute of Aeronautics and Astronautics (AIAA).
- McCabe, J. S. and DeMars, K. J. (2014). Particle filter methods for space object tracking. In *AIAA/AAS Astrodynamics Specialist Conference*. American Institute of Aeronautics and Astronautics (AIAA).
- Mittleman, D. and Jezewski, D. (1982). An analytic solution to the classical two-body problem with drag. *Celestial Mechanics*, 28:401–413.
- Moe, K. and Moe, M. M. (2005). Gas–surface interactions and satellite drag coefficients. *Planetary and Space Science*, 53(8):793–801.
- Montenbruck, O. and Gill, E. (2000). *Satellite Orbits*. Springer Science + Business Media.
- Muylaert, J. (2012). Call for cubesat proposals for qb50. *Von Karman Institute for Fluid Dynamics*.
- Muylaert, J., Reinhard, R., Asma, C., Buchlin, J., Rambaud, P., and Vetrano, M. (2009). Qb50: an international network of 50 cubesats for multi-point, in-situ measurements in the lower thermosphere and for re-entry research. In *ESA Atmospheric Science Conference, Barcelona, Spain*, pages 7–11.
- Naasz, B. J., Berry, K., and Schatten, K. (2007). Orbit decay prediction sensitivity to solar flux variations. In *Proceedings of the AAS/AIAA Space Flight Mechanics Conference*, number 2007–264.
- Nesterov, Y. (2000). Squared functional systems and optimization problems. In Frenk, H., Roos, K., Terlaky, T., and Zhang, S., editors, *High Performance Optimization*, volume 33 of *Applied Optimization*, pages 405–440. Springer US.
- Ng, A. (2010). Overview of Japan-Canada joint collaboration satellites (jc2Sat) gnc challenges and design. *AIAA Guidance, Navigation, and Control Conference*.

- Øksendal, B. (1992). *Stochastic Differential Equations*. Springer Berlin Heidelberg.
- Oltrogge, D. et al. (2011). An evaluation of cubesat orbital decay. In *25th Annual AIAA/USU Conference on Small Satellites*, number AIAA Paper SSC11-VII-2, Logan.
- Ono, M. and Williams, B. C. (2008). An efficient motion planning algorithm for stochastic dynamic systems with constraints on probability of failure. In *AAAI*, pages 1376–1382.
- Pardini, C., Moe, K., and Anselmo, L. (2012). Thermospheric density model biases at the 23rd sunspot maximum. *Planetary and Space Science*, 67(1):130–146.
- Park, R. S. and Scheeres, D. J. (2006). Nonlinear mapping of Gaussian statistics: Theory and applications to spacecraft trajectory design. *Journal of Guidance, Control, and Dynamics*, 29(6):1367–1375.
- Parks, A. D. (1983). A Drag-Augmented Brouwer-Lyddane Artificial Satellite Theory and Its Application to Long-Term Station Alert Predictions. Technical Report NSWC TR 83-107, Naval Surface Weapons Center, Dahlgren, VA.
- Peck, M., Streetman, B., Saaj, C., and Lappas, V. (2007). Spacecraft formation flying using lorentz forces. *Journal of the British Interplanetary Society*, 60:263–267.
- Pérez, D. and Bevilacqua, R. (2013). Differential drag spacecraft rendezvous using an adaptive lyapunov control strategy. *Acta Astronautica*, 83:196–207.
- Petro, A. J. (1992). Techniques for orbital debris control. *Journal of Spacecraft and Rockets*, 29(2):260–263.
- Picone, J. M. (2002). Nrlmsise-00 empirical model of the atmosphere: Statistical comparisons and scientific issues. *Journal of Geophysical Research*, 107(A12).
- Pilinski, M. D., Argrow, B. M., and Palo, S. E. (2011a). Drag coefficients of satellites with concave geometries: Comparing models and observations. *Journal of Spacecraft and Rockets*, 48(2):312–325.
- Pilinski, M. D., Argrow, B. M., and Palo, S. E. (2011b). Drag coefficients of satellites with concave geometries: Comparing models and observations. *Journal of Spacecraft and Rockets*, 48(2):312–325.
- Pontryagin, L. (1987). *Mathematical Theory of Optimal Processes*. Classics of Soviet Mathematics. Taylor & Francis.
- Prieto, D. M., Graziano, B. P., and Roberts, P. C. (2014). Spacecraft drag modelling. *Progress in Aerospace Sciences*, 64:56–65.

- Ries, J. C., Eanes, R. J., Shum, C. K., and Watkins, M. M. (1992). Progress in the determination of the gravitational coefficient of the earth. *Geophysical Research Letters*, 19(6):529–531.
- Roberts, P. C. E. and Harkness, P. G. (2007). Drag sail for end-of-life disposal from low earth orbit. *Journal of Spacecraft and Rockets*, 44(6):1195–1203.
- Ross, I. and Fahroo, F. (2004). Pseudospectral methods for optimal motion planning of differentially flat systems. *IEEE Trans. Automat. Contr.*, 49(8):1410–1413.
- Ross, I. M., Proulx, R., and Karpenko, M. (2014). Unscented optimal control for orbital and proximity operations in an uncertain environment: A new zermelo problem. *AIAA/AAS Astrodynamics Specialist Conference*.
- Roy, A. (2004). *Orbital Motion*. CRC Press.
- Ruf, C., Gleason, S., Jelenak, Z., Katzberg, S., Ridley, A., Rose, R., Scherrer, J., and Zavorotny, V. (2013). The nasa EV-2 Cyclone global navigation satellite system (cygnss) mission. *2013 IEEE Aerospace Conference*.
- Ryden, K., Fearn, D., and Crowther, R. (1997). Electric propulsion: a solution to end-of disposal of satellites? In *Second European Conference on Space Debris*, volume 393, page 709.
- Saleh, J. H., Hastings, D. E., and Newman, D. J. (2002). Spacecraft design lifetime. *Journal of Spacecraft and Rockets*, 39(2):244–257.
- Saltelli, A., Ratto, M., Andres, T., Campolongo, F., Cariboni, J., Gatelli, D., Saisana, M., and Tarantola, S. (2007). *Global Sensitivity Analysis. The Primer*. Wiley-Blackwell.
- Saunders, A., Swinerd, G. G., and Lewis, H. G. (2012). Deriving accurate satellite ballistic coefficients from two-line element data. *Journal of Spacecraft and Rockets*, 49(1):175–184.
- Schaub, H. (2003). Incorporating secular drifts into the orbit element difference description of relative orbits. *Advances in the Astronautical Sciences*, 114:239–257.
- Schaub, H. and Junkins, J. (2003). *Analytical Mechanics of Space Systems*. AIAA, New York.
- Schaub, H., Vadali, S. R., Junkins, J. L., and Alfriend, K. T. (2000). Spacecraft formation flying control using mean orbit elements. *Journal of the Astronautical Sciences*, 48(1):69–87.
- Scheeres, D. J., Hsiao, F.-Y., Park, R. S., Villac, B. F., and Maruskin, J. M. (2006). Fundamental limits on spacecraft orbit uncertainty and distribution propagation. *The Journal of the Astronautical Sciences*, 54(3-4):505–523.

- Scholz, T., Asma, C. O., and Aruliah, A. (2012). Recommended set of models and input parameters for the simulations of orbital dynamics of the qb50 cubesats. In *Proceedings of the 5th International Conference on Astrodynamics Tools and Techniques*, Noordwijk, The Netherlands.
- Schweighart, S. A. and Sedwick, R. J. (2002). High-fidelity linearized j model for satellite formation flight. *Journal of Guidance, Control, and Dynamics*, 25(6):1073–1080.
- Sentman, L. H. (1961). Free molecule flow theory and its application to the determination of aerodynamic forces. Technical report, DTIC Document.
- Shannon, C. E. (1948). A mathematical theory of communication. *Bell System Technical Journal*, 27(4).
- Silverman, L. (1966). Transformation of time-variable systems to canonical (phase-variable) form. *IEEE Transactions on Automatic Control*, 11(2):300–303.
- Sobol', I. M. (1990). On sensitivity estimation for nonlinear mathematical models. *Matematicheskoe Modelirovanie*, 2(1):112–118.
- Soize, C. (2008). Construction of probability distributions in high dimension using the maximum entropy principle: Applications to stochastic processes, random fields and random matrices. *Int. J. Numer. Meth. Engng*, 76(10).
- Sterne, T. E. (1958). An atmospheric model, and some remarks on the inference of density from the orbit of a close earth satellite. *The Astronomical Journal*, 63:81.
- Storz, M. F., Bowman, B. R., Branson, M. J. I., Casali, S. J., and Tobiska, W. K. (2005). High accuracy satellite drag model (HASDM). *Advances in Space Research*, 36(12):2497–2505.
- Sutton, E. K. (2009). Normalized force coefficients for satellites with elongated shapes. *Journal of Spacecraft and Rockets*, 46(1):112–116.
- Svestka, P. and Overmars, M. H. (1998). Probabilistic path planning. *Lecture Notes in Control and Information Sciences*, page 255–304.
- Tapley, B. D., Neto, A. R., and Schutz, B. E. (1975). Orbit determination in the presence of atmospheric drag errors. *Satellite Dynamics*, page 154–169.
- Tapley, B. D., Schutz, B. E., and Born, G. H. (2004). Fundamentals of orbit determination. *Statistical Orbit Determination*, page 159–284.
- Tschauner, J. and Hempel, P. (1964). Optimale beschleunigungsprogramme fur das rendezvous-manover. *Astronautica Acta*, 10:296–307.

- Vallado, D. et al. (2011). Verifying observational data for real world space situational awareness. In *Proceedings of the AAS/AIAA Astrodynamics Specialist Conference*, number AAS Paper 11-439, Girdwood, US.
- Vallado, D. A. (2001). *Fundamentals of Astrodynamics and Applications*. Microcosm.
- van den Berg, J., Abbeel, P., and Goldberg, K. (2011). Lqg-mp: Optimized path planning for robots with motion uncertainty and imperfect state information. *The International Journal of Robotics Research*, 30(7):895–913.
- Van Nieuwstadt, M. J. and Murray, R. M. (1998). Real-time trajectory generation for differentially flat systems. *Int. J. Robust Nonlinear Control*, 8(11):995–1020.
- Vinh, N. X., Longuski, J. M., Busemann, A., and Culp, R. D. (1979). Analytic theory of orbit contraction due to atmospheric drag. *Acta Astronautica*, 6:697–723.
- Vinti, J. P. (1960). Theory of the Orbit of an Artificial Satellite with Use of Spheroidal Coordinates. *Astronomical Journal*, 65:353–354.
- Watari, S. (1996). Separation of periodic, chaotic, and random components in solar activity. *Solar Physics*, 168(2):413–422.
- Wertz, J. R., editor (1978). *Spacecraft Attitude Determination and Control*. Springer Netherlands.
- Wie, B. (2008). *Space Vehicle Dynamics and Control, Second Edition*. American Institute of Aeronautics and Astronautics (AIAA).
- Williams, T. and Wang, Z.-S. (2002). Uses of solar radiation pressure for satellite formation flight. *International Journal of Robust and Nonlinear Control*, 12(2-3):163–183.
- Winn, C. B. (1975). Optimal estimation of unmodeled accelerations on the ONERA navigational satellite. *Journal of Spacecraft and Rockets*, 12(2):79–82.
- Woodburn, J. and Lynch, S. (2005). A numerical study of orbit lifetime. In *Proceedings of the AAS/AIAA Astrodynamics Specialist Conference*, number AAS 05-297, Lake Tahoe, US.
- Wu, Q., Killeen, T. L., and Spencer, N. W. (1994). Dynamics explorer 2 observations of equatorial thermospheric winds and temperatures: Local time and longitudinal dependences. *Journal of Geophysical Research*, 99(A4):6277.
- Yan, H., Gong, Q., Park, C. D., Ross, I. M., and D’Souza, C. N. (2011). High-accuracy trajectory optimization for a trans-earth lunar mission. *Journal of Guidance, Control, and Dynamics*, 34(4):1219–1227.

- Zeng, G., Hu, M., and Yao, H. (2012). Relative orbit estimation and formation keeping control of satellite formations in low earth orbits. *Acta Astronautica*, 76:164–175.
- Zhang, J., Zhang, K., Grenfell, R., and Deakin, R. (2006). GPS satellite velocity and acceleration determination using the broadcast ephemeris. *J. Navigation*, 59(02):293.
- Zijlstra, M., Theil, S., and Scheithauer, S. (2005). Model for short-term atmospheric density variations. In *Earth Observation with CHAMP*, pages 489–494. Springer Science + Business Media.

List of Journal Publications

- L. Dell'Elce, M. Arnst, and G. Kerschen. Probabilistic Assessment of the Lifetime of Low-Earth-Orbit Spacecraft: Uncertainty Characterization. *Journal of Guidance, Control, and Dynamics*, in press, 2014. DOI: 10.2514/1.G000148.
- L. Dell'Elce and G. Kerschen. Probabilistic Assessment of the Lifetime of Low-Earth-Orbit Spacecraft: Uncertainty Propagation and Sensitivity Analysis. *Journal of Guidance, Control, and Dynamics*, in press, 2014. DOI: 10.2514/1.G000149.
- L. Dell'Elce and G. Kerschen. Optimal propellantless rendez-vous using differential drag. *Acta Astronautica*, 109:112–123, 2015. DOI: 10.1016/j.actaastro.2015.01.011.

Under review:

- V. Martinusi, L. Dell'Elce, and G. Kerschen. Analytical propagation for the near-circular satellite motion in the atmosphere of an oblate planet: The case of constant density. *Celestial Mechanics and Dynamical Astronomy*, in review.
- L. Dell'Elce, O. Brüls, and G. Kerschen. Chance-constrained trajectory planning of differentially flat systems. *Automatica*, in review.

List of Conference Publications

- V. Martinusi, L. Dell'Elce, and G. Kerschen. Analytic solution for the relative motion of satellites in near-circular low-Earth orbits. In *Proceedings of the 25th AAS/AIAA Space Flight Mechanics Meeting*, Williamsbug, Virginia, US, 2015.
- L. Dell'Elce, V. Martinusi, and G. Kerschen. Robust optimal rendezvous using differential drag. In *Proceedings of the 2014 AIAA/AAS Astrodynamics Specialist Conference*, San Diego, California, US, 2014.
- V. Martinusi, L. Dell'Elce, and G. Kerschen. Analytic Propagation for Satellites in Near-Circular Low-Earth Orbits. In *Proceedings of the 2014 AIAA/AAS Astrodynamics Specialist Conference*, San Diego, California, US, 2014.
- L. Dell'Elce and G. Kerschen. Validation of differential drag propellantless maneuvers using 6 DoF simulations and stochastic dynamics. In *Proceedings of the 5th International ESA Conference on Guidance Navigation & Control*, Porto, Portugal, 2014.
- L. Dell'Elce and G. Kerschen. Robust rendez-vous planning using the scenario approach and differential flatness. In *Proceedings of the 2nd IAA Conference on Dynamics and Control of Space Systems*, Rome, Italy, 2014.
- V. Martinusi, L. Dell'Elce, and G. Kerschen. Analytic Model for the Motion about an Oblate Planet in The Presence of Atmospheric Drag. In *Proceedings of the 2nd IAA Conference on Dynamics and Control of Space Systems*, Rome, Italy, 2014.
- L. Dell'Elce and G. Kerschen. Uncertainty quantification of the orbital lifetime of a LEO spacecraft. In *Proceedings of the 2013 AAS/AIAA Astrodynamics Specialist Conference*, Hilton Head, South Carolina, US, 2013.
- L. Dell'Elce and G. Kerschen. Comparison between analytical and optimal control techniques in the differential drag based rendez-vous. In *Proceedings of the 5th International Conference on Spacecraft Formation Flying Missions & Technologies*, Munich, Germany, 2013.

- L. Dell'Elce, G. Kerschen, T. Delabie, D. Vandepitte, K. Fleury-Frenette, J.H. Lecat, T. Walewyns, and L.A. Francis. Scientific and Technological Payloads Aboard the B3LSat CubeSat of the QB50 Network. In *Proceedings of the 2nd IAA Conference on University Satellite Missions and CubeSat Workshop*, Rome, Italy, 2012.
- L. Dell'Elce and G. Kerschen. Propellantless rendez-vous of QB50 nanosatellites. In *Proceedings of the 63rd International Astronautical Congress*, Naples, Italy, 2012.
- L. Dell'Elce and G. Kerschen. Orbital rendez-vous using differential drag in the QB50 constellation. In *Proceedings of the 2013 AIAA/AAS Astrodynamics Specialist Conference*, Minneapolis, Minnesota, US, 2012.